Probing the gravitational potential of Sagittarius A* with stars and flares

Antonia Drescher

München 2025

Probing the gravitational potential of Sagittarius A* with stars and flares

Antonia Drescher

Dissertation
der Fakultät für Physik
der Ludwig-Maximilians-Universität
München

vorgelegt von
Antonia Drescher
aus München

München, den 10.06.2025

Erstgutachter: Professor Dr. Reinhard Genzel
Zweitgutachterin: Professor Dr. Barbara Ercolano
Tag der mündlichen Prüfung: 24.07.2025

Contents

List of Figures

List of Tables

Zusammenfassung

Im Zentrum unserer Milchstraße liegt das supermassereiche Schwarze Loch, Sagittarius A*. Mit einer Entfernung von 8276 Parsek und einer Masse von 4,3 Millionen Sonnenmassen ist es das zu uns nächste supermassereiche Schwarze Loch. Alte und junge Sterne sowie verschiedene Gasströme umgeben Sagittarius A* und bilden ein komplexes System, das ein einzigartiges Labor für die Erforschung astrophysikalischer Prozesse darstellt. Das Verfolgen von Sternen und heißem Gas auf ihren Umlaufbahnen um Sagittarius A* bietet die außergewöhnliche Möglichkeit, die Allgemeine Relativitätstheorie in der Nähe eines massiven Schwarzen Lochs zu testen und das starke Gravitationspotential zu untersuchen. Mit dem GRAVITY Interferometer am Very Large Telescope in Chile können wir solche Tests durchführen. In dieser Dissertation stelle ich GRAVITY-Beobachtungen von Sternen und Flares, die Sagittarius A* umkreisen, sowie die Entwicklung eines neuen Beobachtungsmodus namens GRAVITY Wide vor.

In Kapitel 2 präsentiere ich hochauflösende Bilder von Sternen im galaktischen Zentrum, die aus Daten vom Jahr 2021 rekonstruiert wurden. Die Bildgebung der inneren 100 Millibogensekunden um Sagittarius A* ist wichtig, um die Bahnen bekannter Sterne zu vermessen und auch um neue Sterne auf stark exzentrischen und kurzperiodischen Umlaufbahnen zu finden. Diese Sterne könnten helfen, den Spin von Sagittarius A* zu messen und somit höhere Effekte der Allgemeinen Relativitätstheorie. Die Bilder wurden mit einer neuen Analysemethode rekonstruiert und zeigen die bekannten Sterne S29, S55, S62, S38, S42, S60 und S63. Zusätzlich enthüllen die bisher tiefsten Bilder des galaktischen Zentrums einen bisher unbekannten, dunklen Stern mit einer Helligkeit von $m_K \simeq 19{,}0$–$19{,}3$, der sich mit hoher Geschwindigkeit nach Westen bewegt. Wir nennen diesen Stern S300. Zusätzlich zeige ich mit dem CLEAN-Algorithmus rekonstruierte Bilder, die die Entdeckung von S300 bestätigen. Abschließend schätzen wir, dass die neue Bildgebungsmethode in der Lage ist, Sterne mit einer Helligkeit von nur $m_K \sim 20$ zu finden. Dies ermöglicht eine verbesserte Charakterisierung des Gravitationspotentials um Sagittarius A*.

In Kapitel 3 stelle ich astrometrische und polarimetrische Beobachtungen von Flares vor, dem plötzlichen Anstieg der Helligkeit von Sagittarius A*. Flares modellieren wir als relativistisches Gas, das um Sagittarius A* kreist. Zwischen 2018 und 2022 haben wir vier astrometrischen und sechs polarimetrischen Flares beobachtet, die alle ein ähnliches Verhalten aufzeigen: eine Bewegung im Uhrzeigersinn, mit einem ähnlichen Radius und einer ähnlichen Umlaufzeit. Darüber hinaus messen wir eine Polarisationsumdrehung pro astrometrischer Umdrehung. Die Ähnlichkeiten unter den Flares erlauben es uns, sie zu

kombinieren und gemeinsam zu analysieren. Der kokmbinierte Datensatz zeigt die Bewegung von heißem Gas um Sagittarius A* auf einem Radius von etwa neun Gravitationsradien (R_g). Des Weiteren messen wir eine überwiegend vertikale Magnetfeldkonfiguration, eine niedrige Inklination und einen Positionswinkel, der mit der Ausrichtung einer stellaren Scheibe junger Sterne übereinstimmt, die sich im Uhrzeigersinn um Sagittarius A* dreht. Dies lässt uns schließen, dass die Winde der massereichen jungen Sterne in der Scheibe den Akkretionsstrom von Sagittarius A* antreiben. Abschließend zeige ich, dass die Masse von Sagittarius A* innerhalb des Flare Radius mit der Masse übereinstimmt, die mit Sternbahnen bei mehreren tausend R_g gemessen wurde.

Kapitel 4 befasst sich mit Beobachtungen von Sternen in den inneren 400 Millibogensekunden von Sagittarius A*, den sogenannten S-Sternen, die von 2017 bis 2025 mit GRAVITY beobachtet wurden. Die hohe Präzision von GRAVITY ermöglicht es, Sternpositionen mit einer Genauigkeit von einigen zehn Mikrobogensekunden zu messen und dadurch präzise Umlaufbahnen zu bestimmen. Ich beschreibe die Beobachtungsstrategie, die instrumentellen Upgrades sowie die Methoden, mit denen wir die Positionen der S-Sterne relativ zu Sagittarius A* bestimmen. Außerdem präsentiere ich aktualisierte Umlaufbahnen von 11 S-Sternen aus unserer Beobachtungskampagne von insgesamt 15 S-Sternen. Wir stellen fest, dass einzelne Parameter um bis zu einen Faktor von über 1000 besser bestimmt sind im Vergleich zu früheren Messungen mit adaptiver Optik an einzelnen 8 m Teleskopen. Wir untersuchen die Verteilung der Bahnelemente, die Rückschlüsse auf den Ursprung der S-Sterne zulassen könnten. Von insgesamt 41 Sternen, darunter 30 mit bereits bekannten Bahnlösungen, stellen wir fest, dass die meisten Sterne zufällig orientiert sind, im Einklang mit früheren Studien, während eine kleine Untergruppe Teil der im Uhrzeigersinn rotierenden Scheibe junger Sterne ist. Darüber hinaus sind die Exzentrizitätsverteilungen von 22 frühen und 7 späten S-Sternen konsistent mit einer thermischen Verteilung. Dies kann darauf hindeuten, dass die Entstehung der S-Sterne den Hills Mechanismus beinhaltet, bei dem Sterne anfänglich auf stark exzentrische Bahnen gebracht werden und deren Bahnen sich anschließend durch resonante Relaxation weiterentwickeln.

In Kapitel 5 stelle ich das Design und die ersten Ergebnisse von GRAVITY Wide vor, einem neuen Beobachtungsmodus innerhalb des GRAVITY+ -Projekts. GRAVITY Wide erweitert die Himmelsbedeckung von GRAVITY um zwei Größenordnungen, indem es den Abstand zwischen dem beobachteten Objekt und dem Phasenreferenzstern vergrößert. GRAVITY Wide ermöglicht die Messung der Masse Schwarzer Löcher in aktiven Galaxienkernen bei Rotverschiebung ~ 2, was entscheidend für unser Verständnis der Koevolution supermassereicher Schwarzer Löcher und ihrer Heimatgalaxien ist. Ich untersuche außerdem den Kohärenzverlust des beobachteten Objekts bei zunehmendem Abstand zum Phasenreferenzstern und stelle fest, dass dieser gut durch atmosphärische Turbulenzen beschrieben wird. Diese Erkenntnisse wurden seit der Inbetriebnahme von GRAVITY Wide im Jahr 2022 erfolgreich in der Beobachtungsplanung angewendet und verdeutlichen das Potenzial dieses Modus, unser Wissen über lichtschwache Objekte, insbesondere extragalaktische Objekte, zu erweitern.

Im letzten Kapitel, Kapitel 6, fasse ich die wichtigsten Ergebnisse und Schlussfolgerungen dieser Arbeit zusammen und gebe einen kurzen Ausblick in die Zukunft.

Summary

The Milky Way's central supermassive black hole, Sagittarius A*, is the closest to Earth, located 8276 parsecs away with a mass of 4.3 million solar masses. Old and young stars and different gas streamers surround Sagittarius A*, forming a complex system that provides a unique laboratory for studying astrophysical processes. Tracing the motions of stars and hot gas around Sagittarius A* offers the unique possibility to test General Relativity near a massive black hole and to study the strong gravitational potential. The near-infrared beam combiner GRAVITY at the Very Large Telescope Interferometer in Chile makes such tests possible. In this thesis, I present GRAVITY observations of stars and flares orbiting Sagittarius A* in the Galactic Center and the development of a new observing mode within the GRAVITY+ project.

In Chapter 2, I present deep images of stars in the Galactic Center reconstructed from 2021 GRAVITY data. Imaging the inner 100 milli-arcseconds around Sagittarius A* is essential to trace known stars on their orbits and search for faint, unknown stars on highly eccentric, short-period orbits. These stars could help detect the black hole's spin, thus measuring higher-order effects of General Relativity. The images are reconstructed with a newly developed imaging tool, G^R, and the known stars S29, S38, S42, S55, S60, S62, and S63 are detected. Additionally, the to-date deepest images of the Galactic Center reveal a previously unknown, faint star with a magnitude of $m_K \simeq 19.0$–19.3, which moves to the West at high angular velocity. We call the new star S300. I reconstruct images using the CLEAN algorithm and use these images to provide a crucial, independent perspective on the data. The CLEAN images clearly show all known stars listed above and S300, confirming the detection of the new star. Finally, we estimate the new imaging code to be able to detect stars as faint as $m_K \approx 20$, thereby opening up the possibility of finding even more stars and enabling an improved characterization of the gravitational potential around Sagittarius A*.

In Chapter 3, I present astrometric and polarimetric observations of flares, the sudden increase in Sagittarius A*'s near-infrared emission, modeled as an orbiting relativistic hot spot around a non-spinning black hole. Our observations of four astrometric and six polarimetric flares between 2018 and 2022 reveal a consistent behavior: a clockwise looped motion in the sky on a similar radius and a period of around an hour. Further, we measure one polarization loop per astrometric loop. The similarities between the flares allow us to combine and fit them together. The combined fit reveals orbiting hot spots on a radius of around nine gravitational radii, consistent with Keplerian motion close to the innermost

stable circular orbit. Further, we find a predominantly vertical magnetic field configuration, a close-to-face-on inclination, and a position angle consistent with the orientation of the inner clockwise disk of young stars. These results suggest that the winds of the massive young stars in the disk fuel the accretion flow. Finally, we show that the mass of Sagittarius A* measured within the flare radius is consistent with the mass measured from stellar orbits at several thousand gravitational radii.

Chapter 4 is dedicated to observations of stars in the inner 400 milli-arcseconds of Sagittarius A*, called S-stars, conducted with GRAVITY from 2017 to 2025. GRAVITY's high precision allows us to measure stellar positions down to 30 micro-arcseconds, enabling precise determinations of stellar orbits. I describe the observing strategy, instrumental upgrades, and analysis techniques used to obtain the astrometric separations between the stars and Sagittarius A* and present updated orbital solutions for 11 stars from our monitoring campaign of 15 stars. We improve orbital parameter precision by factors ranging from 3 to more than 1000 compared to earlier single 8 m-class adaptive optics measurements. We further analyze the distribution of orbital parameters, which may contain information about the still unresolved origin of the S-stars. Based on a sample of 41 stars, including 30 stars with previously known orbits, we find that most stars are randomly oriented, consistent with earlier findings, while a small subset is part of the clockwise stellar disk. In addition, the eccentricity distributions of 22 early-type and seven late-type stars are consistent with a thermal distribution. This hints towards a formation scenario involving the Hills mechanism, where stars are initially placed on highly eccentric orbits, with subsequent evolution of their orbits through resonant relaxation.

In Chapter 5, I introduce the design and first results of GRAVITY Wide, a new observing mode developed as part of the GRAVITY+ project. GRAVITY Wide significantly enhances the sky coverage of GRAVITY by two orders of magnitude by increasing the separation between the science object and the phase reference star from 2 arcseconds up to 30 arcseconds. GRAVITY Wide enables the measurement of black hole masses in active galactic nuclei at redshift $z \sim 2$, which is crucial to advance our understanding of the co-evolution of supermassive black holes and their host galaxies. One of the targets observed for on-sky verification of GRAVITY Wide was the Orion Trapezium Cluster, where I determined the positions and orbits of three multiple-star systems in the cluster. Further, I investigate the coherence loss of the science target for increasing separations to the phase reference star, finding that it is well described by atmospheric turbulence and anisoplanatism. These findings have been successfully applied to observation planning since GRAVITY Wide's commissioning in 2022, demonstrating the mode's potential to expand our knowledge of faint targets, especially the extragalactic sky.

In the final chapter, Chapter 6, I summarize this thesis's key findings and conclusions and provide a brief forward look.

Chapter 1

Introduction

1.1 The Galactic Center black hole Sagittarius A*

Today, we know that black holes are ubiquitous across the Universe and that supermassive black holes reside in the centers of most galaxies. The closest supermassive black hole to Earth lies in the center of our own Galaxy and is called Sagittarius A* (Sgr A*). At a distance of 8.276 kilo-parsec (kpc) and with a mass of $4.2996 \times 10^6 M_\odot$ (Gravity Collaboration et al., 2024), Sgr A* is surrounded by a dense star cluster and different components of gas. The central 1.5 pc of the Milky Way contain a complex system of ionized gas streamers, known as the *minispiral*, which orbits Sgr A* (Lo and Claussen, 1983). The minispiral, on the other hand, is surrounded by the *circumnuclear disk*, a rotating, clumpy ring of dense molecular gas, extending from 1.5 pc to about 4 pc (Becklin et al., 1982; Guesten et al., 1987; Jackson et al., 1993; Christopher et al., 2005; Genzel et al., 2010). The first time similar systems like black holes were noted was at the end of the 18th century when Michell (1784) and Laplace (1795) proposed "dark stars," extremely compact, massive stars with surface escape velocities surpassing the speed of light. In 1915, Albert Einstein postulated his theory of General Relativity (GR; Einstein, 1916), presenting the interaction between matter, space, and time. GR describes gravity between two bodies as a result of the curvature of spacetime around these bodies. One year later, in 1916, Karl Schwarzschild (Schwarzschild, 1916) found an exact solution to the Einstein field equations for a spherically symmetric spacetime. The solution predicts that an extremely compact mass can curve spacetime such that a region is formed inside which gravity is so strong that nothing, not even light, can escape. This boundary of no escape is called the *event horizon*. Furthermore, a black hole contains a *singularity* at its center, a point where density is infinite and time ends. In the following century, astronomers collected more and more BH candidates until we ultimately had experimental evidence that BHs exist in the Universe. In 2020, the Nobel Prize in Physics was awarded to Reinhard Genzel and Andrea Ghez *"for the discovery of a supermassive compact object at the centre of our galaxy".*

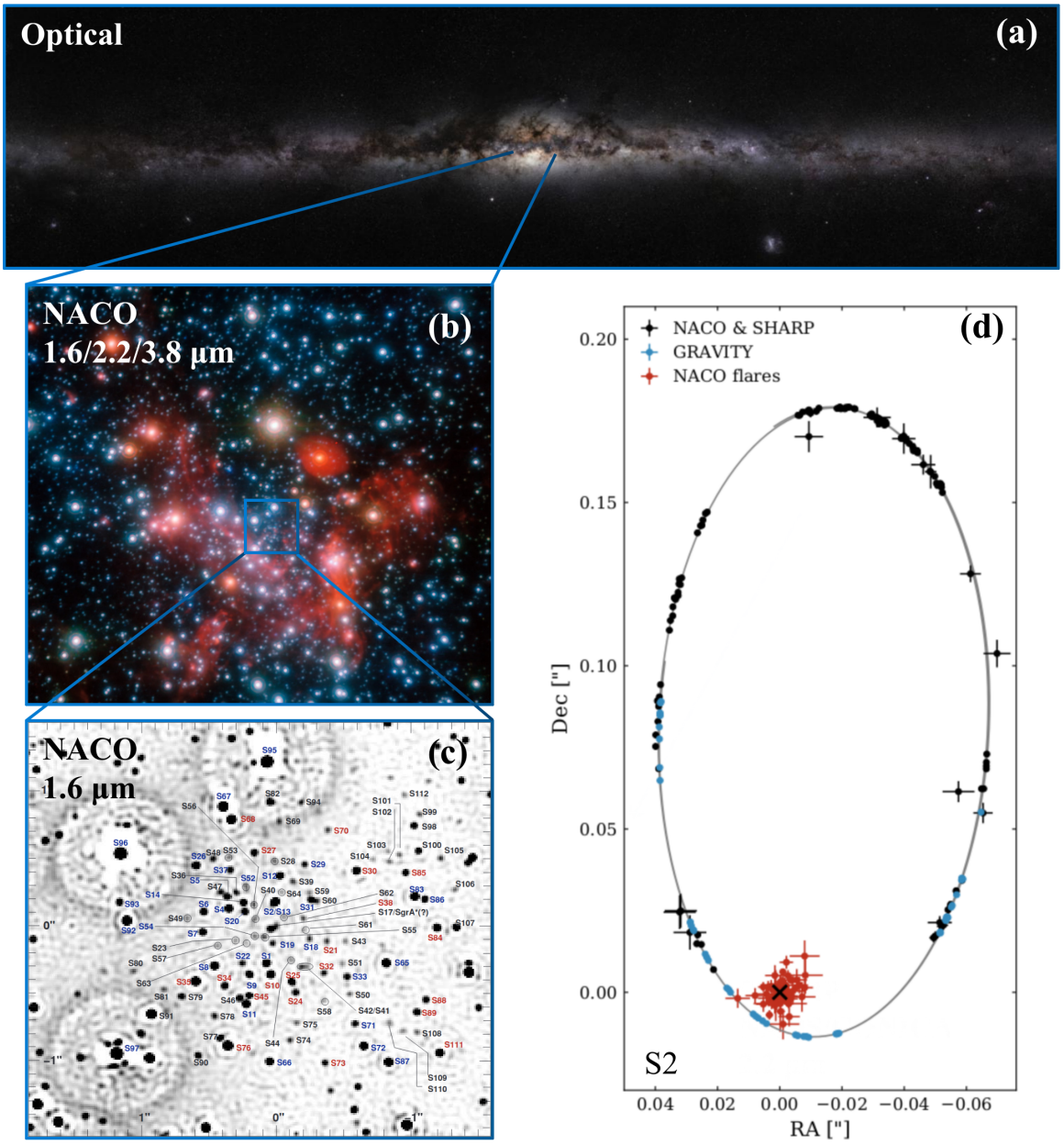

Figure 1.1: A zoom into the Galactic Center. (a) Image of the Galactic plane as seen in the optical. Interstellar dust particles obscure the center of the Milky Way. Credit: ESO/S. Brunier. (b) Three-color image of the central parts of our Galaxy as observed in the near-infrared with the NACO instrument at the VLT. Credit: ESO/S. Gillessen et al. (c) Image of the S-star cluster in the inner 1.5 arcseconds of Sgr A* as observed in the H-band with NACO at the VLT. S-stars as faint as $m_K = 17.7$ are detected and labeled as S1 to S112. Early-type stars are indicated in blue, late-type stars in red, and stars of unknown spectral type in black. Image from Gillessen et al., 2009. (d) The orbit of the star S2 around the black hole Sgr A*. Figure from GRAVITY Collaboration et al., 2020c.

1.1.1 Observations of Sagittarius A*

The discovery of distant "star-like objects" (distant, luminous quasars) by Schmidt, 1963 provided the first astronomical evidence for the existence of black holes. Building on this discovery, Lynden-Bell, 1969 and Rees, 1984 proposed that the powerful emission from centers of galaxies can only come from accreting black holes. Further, Lynden-Bell, 1969 and Lynden-Bell and Rees, 1971 even proposed that most galactic nuclei, including the Galactic Center, harbor massive black holes. Since the most central parts of our Galaxy are obscured by interstellar dust particles in the Galactic plane, it is not possible to observe the Galactic Center in the visible part of the electromagnetic spectrum (see Fig. 1.1 (a)). However, the dust becomes transparent when switching to longer wavelengths, i.e., the infrared, microwave, and radio bands, and shorter wavelengths, i.e., the hard X-ray and γ-ray bands. As a result, astronomers began using and developing telescopes and observational techniques that could peer through the dust and observe the Galactic Center in these wavelengths, thereby enabling the search for a central black hole.

In the early 1970s, Balick and Brown, 1974 detected a bright, compact radio source in the innermost region of our Galaxy. This further supported the idea of a massive black hole in galactic centers. In the late 1970s and early 1980s, the group of Charles Townes detected increasing radial velocities of ionized gas components in the innermost parsec of the Milky Way (Wollman et al., 1977). Analyzing the motion and distribution of the ionized gas, they concluded that the inner parsec of our Galaxy must contain a central point-like mass of $\sim 3 \times 10^6 M_\odot$ (Lacy et al., 1980) and that this object must be a black hole (Lacy et al., 1982). Throughout the 1980s, the case for a central mass concentration continued to improve. Crawford et al., 1985 observed the ionized gas streamers in the central 10 pc with near-infrared and sub-millimeter spectroscopy and found that the mass distribution in the Galactic Center would be consistent with a point mass of $\sim 4 \times 10^6 M_\odot$, or a point mass surrounded by a stellar cluster. Genzel and Townes, 1987 reviewed and discussed observations and theoretical models of the Galactic Center. They found the case for a black hole in the center of our Galaxy "substantial but not fully convincing," as physical forces other than gravity could cause the observed gas dynamics.

Further progress came in the 1990s from observations of stellar motions by two different groups. Eckart and Genzel, 1996 and Eckart and Genzel, 1997 used near-infrared speckle imaging at the 3.5 m New Technology Telescope (NTT) of the European Southern Observatory (ESO) in Chile to determine proper motions of stars in the inner 0.4 parsec of the Galactic Center. They find strong evidence for a central mass of $\sim 2.45 \times 10^6 M_\odot$, suggesting that the object is a massive black hole. Ghez et al., 1998 improved and supported these observations using the W. M. Keck 10 m telescope. Ghez et al., 2000 determined the acceleration of stars in their orbits around the central mass, in particular of three stars, which could have orbital periods as short as 15 years, making it possible to observe an entire orbit in the near future. Both groups concluded that the center of our galaxy harbors a massive black hole of several million solar masses. Further, Very Long Baseline Array (VLBI) measurements of the radio source Sgr A* showed only a little motion of the source itself with respect to extragalactic sources (Reid and Brunthaler, 2004; Reid, 2009),

providing observational evidence that the mass of Sgr A* is $4 \times 10^6 M_\odot$ and is enclosed within a radius of 100 AU.

The two groups reached diffraction-limited imaging through the implementation of adaptive optics (AO) at the VLT (Rousset et al., 2003) and Keck observatory (Wizinowich et al., 2000). This allowed individual stellar orbits close to the massive black hole to be determined at the highest angular resolution possible until then (see Fig. 1.1 (b) and (c)). The next breakthrough came with AO-supported spectroscopy, which allows the measurement of radial velocities of the stars around Sgr A*. Long slit spectroscopy was used at the Keck telescope (Ghez et al., 2003) and especially integral field spectroscopy at the VLT (Eisenhauer et al., 2003) revolutionized the exploration of the innermost stars through radial velocity measurements. Ultimately, the final evidence came from determining the first complete orbit solution of a star close to Sgr A*, the star S2, combining spectroscopy and astrometry (Schödel et al., 2002). Observations of both pericenter and apocenter passage revealed a star on a highly elliptical orbit, with a pericenter distance of 17 light hours and a period of 15.2 years. The best-fit orbit requires a central point mass of $(3.7 \pm 1.5) \times 10^6 M_\odot$, making it highly plausible that the center of our galaxy harbors a supermassive black hole: Sgr A* (Schödel et al., 2002; Ghez et al., 2003; Ghez et al., 2005; Eisenhauer et al., 2005). This groundbreaking discovery has been further refined through ongoing observations of S2 (see Fig. 1.1 (d)) and other stars closely orbiting Sgr A*, as stars provide the unique opportunity to test the massive black hole paradigm within the strong gravitational potential of the central black hole.

1.1.2 The S-star cluster

The nuclear star cluster at the center of the Milky Way has been extensively studied through photometry, imaging, and spectroscopy. The first near-infrared observations of the cluster were made by Becklin and Neugebauer, 1968, who later identified many bright stars in the region (Becklin and Neugebauer, 1975). Further studies by Becklin et al., 1978 revealed that some of these stars are older, late-type (red) giants or supergiants, such as the star IRS 7, based on photometric and spectrophotometric analysis. Higher angular resolution observations have since shown that many of the bright stars in the cluster are actually massive, hot early-type stars (Allen et al., 1990; Krabbe et al., 1991; Krabbe et al., 1995; Blum et al., 1995; Genzel et al., 1996; Tamblyn et al., 1996; Paumard et al., 2001; Paumard et al., 2006). These stars include blue supergiants and Wolf-Rayet stars with zero-age main-sequence (ZAMS) masses of up to $\sim$100 $M_\odot$ (Krabbe et al., 1995; Najarro et al., 1997), as well as giant main-sequence O and B-type stars (Paumard et al., 2006; Bartko et al., 2009; Bartko et al., 2010). The formation history of these massive stars has been investigated by several studies. Krabbe et al., 1995 found that the stars formed in a burst of star formation approximately 3–7 Myr ago. This finding was later confirmed by Paumard et al., 2006 and Bartko et al., 2010, who estimated a common age of $\sim$6 Myr for the stars.

Measurements from stellar kinematics in the central few arcseconds of Sgr A* have revealed that the massive, young stars reside in two moderately thin disks (Genzel et al.,

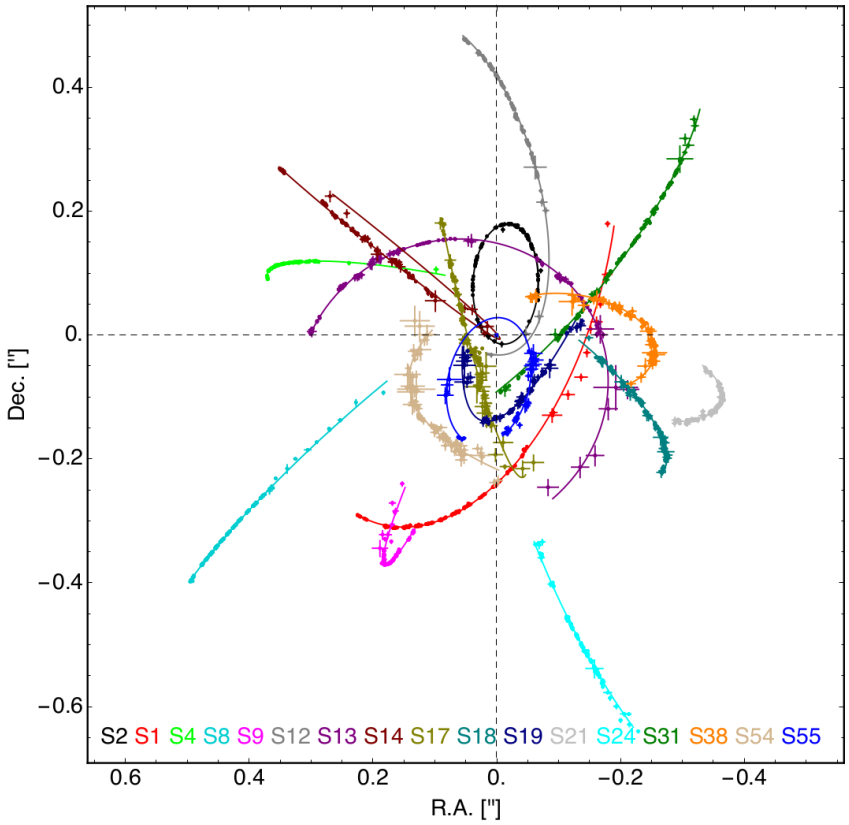

Figure 1.2: Orbits of 17 stars in the inner 500 milli-arcseconds of Sgr A*. The stars belong to the "S-star cluster", a compact cluster of mainly older, B-type stars in the central arcsecond of Sgr A*. The stars are on preferably high eccentricity and randomly oriented orbits. Figure taken from Gillessen et al., 2017.

2000; Levin and Beloborodov, 2003; Paumard et al., 2006; Genzel et al., 2003b; Lu et al., 2006; Lu et al., 2009; Bartko et al., 2009; Yelda et al., 2014). One disk rotates in a clockwise direction and appears to lie inside the other disk, which rotates in a counterclockwise direction. A recent spectroscopic survey of over 2800 stars within a $\sim 30 \times 30$ arcseconds region (von Fellenberg et al., 2022) has confirmed the existence of the clockwise disk and revealed a previously reported warp in the disk‘. Further, the authors confirmed the counterclockwise disk at larger distances from Sgr A*and discovered two new overdensities. It is now understood that the stars formed *in situ* within at least one self-gravitating massive gaseous disk (Bonnell and Rice, 2008; Hobbs and Nayakshin, 2009; von Fellenberg et al., 2022). The disk is thought to have formed from an infalling giant molecular cloud of $\sim 10^5\ M_\odot$ that interacted with Sgr A* a few million years ago. As the disk became bound to the black hole, fragmentation started, and the temperature of the gas increased, leading to the formation of relatively massive stars.

In the central arcsecond of Sgr A*, the stellar landscape yet takes a new turn. A compact cluster of mainly B-type stars with masses ranging from $\simeq$ 3.5 to 20 $M_\odot$ is

found to reside in this region (Genzel et al., 2010; Habibi et al., 2017). This central concentration of stars is known as the *S-star cluster* (Eckart and Genzel, 1996). The S-stars are characterized by their highly eccentric and randomly oriented orbits (see Fig. 1.2, Gillessen et al., 2009; Gillessen et al., 2017). To date, more than 200 S-stars have been identified, with some of them having well-determined individual orbits, such as the well-known star S2 (Ghez et al., 1998; Ghez et al., 2005; Gillessen et al., 2009; Gillessen et al., 2017). The faintest S-star known to date is S301, with a magnitude of $m_K \approx 19.0 - 19.5$. It was identified using an updated version of the imaging code G^R, based on the G^R imaging tool presented in Chapter 2. The detection and orbital motion of S301 is currently being analyzed and prepared for publication (GRAVITY Collaboration et al., 2025, in prep.). The GRAVITY interferometer has enabled the precise measurement of S-star positions, and thus their orbits, with a level of accuracy that is unmatched by any previous instrument. By monitoring these stars over several years, particularly during their pericenter passage, it is possible to determine the mass of and distance to Sgr A* with high precision. The most recent and accurate values for these parameters come from a combined fit of the four S-stars S2, S29, S38, and S55 and yield (Gravity Collaboration et al., 2024):

$$R_0 = (8275.9 \pm 8.6)\ \text{pc} \tag{1.1}$$

$$M_\bullet = (4.2996 \pm 0.0118) \times 10^6 M_\odot\ . \tag{1.2}$$

Finally, the presence of young stars in the Galactic Center is puzzling. How could they form in the strong gravitational field around the black hole, as the strong tidal forces of Sgr A* should suppress star formation? Or were the stars formed further out and subsequently transported to the center? This paradox, known as the *paradox of youth*, has been the subject of ongoing debate. One possible scenario is the Hills-mechanism (Hills, 1988), in which a tightly bound binary interacts with the massive black hole and gets disrupted. One member becomes bound to the black hole, while the other is being ejected at high velocity.

1.1.3 Testing General Relativity in the Galactic Center

Observing stars orbiting Sgr A* offers the unique possibility of testing General Relativity near a massive black hole. One star, S2, is particularly interesting for these tests. S2 is a massive B-type star with an apparent magnitude of $m_K \approx 14$ in the astronomical K-band (Martins et al., 2008) and belongs to the S-star cluster. It is on a highly elliptical orbit with an eccentricity of $e = 0.88$ and a period of about 16 years. The star passed its most recent pericenter in May 2018 at a distance of about 17 light hours, or approximately 1400 Schwarzschild radii, R_S (GRAVITY Collaboration et al., 2018b; Gravity Collaboration et al., 2024).

S2 has been observed for more than three decades, making it an ideal probe for testing General Relativity by measuring deviations from a Keplerian orbit in the data. The implementation of the GRAVITY interferometer at the Very Large Telescope Interferometer (VLTI) in Chile (GRAVITY Collaboration et al., 2017) was crucial for the next breakthrough to come. GRAVITY combines the light from four 8 m Unit Telescopes at the

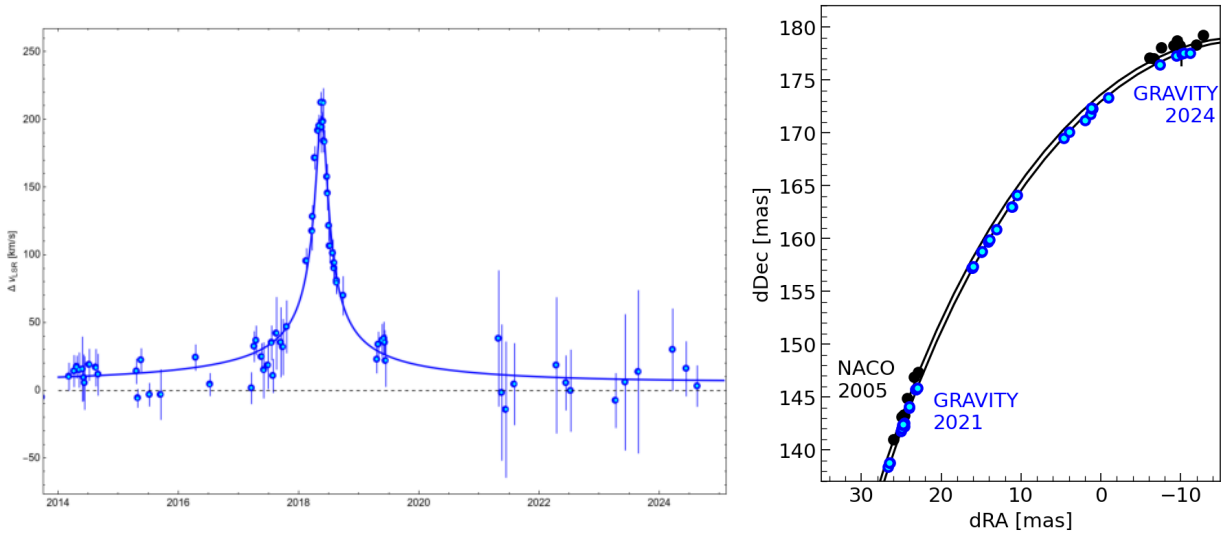

Figure 1.3: Testing General Relativity in the orbit of the star S2. *Left*: Detection of the gravitational redshift using spectroscopic data from SINFONI and ERIS. The horizontal grey line corresponds to a Keplerian orbit. The blue line represents a GR orbit. The measurements (blue circles) around the pericenter of S2 fall on the predicted GR orbit, excluding pure Newtonian dynamics in the S2 data. Figure adapted from Genzel et al., 2024. *Right*: Detection of the Schwarzschild precession using astrometric data from NACO (black) and GRAVITY (blue). We measure a prograde in-plane precession of 12.1' in the orbit of S2 in clockwise direction, consistent with a GR orbit. Figure adapted from GRAVITY Collaboration et al., 2022.

VLTI, achieving a resolution of about 3 milli-arcseconds and an astrometric precision of a few tens of micro-arcseconds. This enables the disentanglement of Sgr A* from the surrounding stars, allowing for precise orbit determination and the observation of the position and emission of Sgr A* itself at almost all times.

The first effect predicted by General Relativity that we were able to detect is the gravitational redshift. This effect stretches the observed light emitted by a star to longer wavelengths, λ, as the star moves through the strong gravitational field of the black hole. We detected the gravitational redshift together with the transverse Doppler effect, predicted by Special Relativity. The combination of the two effects gives a contribution to the redshift of $z = \Delta\lambda/\lambda \approx 200$ (km s^{-1})/c, where c is the speed of light (see Fig. 1.3 left). If the total redshift z_{tot} is separated into a Newtonian/Keplerian part z_K and a relativistic correction, one can write $z_{tot} = z_K + f(z_{GR} - z_K)$, where f corresponds to zero for a purely Keplerian orbit and one for a relativistic orbit. In 2018, S2 data from mainly SINFONI, NACO, and GRAVITY at the VLT(I) enabled the detection of the gravitational redshift with a measurement of $f = 0.90 \pm 0.09|_{stat} \pm 0.15|_{sys}$ (GRAVITY Collaboration et al., 2018b). In 2019, the detection was confirmed using data from the Keck telescope, with a measurement of $f = 0.88 \pm 0.17$ (Do et al., 2019a). In 2020, the significance was

improved to 20σ through the addition of astrometric data points from GRAVITY, with a measurement of $f = 1.04 \pm 0.05$ (GRAVITY Collaboration et al., 2019a).

Due to GRAVITY's high precision, it is also possible to detect another effect predicted by General Relativity, the Schwarzschild precession, which is a prograde in-plane precession of the orbit of $\delta\phi = (3\pi R_S)/(a(1-e^2))$, where a is the semi-major axis and e the eccentricity of the orbit. For S2, this corresponds to a shift of $\sim$ 12.1 arcmin in clockwise direction (see Fig.1.3 right, GRAVITY Collaboration et al., 2020c). Assuming that the observed precession is $f_{SP} \times \delta\phi$, f_{SP} is equal to one for a relativistic orbit and zero for a Keplerian closed orbit. GRAVITY Collaboration et al., 2020c found a value of $f_{SP} = 1.10 \pm 0.19$ fitting the S2 data up to 2019. Using GRAVITY data up to 2022, Genzel et al., 2024 improved the measurement to $f_{SP} = 1.2 \pm 0.1$.

Furthermore, the orbits of S-stars, and, in particular, S2, can be used to constrain any extended mass distribution around Sgr A* (GRAVITY Collaboration et al., 2022), as any extended mass would cause a retrograde precession in the star's orbits. A multi-star fit using astrometric and spectroscopic data from S2, S29, S38, and S55 limits any extended mass surrounding Sgr A* to approximately $1200 M_\odot$ within the orbit of S2, for both a power law and Plummer density profile (Gravity Collaboration et al., 2024).

The detection of the gravitational redshift and Schwarzschild precession in the S2 data shows that the orbits of stars around the single central point mass, Sgr A*, are in excellent agreement with General Relativity and can accurately be described by the Schwarzschild metric. Moreover, there is no evidence of any extended mass distribution around Sgr A*.

1.2 Observations of the accretion flow of Sagittarius A*

The supermassive black hole Sgr A* is detectable at all times and shows variability across the electromagnetic spectrum. The amplitude of variability, however, changes for different observed wavelengths. Radio observations of Sgr A* have been conducted since the 1980s (Zhao et al., 2001; Herrnstein et al., 2004; Event Horizon Telescope Collaboration et al., 2022), revealing a variability of 20–40% over timescales of years to days in the $\sim$4–11 cm wavelength range (Brown and Lo, 1982), and 30–40% at wavelengths of 0.7–20 cm (Macquart and Bower, 2006). Similar trends are observed at millimeter wavelengths (Falcke et al., 1998; Zhao et al., 2003; Miyazaki et al., 2004; Yusef-Zadeh et al., 2006), with fractional variations of $\sim$20–30 % within 2 to 2.5 hr (Li et al., 2009). Sgr A* exhibits variable emission also in the sub-millimeter range (Marrone et al., 2006; Yusef-Zadeh et al., 2006; Kunneriath et al., 2008; Bower et al., 2019). In contrast, the amplitude of variability in the near-infrared is about an order of magnitude larger than in the radio regime (Genzel et al., 2010), increasing by a factor of a few in bright states compared to quiescent states. Fig. 1.4 shows the light curve of Sgr A* as observed with the GRAVITY interferometer at 2.2 microns in the years 2017 to 2019. The sudden increases in Sgr A*'s emission, known as *flares*, most likely come from heated electrons emitting synchrotron

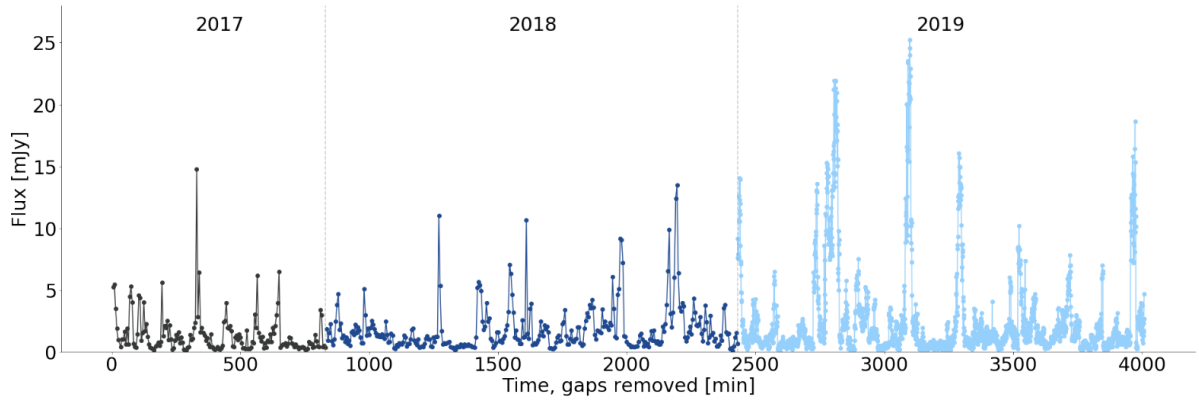

Figure 1.4: Light curve of Sgr A* as observed with the GRAVITY interferometer at the VLTI at 2.2 microns in the years 2017 to 2019. The time gaps between the observations were removed. The flux of Sgr A* increases sporadically during so-called flares. Figure from GRAVITY Collaboration et al., 2020g.

radiation (Genzel et al., 2010). Flares are observed roughly once or twice per day (Genzel et al., 2003a; Eisenhauer et al., 2005; Dodds-Eden et al., 2011; Dodds-Eden et al., 2011; Witzel et al., 2018; GRAVITY Collaboration et al., 2018a; GRAVITY Collaboration et al., 2020g). In 2019, an extremely bright flare was observed at 2.2 microns, with a change in Sgr A*'s flux by a factor of 75 within 2 hours (Do et al., 2019b). Further, infrared flares are often accompanied by increased X-ray emission. The largest variability is observed in the X-ray regime (Baganoff et al., 2001), where the brightness can increase by as much as about 160 times in bright states compared to quiescent states in less than one hour (Porquet et al., 2003). Combined observations across the electromagnetic spectrum aim to investigate a common origin and mechanism of the flares (Eckart et al., 2006b; Marrone et al., 2008; Yusef-Zadeh et al., 2008; Yusef-Zadeh et al., 2009; Witzel et al., 2021).

Fig. 1.5 presents the spectral energy distribution of Sgr A*, illustrating the flux distribution of the black hole across different wavelengths. Notably, the emission of the black hole is in a constant state at radio and (sub-)millimeter wavelengths and highly variable in the near-infrared and X-ray regimes. The red data point is a measurement in the K-band using the GRAVITY interferometer and indicates the median flux density (GRAVITY Collaboration et al., 2020g). Additional flux density percentiles are labeled. In the X-ray, the flux of Sgr A* can range from a quiescent state (Baganoff et al., 2003) to a bright flare (Ponti et al., 2017), highlighting the complex and dynamic nature of the black hole's emission.

High-precision astrometric and polarimetric observations of flares provide key information about the properties of Sgr A*'s accretion flow and the black hole itself. Recent studies have demonstrated that GRAVITY can resolve flares and measure hot spots, the centroid motion of the emission, around Sgr A*'s innermost stable circular orbit (Broderick and Loeb, 2006). For example, GRAVITY Collaboration et al., 2018a used three observed flares to constrain the properties of the black hole, finding that the hot spot orbits a 4 $\times 10^6 M_\odot$ black hole at a radius of 6–10 R_g at about 30 % the speed of light. They

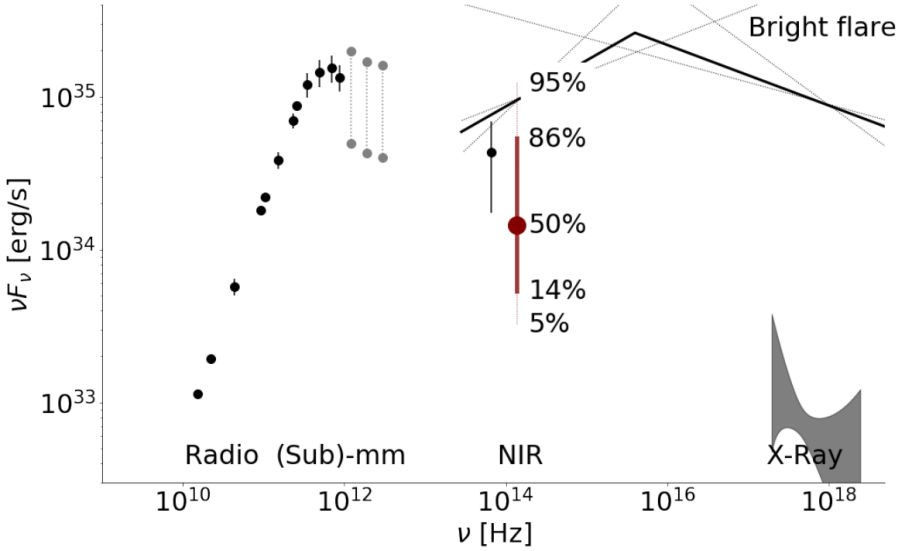

Figure 1.5: Spectral energy distribution of Sgr A*. The emission from the accretion flow around the black hole is roughly constant in the radio and (sub-)mm bands and highly variable in the near-infrared and X-Ray regimes. The red data point is the median flux density from K-band GRAVITY observations of Sgr A*. Figure taken from GRAVITY Collaboration et al., 2020g.

also measured the linear polarization of the flares and determined that the magnetic field around Sgr A* is consistent with a poloidal configuration.

The origin of flares, however, is still under debate. Several models have been proposed to explain the observed phenomena, with many of them based on magnetic reconnection in the accretion flow (Yuan et al., 2009; Dexter et al., 2020; Ripperda et al., 2022). One such model is the magnetic reconnection plasmoid model, proposed by Aimar et al., 2023, which describes flares as the ejection of a plasmoid along a conical orbit near Sgr A*. The plasmoid is a hot plasma region produced by the merging of smaller plasmoids through magnetic reconnection in the magnetosphere of Sgr A*. This model results in an apparent super-Keplerian velocity of the rotating hot spot, which could potentially explain the moderately faster Keplerian velocity measured with GRAVITY data (GRAVITY Collaboration et al., 2018a). Another model, proposed by Lin et al., 2023, is a coronal-mass-ejection model, similar to solar flares, which describes flares as ejected flux ropes resulting from the magnetic reconnection of field lines in the accretion flow. This model also aims to explain the observed GRAVITY results, including the slightly faster than Keplerian velocity of the hot spot. In contrast, Matsumoto et al., 2020 propose a pattern motion as the origin of flares, which could result from magnetohydrodynamic perturbations or a gas outflow interacting with a surrounding disk.

To further refine flare models and accurately determine the parameters of the accretion flow, including the inclination, position angle, and magnetic field configuration, it is

essential to collect additional data in astrometry and polarimetry. This will also allow a precise measurement of the mass of Sgr A* that is enclosed within the flare radius, finally providing independent proof for the existence of a black hole in the center of our galaxy.

1.3 GRAVITY and the Galactic Center

1.3.1 The principle of interferometry

The spatial resolution of a telescope is the smallest distance between two sources at which they can still be distinguished from each other. It is limited by diffraction and given by:

$$\Delta\Theta = 1.22 \, \frac{\lambda}{D} \, , \tag{1.3}$$

for a single telescope with diameter D, observing at a wavelength λ. With current 8 – 10 m class telescopes, the maximum spatial resolution at optical/near-infrared wavelengths is approximately 50 mas. However, to study the effects of General Relativity in the Galactic Center, much higher spatial resolutions and astrometric precisions are needed. This can be achieved by interferometry, which combines the light from two or more telescopes. For s, the spatial resolution in Equ. 1.3 becomes:

$$\Delta\Theta = \frac{\lambda}{B} \, , \tag{1.4}$$

where B is the separation between two telescopes, called *baseline*. Since baselines are usually much larger than the size of a single aperture, s tremendously increase the spatial resolution.

Interferometry is based on the van Cittert-Zernike theorem, which connects the coherent flux $F(u, v)$ measured by the to the sky brightness distribution $I(x, y)$ via a Fourier transform (Glindemann, 2011; Buscher and Longair, 2015):

$$F(u, v) = \int\int I(x, y) e^{-2\pi i(xu+yv)} dxdy \, , \tag{1.5}$$

where $u = B_x/\lambda$ and $v = B_y/\lambda$ are the spatial frequencies and B_x and B_y the projected baselines on sky. The observed complex visibility can be understood as the normalized coherent flux:

$$V(u, v) = \frac{F(u, v)}{F(0, 0)} \, . \tag{1.6}$$

Using Equ. 1.5 and 1.6, we can also write the complex visibility in terms of the properties of the observed object as:

$$V(u, v) = \frac{\int\int I(x, y) e^{-2\pi i(xu+yv)} dxdy}{\int\int I(x, y)} \, . \tag{1.7}$$

The complex visibility is a two-dimensional Fourier transform of the source brightness distribution on the sky. It is measured in the (u, v)-plane, a plane parallel to the coordinate

system of the observed object. Each baseline and spectral channel corresponds to one point in the (u, v)-plane. Using Earth's rotation, we can synthesize a large (u, v)-plane coverage, enabling us to reconstruct high-resolution images of the observed object. The imaging resolution is approximately given by $\Delta\Theta \sim \lambda/|B|_{max}$, where $|B|_{max}$ is the largest projected baseline of the . If the (u, v) coverage is limited, we can still extract information about the observed object by fitting models to the data. In this thesis, we employ both image reconstruction and model fitting to analyze the interferometric data.

The observed complex visibility contains both an amplitude and a phase. The visibility amplitude, a dimensionless quantity ranging from zero to one, describes the contrast of the fringes. For point sources, the visibility amplitude remains constant at one. For extended sources, the visibility amplitude decreases with increasing baseline. Additionally, binary or multiple star systems lead to a modulation of the visibility amplitude. The visibility phase, on the other hand, carries information about the spatial structure of the science target and its position in the sky. This enables precise astrometric measurements, such as those of stars orbiting Sgr A*. However, the main problem of phase measurements is turbulence in the Earth's atmosphere and imperfections in the 's light path. Both can introduce phase perturbations, therefore destroying the visibility phase. To mitigate these effects, two solutions are employed: phase-referenced interferometry, where the phases of the observed object are referenced to those of a known point source, and the use of the *closure phase*. The closure phase is a robust quantity that is insensitive to telescope-based errors. It is formed by combining three phases from baselines of three telescopes $1, 2, 3$ that form a triangle (Buscher and Longair, 2015):

$$\Phi_{123} = \Phi_{12} + \Phi_{23} + \Phi_{31} \ . \tag{1.8}$$

For a symmetric source, the closure phases are zero. Any deviation from zero indicates an asymmetry in the observed brightness distribution. Moreover, the closure phase is translation invariant, which means that it is insensitive to the absolute position of the source in the sky. As a result, we obtain information about the astrometry of sources only when they are observed simultaneously within the same beam. For targets farther away than one beam, we rely on phase-referenced interferometry to enable precise astrometric measurements. In the context of this thesis, we use all the interferometric quantities described above, for both model fitting and image reconstruction.

1.3.2 The GRAVITY interferometer

The data presented in this thesis were collected with GRAVITY (GRAVITY Collaboration et al., 2017), a second-generation beam combiner at ESO's Very Large Telescope (VLTI) at Cerro Paranal in the Atacama Desert in northern Chile. GRAVITY operates in the K-band, from 1.95 – 2.45 microns. It coherently combines the light from either the four 8.2 m Unit Telescopes (UTs) or the four 1.8 m Auxiliary Telescopes (ATs). With baselines of up to 130 m for the UTs (200 m for the ATs), GRAVITY reaches an imaging resolution of about 3 milli-arcseconds and precise astrometry at a level of a few 10 micro-arcseconds,

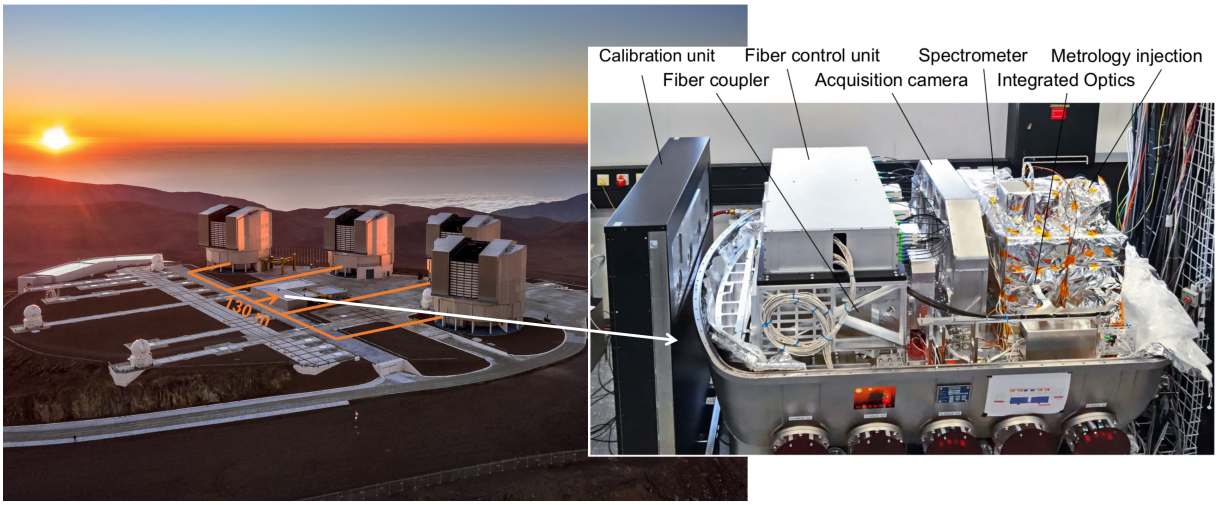

Figure 1.6: *Left:* The Very Large Telescope on top of Cerro Paranal in Chile. The four 8.2 m Unit Telescopes (UTs) have baselines up to 130 m and are installed on fixed positions. The four 1.8 m Auxiliary Telescopes (ATs) reach baselines up to 200 m and can be moved to different positions. *Right:* The open GRAVITY beam combiner instrument with its different subsystems labeled. GRAVITY coherently combines the light from either the four UTs or the four ATs. Image credits: G. Hüdepohl/ESO and GRAVITY Collaboration et al., 2017.

which is an improvement of 10–20 times compared to an individual 10 m-class telescope. GRAVITY offers astrometric, polarimetric, and spectroscopic observing modes (GRAVITY Collaboration et al., 2017; GRAVITY Collaboration et al., 2024) and wide and deep imaging modes (GRAVITY Collaboration et al., 2022; GRAVITY+ Collaboration et al., 2022; Abuter et al., 2024). Three spectral resolutions are available: Low with $R = \lambda/\Delta\lambda \approx 20$, Medium with $R \approx 500$, and High with $R \approx 4500$. Further, GRAVITY can observe objects as faint as $m_K = 19.7$ (GRAVITY Collaboration et al., 2022), which is an increase in sensitivity of more than a factor of a thousand compared to previous interferometers.

Fig. 1.6 shows the VLTI platform on the left. The light from the four UTs or four ATs is propagated to the VLTI lab, where it is combined using GRAVITY. The image to the right shows the open GRAVITY beam combiner instrument with the subsystems labeled. An overview of the entire instrument is given in Fig. 1.7, and its working principle is described in the following. An observation with GRAVITY requires three targets: a bright wavefront reference star for the adaptive optics (AO) system, a point source with a limiting magnitude of $m_K \approx 11$ as a phase reference (FT) star, and a science target (SC). The PRIMA star separator (Delplancke et al., 2004) splits the light from the AO star and the science target at the Coudé focus of each telescope and feeds the light into an AO system, where the wavefront correction is applied. For the UTs, two different AO systems are available: MACAO (until the end of 2024) in the visible (Arsenault et al., 2003), GPAO (since early 2025) both in the visible and near-infrared (Bourdarot et al.,

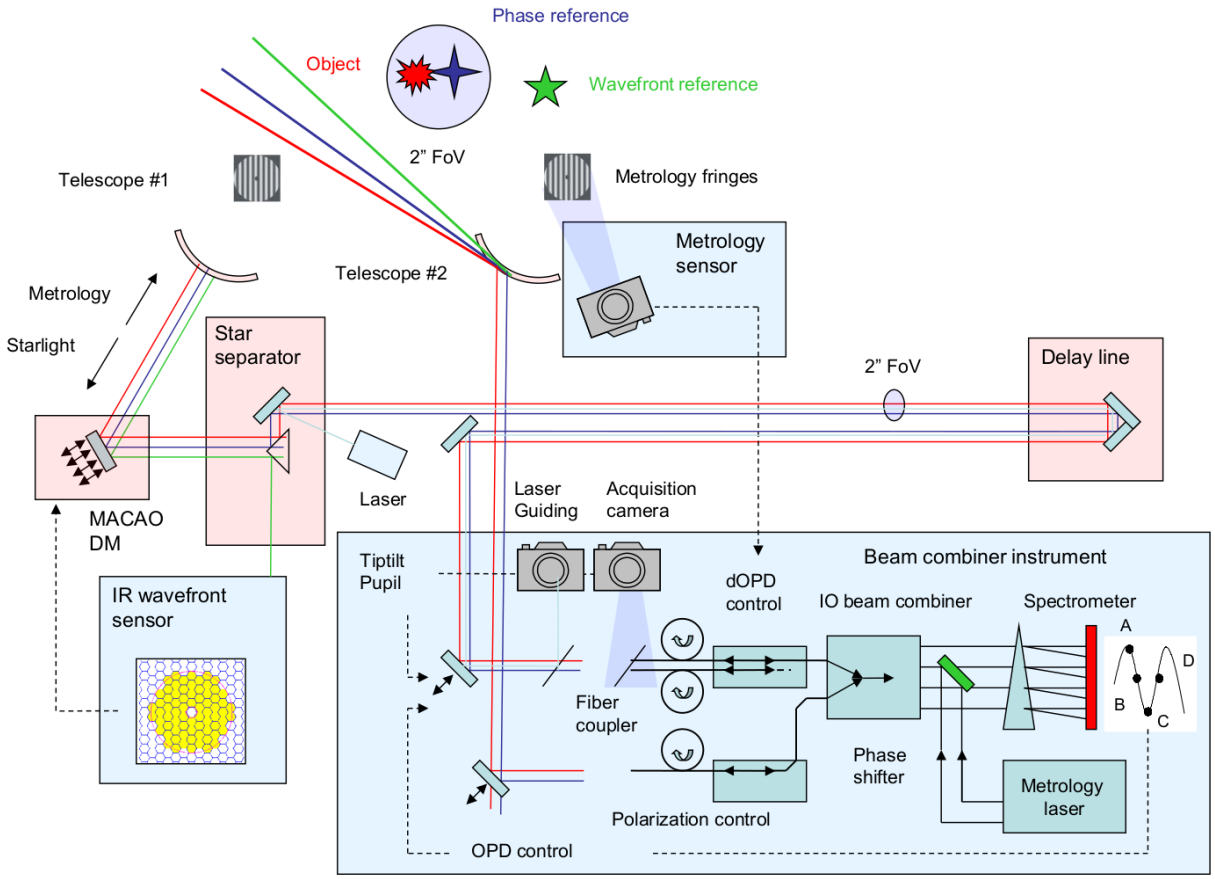

Figure 1.7: The working principle of GRAVITY. GRAVITY subsystems are shown in the blue boxes and the used VLTI substructure in the red boxes. The light of the wavefront reference star (green) is propagated to the infrared adaptive optics wavefront sensor. The light of the science object (red) and phase reference star (blue) travel through the delay lines until they are combined in the beam combiner instrument. The metrology laser is propagated backwards through the light path of GRAVITY and the VLTI and measures the differential optical path difference between the science object and phase reference star for astrometric observations. Figure taken from GRAVITY Collaboration et al., 2017.

2024), and CIAO in the near-infrared (Kendrew et al., 2012; Scheithauer et al., 2016). For the ATs, the available AO system is NAOMI, which operates in the visible (Woillez et al., 2019).

The 2 arcsecond field of view of the VLTI for the UTs (and 4 arcseconds for the ATs) contains the light of the FT and SC, which is propagated through the main delay lines for optical path difference (OPD) compensation between the telescopes to GRAVITY. The fiber coupler unit de-rotates the field, splits the light of the FT and SC, and couples it into individual fibers, which can be stretched to compensate for the differential OPD (dOPD) between the SC and FT (Perrin et al., 2024; Pfuhl et al., 2014). Further, a half-wave plate enables polarization alignment for maximum contrast and polarimetric observations by measuring the light in two linear polarization states. The beam combination is then performed in an integrated optics (IO) chip (Jocou et al., 2014; Perraut et al., 2018), providing simultaneous interference for all six baselines. The FT light goes to the FT detector, which runs at a high frequency of 300 Hz or 1 kHz and measures the phase and group delay (Lacour et al., 2019). This OPD is then compensated via internal piezo mirrors, thus stabilizing the fringes of both FT and SC, which allows for second to minute-long integration times on the science detector.

One of the subsystems of GRAVITY is the acquisition camera (Amorim et al., 2012), which operates in the H-band (1.45 – 1.85 microns). It shows an image of the observed field and pupil, of the Shack-Hartmann wavefront sensor and the pupil tracker for each of the four telescopes. The field image on the acquisition camera is used to control pupil drifts at low frequency. For stabilizing the field and pupil, GRAVITY uses two laser tracking systems. One system is the pupil tracker, a 2x2 Shack-Hartmann sensor, which is fed by a laser launched from the spider arms of each telescope. The pupil tracker measures both lateral and longitudinal pupil motion. Internal pupil actuators and the curvature mirror in the VLTI delay line then correct this motion in real-time. The other system controls image drifts at high frequency, coming from air turbulence in the VLTI optical train. They are measured by laser beacons, which are launched at the star separator and detected with position-sensitive diodes (Pfuhl et al., 2014).

Another critical subsystem is GRAVITY's laser metrology system (Lippa et al., 2016). It measures the dOPD between the FT and SC for each telescope, allowing for astrometric measurements by phase referencing the science light to the fringe tracker light. The metrology system consists of three beams from the same 1908 nm laser. It is launched in the fiber coupler, propagated backward through the light path of GRAVITY and the VLTI, and measured by metrology receivers mounted on the spider arms of each telescope. Two beams (one for the FT and SC beam, respectively) are fed into both of the GRAVITY beam combiners; the third beam, the *carrier beam*, has a significantly higher laser power and is injected into the system after the fiber coupler. The metrology receivers measure the interference pattern between the carrier beam and each of the FT and SC beams individually, finally measuring the dOPD and, thus, the precise distance between the two targets.

The brightness of the science target and the separation from the fringe tracking star dictates whether the observations are conducted in single-field or dual-field mode. If the SC

is bright enough, its light is split by a beam splitter, and 50% goes to the SC channel and 50% to the FT channel. This is the single-field on-axis mode of GRAVITY. The dual-field mode in on-axis, off-axis, or wide is used for science targets fainter than $m_K = 11$ for the UTs ($m_K = 9$ for the ATs). Dual-field off-axis is chosen for FT – SC separations between 0.27 arcsec and 2.0 arcseconds for the UTs (1.17 arcseconds to 4 arcseconds for the ATs), which is the mode for Galactic Center observations (see Section 1.3.3 for more details). Dual-field wide is used for separations larger than 2 arcseconds for the UTs (4 arcseconds for the ATs; see Section 1.3.4 and Chapter 5 for more details).

GRAVITY had its first light in 2017 and has delivered groundbreaking results in different fields of astronomy since then. Due to its high angular resolution, precise astrometry, and high sensitivity, GRAVITY is able to observe stars orbiting the black hole at the center of our galaxy, exoplanets orbiting their host star, disks of young stellar objects, gravitational microlenses, broad line regions of active galactic nuclei, multiple-star systems, and high mass x-ray binaries. The following Section will describe how we observe the Galactic Center with GRAVITY.

1.3.3 Observing the Galactic Center with GRAVITY

From Cerro Paranal, the Galactic Center is observable from March to September each year, and we collect data almost every month during this period. The 2017 – 2025 observations are part of the GRAVITY or GRAVITY+ long-term Guaranteed Time Observations (GTO) program of probing physics near the event horizon of Sgr A* with stars and flares. This program focuses on obtaining the astrometry of objects near Sgr A* and sampling stellar motions each month. Further, long integrations on the central field aim to detect previously unknown faint stars via deep imaging. Finally, whenever an increase in Sgr A*'s brightness is detected, we integrate on the central field to follow the motion of the gas around the event horizon of Sgr A* during a flare, both in astrometry and polarimetry. The observing mode we use for Galactic Center observations with GRAVITY is the dual-field off-axis mode in low spectral resolution and split polarization. As described above and shown in Fig. 1.8, this mode requires three targets: an AO star, a fringe tracking star, and a science object. We use IRS 7 ($m_K = 6.5$) as the AO star and CIAO as the AO system and GPAO since 2025, respectively. For fringe tracking, we usually choose IRS 16C ($m_K = 9.7$), but other stars are possible too, such as IRS 16NW ($m_K = 9.7$). Once the telescopes are preset to the AO and FT stars, we can point to any science target within 2 arcseconds from the FT.

Each observing night, we collect data on Sgr A*, on our local calibrator, and S2 or any of the stars in the inner 400 milli-arcseconds of Sgr A*. The calibrator should be a single star with visibility amplitudes close to one and closure phases close to zero. The calibrators we choose are R2 ($m_K = 12.4$), S2 ($m_K = 14.1$) or S4 ($m_K = 14.6$). We obtain the positions of the stars relative to Sgr A* in two different ways. If the star is within the same ∼70 milli-arcsecond interferometric field of view as Sgr A*, we fit a black-hole-star model to the visibility amplitudes and closure phases. Suppose the star is further away than ∼70 milli-arcseconds. In that case, we observe Sgr A* and the star separately and

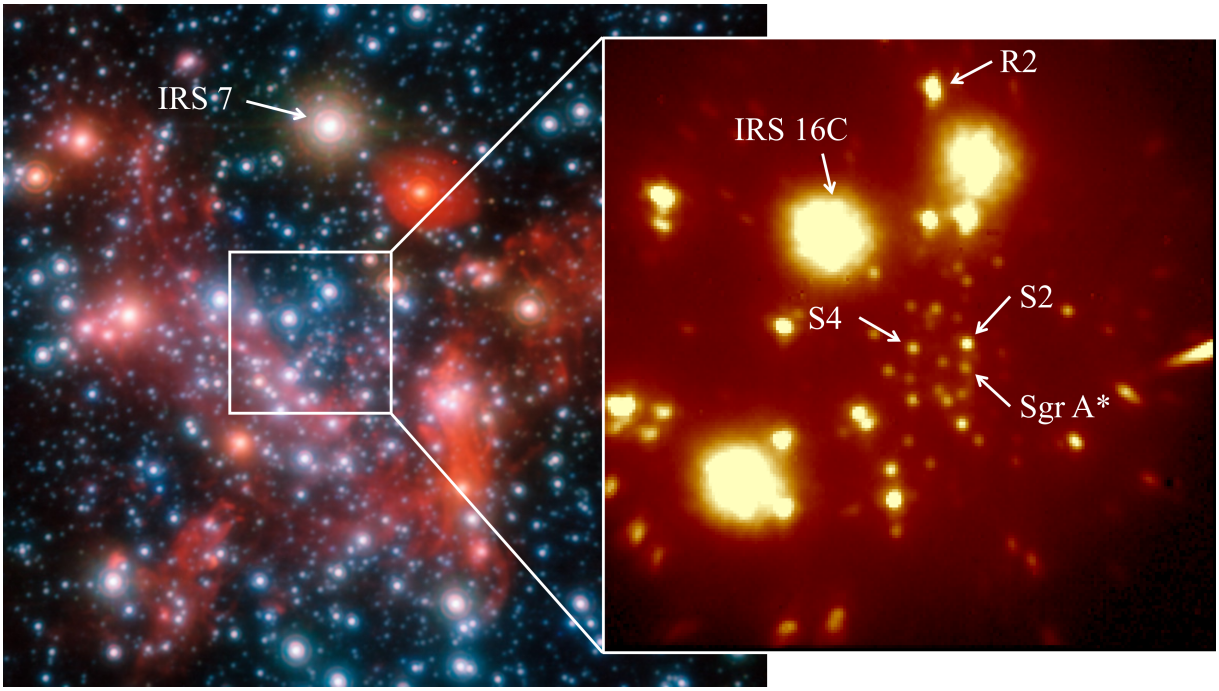

Figure 1.8: Setup for GRAVITY observations of the Galactic Center. *Left:* Image of the Galactic Center as seen by the NACO instrument at the VLT. We use IRS 7 ($m_K = 6.5$) as the adaptive optics star for CIAO. Credit: ESO/S. Gillessen et al. *Right:* Acquisition camera field image of the inner 2 arcseconds of Sgr A*. We use IRS 16C ($m_K = 9.7$) as the fringe tracking star, and R2 ($m_K = 12.4$), S2 ($m_K = 14.1$) or S4 ($m_K = 14.6$) as the calibrator. Our science targets are Sgr A* and stars in the inner 400 milli-arcseconds of Sgr A*.

reference the two fields to each other by fitting the visibility phases, which are referenced to the FT via GRAVITY's metrology system. The model used for the star field is a single-star or multiple-star model, depending on how many stars are in the field of view.

For a comprehensive description of the Galactic Center observing strategy, the observational techniques employed, and the methods used to determine astrometric positions of stars around Sagittarius A*, the reader is referred to Chapter 4. This chapter presents the monitoring of stellar orbits in the Galactic Center with GRAVITY based on data collected between 2017 and 2025.

1.3.4 Towards the spin of Sagittarius A* with GRAVITY+

GRAVITY and the VLTI have revolutionized optical/infrared interferometry through various technical breakthroughs and have provided groundbreaking results on the Galactic Center, exoplanets, and active galactic nuclei. Another boost towards ever-fainter, all-sky, and high-contrast interferometry will come with GRAVITY+ (Eisenhauer, 2019), an upgrade to GRAVITY and parts of the VLTI. GRAVITY+ aims to open the sky for extragalactic science and observe targets as faint as $m_K = 22$. Science goals of GRAVITY+ include the observations of faint active galactic nuclei, faint stars in the Galactic Center, and massive stars. They further include the exploration of cold exoplanets and low-mass young embedded stars, resolving microlenses, and, finally, revealing the presence of an intermediate-mass black hole.

Fig. 1.9 shows an overview of the different GRAVITY+ upgrades. The first upgrade was the grism upgrade in 2019 (Yazici et al., 2021), which increased the science channel throughput by a factor of 2 – 3 in medium and high spectral resolution. Subsequent upgrades include the implementation of state-of-the-art adaptive optics (GPAO), which were commissioned at the end of 2024 and are now available to the community. Additionally, laser guide stars are planned to be commissioned in late 2025 for all four 8 m UTs, which will improve high-contrast observations and enable all-sky coverage (Bourdarot et al., 2024; More et al., 2024; Berdeu et al., 2024; Millour et al., 2024; Booth et al., 2024). The performance of interferometric observations is also being improved through better vibration control (Laugier et al., 2024). Furthermore, GRAVITY+ includes an upgrade of the GRAVITY fringe tracker (Nowak et al., 2024) and the implementation of two new observing modes: GRAVITY Wide (see Chapter 5, GRAVITY+ Collaboration et al., 2022; Drescher et al., 2022; Fabricius et al., 2024)) and GRAVITY-Faint (Widmann et al., 2022), which has been used for Galactic Center observations since 2023. Finally, a new Germanium grism for high-spectral resolution observations with R $\sim$ 15000 is being developed (Sanchez-Bermudez et al., 2024).

GRAVITY+ will have a resolution, accuracy, and sensitivity that is unmatched by any other observatory. This will give the chance to answer some of the most unique questions on the innermost region of the Galactic Center. The GRAVITY+ science goals of the Galactic Center are threefold: to investigate the accretion flow, explore the structure of the S-star cluster, and test General Relativity.

The improved astrometry of GRAVITY+, with an accuracy of 10 – 30 micro-arcseconds,

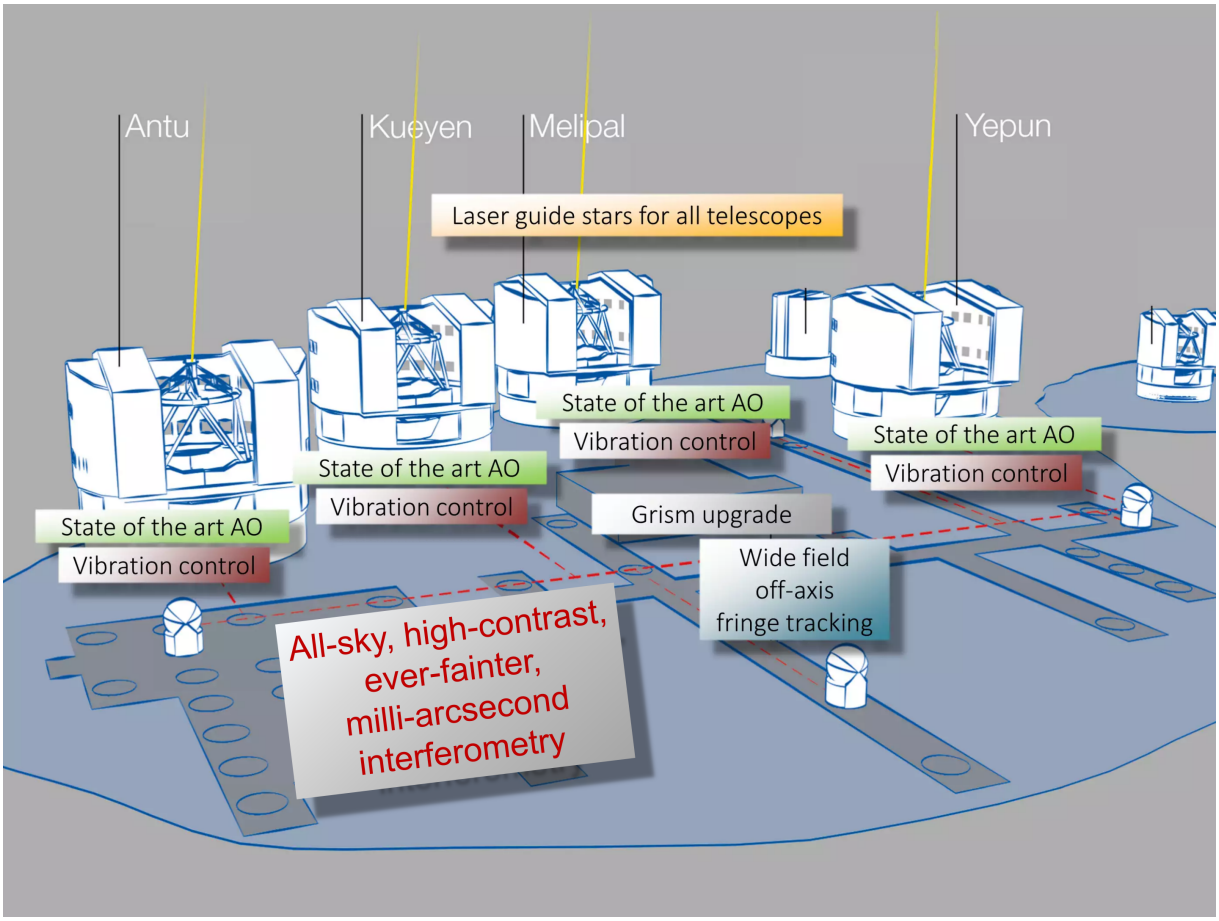

Figure 1.9: Overview of the upgrades of GRAVITY and parts of the VLTI to GRAVITY+ for all-sky, high-contrast, ever-fainter milli-arcsecond interferometry. GRAVITY+ includes implementing state-of-the-art adaptive optics and laser guide stars on all four 8 m UTs, wide field off-axis fringe tracking, an improved vibration control, and a grism upgrade. Figure adapted from Eisenhauer, 2019.

will deepen our understanding of the innermost accretion zone. We can obtain insights into the physical conditions governing this region by following the motions of hot gas around Sgr A* in space and time. Furthermore, combining astrometry with polarimetry will provide a more detailed picture of the magnetic field configuration in the Galactic Center. GRAVITY data have already vastly improved our understanding of the innermost accretion zone (Gravity Collaboration et al., 2023a, see Chapter 3), but especially the improved astrometry of GRAVITY+ will enable precise comparisons with different flare models, shedding new light on the nature of Sgr A* flares.

Secondly, GRAVITY+ will enable even more precise astrometric measurements of stars in the Galactic Center, allowing for a better characterization of the gravitational potential. The improved astrometric accuracy of GRAVITY+ will increase the chances of detecting the eventual presence of an intermediate-mass black hole and stellar-mass black holes in the Galactic Center. The observed signature would be a sudden deviation of a star from its orbit due to the gravitational pull of the black hole (Merritt et al., 2010). GRAVITY data have already ruled out an intermediate-mass black hole with masses larger than 1200 $M_\odot$ within the orbit of S2 (Gravity Collaboration et al., 2024; GRAVITY Collaboration et al., 2022; Gravity Collaboration et al., 2023b). Observing the orbits of fainter stars with higher precision will further constrain the possibility of an IMBH in the Galactic Center. Further, the detection of faint stars, stellar mass, and intermediate-mass black holes will give important information for the upcoming LISA mission (Thorpe et al., 2019), which will be able to detect intermediate and extreme mass ratio inspirals into the supermassive black hole (Amaro Seoane et al., 2024).

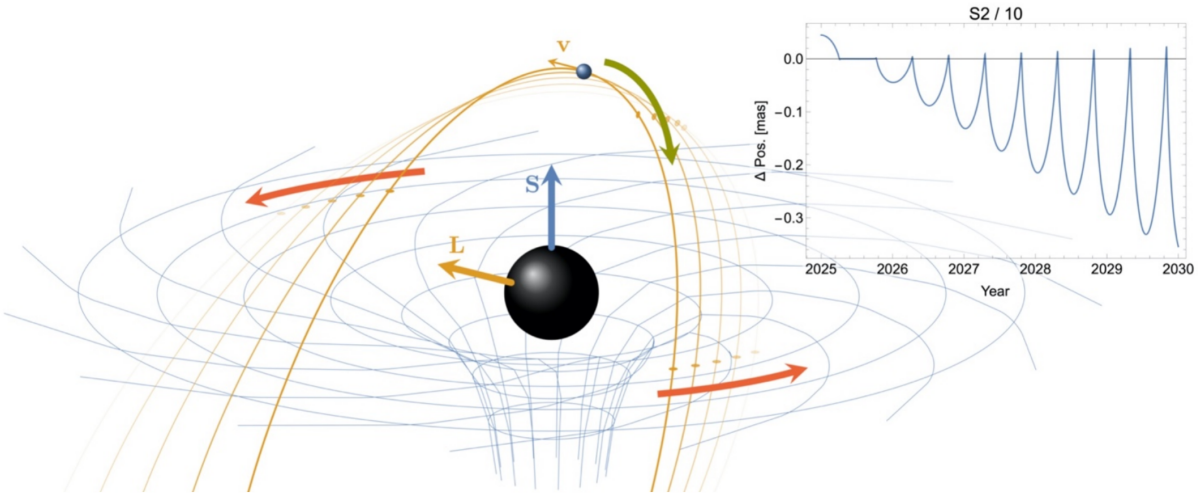

Figure 1.10: Illustration of the Lense-Thirring precession of a star around a spinning black hole. The effect depends on the black hole spin vector **S** and orbital angular momentum vector **L** and causes a rotation of the spacetime around the black hole with the spin. The top right panel shows the difference between the orbits of a non-spinning and a maximally spinning black hole for a hypothetical S2/10 star, an S2-like star with a ten times smaller semi-major axis. Figure taken from Gravity+ Collaboration et al., 2022.

Finally, the third goal for Galactic Center science with GRAVITY+ is to measure higher-order effects of General Relativity, such as the spin of Sgr A*. This can be achieved by measuring the effect of the spin on stellar orbits. The signature one would measure is the Lense-Thirring precession, which causes a precession of the star's orbital plane. The spin effect falls off with r^{-3} from the mass center; thus, stars on short orbits would be affected much more strongly than stars further out. Fig. 1.10 illustrates the Lense-Thirring precession for a star around a spinning black hole. The inset to the upper right presents the difference between the orbits of a non-spinning and a maximally spinning black hole for a hypothetical S2/10 star, an S2-like star with a ten times smaller semi-major axis (Waisberg et al., 2018). Since no star on a suitable orbit has been found from adaptive optics data, they must be fainter than $m_K = 18$. GRAVITY has already detected S62 with $m_K = 18.9$ and S300 with $m_K \sim 19.3$ via imaging (GRAVITY Collaboration et al., 2021b; GRAVITY Collaboration et al., 2022, see Chapter 2), but both stars are not on a suitable orbit for a spin measurement. The full potential will come with GRAVITY+. Its improved sensitivity to $m_K = 22$ will increase the probability of finding a faint star on a short-period, high-eccentricity orbit via imaging. Precise astrometry from GRAVITY+ together with spectroscopy from the Extremely Large Telescope's (ELT) instrument MICADO (Davies et al., 2018) will enable complete orbit monitoring, making it possible to measure the spin of Sgr A*.

1.4 This thesis

The work collected in this thesis focuses on near-infrared interferometric observations with GRAVITY and data analysis of stars and flares in the Galactic Center. Additionally, it includes the presentation and demonstration of a new observing mode developed within the GRAVITY+ project.

- Chapter 2 presents images of stars within the central 100 milli-arcseconds of Sgr A*. Imaging is essential for searching for unknown, faint stars on highly eccentric, short orbits, which could help constrain the spin of Sgr A*. The images shown in chapter 2 are reconstructed with a newly developed imaging code called G^R, which is specifically designed for Galactic Center observations with GRAVITY. We detect the known stars S29, S55, S62, S38, S42, S60, and S63 in a series of exposures. Additionally, the images reveal a previously unknown faint star called S300. It has a magnitude of $m_K \simeq 19.0 - 19.3$ and moves to the west at a high angular velocity. Finally, images reconstructed with the CLEAN algorithm confirm the detection of S300.

- Chapter 3 presents astrometric and polarimetric observations of the positional change of Sgr A*'s near-infrared emission during bright states, called *flares*. Flares are an excellent probe for the mass of the black hole and the physics in its environment. We have observed four astrometric and six polarimetric flares with GRAVITY since 2018. All astrometric flares show clockwise motion in the sky with a period of around an hour, and we observe one polarization loop per astrometric loop. The striking

similarities of the flares allow us to combine the data. We present a common fit that enables us to measure the mass and radius of the black hole and the inclination and position angle of the accretion flow. Finally, we show that the accretion flow geometry is consistent with the angular momentum of the inner clockwise disk of young stars, suggesting that the winds of the massive young stars of this disk fuel the accretion flow.

- Chapter 4 presents orbital motions of 15 S-stars in the inner 400 milli-arcseconds of Sgr A*, observed with GRAVITY from 2017 to 2025. We explain the observing strategy, instrumental upgrades to GRAVITY, and the methods used to determine astrometric separations between Sgr A* and individual S-stars in the Galactic Center. We present updated and refined orbital solutions for 11 S-stars and fit linear or quadratic motions for the remaining four S-stars. We also analyze the angular momentum and eccentricity distributions of the observed S-stars, including 30 stars with previously published orbital solutions. Our findings are that most stars are randomly oriented, except eight stars, which are members of the clockwise stellar disk. Additionally, the eccentricity distributions of both early-type and late-type stars are consistent with a thermal distribution.

- Chapter 5 presents the design and first results of GRAVITY Wide, a new observing mode implemented in the first phase of the GRAVITY+ upgrade. This upgrade significantly improves the sky coverage of GRAVITY, increasing it by two orders of magnitude, which enables the observation of faint targets and, in particular, active galactic nuclei at redshift $z \sim 2$. These observations are crucial for understanding the co-evolution of supermassive black holes and their host galaxies. The new observing mode is limited by turbulence in the Earth's atmosphere, which is a major factor in the coherence loss between the science object and the fringe tracking star. We use the data collected during the GRAVITY Wide commissioning runs to test the new observing mode and predict the coherence loss based on the atmospheric conditions at the observation time. This prediction has been successfully applied to observing planning since GRAVITY Wide became available to the community in October 2022.

- Finally, Chapter 6 presents the overall conclusions of this work and an outlook within the context of expected scientific advancements in the upcoming years.

Chapter 2

Deep images of the Galactic center with GRAVITY

Original Publication: GRAVITY Collaboration: R. Abuter, N. Aimar, A. Amorim, P. Arras, M. Bauböck, J.-P. Berger, H. Bonnet, G. Bourdarot, W. Brandner, V. Cardoso, Y. Clénet, R. Davies, P.T. de Zeeuw, J. Dexter, Y. Dallilar, A. Drescher, F. Eisenhauer, T. Enßlin, N.M. Förster Schreiber, P. Garcia, F. Gao, E. Gendron, R. Genzel, S. Gillessen, M. Habibi, X. Haubois, G. Heißel, T. Henning, S. Hippler, M. Horrobin, A. Jiménez-Rosales, L. Jochum, L. Jocou, A. Kaufer, P. Kervella, S. Lacour, V. Lapeyrère, J.-B. Le Bouquin, P. Léna, D. Lutz, F. Mang, M. Nowak, T. Ott, T. Paumard, K. Perraut, G. Perrin, O. Pfuhl, S. Rabien, S. Scheithauer, J. Shangguan, T. Shimizu, J. Stadler, O. Straub, C. Straubmeier, E. Sturm, L.J. Tacconi, K. R. W. Tristram, F. Vincent, S. von Fellenberg, I. Waisberg, F. Widmann, E. Wieprecht, E. Wiezorrek, J. Woillez, S. Yazici, A. Young, and G. Zins
CORRESPONDING AUTHORS: J. Stadler, A. Drescher
DOI: 10.1051/0004-6361/202142459

ABSTRACT: Stellar orbits at the Galactic Center provide a very clean probe of the gravitational potential of the supermassive black hole. They can be studied with unique precision, beyond the confusion limit of a single telescope, with the near-infrared interferometer GRAVITY. Imaging is essential to search the field for faint, unknown stars on short orbits which potentially could constrain the black hole spin. Furthermore, it provides the starting point for astrometric fitting to derive highly accurate stellar positions. Here, we present G^R, a new imaging tool specifically designed for Galactic Center observations with GRAVITY. The algorithm is based on a Bayesian interpretation of the imaging problem, formulated in the framework of information field theory and building upon existing works in radio-interferometric imaging. Its application to GRAVITY observations from 2021 yields the deepest images to date of the Galactic Center on scales of a few milliarcseconds. The images reveal the complicated source structure within the central 100 mas around Sgr A*, where we detected the stars S29 and S55 and confirm S62 on its trajectory, slowly approaching Sgr A*.

Furthermore, we were able to detect S38, S42, S60, and S63 in a series of exposures for which we offset the fiber from Sgr A*. We provide an update on the orbits of all aforementioned stars. In addition to these known sources, the images also reveal a faint star moving to the west at a high angular velocity. We cannot find any coincidence with any known source and, thus, we refer to the new star as S300. From the flux ratio with S29, we estimate its K-band magnitude as $m_{\mathrm{K}}\,(\mathrm{S300}) \simeq 19.0 - 19.3$. Images obtained with CLEAN confirm the detection. To assess the sensitivity of our images, we note that fiber damping reduces the apparent magnitude of S300 and the effect increases throughout the year as the star moves away from the field center. Furthermore, we performed a series of source injection tests. Under favorable circumstances, sources well below a magnitude of 20 can be recovered, while 19.7 is considered the more universal limit for a good data set.

2.1 Introduction

he Galactic Center (GC) is a unique laboratory for probing general relativity (GR; Genzel et al. 2010), where stars orbiting Sagittarius A* (Sgr A*) serve as clean test particles in the gravitational field of a supermassive black hole (SMBH). With near-infrared (near-IR) interferometry, it is not only possible to peer through the dust obscuring the GC, but to also push the angular resolution beyond a single telescope's diffraction limit. Down to an astrometric accuracy of $\sim 65\,\mu$as, this technique has been pioneered by the GRAVITY instrument (GRAVITY Collaboration et al., 2017), which couples the four 8m telescopes at the ESO Very Large Telescope (VLT). At the available telescope separation of $\lesssim 130\,$m, Sgr A* and the stars in its vicinity still appear as point sources, but their positions can be determined by a factor of ~ 20 more accurately compared to adaptive optics (AO) assisted imaging with a single telescope of similar size. Most importantly, the high angular resolution of GRAVITY allows to overcome the confusion limit of AO imaging.

There are about 50 stars with known orbits within 1 arc second (as) of Sgr A* (Gillessen et al., 2017). The most prominent of them, S2, passed its pericenter in 2018. The close monitoring of this event allowed for the detection of the gravitational redshift (GRAVITY Collaboration et al., 2018b; Do et al., 2019a) and the Schwarzschild precession (GRAVITY Collaboration et al., 2020c) in the S2 orbit. In 2019, S2 still was the brightest source next to Sgr A* within the GRAVITY field of view (FOV) (GRAVITY Collaboration et al., 2021b); in 2021, it moved to a separation that is sufficiently large such that the two sources cannot be detected in a single pointing. Two other stars, however, approach Sgr A* and go through their pericenters in 2021 – S29 and S55 (Gillessen et al., 2017), which we have detected within 50 mas from Sgr A*. In comparison with S2, S29 approaches the black hole even more closely, while S55 has a shorter orbital period (Meyer et al., 2012). We present updated results from their GR orbits in a second paper (GRAVITY Collaboration et al., 2022).

The magnitude at which gravitational redshift and Schwarzschild precession affect stellar orbits are on the order of β^2 (where $\beta = v/c$, Zucker et al., 2006), while the Lense-Thirring precession due to the black hole spin falls off faster with the distance to the black hole. It

is thus not clear whether any of the known stellar orbits allow for the detection of higher-order GR effects (Merritt et al., 2010; Zhang and Iorio, 2017). A faint star at a smaller radius, on the other hand, could provide an opportunity to measure the spin of the SMBH (Waisberg et al., 2018). The expected number of stars suitable for such a measurement has been estimated around unity from extrapolation of the density profile and mass function observed at the GC (Genzel et al., 2003b; Do et al., 2013; Gallego-Cano et al., 2018) to small radii and faint stars, respectively (Waisberg et al., 2018).

With the interferometry approach, each baseline between two telescopes represents a point in Fourier space and the correlation of their signal corresponds to the Fourier transform of the image at this coordinate, in accordance with the well-known van Cittert-Zernike theorem (van Cittert, 1934; Zernike, 1938). Taking advantage of the Earth's rotation over a longer observing sequence and multi-wavelength observations help to fill the so-called (u, v)-plane. If sufficient prior knowledge on the observed flux distribution exists, model fitting is a powerful method to extract the desired information from the data. Without any prior indication of where a source might be expected, on the other hand, image reconstruction is the technique of choice in the search for faint, as-yet-unknown stars.

Consequently, deep imaging is essential in pushing the exploration of the GC further. Beyond the quest for faint stars, it is also the method of choice for exploring a lesser known field and serves as the starting point for astrometric fitting. The detection of S62, a slowly moving star at the K-band magnitude of $m_{\mathrm{K}}\,(\mathrm{S62}) \simeq 18.9$, in GRAVITY images reconstructed with the radio-interferometry algorithm CLEAN (Högbom, 1974), clearly demonstrates the power and value of the imaging approach (GRAVITY Collaboration et al., 2021b). CLEAN views the image as a collection of point sources, whose signal it subtracts iteratively from the measured coherent flux until only the noise is left. The question of where to place those point sources and when to stop iterations is guided by the Fourier inversion of the data. Because the (u, v)-space is only sparsely sampled, this "dirty image" is usually dominated by the inverse Fourier transform of the sampling pattern (the so-called dirty beam) and only the most prominent sources in the field are apparent. After subtracting their signal, fainter sources become recognizable in the residual images. As such, CLEAN depends on the linearity and invertibility of the Fourier transform that relates the image to the data.

Both conditions are not strictly satisfied for near-IR interferometry, where instrumental and observational effects, such as the finite bandwidth size and optical aberrations introduced by the instrument (GRAVITY Collaboration et al., 2021c), complicate the measurement equation. This is similar to what is known as direction-dependent effects (DDEs) in radio interferometric imaging (see e.g. Bhatnagar et al., 2008; Smirnov, 2011). Furthermore, the requirement for a linear measurement equation impedes the use of closure quantities (Rogers et al., 1974), non-linear combinations of the data on different baselines that are insensitive to any telescope-based errors and thus provide more robust measurements.

Bayesian forward modeling offers an alternative approach to image reconstruction in which possible flux distributions are quantified by the prior and the optimal image is found from exploration of the joint prior and likelihood, that is, the posterior. In this

fashion, only the forward implementation of the measurement equation (and possibly its derivative for effective minimization) are needed, such that non-linear and non-invertible terms can be handled straightforwardly. The method, however, comes at the disadvantage of increased computational costs required to perform the posterior search.

Existing tools for optical and near-IR interferometric imaging, such as MIRA (Thiébaut, 2008) and SQUEZZE (Baron et al., 2010), perform the posterior search either by descent minimization or with Monte Carlo Markov chains (MCMC). While it may be faster, the former method is limited to convex likelihood and prior formulations. The MCMC method, on the other hand, becomes very inefficient for high-dimensional problems. For imaging, where every pixel is a free parameter to be inferred, this limits the applicability to rather small grids. Furthermore, these are general-purpose codes intended for the application to a range of instruments and, therefore, they do not account for all instrumental effects known to impact GRAVITY data. Finally, imaging the GC is complicated by the variability of Sgr A* on a timescale of five minutes (Genzel et al., 2003a; Ghez et al., 2004; Eisenhauer et al., 2005; Gillessen et al., 2006; Eckart et al., 2008b; Do et al., 2009; Dodds-Eden et al., 2011; Witzel et al., 2018; GRAVITY Collaboration et al., 2020g; GRAVITY Collaboration et al., 2020e). Naively combined over a longer period, the data become inconsistent, but (u, v)-sparsity prevents snapshot images over such a short duration. Rather, a prior model beyond those currently available in public codes is required, which can accommodate flux variations of the central source in a otherwise static field of point sources.

In this paper, we present our new imaging code GRAVITY-RESOLVE ($\mathrm{G^R}$)[1]. It builds upon RESOLVE (Arras et al., 2021b; Arras et al., 2018), a Bayesian algorithm for radio interferometry, but it is tailored to GC observations with GRAVITY in its measurement equation and its prior model. For exploring the posterior distribution, we employed Metric Gaussian Variational Inference (MGVI, Knollmüller and Enßlin, 2019), an algorithm that aims to provide a trade-off between robustness to complicated posterior shapes and applicability to high-dimensional problems. We present the details of $\mathrm{G^R}$ in Sect. 2.2, describe the GRAVITY data in Sect. 4.5 and apply $\mathrm{G^R}$ to it in Sect. 3.5. The images reveal the rich structure of sources around the SMBH and a previously unknown faint star, moving to the west at high angular velocity. In Sect. 5.4, we first compare the results of the new algorithm to image reconstruction with CLEAN, before we discuss the properties and implications of the newly detected star. Finally, we present our conclusions in Sect. 4.8.

2.2 Imaging method

The backbone of our method is a Bayesian interpretation of the imaging process, in which the posterior probability for a certain image, I, given the data, d, is proportional to

$$\mathcal{P}\left(I|\, d\right) \propto \mathcal{P}\left(d|\, I\right)\, \mathcal{P}\left(I\right)\,, \tag{2.1}$$

that is, the prior times the likelihood. The proportionality arises because we have omitted the notoriously difficult-to-calculate evidence term $\mathcal{P}\left(d\right)$, which is insensitive to the

[1]The $\mathrm{G^R}$ source code is available at `https://gitlab.mpcdf.mpg.de/gravity/gr_public.git`

particular image realization (we come back to this choice in Sect. 2.2.5). If the posterior distribution is known, we can easily find the most likely image from it or we can compute the expected image and its variance from the first two posterior moments. In practice, however, the posterior is a very high-dimensional scalar function (each image pixel contributes one dimension), and we cannot evaluate its moments analytically. It is then necessary to resort to numerical methods, such as descent minimization to find a (local) maximum or to sampling techniques.

In this section, we introduce all the necessary ingredients to implement the Bayesian inference scheme in practice. We start with the prior (Sect. 2.2.1), which is formulated as a generative model such that random samples can be drawn from it. Each sample constitutes a possible realization of the image before knowledge of the data. It is then processed by the instrumental response function (Sect. 2.2.2) to arrive at a prediction of the data. Some time-varying instrumental effects, such as coherence loss over a baseline, cannot be described to sufficient accuracy by a deterministic model, and we account for them in a self-calibration approach (Sect. 2.2.3). The agreement between predicted and actual data is then quantified by the likelihood (Sect. 2.2.4). With this, all the components are in place to compute the posterior of a certain sample. Finally, the exploration of the posterior is performed with the MGVI algorithm (Sect. 2.2.5).

2.2.1 Prior model for the Galactic Center

A major challenge in imaging the GC is the variability of Sgr A*. During very bright epochs, it can outshine ambient stars and the signal more strongly resembles the expectation for a single point source. When Sgr A* is fainter, on the other hand, signatures of the stars in its vicinity become very apparent. Continuous alteration of the flux, between the two extreme cases, prevents the naive combination of exposures over a longer observing period. We account for it by describing Sgr A* as a time-variable point source that we superimpose on the actual, static image.

In our prior model, the position of Sgr A*, $\vec{s}_{\mathrm{SgrA}}$, follows a Gaussian distribution with user-defined mean and variance. For the flux $I_{\mathrm{SgrA}}(t, p)$, we impose a log-normal distribution, and account for the variability by inferring an independent flux value for each exposure t. While it would, in principle, be possible to explicitly model the temporal correlation, namely, along the lines of Arras et al., 2020, this further increases the size and complexity of the parameter space, introduces additional hyper-parameters, and makes the sampling more demanding. We therefore leave the exploration of this option to future studies. Furthermore, the emission from Sgr A* is known to be polarized, with the polarization also varying on short timescales (Trippe et al., 2007; Zamaninasab et al., 2010; Shahzamanian et al., 2015; GRAVITY Collaboration et al., 2018a; GRAVITY Collaboration et al., 2020d). We thus also allow for Sgr A* to have differing, independent fluxes in each of the two polarization states observed by GRAVITY and which we have labeled as p.

The actual image, $I_{\mathrm{Img}}(\vec{s})$, then contains the stars in the vicinity of Sgr A*, where $\vec{s}$ refers to the angular direction relative to the phase center. It must be large enough to cover

the full FOV of the GRAVITY fibers, which have a full width half maximum (FWHM) of about 65 mas. On the other hand, the pixel scale $\delta\alpha$ needs to be sufficiently small to describe the highest spatial frequencies or smallest scales observed by GRAVITY. The latter requirement is the Nyquist–Shannon theorem to avoid spectral aliasing and imposes $\delta\alpha \leq \lambda/(2b_{\max})$ (Thiébaut, 2008). With the longest baseline of 130 m and the smallest used spectral channel at $\lambda_{\min} = 2.11\,\mu$m, this requires $\delta\alpha \lesssim 1.7$ mas. By using a grid with 256^2 pixels of 0.8 mas size, we can meet both requirements simultaneously at manageable computational costs.

To GRAVITY, stars in the GC appear as unresolved point sources. Consequently, we assume that all pixels in the image are statistically independent. We note that this statement applies to the sky prior model and that correlations between nearby pixels introduced by the instrument's finite spatial resolution are described by the response function (Sect. 2.2.2). Furthermore, we expect to see only $\mathcal{O}(1)$ stars in the image such that the vast majority of pixels will be dark. We describe this situation by imposing an inverse-Gamma prior on the brightness of each pixel:

$$\mathcal{P}(I_{\mathrm{Img}}) = \prod_i^{N_{\mathrm{pix}}} \frac{q^\alpha}{\Gamma(\alpha)} I_{\mathrm{Img}}(i)^{-\alpha-1} \exp\left[\frac{-q}{I_{\mathrm{Img}}(i)}\right]. \tag{2.2}$$

Here, the index i labels all pixels in the image, Γ is the Gamma function, and q and α are two parameters that need to be specified before applying the code. They determine the a priori probability of encountering a bright star (where larger α implies a smaller probability) and allow for the mode of the distribution, $q/(\alpha+1)$, to be set to some background level.

As discussed at length in the following section, the primary observables in optical and near-IR interferometry are the complex visibilities (cf. Eq. 2.3), given by the ratio between the coherent flux of a baseline and the flux on each of its two telescopes. Consequently, the data is only sensitive to the relative brightness of all sources. The maximum possible value for the visibility amplitude equals unity and decreases in the presence of a homogeneous background. With this in mind, we set $q = 10^{-4}$ and $\alpha = 1.5$. In a typical GC observation, the instrumental visibilities are on the order of 0.5, such that this setup implies $\mathcal{O}(1)$ point sources. The probability of encountering a unit point source in the image of faint sources, on the other hand, is $\sim 5\%$. We further chose zero as the mean and unity as the variance for the Sgr A* log-flux prior, whereby the large flexibility of the log-normal distribution can easily accommodate changes by an order of magnitude.

In many observations, there are bright stars within the FOV around Sgr A*, whose positions can be adequately predicted from their known orbits. We incorporate them into our model by allowing for additional point sources with a Gaussian prior on their position and a log-normal flux prior. In contrast to Sgr A*, we assume the flux to be constant in time and the same for both polarization states. In principle, these stars could also be attributed to the image; modeling them explicitly helps to mitigate pixelization errors and improves the convergence.

Finally, the model describes the spectral distribution of Sgr A* and the stars as two power laws with different spectral indices. These follow a Gaussian prior whose mean

we set to -1 and $+2$ for Sgr A* (Genzel et al., 2010; Witzel et al., 2018) and the stars respectively. As variance, we assume 3 for both the stars and Sgr A*. A mathematical description of the sky model is provided in Eq. (3), and the priors on each of its components are noted down explicitly in Eq. (8) to Eq. (13).

2.2.2 Instrumental response function

The primary observable of GRAVITY is the complex visibility, measured as the coherent flux over a baseline, $\boldsymbol{b}$, divided by the flux on each telescope forming that baseline. In an idealized setting, it is related to the sky flux distribution, $I(\boldsymbol{s}, \lambda)$, by

$$v(\boldsymbol{b}/\lambda) = \frac{\int_{\mathrm{FOV}} \mathrm{d}\boldsymbol{s}\ I(\boldsymbol{s}, \lambda)\ \mathrm{e}^{-2\pi \boldsymbol{b}\cdot\boldsymbol{s}/\lambda}}{\int_{\mathrm{FOV}} \mathrm{d}\boldsymbol{s}\ I(\boldsymbol{s}, \lambda)}\,, \tag{2.3}$$

where λ is the wavelength. In reality, instrumental effects render the response equation more complicated. We discuss the modifications qualitatively in the following and the generalized expression is given in Eq. (1).

The relevance of the denominator in Eq. (2.3) is most intuitively understood by considering a homogeneous background flux, which averages out in the numerator term for $\boldsymbol{b} \neq 0$ but affects the denominator. We therefore implemented the Fourier transform and the normalization term explicitly in the response function.

Equation (2.3) constitutes a simplification in that not all sources are coupled into the fiber equally. GRAVITY uses single mode fibers, which have a Gaussian acceptance profile, to transport the light from the telescope to the beam combiner (GRAVITY Collaboration et al., 2017). The coupling of light into the instrument is further affected by diffraction (Shaklan and Roddier, 1988; Guyon, 2002) and residual tip-tilt jitter from the AO system (Perrin and Woillez, 2019). Both effects lead to a wider FOV than implied by the fiber profile alone. Furthermore, there are static optical aberrations along the GRAVITY light path which impact also the phase of the transmitted light (GRAVITY Collaboration et al., 2021c). These aberrations are different for each of the four telescopes.

Taken together, fiber damping and optical aberrations act as a position dependent phase screen which multiplies the image inside the Fourier transform. With the measurement of these so-called phase- and amplitude-maps in GRAVITY Collaboration et al., 2021c, we are able to provide a full model of the optical aberrations and fiber damping, which we include in the implementation of the response function.

GC observations with GRAVITY are carried out in low spectral-resolution mode and the effect of the spectral bandwidth on the measurement needs to be taken into account. This is known as bandwidth smearing and it leads to a further modification of Eq. (2.3), where the numerator and denominator are independently integrated over the bandpass, namely, $\int \mathrm{d}\lambda P(\lambda)$. In the most simple case of flat spectral distributions, bandwidth smearing multiplies the visibility amplitudes by a sinc function. For a more realistic scenario in which the source's spectral distribution is modeled as a power law, bandwidth smearing is described by a generalized complex gamma function and, thus, it also affects the visibility

phases. Either way, the effect on the measured visibilities increases with the source distance from the image center.

We account for the finite bandpass size by evaluating the Fourier transform in Eq. (2.3) at multiple values of λ, spread equally over a top-hat bandpass and taking the average. The complete response equation and details about its efficient implementation are provided in Appendix A1.1.

2.2.3 Self-calibration

There are time-variable instrumental effects that our response function does not capture, such as coherence loss on a baseline or telescope-dependent phase errors, for instance, from atmospheric conditions or instrumental systematics. The former leads to a reduction of the measured visibility amplitude, while the latter impacts the visibility phase. If unaccounted for, either of these effects can significantly degrade the imaging solution.

We resolve telescope-dependent phase errors by working with closure phases (Rogers et al., 1974),

$$\phi_{i,j,k} = \arg\left(v_{i,j}\, v_{j,k}\, v_{k,i}\right) , \tag{2.4}$$

which are formed over a triangle of telescopes i, j, and k, such that telescope-based errors are canceled out. The VLTI consists of four telescopes, implying that six visibility phases and four closure phases can be measured per spectral channel.

GRAVITY carries out a visibility measurement for each baseline. With regard to the amplitudes, we thus adopted a self-calibration approach in which we infer an independent scaling factor, $C\left(t,\, b\right)$, for each exposure and baseline, b. This factor joins the list of free model parameters in Appendix A1.2. We impose a Gaussian prior on the scaling factor with unit mean and standard deviation 0.1, as given by Eq. (13).

Visibility amplitudes and closure phases are both translation-invariant, that is to say that in the absence of absolute phase information, any global shift of the image will not affect the posterior. Phase- and amplitude maps as well as bandwidth smearing partly break the degeneracy, but these instrumental effects are not sufficiently strong to reliably center the image, particularly if the brightest sources are located close to the image center. Instead, we fix the position of one point source, usually Sgr A*, which we refer to as as the anchor for our images.

2.2.4 Likelihood

In the limit of sufficiently high signal-to-noise ratios (S/N), that is S/N $\gtrsim 2-5$, the noise properties of visibility amplitudes and closure phases are well approximated by a Gaussian distribution (Blackburn et al., 2020). This condition is well satisfied for typical GC observations with GRAVITY.

However, only three of the four closure triangles available to GRAVITY are statistically independent. In principle, we need to account for this by selecting a reduced, non-redundant closure set whose cross-correlations are captured by a non-diagonal covariance.

In practice, and in the limit of equal S/N on all telescopes, equivalent likelihood contours can be obtained from the full closure set without accounting for cross-correlations by up-scaling the error bars with a redundancy factor $N/3$, where N is the number of telescopes (Blackburn et al., 2020). In this work, we adopt the latter formulation.

Forward modeling approaches are rather sensitive to underestimated error bars. In the case of our imaging code, we observe that overfitting the data can introduce spurious sources in the images. To avoid any potential bias, we applied a conservative $\mathcal{O}(1)$ factor to the error bars in the first imaging iteration. This factor may differ for closures and amplitudes but it is common to all frames and baselines. We then checked the residuals and adjust the error scaling for subsequent runs, aiming for a reduced χ^2 of $0.95 - 1.0$ for visibility amplitudes. To realize the aforementioned redundancy factor, the targeted reduced χ^2 for the closure phases is smaller than the noise expectation from Gaussian statistics and in the range of $0.7 - 0.75$.

2.2.5 Inference strategy

The goal of the inference is to explore the posterior distribution in Eq. (2.1) around its maximum over a very high dimensional parameter space. Indeed, for a data set consisting of N_{exp} individual exposures and considering N_{PS} static point sources in the prior model, the dimensionality is

$$
\begin{aligned}
d &= 256^2 && \text{image of faint sources} \\
&+ 2 \times N_{\mathrm{exp}} && \text{Sgr A* light curves} \\
&+ 2 && \text{Sgr A* position} \\
&+ 3 \times N_{\mathrm{PS}} && \text{point sources position and flux} \\
&+ 6 \times N_{\mathrm{exp}} && \text{amplitude self-calibration} \\
&+ 2 && \text{spectral indices} \\
&\sim 7 \times 10^4 \,. &&
\end{aligned}
\tag{2.5}
$$

Here, the factor of two in the light curves arises from the two polarization states observed by GRAVITY and there are six baselines available. Dealing with such high-dimensional distributions is notoriously difficult and computationally expensive.

The MGVI algorithm (Knollmüller and Enßlin, 2019) used in this study searches for a multivariate Gaussian distribution $\mathcal{G}\left(\xi|\,\vec{\bar{\xi}},\,\Xi\right)$ that best approximates the full posterior. Here, $\vec{\xi}$ are standardized coordinates, thus we mapped each degree of freedom to an auxiliary parameter or excitation ξ, whose prior is given by a unit Gaussian with zero mean. The inference targets the excitations rather than the physical quantities, however, the two are uniquely related by a mapping (given in Appendix A1.2). As an advantage, this setup makes it fast and easy to draw samples from the prior.

The mean $\vec{\bar{\xi}}$ and covariance Ξ of the posterior approximation are found in an iterative procedure. Starting at some initial position $\vec{\bar{\xi}}_i$ $(i = 0)$, MGVI uses a generalization of the

Fisher metric (cf. Eq. 17) to approximate the covariance. This is a $d \times d$ matrix, and by allowing for non-zero off-diagonal elements, MGVI is able to capture cross-correlations between individual model parameters. Since the explicit storage of d^2 matrix elements becomes prohibitive for large inference problems, an implicit representation in the form of a numerical operator is used internally.

In the next step, the mean of the approximate distribution $\bar{\xi}$ is updated with the aim to increase the overlap between approximate and true posterior $\mathcal{P}(\xi|d)$. This overlap is quantified by the Kullback-Leibler divergence (KL), such that updating $\bar{\xi}$ amounts to minimizing the KL, that is,

$$\bar{\xi}_{i+1} = \min_{\bar{\xi}} \int \mathrm{d}\xi \; \mathcal{G}\left(\xi|\,\bar{\xi}, \Xi_i\right) \ln \left[\frac{\mathcal{G}\left(\xi|\,\bar{\xi}, \Xi_i\right)}{\mathcal{P}\left(\xi|\,d\right)}\right] . \tag{2.6}$$

The minimum is insensitive to any multiplicative factors applied to the true posterior as long as they are independent of ξ, thus, the omission of the evidence term in Eq. (2.1), in fact, does not affect our analysis. To estimate the expectation value in the KL numerically, MGVI draws samples from the approximate posterior distribution and replaces the integral in Eq. (2.6) by the sample mean. Once $\bar{\xi}$ has been updated, MGVI computes the covariance at the new position and henceforth alternates between the Ξ and $\bar{\xi}$ determination.

After the final iteration, the primary product is a set of samples distributed according to the approximate posterior distribution. These samples can then be used to compute expectation values and their standard deviations, which we report as our main results.

We note that MGVI leaves it to the user to set the number of samples and minimization steps at each iteration as well as the total number of iterations. A good practice is to start with few samples and steps, then increase both quantities as the inference approaches the posterior maximum. Details about the scheme used for this work are given in Appendix A1.3, where we also specify the minimizers and iteration controllers used. For the initial position from which to start the inference, we align all parameters with the mode of their respective priors.

Two obstacles in the minimization procedure demand special attention, namely: the convergence of our results and the possibility of multi-modal posterior distributions. In case of the latter, the Gaussian approximation obtained from MGVI captures one typical posterior mode. Exploring multi-modal distributions in such high-dimensions is genuinely a very difficult, computationally expensive problem for which there currently exists no standard practice. To maintain some handle on the multi-modality of the posterior and to judge how well the algorithm has converged, we exploit the inherent stochasticity of MGVI that arises when the KL is estimated from random samples. As our results below indicate, changing the random seed from which samples are drawn can nudge the algorithm to explore different posterior modes. In addition, poorly converged runs – which are typically more noisy and might contain over-fitted sources or might fail to detect a faint source – also occur just for individual random seeds, such that they can be judged and eliminated by comparing results from multiple random seeds.

For a typical data set, we performed ten independent imaging runs with different random

seeds. This number is large enough to capture the dominant modes of the posterior but too low to determine their relative weights reliably. Instead, we used the fact that we have multiple data sets available and judged the images by their consistency over the full 2021 observing period.

2.3 Data

For this study, we considered GC observations with GRAVITY from 2021. They are separated into four epochs taking place at the end of March, May, June, and July, respectively. The data were obtained with GRAVITY's low spectral-resolution, split-polarization mode. Each exposure consists of 32 individual frames with 10 s integration time. Most of them are centered on Sgr A*, and the Sgr A* observing blocks are bracketed by S2 and R2 pointings that are required for calibration and to monitor the S2 orbit. The data were reduced by the GRAVITY standard pipeline and calibrated with a single, carefully chosen S2 exposure from the same night.

We used the data to obtain night-wise images of Sgr A* and its vicinity. To have sufficient (u, v)-coverage, we required $\mathcal{O}(10)$ exposures at least and selected those nights with a larger number of Sgr A* pointings available. The selection is summarized in Table 2.1.

Table 2.1: GC observing nights selected for Sgr A* imaging.

Date	Available exposures	N_{exp}	$\langle\sigma_\rho\rangle$	$\langle\sigma_\phi\rangle$
2021-03-30	13	13	4.5×10^{-2}	33.2°
2021-05-22	20	19	3.3×10^{-2}	10.5°
2021-05-29	22	21	3.5×10^{-2}	19.3°
2021-05-30	20	20	3.7×10^{-2}	24.3°
2021-06-24	32	29	3.6×10^{-2}	20.7°
2021-07-25	28	22	3.1×10^{-2}	15.3°
2021-07-26	20	20	3.6×10^{-2}	19.6°
2021-07-27	20	19	2.8×10^{-2}	10.3°

Notes. Each exposure amounts to a 320 s integration time. For some nights, we deselected exposures which were affected by bad weather or instrumental problems, such that the number of exposures used in the imaging, N_{exp}, is smaller than the total number of exposures available. The last two columns give the mean standard deviation of the closure phases and amplitudes. If a scaling factor was applied to the error bars, this is included.

The Sgr A*-centered images from March to June revealed a faint object, moving to the west at high angular velocity. To track this new star and to also scan a wider field, we performed a series of pointings in July, where we offset the fiber from Sgr A*. Further, to the south west of Sgr A* there is S38 with a separation too large to be detected in the Sgr A*-centered images. For the July observing run, there are a sufficiently large number

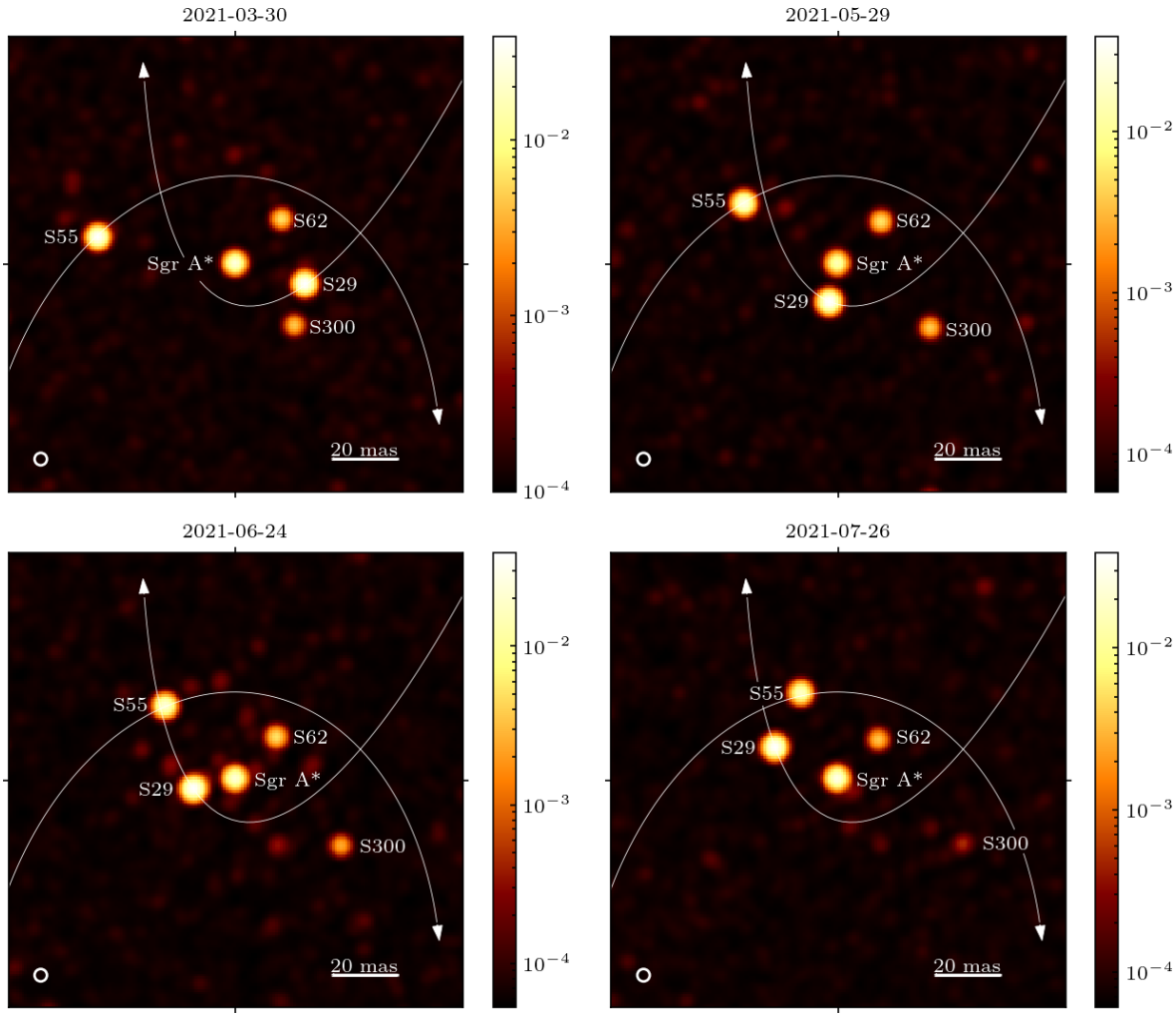

Figure 2.1: Images for one night per observing epoch in 2021, where north is up, east to the left, and the flux normalized to S29. For each night, we performed ten imaging runs with varying random seeds and then picked the cleanest result with the highest degree of consistency over the full year. Images are computed as mean over all samples in the chosen run, centered on Sgr A*, and smoothed with a Gaussian of 1.6 mas standard deviation, whose FWHM is indicated in the bottom left corner. Sgr A* varies in flux, and we here show its mean brightness over all exposures and polarization states. On each image, we overdraw the orbits of S29 and S55 and the labels of all identified sources to give a better orientation. We note that due to the large dynamical range and the logarithmic color scaling, sources appear more widespread.

Table 2.2: Overview of the mosaicing data set.

Name	Date	# of exposures	Pointing offset w.r.t Sgr A* (RA, Dec [mas])	Preset sources	Anchor
S2	2021-05-29 & 30	13	24.8, 142.4	S2	S2
NW	2021-07-29	8	−45.0, 45.0	Sgr A*, S29, S55, S42	S42
SE	2021-07-29	8	45.0, −45.0	Sgr A*, S29, S55	Sgr A*
mid	2021-07-29	7	−24.8, −31.4	Sgr A*, S29, S55	Sgr A*
S38	2021-07-25 & 26	8	−38.6, −76.8	S38	S38

Notes. The second to last column lists all sources which are modeled as point sources with a Gaussian position prior. To break the translation invariance inherent to closure phases and visibility amplitudes, we fix the location of one bright point source, which we call the anchor for that image.

of S38-centered exposures available to attempt reconstructing an image from them. Just as with the Sgr A*-centered exposures, the data were reduced by the standard pipeline and calibrated with a single S2 file. Finally, we also considered S2-pointings from May, which were calibrated with R2. The so-called "mosaicing data set" is summarized in Table 2.2.

2.4 Results

We apply the G^R imaging algorithm (introduced in Sect. 2.2) to obtain night-wise images from the data summarized in Tables 2.1 and 2.2. Here, we first focus on observations with Sgr A* at the center and come back to the mosaicing data set later on.

The final output of the MGVI algorithm is a set of samples drawn from the approximate posterior. Our best image is computed as the mean over these samples and we add the flux of all additional point sources to the appropriate pixels. Because of the normalization term in the instrumental response function (cf. Eq. 2.3), the likelihood is insensitive to a global scaling of the flux. In a post-processing step, we therefore normalize our images to the flux of S29 ($m_K\,(\mathrm{S29}) \simeq 16.6$, GRAVITY Collaboration et al., 2021b), which is the brightest static source in the field. The implementation of the response function presented in Appendix A1.1 explicitly takes into account fiber damping, which reduces the flux transmission for off-center sources; thereby, our images are automatically corrected for this effect. Finally, we smoothed the images with a Gaussian of 1.6 mas standard deviation. This corresponds to the typical size of the CLEAN beam, that is, a Gaussian fit to the central part of the dirty beam pattern.

2.4.1 Detection of S29 and S55 within 50 mas of Sgr A*

In 2021, there are two relatively bright stars in the FOV around Sgr A*, which are S29 with a K-band magnitude of $m_K\,(\mathrm{S29}) \simeq 16.6$ (GRAVITY Collaboration et al., 2021b) and S55 with $m_K\,(\mathrm{S55}) \simeq 17.6$ (Gillessen et al., 2017). In particular the cross-identification of S29 in earlier AO-based NACO images has been subject of debate recently (Peißker et al., 2021). We discuss this in Appendix A1.4.

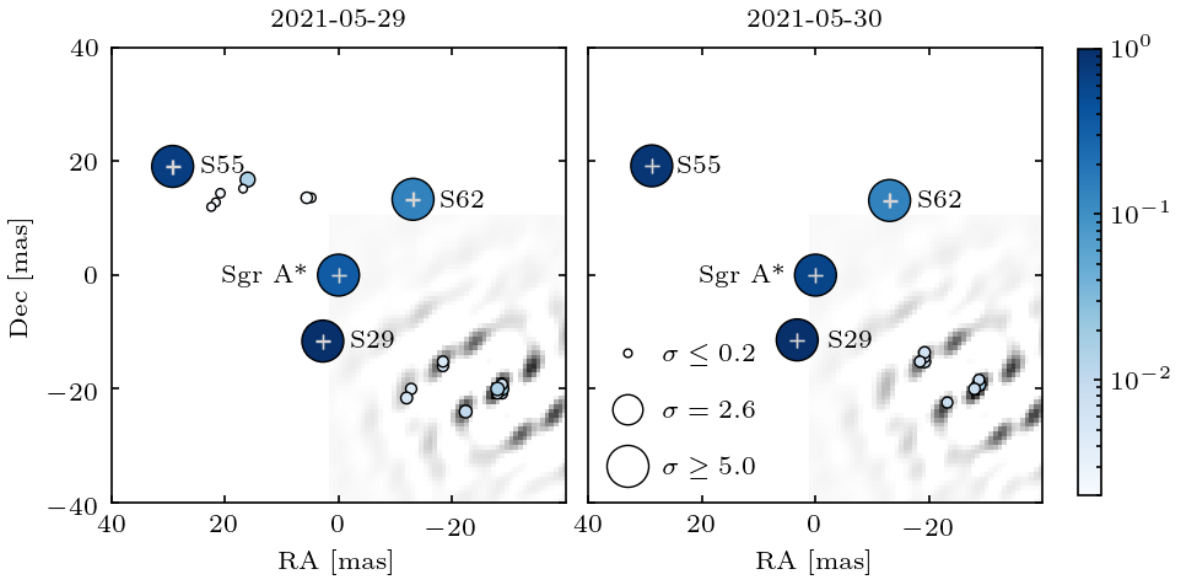

Figure 2.2: Combined view on all imaging runs from a single night (see Appendix A1.5 for details on the illustration). The symbol color indicates the flux of a source candidate, normalized to S29, while the symbol size represents its significance. The Sgr A* flux depicted here has to be multiplied by the light curve at each exposure to arrive at the true flux ratio. For stars that are modeled as a point source, the position uncertainty is indicated in gray. Sources are shown superimposed on the dirty beam pattern of the imaging night, which we have centered at the position of S300.

The orbital motions of S29 and S55 around the black hole are overdrawn on the images in Fig. 2.1. In a couple of test runs, we find that our algorithm is easily capable of detecting each of them. The detection of S29 and S55 in the 2021 Sgr A*-centered exposures also is a prerequisite and starting point for astrometric fitting to extract high-accuracy stellar positions.

In what follows, we model S29 and S55 as point sources, superimposed on the image as described in Sect. 2.2.1. Each of the sources has a Gaussian prior on its position, whose mean we obtain either from orbit predictions or from the pixel position in a pre-imaging run. To avoid any bias arising from the latter procedure, we chose a deliberately large standard deviation for the sources' position priors of 2.4 mas in RA and Dec. This corresponds to three pixels in our image and is larger than the beam width in any of the observations considered. Since Sgr A* is fixed at the image center to break the translation invariance inherent to closure phases, mapping the stars' separation vector to an image position is straightforward.

Table 2.3: Separation between S62 and Sgr A* obtained from imaging runs in which S62 was modeled as point source with a Gaussian position prior.

Epoch	RA [mas]	Dec [mas]
2021.2453	-13.85 ± 0.11	14.00 ± 0.10
2021.3902	-13.03 ± 0.05	13.12 ± 0.06
2021.4093	-13.12 ± 0.06	13.33 ± 0.07
2021.4120	-13.05 ± 0.06	13.13 ± 0.08
2021.4803	-12.78 ± 0.04	12.84 ± 0.05
2021.5649	-12.60 ± 0.04	12.67 ± 0.05
2021.5657	-12.74 ± 0.05	12.64 ± 0.07
2021.5703	-12.71 ± 0.09	12.57 ± 0.14

Notes. The epoch is computed as mean over all exposures used for the image. For each night we performed ten G^R runs with varying random seeds and combined the samples from all runs into an estimate of the S62 position and its standard deviation. We note that the standard deviation only accounts for the statistical position uncertainty, but not for any systematic error.

2.4.2 Detection of S62

In GRAVITY Collaboration et al., 2021b, CLEAN images revealed a 18.9 K-band magnitude star which slowly approaches Sgr A* and was identified as S62. Extrapolating the motion observed in 2019, we expect S62 at RA = (-14.1 ± 0.4) mas, Dec = (13.6 ± 0.8) mas in March 2021. By July, it should move to RA = (-13.2 ± 0.4) mas, Dec = (12.3 ± 0.9) mas.

An important test for the new imaging method is whether it is also able to detect S62. Indeed, for all nights we infer flux at the expected position. This detection is very robust, namely, $> 5\sigma$ for almost all random seeds and even holds if the error bars are moderately over-scaled. To determine the S62 coordinates beyond the accuracy of the pixel size, we then include it into the set of point sources inferred on top of the image and perform ten imaging runs with varying random seeds for each night. The results are consistent between all runs of an individual night. We are thus able to combine the samples from all ten runs into an estimate on the mean S62 position and its variance. This is summarized in Table 2.3 and it does match the prediction from GRAVITY Collaboration et al., 2021b very well.

Furthermore, we use the positions in Tab 2.3 to provide an updated on the motion of S62. From a linear fit that also considers the results from 2019 observations (GRAVITY Collaboration et al., 2021b), we obtained the following for the relative velocity w.r.t. Sgr A*:

$$v_{\mathrm{RA}} = (2.97 \pm 0.05)\ \mathrm{mas\ yr}^{-1},$$
$$v_{\mathrm{Dec}} = (-3.58 \pm 0.09)\ \mathrm{mas\ yr}^{-1}.$$

The slow linear motion of S62, observed with GRAVITY consistently in 2019 and 2021, does not fit a star with a 9.9 year orbital period as reported in Peißker et al., 2020. In

Appendix A1.4, we explain in detail the cross-identification of all further sources in the FOV, S29, and S55, namely, between GRAVITY and earlier AO-based images. Thus, the GRAVITY images do not support the existence of a star that orbits Sgr A* with a 9.9 year period.

2.4.3 Discovery of S300, a faint fast-moving star

The main goal of our imaging analysis is to search the vicinity of Sgr A* for faint, as-yet-unknown stars. To this end, we used the same ten imaging runs per night from which we measured the S62 position (detailed in Sect. 2.4.2). A representative image for each epoch is shown in Fig. 2.1. In Appendix A1.5, we provide a complementary view of the imaging results for all nights listed in Table 2.1, which accounts for the statistical nature of our algorithm.

In addition to the four expected sources – Sgr A*, S29, S55, and S62 – our images contain a fifth object that is fainter than all aforementioned stars. It moves to the west with a high angular velocity, so that the change in position can be recognized very clearly between individual months. In the following, we discuss this detection for each epoch separately.

March 2021

Due to the limited observability of the GC in March, this is the data set with the sparsest (u, v)-coverage. However, it is also the epoch where the new source is closest to the center of the FOV and thus it is the least affected by fiber damping. Of the ten imaging runs we performed, five detected the new source as a single bright pixel with high significance ($> 5\sigma$). Its location on the grid can vary by one pixel between runs. Two further runs infer flux at the same position, but smeared out over multiple neighboring pixels.

May 2021

In Sect. 2.2.5, we mention the possibility of multi-modal posterior distributions. Indeed, the only data set where we have clear signs of such an issue are the three Sgr A*-centered images from May 2021.

All ten imaging runs for May 29 infer a single bright pixel to the south west of Sgr A* at a high significance. In three instances, however, the location of this pixel is shifted towards the image center. A similar situation arises for May 30. In four instances, the location of the bright pixel coincides with the position found for the previous night, otherwise it is shifted inwards.

We illustrate this situation in Fig. 2.2, where we have combined the samples from all ten imaging runs into a single figure for each night. Even though the new source is detected with a high significance in individual $\mathrm{G^R}$-runs, the fact that its location varies between runs makes the overall significance estimate decrease in Fig. 2.2 (cf. Appendix A1.5). The sources detected in the image are superimposed on the dirty beam pattern of the respective

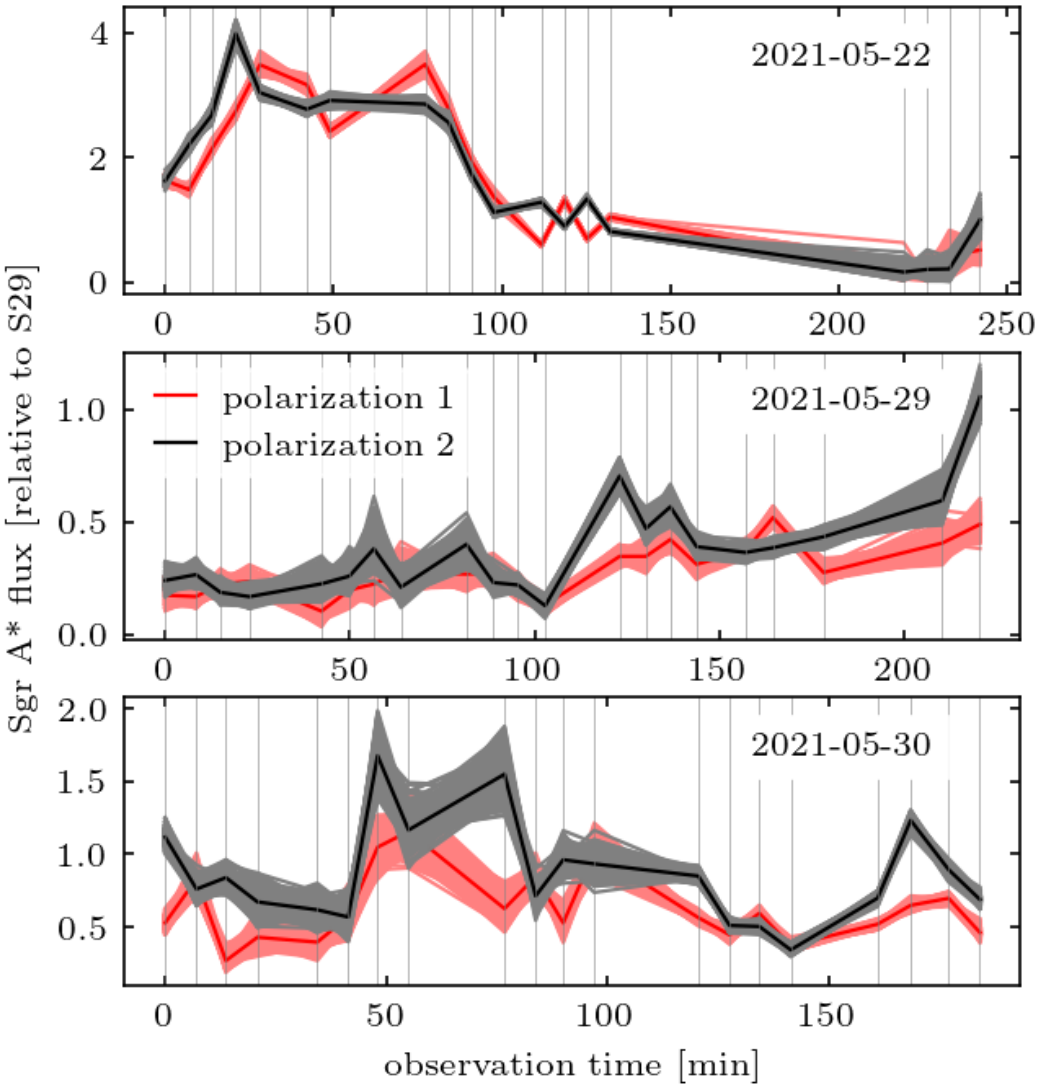

Figure 2.3: Light curves inferred with the G^R-code for the May observing nights. Light lines in gray and red indicate the individual samples and dark lines show the sample mean. Here, we combined all samples from all imaging runs of a particular night. The time of the individual exposures is indicated by vertical lines. We note that S2 is about 11 times as bright as S29.

nights to illustrate the reason behind the observed multi-modality. This shows that the inward-shifted detections of the new source correspond to side-maxima or side-lobes of the dirty beam pattern.

On May 29, the algorithm apparently is somewhat more successful at disentangling the true source position and its side-lobes than on May 30. There are two possible reasons for this, the first being that the data set for May 29 contains one more exposure and on average exhibits smaller error bars than that of May 30, as Table 2.1 indicates. Secondly, the light curves that we obtain as part of the inference are shown in Fig. 2.3 for all May nights. They disclose that Sgr A* was slightly brighter on May 30 than on the 29th. When the complex visibilities are dominated by the central source more strongly, the detection of the faint source further out in the field becomes more difficult.

The images that we infer for May 22 also are consistent with that line of reasoning. As Fig. 2.3 shows, Sgr A* went through a moderate flare in the beginning of the night. While all imaging runs for May 22 clearly exhibit some flux to the south west of Sgr A*, no consistent source position can be identified from the comparison of multiple runs (cf. Fig. 4).

June 2021

For the large June imaging data set, all ten imaging runs exhibit flux at the same location to the south west of Sgr A*. In five instances, this flux is detected in a single pixel with high significance ($> 5\sigma$). Its position scatters by at most a pixel. In the other five instances, the flux is spread out over several connected pixels, which exhibit larger flux variations between the individual samples.

Since the source has moved further away from the field center and is more strongly affected by fiber damping than it was in May, the question arises why no similar multi-modality of the posterior is observed. On June 24, we have a much better (u, v)-coverage and the dirty beam pattern becomes considerably smoother without the isolated, strongly peaked side-maxima that induce the misplacement in the May images.

July 2021

We are able to detect the new source only in one of the July observing nights which is July 26. Even so, it is found in five of the ten imaging runs at a low significance smeared out over multiple pixels. Correspondingly, the source appears fainter in the final image of Fig. 2.1. Since the new star is most strongly affected by fiber damping in July, this loss of sensitivity does not come as a surprise. We discuss it further in Sect. 2.4.5.

We summarize the source position inferred for each night in Table 2.4, along with its flux relative to S29. For the latter, we selected all runs in which the new source is found as a single bright pixel in the correct location and combined all samples in these runs. That is, we exclude runs from the flux estimate that failed to identify the new source, where the new source was misplaced at a side-lobe, or where its flux was smeared out over multiple pixels.

Table 2.4: Position of S300, the newly detected star, with respect to Sgr A*.

Epoch	RA [mas]	Dec [mas]	Flux/S29
2021.2453	-18.0 ± 0.8	-19.6 ± 0.8	0.11 ± 0.01
2021.4093	-28.4 ± 0.8	-20.4 ± 0.8	0.09 ± 0.01
2021.4120	-28.4 ± 0.8	-18.8 ± 0.8	0.08 ± 0.01
2021.4803	-33.4 ± 0.8	-20.4 ± 0.8	0.05 ± 0.02
2021.5657	-39.6 ± 0.8	-19.6 ± 0.8	–

Notes. The flux ratio relative to S29, is already corrected for fiber damping and the epoch is computed as mean over all exposures used in the imaging.

The position and motion of the new star matches none of the known S-stars (Gillessen et al., 2017) and we conclude that we have detected a new star, which we refer to as S300. We further discuss the possibilities for its nature in Sect. 2.5.2.

2.4.4 Images for the mosaicing data set

To produce images for the mosaicing data set, we used the exact same strategy as for the Sgr A*-centered exposures. The pointing directions and the known stars in the field are summarized in Fig 2.4. In Table 2.2, we list all stars that we model as point sources with a Gaussian position prior and the anchor, whose positional variance we set to zero in order to break the translation invariance inherent to closure phases and visibility amplitudes (cf. Sect. 2.2.3).

In contrast to the Sgr A*-centered images and with exception of the S2 pointings, we now have fewer than ten exposures available for each individual image. We thus expect (and also go on to find) that the solutions become more noisy and that there is a greater variability between the ten runs which we perform for each data set. The images obtained for the mid, NW, and S38 pointings are shown in Fig. 2.5, and the full statistical view over all results is provided in Appendix A1.5 and in Fig. 5.

The mid pointings were specifically designed to provide an additional test of the S300 detection. The fiber position is such that S300 is close to the center of the field, but Sgr A*, S63, and S38 can also be observed within the same pointing; Fig. 2.5 very clearly shows all the expected sources. The new source, S300, is detected with high significance ($> 5\sigma$) in each of the imaging runs, its position varies by at most one pixel in RA and two pixels in Dec. Combining all mid-pointing imaging runs, we obtain:

$$\begin{aligned} \mathrm{RA} &= (-38.8 \pm 0.8)\,\mathrm{mas}\,, \\ \mathrm{Dec} &= (-19.4 \pm 1.6)\,\mathrm{mas}\,, \\ \mathrm{flux/S38} &= 0.15 \pm 0.10\,, \end{aligned}$$

which is fully consistent with the position obtained from Sgr A*-centered images in Table 2.4.

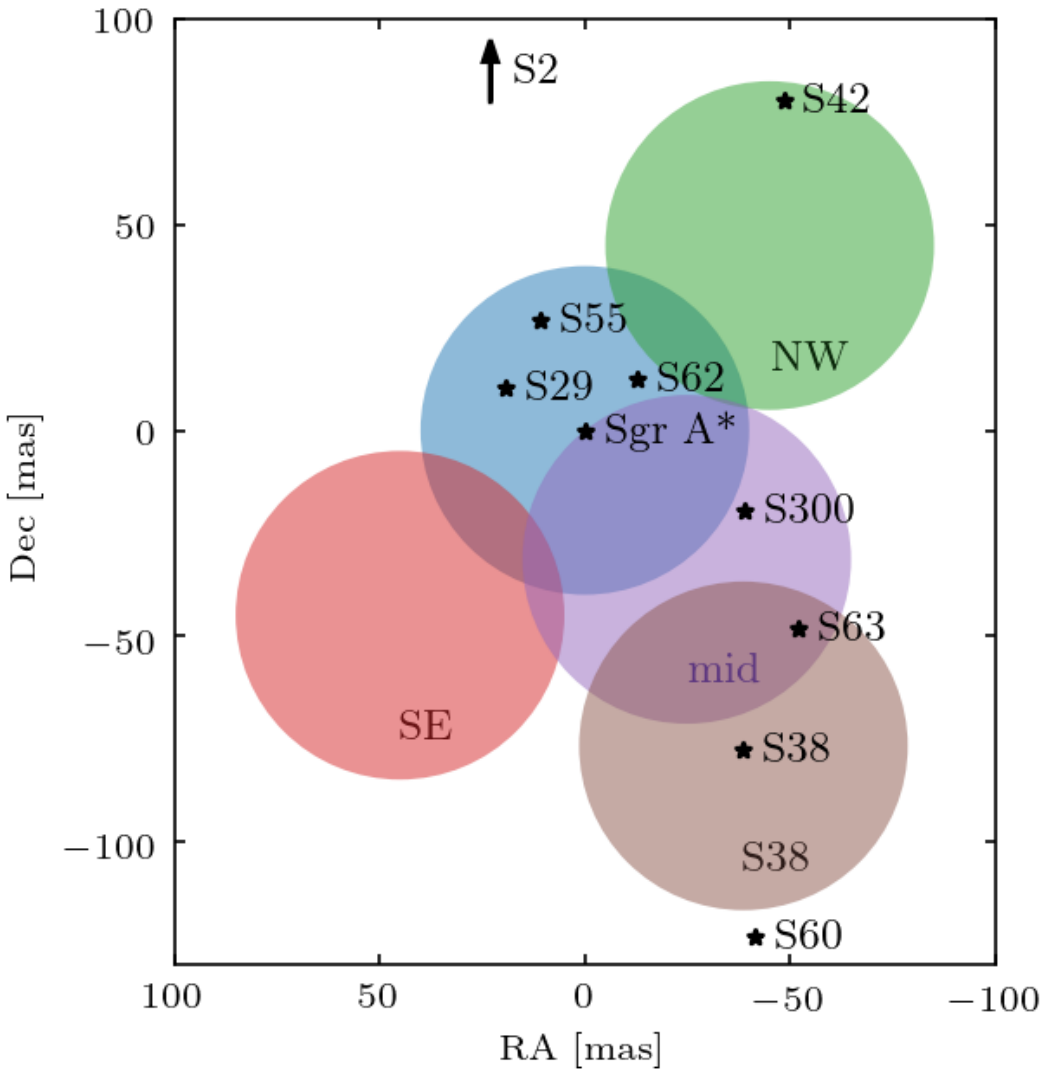

Figure 2.4: Summary of pointings in the mosaicing data set in the relation to the positions of all detectable stars during the July observing run. For completeness, we further include the Sgr A*-centered exposures (blue). Colored circles indicate the individual pointings and have diameters of 40 mas, which is half the extent of the images in Fig. 2.5.

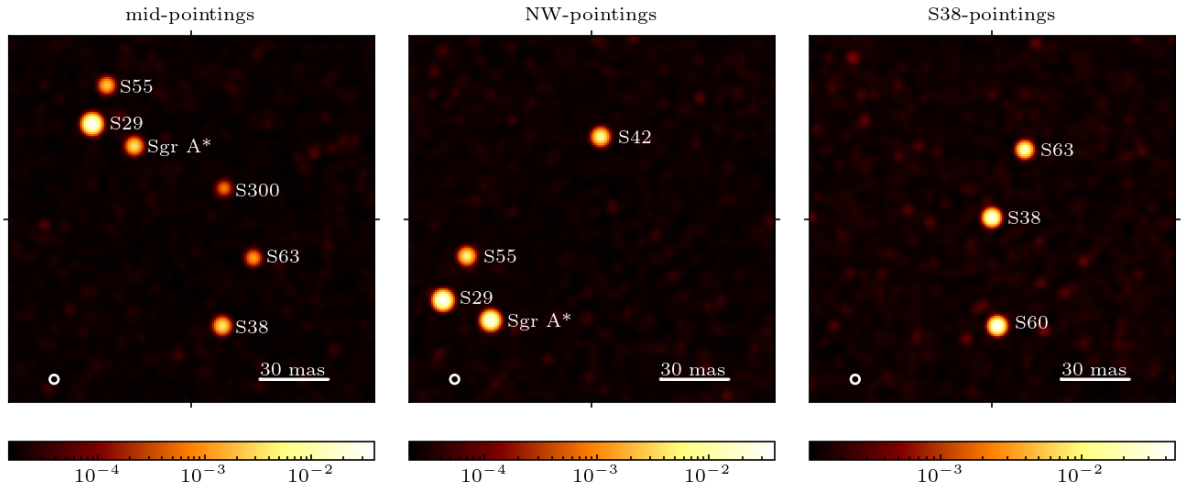

Figure 2.5: Images obtained for the mosaicing data set, where north is up and east to the left. The flux is normalized by S29 in the mid and northwest pointings and by S38 in the rightmost panel. Images are computed as sample mean over all samples of a single G^R run and have been convolved with a Gaussian of 1.6 mas standard deviation whose FWHM is indicated in the bottom left corner. The mid- and the S38-pointings extend the Sgr A*-centered images to the south west. S62 is not detectable in these images due to a combination of two effects. First, at this large distance from the image center, the already faint flux is further damped by the fiber profile; and secondly, the overall sensitivity of the images is reduced in comparison to the Sgr A* pointings because of the smaller number of exposures available.

An important difference to the Sgr A*-centered images, in particular, for the mid and S38 pointings, is that we did not pre-set all known sources in the field. In the former case, it was left to our algorithm to detect S300, S63, and S38; in the latter case, S63 and S60. In this context, the images in Fig. 2.5 also demonstrate how G^R is able to orient in a field with limited prior knowledge about the overall source structure. Apart from the stars that are sketched in Fig. 2.4 – namely Sgr A*, S2, S29, S38, S42, S55, S60, S63, and S300 – we do not detect any other objects.

The detection of all the aforementioned sources in the images also serves as a starting point for astrometric fitting to obtain high accuracy source positions (see GRAVITY Collaboration et al., 2020c, for details on the fitting procedure), which, in turn, allows us to determine the stars' orbits. We give an update on the orbital elements of all stars detected in the 2021 images in Table 2.5.

2.4.5 Sensitivity estimation

As a first step to estimate the sensitivity in our images, we performed a series of injection tests that are reported in Appendix A1.6. They consider sources at two different locations

Table 2.5: Orbital elements for six stars detected in the 2021 images.

Star	a[mas]	e	i [°]	Ω [°]
S2	124.95 ± 0.04	0.88441 ± 0.00006	134.70 ± 0.03	228.19 ± 0.03
S29	397.50 ± 1.56	0.96927 ± 0.00011	144.37 ± 0.07	7.00 ± 0.33
S38	142.54 ± 0.04	0.81451 ± 0.00015	166.65 ± 0.40	109.45 ± 1.00
S42	411.42 ± 7.14	0.77385 ± 0.00309	39.57 ± 0.19	309.60 ± 1.06
S55	104.40 ± 0.05	0.72669 ± 0.00020	158.52 ± 0.22	314.94 ± 1.14
S60	489.21 ± 18.55	0.77733 ± 0.00806	126.60 ± 0.15	178.03 ± 0.80
	ω [°]	t_P[yr]	T[yr]	m_K
S2	66.25 ± 0.03	2018.38 ± 0.00	16.046 ± 0.001	13.95
S29	205.79 ± 0.33	2021.41 ± 0.00	91.04 ± 0.54	16.6
S38	27.17 ± 1.02	2003.15 ± 0.01	19.55 ± 0.01	17.
S42	48.29 ± 0.46	2022.12 ± 0.02	95.9 ± 2.5	17.5
S55	322.78 ± 1.13	2009.44 ± 0.01	12.25 ± 0.01	17.5
S60	30.43 ± 0.21	2023.62 ± 0.05	124.3 ± 7.1	16.3

Notes. The parameters listed are the semi major axis, eccentricity, inclination, position angle of the ascending node, longitude of periastron, epoch of periastron passage, orbital period, and K-band magnitude. The stars S62 and S300 are not listed here, as their movement observed so far is consistent with a linear motion. Images serve as starting point for high-accuracy astrometric fitting, and the orbits are determined from positions provided by the latter.

and four magnitudes, between 19.7 and 22.7, which are inserted into the May 29 data set.

The ability of G^R to recover the injected source depends on its position. In the first scenario, the new star is located close to S300, and we managed a high-significance detection only at 19.7th magnitude. In addition, we observed a larger scatter around S300, and more flux is placed in its side-lobes. In the second case, the source is injected at same distance but to the north east of Sgr A*. Here, we can reach significantly deeper and manage a robust detection even at 21.0th magnitude.

We can also use S300 itself to estimate the sensitivity in our images. As the star moves away from the field center, it is more strongly affected by fiber damping and appears fainter to the GRAVITY instrument. Since S300 is most robustly detected close to the field center, we use the images from March, May, and the mid pointing in July to estimate its magnitude from which we obtain $m_{\mathrm{K}}\,(S300) \simeq 19.0 - 19.3$. The corresponding apparent magnitudes, that is, the magnitude corrected for fiber damping, are listed in Table 2.6 for all observing epochs.

Until June 2021, S300 is very robustly detected in our images which also matches the results of the mock tests above. In July, on the other hand, the apparent magnitude of S300 is already below 20, and we only managed a weak detection at low significance.

In addition to the heightened fiber damping, the large distance to the field center in

Table 2.6: Apparent magnitude of S300 in all four 2021 observing epochs.

Date	min $m_{\mathrm{K,app}}$	max $m_{\mathrm{K,app}}$
March 2021	19.3	19.7
May 2021	19.6	19.9
June 2021	19.8	20.1
July 2021	20.1	20.5

Notes. The apparent magnitude of a star accounts for corrections due to fiber damping if it is not located at the center of the FOV. The minimum and maximum values correspond to our bracketing estimates for the intrinsic S300 brightness.

combination with systematic effects can also affect the ability to detect S300 in July. In the context of our forward model, we can understand systematics as a mismatch between the predicted signal of the source and its actual effect on the data. It is expected that the quality of our modeling decreases for sources further away from the field center. The possible reasons for this include bandwidth smearing and optical aberrations in the instrument. Both effects become stronger further off axis, and, consequently, their modeling is more sensitive to approximations and calibration data, such as the bandpass shape or the aberration maps. It is important to note in this context, that Bayesian analyses in high dimensions are particularly vulnerable to model mismatches and that alternative tools can have a higher degree of robustness under such circumstances. We come back to this issue in Sect. 2.5.1, when we compare the new imaging algorithm to CLEAN.

At this point, we have encountered several factors beyond (u, v)-coverage and data quality that can considerably impact the sensitivity of our images, such as the brightness of Sgr A*, proximity to another faint source and the distance to the image center. Rather than giving a single estimate for the limiting magnitude, we therefore decided to highlight two bracketing values. Even under somewhat difficult circumstances – in June, S300 is already seen to be outside the FWHM of the fiber and in the first mock test, the injected source is very close to S300 – we are able to recover a source of at least $m_{\mathrm{K}} \simeq 19.7$ magnitude when corrected for fiber damping. On the other hand, mock tests at position 2, and also the low noise levels reported in Appendix A1.7, indicate that under favorable circumstances, we are able to push the sensitivity significantly beyond a magnitude of 20 with the newly developed $\mathrm{G^R}$ imaging algorithm.

2.5 Discussion

2.5.1 Confirmation of S300 with CLEAN

So far, the standard for deep imaging of the GC with GRAVITY has been set by CLEAN (GRAVITY Collaboration et al., 2021b), and comparing both methods is important to judge the performance of our new $\mathrm{G^R}$ algorithm. We therefore carried out an independent

analysis of the 2021 data with CLEAN (using the AIPS implementation, Greisen, 2003), which was already informed of the detection of S300 with G^R. In Fig. 2.6, we provide a representative image for each observing epoch and in Table 2.7, we list the corresponding data sets.

To successfully apply CLEAN to GRAVITY GC observations, a distinct procedure was developed and described in GRAVITY Collaboration et al., 2021b. Here, we adapt it to the changed field configuration in 2021. The major steps are laid out in the following.

Just as in 2019, we start by computing the coherent flux from the complex visibilities and the photometric flux observed at each telescope. To correct for flux variations (introduced e.g., by changes in air mass or the performance of the adaptive optics system), we interpolated the photometric flux of S2 across all frames collected for a night and normalized the coherent flux in the Sgr A*-centered pointings by this value.

We then cleaned on Sgr A* and S29 on an exposure-by-exposure basis. In particular, S29 is the brightest source in the field, but cleaning on Sgr A* is important due to its flux variations, which would otherwise render the data mutually inconsistent. After this has been resolved, we combine all Sgr A*- and S29-cleaned exposures from the night. In the resulting residual image, S55 is clearly visible and we jointly clean on the remains of Sgr A* and S29, as well as on S55. At this point, S62 usually becomes apparent. For three of the four nights shown in Fig. 2.6, it was the brightest residual, and it was only in the May imaging that it appeared as the second brightest.

The images obtained with CLEAN (cf. Fig. 2.6) agree very well with the G^R results (cf. Fig. 2.1). Both methods recover an identical image structure that is dominated by the four established stars and matching source positions. Further, the CLEAN images confirm the detection of S300. For the March and May nights shown in Fig. 2.6, after S62 has been cleaned, a bright residual becomes visible whose location is consistent with the G^R discovery. It corresponds to the second-brightest residual on March 27 and the third-brightest on May 29. Also on the June night, a residual is visible at the expected S300 position; however, in this case, it is not among the few brightest ones. Here, fiber damping considerably impacts the ability to detect S300 in the CLEAN images. Bandwidth smearing, which becomes more severe for sources further away from the image center and is not modeled by CLEAN, can also diminish the sensitivity to S300 for the later 2021 observing runs. Finally, the images in Fig. 2.6 were obtained by cleaning on S300.

The most powerful confirmation of S300 in the CLEAN images, however, is provided by the July mid pointings in Fig. 2.7. The image is obtained from a total of 16 frames collected over three consecutive nights from July 25 to July 27, 2021. After cleaning on Sgr A* in each individual exposure and combining all files, S38, S63, and S300 become apparent in the residual image, and we clean on the sources in this order. Subsequently, S29 can be recognized, which appears fainter in the mid pointings due to the larger fiber damping, and we also cleaned on it. Again, the CLEAN image shows excellent consistency with the G^R result in Fig. 2.5.

As in GRAVITY Collaboration et al., 2021b, we computed the root mean square (rms) value of the residual image in the central 74×74 mas for the Sgr A* centered images, see Table 2.7. The rms of the complex visibilities and the residual image are directly

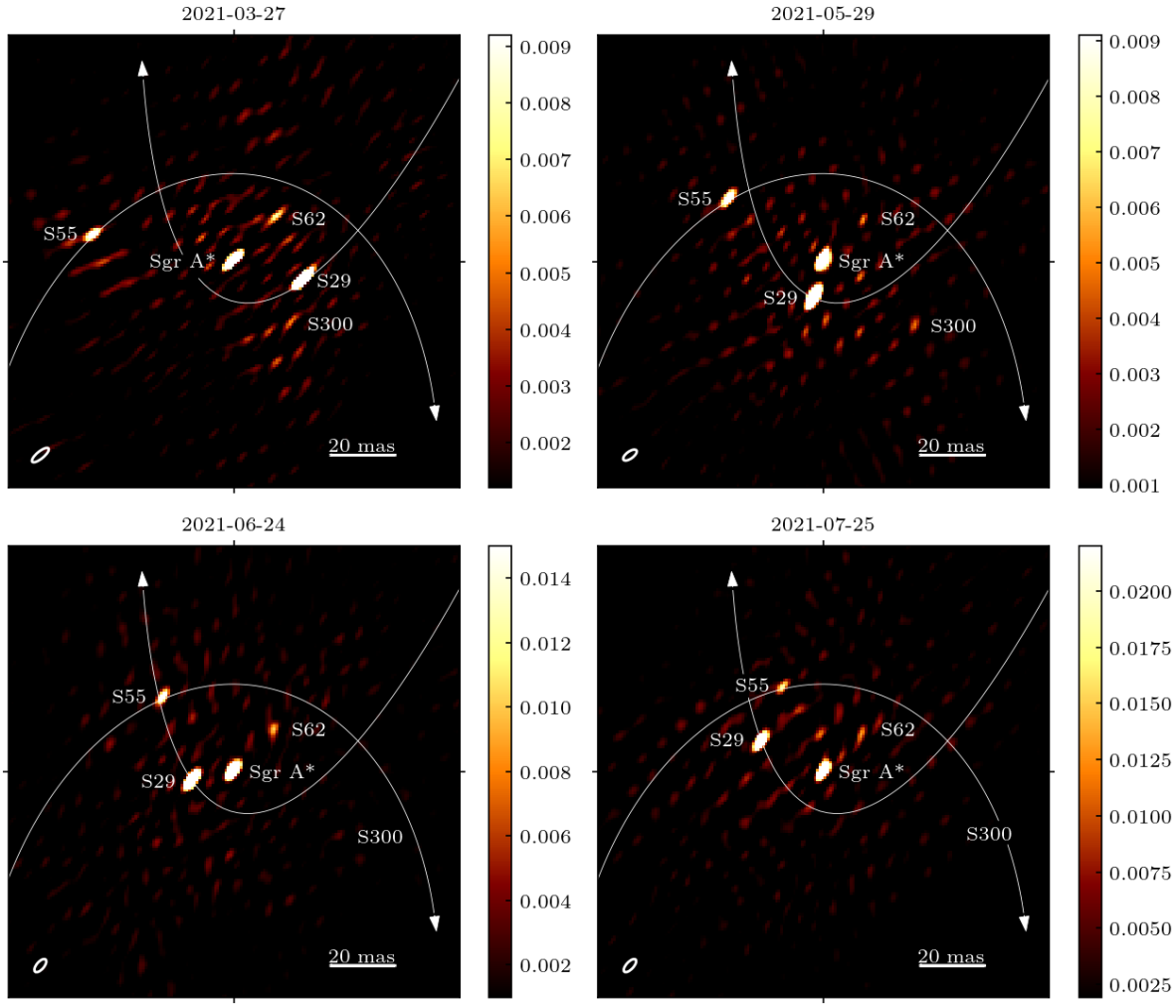

Figure 2.6: Representative image for each observing epoch obtained with CLEAN (north is up, east to the left, and the flux is normalized to S2). We show the model convolved with the CLEAN beam on top of the residual images and indicate the FWHM of the CLEAN beam in the bottom left corner. To obtain the model, we cleaned Sgr A*, S29, S55, and S62; for the images from March to June, we also cleaned S300.

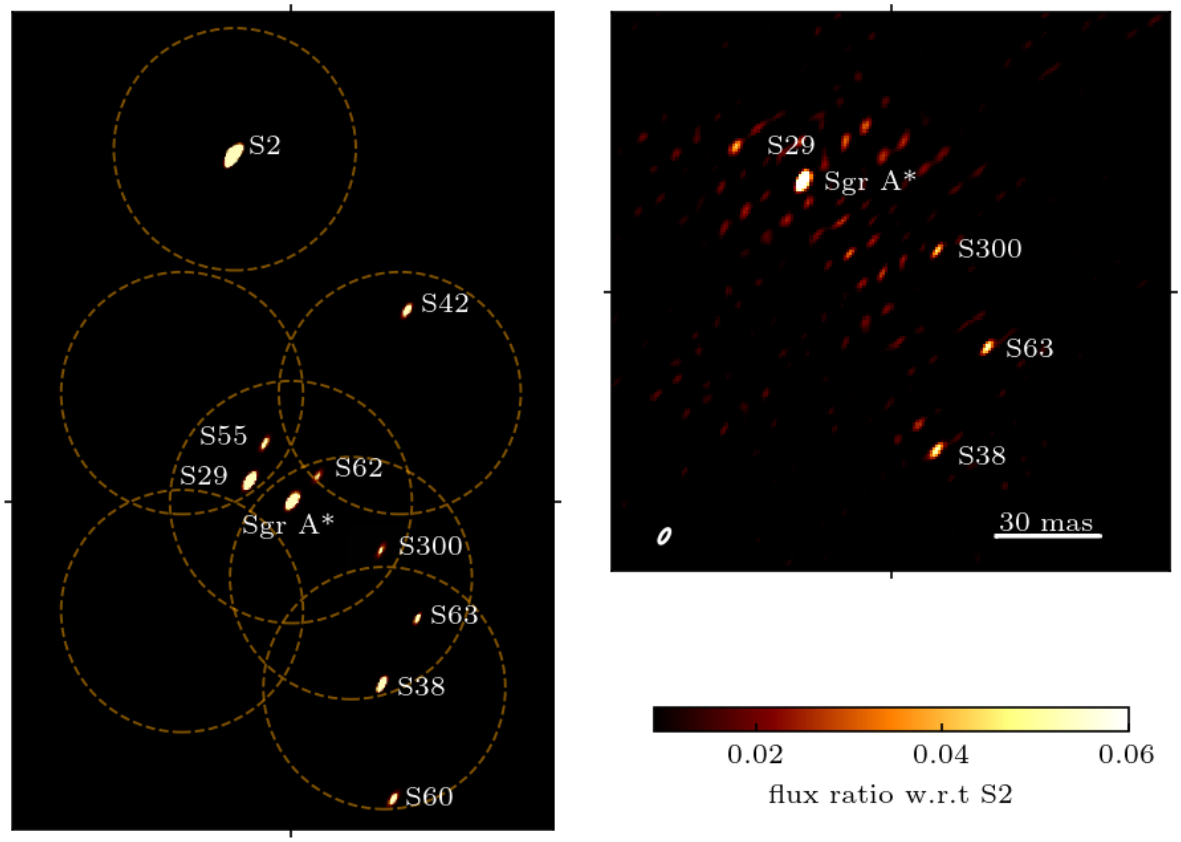

Figure 2.7: Imaging results for the wide field data set obtained with CLEAN, where north is up, east to the left, and the flux is normalized to S2. In the left panel, we combine the CLEAN model from all pointings in the July 2021 mosaicing data set (see Table 2.2) and indicate the pointing direction by a circle with 50 mas radius. Apart from the expected stars, which are also summarized in Fig. 2.4, we do not detect any additional sources. In the right panel, we show the mid pointings from July 25, 26, and 27 (16 exposures in total) imaged with CLEAN. The image displays the model convolved with the CLEAN beam on top of the residuals and the beam size is indicated in the bottom left corner. To obtain the model, we have cleaned on Sgr A*, S38, S63, S300, and S29.

Table 2.7: Summary of the data set from which the CLEAN images in Fig. 2.6 were obtained.

Date	N_{exp}	rms/S2	Corresponding m_{K}
2021-03-27	12	1.5×10^{-3}	21.2
2021-05-29	20	1.2×10^{-3}	21.4
2021-06-24	32	1.4×10^{-3}	21.2
2021-07-25	28	2.5×10^{-3}	20.6

Notes. Here, N_{exp} gives the number of exposures used for imaging. In addition, we also provide the rms in the residual image normalized to S2 and translate the value to a K-band magnitude in the final column.

related by Parseval's theorem, such that the latter quantity measures how well the model is able to reproduce the data. The flux in the CLEAN images as well as the rms values are normalized to S2, a 14.1 magnitude star in K-band (GRAVITY Collaboration et al., 2017). Equivalent values for the $\mathrm{G^R}$ results are estimated in Appendix A1.7 and are given in Table 2.

The low brightness of S300 in the June CLEAN residual image, where $\mathrm{G^R}$ still manages a robust detection, already illustrates the increased sensitivity of the latter method. Furthermore, for the May and June observing nights, where we can directly compare the results in Table 2.7 and Table 2, $\mathrm{G^R}$ improves the rms over the CLEAN result by $\Delta m_{\mathrm{K}} \simeq 0.3 - 0.4$. At this point, we want to emphasize that the comparison of residual images is rather unfavorable for $\mathrm{G^R}$, which reconstructs the image from closure phases and visibility amplitudes. Residual images are only computed retroactively and require some additional alignment steps which are described in Appendix A1.7 and can increase the noise level by themselves.

Apart from being better able to describe instrumental effects, $\mathrm{G^R}$ has another advantage. The residual images are essential within CLEAN to search for new sources. They do not, however, contain any information about the error bars in the data domain. Even if the residual visibilities were completely consistent with the Gaussian noise expectation, the inhomogeneous sampling pattern of the Fourier plane would introduce structures in the residual images. It can be challenging to judge whether a bright spot in the residual image is consistent with noise expectations or corresponds to a faint source. In contrast, $\mathrm{G^R}$ judges the match between model and data directly in the domain of the data and thus can compare the residuals directly with the error bars of the individual data points.

On the other hand, a clear advantage of CLEAN is its speed and the significantly smaller computational demands in comparison to $\mathrm{G^R}$. A full image reconstruction starting from data conversion with CLEAN only requires a single CPU and takes one to one and a half hours, which are dominated by data selection and inspecting the results rather than computation time. The $\mathrm{G^R}$-code runs for about ten times as long on 16 CPUs, albeit once it has been initiated, it requires no human intervention.

Finally, we note that in some situations, CLEAN appears to be more robust to short-

comings of the response model. For the mid-pointing images with G^R in Sect. 2.4.4, we only used data from a single night. Combining multiple nights with G^R works well for S2 and S38 pointings, but this significantly degrades the imaging solution of the mid pointings by introducing spurious sources, most likely due to the day-to-day movement of S29 and S55. While this further illustrates the heightened sensitivity of G^R, it also implies that additional work on the prior model will be required before one can combine exposures with fast moving sources from multiple nights. CLEAN, on the other hand, is able to image mid pointings from three consecutive nights jointly, without any artifacts from the movement of fainter stars affecting the structure of the brightest sources. In Fig. 2.7, we have Sgr A*, S300, S63, and S38 all correctly recovered, while the fast-moving S29, which is subdominant to the total flux, appears slightly smeared out at an average position. On the other hand, S55, which is even fainter and further off axis than S29, cannot be recovered.

2.5.2 Possible S300 positions in the Milky Way

The observed S300 positions from March to July (cf. Table 2.4 and Sect. 2.4.4) are fully consistent with a linear motion. Fitting for the angular velocity, we obtain:

$$v_{\mathrm{RA}} = (-65.6 \pm 1.8)\ \mathrm{mas\ yr^{-1}},$$
$$v_{\mathrm{Dec}} = (-0.5 \pm 2.7)\ \mathrm{mas\ yr^{-1}}.$$

Its high angular velocity makes it very unlikely that S300 is a background star. In the following, we discuss possible options for describing its nature, namely, as a star located in the CG and a foreground star in the galactic disk.

If the star is at the same distance as the GC, its projected velocity with respect to the GC would be $v \simeq 2.6 \times 10^3\,\mathrm{km\ s^{-1}}$. The 2σ limit on the acceleration of S300 is $-23\,\mathrm{mas\,yr^{-2}}$. This, in combination with requiring it to be gravitational bound to the black hole, limits the possible range of perpendicular coordinates to $50\,\mathrm{mas} \leq |z| \leq 137\,\mathrm{mas}$. Furthermore, for each possible value of z there is a maximum velocity v_z beyond which the star would become unbound. Sampling uniformly from the allowed values for z and their corresponding velocities, we can investigate the possible orbits of S300.

We find that the median orbit of this distribution has a 171 mas semi-major axis, 0.6 eccentricity, and a 26 yr orbital period. It thus perfectly fits into the distribution of S-stars. Assuming a similarly accurate position determination as for the 2021 imaging, a single good observing night from 2022 would allow to detect the acceleration of this median orbit. However, the distribution also contains more extreme solutions with larger semi-major axis and orbital period. For them, the apparently linear motion could continue throughout 2022. Even though, the continued observation of S300 over the coming year will allow to considerably constrain the family of allowed orbits.

Until then, in the absence of a significant acceleration detection, the possibility remains that S300 is a foreground star rather than being located in the GC. In this case, there would be little dust attenuation and S300 should also be detectable in the optical. We therefore checked the *Gaia* EDR3 catalog (Gaia Collaboration et al., 2021), which lists

sources down to a G-band magnitude of 21, but we do not obtain a match. In a circle with 4 arc min diameter around Sgr A*, *Gaia* lists 285 stars fainter than $m_{\mathrm{G}} > 17$. If we use this number at face value to estimate the number density of stars towards the GC, the probability for a star crossing our 100×100 mas image is small $\simeq 6 \times 10^{-5}$.

Further, if S300 was a disk star, there would be only a narrow range of possible distances from the sun consistent with our observations. While the high angular velocity implies that S300 must be close, the linear motion and the absence of a parallax also impose a minimum distance. Taken together, in addition to the low probability of a foreground star crossing the narrow GRAVITY FOV, its distance to the sun is limited to $\mathcal{O}$ (kpc).

2.6 Conclusions

In this paper, we present GRAVITY-RESOLVE (G^{R}), a new imaging code, specifically tailored to GRAVITY observations of the Galactic Center (GC). The tool is based on a Bayesian interpretation of the imaging process and builds upon RESOLVE (Arras et al., 2021b; Arras et al., 2018), an imaging tool for radio interferometry developed in the framework of information field theory (Enßlin, 2019). In this context, we implemented an instrument model which accounts for all relevant effects in GRAVITY and developed a prior that is specifically designed for the GC and can, for instance, accommodate the variability of Sgr A*. The posterior exploration was performed with Metric Gaussian Variational Inference (MGVI, Knollmüller and Enßlin, 2019).

We then applied G^{R} to GC observations in 2021. The resulting images reveal a complicated structure, composed of several point sources of different brightness with a time-variable central object. We note that while our prior model is specifically tailored to the GC and only considers point sources, there are also methods available to model an extended emission within a similar framework (Arras et al., 2020; Arras et al., 2021b).

The stars S29 and S55 (Gillessen et al., 2017) both pass their pericenters in 2021 and we detected them within a 50 mas radius from Sgr A*. Their position in the images is also the starting point for astrometric model fitting which allows to determine the sources' positions to a very high accuracy of $\sim 100\,\mu$as. We present a detailed study of the resulting GR orbits in a second publication (GRAVITY Collaboration et al., 2022). Further, G^{R} yields a very robust night-by-night detection of S62, a $m_{\mathrm{K}} = 18.9$ star that slowly approaches Sgr A* and has already been found in GRAVITY GC images from 2019 obtained with CLEAN (GRAVITY Collaboration et al., 2021b). None of the sources S29, S55, S62, and S300 identified in the GRAVITY observations matches a 9.9 year orbital period star as reported in Peißker et al., 2020; Peißker et al., 2021.

In addition to the known stars, a new source is apparent from the images which moves to the west at high angular speed $\simeq 66$ mas yr^{-1}. It is detected at a high significance in the March, May, and June observations, but only dimly recognizable in the July Sgr A*-centered exposures, where it is located at the largest distance from the image center. In July, however, we performed some dedicated mid pointings in which the GRAVITY fibers are offset from Sgr A* and indeed recover the star at the expected location.

The new source neither corresponds to any of the known S-stars (Gillessen et al., 2017) nor is it present in the *Gaia* catalog (Gaia Collaboration et al., 2021), and we refer to it as S300. From the flux ratio with known stars in the field, particularly S29 and S38, we estimate that $m_{\mathrm{K}}\,(S300) = 19.0 - 19.3$. If fiber damping is taken into account, this source is at the detection limit estimated in GRAVITY Collaboration et al., 2021b in the March images and becomes dimmer during the rest of the year. The detection clearly demonstrates that $\mathrm{G^R}$ can deliver significantly deeper images. With the knowledge of the S300 position, we also searched for it in 2021 CLEAN images and, indeed, we can identify a bright residual at the correct location in March, May, June, and the mid pointings.

The mid pointings are part of a larger mosaicing data set (cf. Table 2.2), obtained to scan a wider field around Sgr A*. In the corresponding images (cf. Fig 2.5), we can detect S38, S42, S60, and S63 in addition to the aforementioned sources. We use the opportunity to give an update on the orbital elements of all stars in Table 2.5. These are based on astrometric fits to the data for which the imaging serves as a starting point.

Struggles to detect S300 in the July Sgr A*-centered frames are partly due to fiber damping, but also the fact that our instrumental model becomes more sensitive to approximations; in addition, uncertainties in the calibration the farther away from the image center a source is located might play a role. To further assess the sensitivity of the new code, we performed a series of injection tests that we compared to the apparent magnitude of S300. As the images from May 22 demonstrate, a flare significantly reduces our sensitivity to faint sources. Under moderately difficult circumstances – if the source is injected close to S300 or in June, where the off-axis separation already exceeds the fiber FWHM – we are still able to robustly recover a source with an apparent magnitude of at least 19.7. Finally, the injection tests show that, under good circumstances, we are able to push the sensitivity significantly below a magnitude of 20 and we are even able to retrieve a injected star of a magnitude of 21.0.

At present, a limiting factor to $\mathrm{G^R}$ is that we have to scale the error bars by hand and to adjust that scaling by trial-and-error, making the application cumbersome. This can be improved in the future by implementing an automated error inference, such as in Arras et al., 2019a. With this method, we can also introduce more elaborate covariance matrices for the likelihood. Indeed, we find that the correlation structure of our residuals is similar to the one reported in Kammerer et al., 2020. This analysis, which was carried out in the context of exo-planet observations with GRAVITY, demonstrated that an improved correlation model increases the achievable contrast. We see a similar potential in the imaging context, which would allow for an improvement in the convergence of the inference and further enhance the sensitivity beyond the capabilities that we have demonstrated with this publication.

Acknowledgements. We are very grateful to our funding agencies (MPG, ERC, CNRS [PNCG, PNGRAM], DFG, BMBF, Paris Observatory [CS, PhyFOG], Observatoire des Sciences de l'Univers de Grenoble, and the Fundação para a Ciência e Tecnologia), to ESO and the ESO/Paranal staff, and to the many scientific and technical staff mem-

bers in our institutions, who helped to make GRAVITY a reality. This publication is based on observations collected at the European Southern Observatory under ESO programme 105.20B2.002. A.A., P.G. and V.C. were supported by Fundação para a Ciência e a Tecnologia, with grants reference SFRH/BSAB/142940/2018, UIDB/00099/2020 and PTDC/FIS-AST/7002/2020. P.A. acknowledges the financial support by the German Federal Ministry of Education and Research (BMBF) under grant 05A17PB1 (Verbundprojekt D-MeerKAT). In the implementation of our code, we relied on the NIFTy and ducc0 Python packages and used the computing resources provided by MPCDF for our inferences.

Chapter 3

Polarimetry and astrometry of NIR flares as event horizon scale, dynamical probes for the mass of Sgr A*

Original Publication: GRAVITY Collaboration: R. Abuter, N. Aimar, P. Amaro Seoane A. Amorim, M. Bauböck, J.-P. Berger, H. Bonnet, G. Bourdarot, W. Brandner, V. Cardoso, Y. Clénet, R. Davies, P.T. de Zeeuw, J. Dexter, A. Drescher, A. Eckart, F. Eisenhauer, H. Feuchtgruber, G. Finger, N.M. Förster Schreiber, A. Foschi, P. Garcia, F. Gao, Z. Gelles, E. Gendron, R. Genzel, S. Gillessen, M. Hartl, X. Haubois, F. Haußmann, G. Heißel, T. Henning, S. Hippler, M. Horrobin, L. Jochum, L. Jocou, A. Kaufer, P. Kervella, S. Lacour, V. Lapeyrère, J.-B. Le Bouquin, P. Léna, D. Lutz, F. Mang, N. More, T. Ott, T. Paumard, K. Perraut, G. Perrin, O. Pfuhl, S. Rabien, D. C. Ribeiro, M. Sadun Bordoni, S. Scheithauer, J. Shangguan, T. Shimizu, J. Stadler, O. Straub, C. Straubmeier, E. Sturm, L.J. Tacconi, F. Vincent, S. von Fellenberg, F. Widmann, M. Wielgus, E. Wieprecht, E. Wiezorrek, and J. Woillez
CORRESPONDING AUTHORS: A. Drescher, D. C. Ribeiro, N. Aimar
DOI: 10.1051/0004-6361/202347416

ABSTRACT: We present new astrometric and polarimetric observations of flares from Sgr A* obtained with GRAVITY, the near-infrared interferometer at ESO's Very Large Telescope Interferometer (VLTI), bringing the total sample of well-covered astrometric flares to four and polarimetric flares to six. Of all flares, two are well covered in both domains. All astrometric flares show clockwise motion in the plane of the sky with a period of around an hour, and the polarization vector rotates by one full loop in the same time. Given the apparent similarities of the flares, we present a common fit, taking into account the absence of strong Doppler boosting peaks in the light curves and the EHT-measured geometry. Our results are consistent with and significantly strengthen our model from 2018. First, we find that the combination of polarization

period and measured flare radius of around nine gravitational radii ($9R_g \approx 1.5R_{ISCO}$, innermost stable circular orbit) is consistent with Keplerian orbital motion of hot spots in the innermost accretion zone. The mass inside the flares' radius is consistent with the $4.297 \times 10^6\,\mathrm{M}_\odot$ measured from stellar orbits at several thousand R_g. This finding and the diameter of the millimeter shadow of Sgr A* thus support a single black hole model. Second, the magnetic field configuration is predominantly poloidal (vertical), and the flares' orbital plane has a moderate inclination with respect to the plane of the sky, as shown by the non-detection of Doppler-boosting and the fact that we observe one polarization loop per astrometric loop. Finally, both the position angle on the sky and the required magnetic field strength suggest that the accretion flow is fueled and controlled by the winds of the massive young stars of the clockwise stellar disk 1-5 arcsec from Sgr A*, in agreement with recent simulations.

3.1 Introduction

The presence of a massive black hole (MBH) in the Galactic center (GC) has been established, beyond any reasonable doubt, in a four-decade-long research by several teams (e.g., Genzel, 2021) Not only is Sagittarius A* (Sgr A*) the best case for the existence of black holes, but unlike any other known black hole, it can be resolved both spatially and temporally, allowing dynamical tests long considered unfeasible. The combination of precise stellar astrometry and spectroscopy has revealed the gravitational redshift signature in the orbit of the star S2 (GRAVITY Collaboration et al., 2018b; Do et al., 2019a). Furthermore, the prograde relativistic precession of the orbit yielding an astrometric signature of around 0.5 mas per revolution was detected employing the ultra-high resolution of the GRAVITY interferometer (GRAVITY Collaboration et al., 2020c; GRAVITY Collaboration et al., 2022). Emission from a distance of just a few R_g ($R_g = GM/c^2$ corresponds to 5.12 µas at our assumed $R_0 = 8.277\,\mathrm{kpc}$ and for $M = 4.297 \times 10^6\,\mathrm{M}_\odot$ from GRAVITY Collaboration et al. 2022) was detected in the X-ray (Baganoff et al., 2001; Neilsen et al., 2013), near-infrared (NIR, Genzel et al., 2003a; Eisenhauer et al., 2005; Dodds-Eden et al., 2011; Do et al., 2019b; Witzel et al., 2021), and radio bands (Balick and Brown, 1974; Lo et al., 1998; Shen et al., 2005; Yusef-Zadeh et al., 2006; Doeleman et al., 2008; Johnson et al., 2015; Event Horizon Telescope Collaboration et al., 2022). The small spatial scales imply that the light arises deep in the strong gravitational field of the MBH, and that its propagation is subject to strong relativistic effects.

The NIR emission of Sgr A* is highly variable, with flares of ten times the quiescent flux occurring once or twice per day (Dodds-Eden et al., 2011; Witzel et al., 2018; GRAVITY Collaboration et al., 2020g). The flare emission most likely comes from locally heated electrons emitting synchrotron emission from the NIR, possibly up to the X-ray band (Yuan et al., 2003; Dodds-Eden et al., 2009; Ponti et al., 2017; GRAVITY Collaboration et al., 2021a). The synchrotron model with emission coming from a compact source also explains the observed variable NIR polarization of a few tens of percent linear polarization and a negligible amount of circular polarization (Eckart et al., 2006a; Eckart et al., 2008a; Trippe et al., 2007; Zamaninasab et al., 2010; Witzel et al., 2011; Shahzamanian et al.,

2015; GRAVITY Collaboration et al., 2020c), as well as the co-evolution of the light curves in the two bands. The estimated source sizes of around 1 R_g and the required magnetic field strengths of around 30-80 G (Dodds-Eden et al., 2010; Eatough et al., 2013; Ripperda et al., 2020) are in agreement with the "hot spot model" with orbital radii close to the innermost circular orbit (Broderick and Loeb, 2005; Broderick and Loeb, 2006; Meyer et al., 2006; Hamaus et al., 2009; Ripperda et al., 2020; GRAVITY Collaboration et al., 2020e). This model has observable signatures in the astrometry and polarimetry of the NIR emission, where the astrometric amplitudes of a few 10 µas were one key driver for the development of GRAVITY (Paumard et al., 2006; GRAVITY Collaboration et al., 2017). Moreover, Dexter et al., 2020 show by means of general relativistic magnetohydrodynamic simulations that for magnetically arrested disks (MADs), flares with properties similar to the observed ones might arise from magnetic reconnection events.

GRAVITY combines the light from either the four Auxiliary Telescopes (1.8 m diameter) or the four Unit Telescopes (8 m diameter) at the Paranal observatory. The spatial resolution in K-band is around 3 mas, and the accuracy by which sources can be located is of a few 10 µas – good enough to follow the motions of orbiting hot spots. In 2018 we observed in three nights flares from Sgr A*, all of which showed astrometrically clockwise motions at radii compatible with the hot spot model. For one flare we also obtained polarimetry in 2018, showing a full rotation of the polarization vector (GRAVITY Collaboration et al., 2018a).

Clearly, the number of such high-precision flares was still small. Hence, we embedded in our nightly observing strategy regular visits to Sgr A* and analyzed in real time the incoming data to monitor for flux increases. If a flare occurred, we continued to observe Sgr A*.

Here we report on one new flare, for which the astrometric and polarimetric data are good enough to resolve orbital motion, and on four additional flares, for which only the polarimetry is of sufficient quality.

3.2 Observations

We observe the GC typically six months per year, with a total allocation of around 90 h. The data serve for the astrometric monitoring of the stellar orbits (GRAVITY Collaboration et al., 2018b; GRAVITY Collaboration et al., 2022) and for observing the emission from Sgr A* itself (GRAVITY Collaboration et al., 2018a). We report on as-yet-unpublished data obtained from observations in 2019, 2021, and 2022 during which Sgr A* exhibited flares. We analyzed them together with previous flare observations. Specifically, we used the observations listed in Table 3.1.

Table 3.1: Observations with astrometric (A) and polarimetric (P) data.

Date of night	UTC interval	# of frames	A	P
27 May 2018	07:02 – 09:15	19	x	
22 Jul. 2018	02:44 – 04:51	19	x	
28 Jul. 2018	00:02 – 04:16	36	x	x
18 Aug. 2019	23:46 – 03:46	32		x
26 Jul. 2021	23:25 – 03:47	36		x
27 Jul. 2021	23:29 – 03:21	33		x
19 May 2022	04:14 – 09:41	45	x	x
16 Aug. 2022	23:40 – 02:06	26		x

Notes. The Program IDs for the 2018 data are 0101.B-0576(C) and 0101.B-0576(E). For 2019, 2020, and 2022 they are respectively 0103.B-0032(C), 105.20B2.004, and 109.22ZA.002.

3.3 Data

Our GRAVITY data deliver position and polarization measurements simultaneously. The former are obtained from the phase measurements, the latter by comparing (interferometric) fluxes behind a Wollaston prism.

3.3.1 Astrometry

For the GC, GRAVITY uses optical fibers to simultaneously observe two objects and record the interference of the two targets on the six baselines formed by the four 8 m telescopes. One target is the star IRS 16C ($m_K = 9.7$), used as a phase reference, and the other is the science target. Each GRAVITY fiber has a field of view of approximately 70 mas, comparable to the diffraction limit of the individual telescopes.

Since the beginning of the GRAVITY observations, stars were always close enough to Sgr A* to be observed in the same field of view, yielding binary, triple, or multiple signatures in the interference pattern. In 2018 the star S2 ($m_K = 14.0$) was observed together with Sgr A* in this way. In this single-beam measurement, information such as the position vector and flux ratio between the two sources, is directly inferred from the measured closure phases and amplitudes. Since 2019, S2 has moved so far out of the interferometric field of view that other fainter stars have been detected close to Sgr A* (GRAVITY Collaboration et al., 2021b; GRAVITY Collaboration et al., 2022). However, during a flare, Sgr A* outshines these fainter stars and effectively appears as a single source. In this case the astrometry of Sgr A* has to be derived from the visibility phases. These are measured relative to the reference target via GRAVITY's metrology system, which traces the optical path differences between the telescopes and the instrument (GRAVITY Collaboration et al., 2020c, Appendix A therein).

Hence, for the new, dual-beam data sets, the astrometry is obtained as a sum of three

measured phases: of Sgr A*, of IRS 16C, and the metrology linkage. The source models are simply unary fits in this case. In practice, we measure the Sgr A* phases and, every few exposures, that of a local phase reference for which we chose S2. Since

$$\left(\varphi_{Sgr\ A*} - \varphi_{IRS16C}\right) - \left(\varphi_{S2} - \varphi_{IRS16C}\right) = \left(\varphi_{Sgr\ A*} - \varphi_{S2}\right) , \tag{3.1}$$

we reference the Sgr A* positions to S2. The proper motion of S2 during a flare is small enough not to affect our measurements.

A significant systematic error in our dual-beam flare astrometry is due to high-order imperfections in the GRAVITY optics. As the metrology sensors cover only four points of the pupil, the high-order aberrations translate into phase errors, and thus astrometric uncertainty. These errors average out effectively by the pupil rotation over the course of the night so that stellar orbits are routinely measured with an accuracy down to $20 - 50\,\mu as$ (e.g., GRAVITY Collaboration et al., 2022). For the individual short exposures of flare observations, however, these metrology footprint errors dominate over the statistical errors. Since 2022, we circumvent this source of error by simultaneously modulating the telescope pupils relative to the metrology receivers such that the high-order aberrations average out. This restores the astrometry to a level similar to what we achieved in the single-beam case. This new observing mode was not yet in place in 2019 and 2021, and the accuracy of the dual-beam astrometry was not at the level needed for flare orbits during this period.

3.3.2 Polarimetry

In its polarimetric mode, GRAVITY splits the light post-beam combination by means of a Wollaston prism into two orthogonal, linear polarization states. Employing a half-wave plate, we rotate the polarization by 45° between exposures, such that for each pair of exposures, we measure the polarized flux in the 0°, 45°, 90°, and 135° directions. The polarization angles are measured with respect to the equatorial system and defined between 0° and 180° east of north.

From the polarized fluxes, the Stokes parameter Q and U are calculated as

$$Q' = \frac{f_0 - f_{90}}{f_0 + f_{90}} \quad , \quad U' = \frac{f_{135} - f_{45}}{f_{135} + f_{45}} \quad , \tag{3.2}$$

where f_θ represents the correlated flux along direction θ and the primes indicate that the values are measured in the detector coordinate system. To get the on-sky polarization state Q and U, it is necessary to correct for the geometric beam propagation and the instrumental polarization. This is done with the model developed by GRAVITY Collaboration et al., 2024. As GRAVITY cannot measure circular polarization, we correct for birefringence with the model presented by Witzel et al., 2011, using the fact that the polarized NIR emission of Sgr A* is predominantly linearly polarized.

Our Q and U values are fractional values normalized to the observed intensity. Unlike at longer wavelengths, the variations of the NIR polarized fluxes are completely dominated

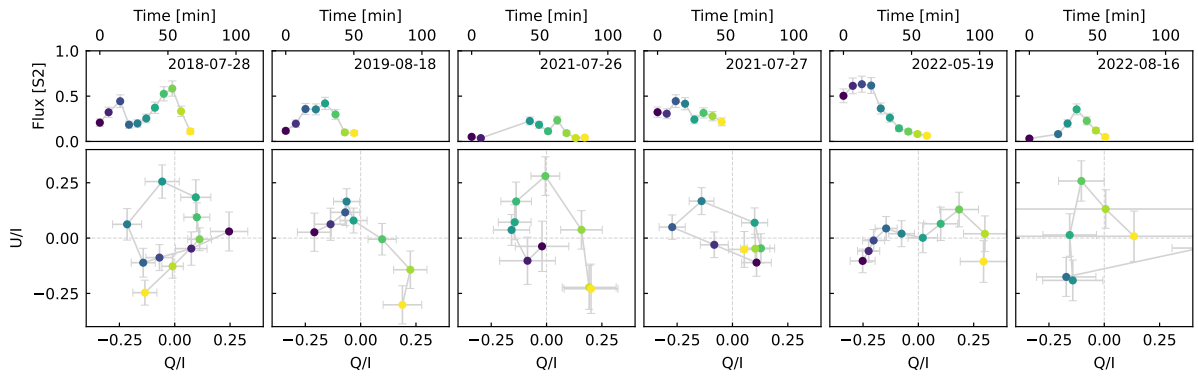

Figure 3.1: Flares with polarimetric signature. Top row: flux evolution for each flare. Bottom row: polarimetric signal in Q/I and U/I, color-coded according to time. The flare from 28 July 2018 was published and analyzed in GRAVITY Collaboration et al., 2018a; GRAVITY Collaboration et al., 2020d. The other five are newly reported here.

by the overall brightness variations – a result of the much shorter heating and cooling timescales in the NIR (von Fellenberg et al., 2023). Thus, the fractional values carry the information on the magnetic field and geometry of the Sgr A* system.

Following GRAVITY Collaboration et al., 2020g, there are two different ways to measure the required fluxes. In the first, if Sgr A* is the dominant (or only) source in the (interferometric) field of view, the coherent flux directly measures the flux of Sgr A*. In the second, if there are multiple sources in the field of view, a multiple source fit to these sources includes the flux ratio of Sgr A* to each star, which, when multiplied with the coherent flux, yields the desired Sgr A* flux. Flux measurements for observations up to 2020 are reported in GRAVITY Collaboration et al., 2020g. For 2021 and 2022 we used binary fits with the stars S29 (2021) and S38 (2022) as the second object beyond Sgr A* (see, e.g., GRAVITY Collaboration et al., 2022 for images of the central region where the stars S29 and S38 are shown).

3.4 Analysis

Our sample of flares with polarimetric coverage has grown from one (GRAVITY Collaboration et al., 2018a; GRAVITY Collaboration et al., 2020d) to six, all of which show a single clockwise loop, or part thereof, in the $Q-U$ plane (Fig. 3.1). The sample of astrometric measurements has also grown and consists now of four events: the three flares from GRAVITY Collaboration et al., 2020g and the addition from 2022 May 19 (Fig. 3.2).

In contrast to the flare astrometry, where we need a precision of $\approx 10-30\,\mu$as per five-minute exposure, polarimetry is less sensitive to observing conditions and is not penalized by the optical imperfections. As a result, we obtained valid polarimetry for flares even if the conditions were not good enough for astrometry. This is the case for the flare from 2019, the two from 2021, and the one from August 2022.

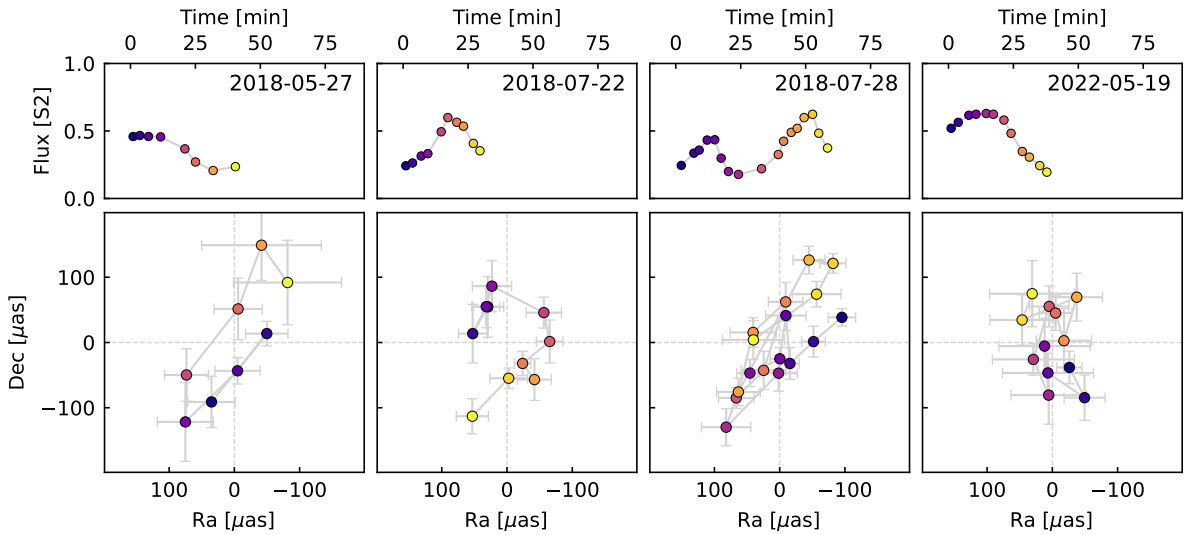

Figure 3.2: Flux and centroid measurement of the four astrometric flares from 2018 and 2022. The three 2018 flares were published in GRAVITY Collaboration et al., 2018a; GRAVITY Collaboration et al., 2020d.

The similarity between the flares motivated us to look at them in an averaged way. We combined the data of the six polarimetric and four astrometric flares by allowing only a relative time shift between the individual events and finding the solution that best represents a sinusoidal in both sky coordinates for the combined flare data. This yields the data shown in Fig. 3.3. Both averaged data sets are very well described by elliptical figures with a common period of around 60 min and constant angular velocity of 6 °/min.

The mean astrometric loop size in Fig. 3.3 of around $r = 61 \pm 9$ µas (corresponding to 0.50 ± 0.07 AU for our assumed R_0) and the polarization period of $P = 60 \pm 3$ min allows us to estimate the enclosed mass M_{enc}. Assuming Keplerian orbital motion, this yields $M_{enc,estimate} = (5.1 \pm 1.6) \times 10^6\,\mathrm{M}_\odot$ (Appendix A2.1). Within the error, this value agrees with that known from stellar orbits, $M = (4.297 \pm 0.012) \times 10^6\,\mathrm{M}_\odot$ (GRAVITY Collaboration et al., 2022) and shows that (within the uncertainties) the mass of Sgr A* is enclosed within the flare orbit.

In the following we refine the value of M_{encl} by modeling the astrometry and polarimetry of the flares. We model the astrometric motion of the combined data set as in GRAVITY Collaboration et al., 2020e by an orbiting relativistic hot spot, including the effects of lensing via ray tracing. However, here we enhance the pure astrometric fit by including more information, mainly from the polarimetry. First, we identify the period of the polarization loop with that of the astrometric loop. Technically this sets a prior on the orbital period. We use $P_{pol} = 60 \pm 3$ min. Second, we show that observing a single polarization loop per astrometric loop yields a strong prior on the allowed range of inclinations (see Sect. 3.4.1). The angular velocity of 6 °/min constrains the inclination to $i = 157° \pm 5°$. Third, the absence of strong spikes from Doppler beaming in the light curves also limits the inclina-

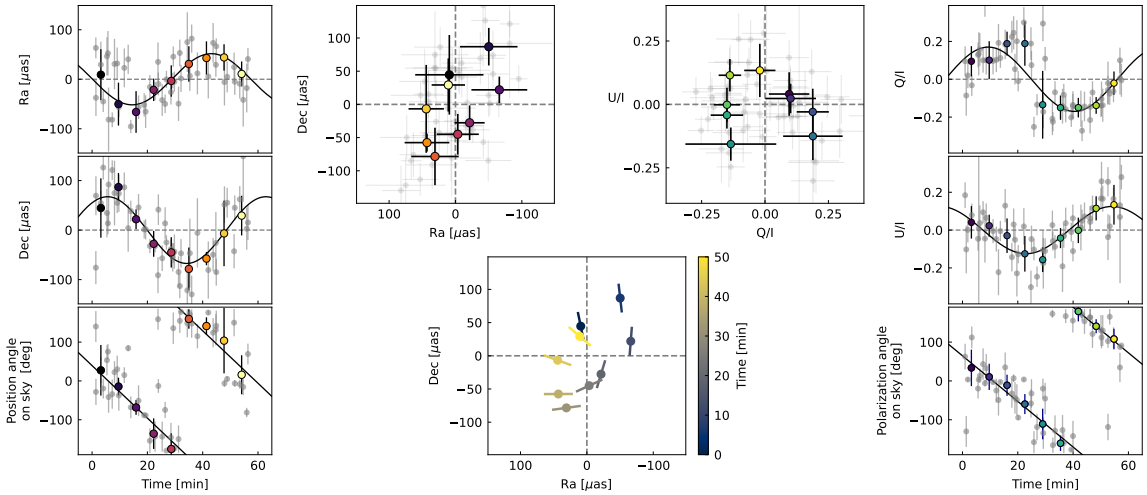

Figure 3.3: Combined astrometric (left) and polarimetric (right) data. The outer left panels show RA, Dec, and position angle on the sky as a function of time. The outer right panels show Q/I, U/I, and polarization angle on the sky vs. time. The full data are shown in gray, the colored points are bins of five minutes, and the color indicates time. The binned data are obtained after wrapping all points around the fit period of 60 minutes, and the error bars are the standard deviation of the binned data. Overplotted on the angle plots are slopes of $6\,^\circ/\mathrm{min} = 360\,^\circ/\mathrm{h}$. The top middle panels illustrate the loops on the sky (left) and in the $Q-U$ plane (right). The bottom middle panel shows the rotation of the polarization for the corresponding astrometric points, one polarization rotation per astrometric orbit. The electric field vector rotates clockwise in the plane of the sky, and in the $Q-U$ plane.

tion to be close to face-on. Following Hamaus et al., 2009 and GRAVITY Collaboration et al., 2018b (Appendix C therein), we place a conservative prior of $i = 180° \pm 40°$. Finally, the Event Horizon Telescope (EHT) image of Sgr A* constrains the inclination to $i = 180° \pm 50°$ (Event Horizon Telescope Collaboration et al., 2022).

We took into account all these constraints by including them in the likelihood function and determined a globally best-fitting orbiting hot spot model. The parameters of the fit are the hot spot's orbital radius R, the inclination i, the position angle Ω, and the enclosed mass M_{enc}.

3.4.1 Modeling the polarization loop

The polarization signal of an orbiting hot spot probes the magnetic field around Sgr A* (Broderick and Loeb, 2005; GRAVITY Collaboration et al., 2018a; GRAVITY Collaboration et al., 2020d; GRAVITY Collaboration et al., 2020e; Wielgus et al., 2022; Michail et al., 2023). Simulations and analytical methods have been used by GRAVITY Collaboration et al., 2020d and Narayan et al., 2021 to investigate the polarization changes associated with such hotspots. A dominantly toroidal or radial field lead in general to two full loops in the $Q-U$ plane, while a dominantly poloidal field produces either no loops for edge-on geometries ($i \sim 90°$), one loop for moderate inclinations ($i \sim 30°/150°$), or two loops for face-on inclinations ($i \sim 0°/180°$). Hence, observing one loop per astrometric revolution severely constrains the configuration space and argues for a vertical magnetic field and moderate inclination. The repeated observations of single loops in the $Q-U$ plane also indicate that the global magnetic field configuration has remained stable over recent years, consistent with the small changes in the circularly polarized emission at sub-millimeter wavelengths (Muñoz et al., 2012).

To derive the inclination constraint, we used the model introduced by Gelles et al., 2021. This semi-analytic model implements an equatorial point-like hot spot orbiting on a Keplerian orbit around a Kerr black hole with a local magnetic field. The model uses the semi-analytic solution for light rays (Gralla and Lupsasca, 2020) to obtain a polarized image of the synchrotron emitting source.

Since the model describes purely linear polarized emission, we extend it to take into account the observed polarization fraction in the data. Although coming from a point-source emitter, the model captures the fundamental features of extended emission regions (GRAVITY Collaboration et al., 2020d; Vos et al., 2022). A more detailed description of the model can be found in Appendix A2.2.

The local magnetic field is given in cylindrical coordinates and allows a clear distinction between radial, toroidal, and poloidal magnetic field configurations. Other free parameters are the inclination of the orbit, the orbital radius, the local boost, and the spin of the black hole. The last only has a minor impact on the polarization signal (Gelles et al., 2021), and hence we choose to work with zero-spin models. Further, we fix the radius to $9R_g$ as this matches the observed astrometric and polarimetric periods. Using radii in the $8-10R_g$ range does not alter our results (see Fig. 9). Fixing the radius also fixes the Lorentz boosting factor to $\beta = 0.37$. The model does not take radiative transfer effects

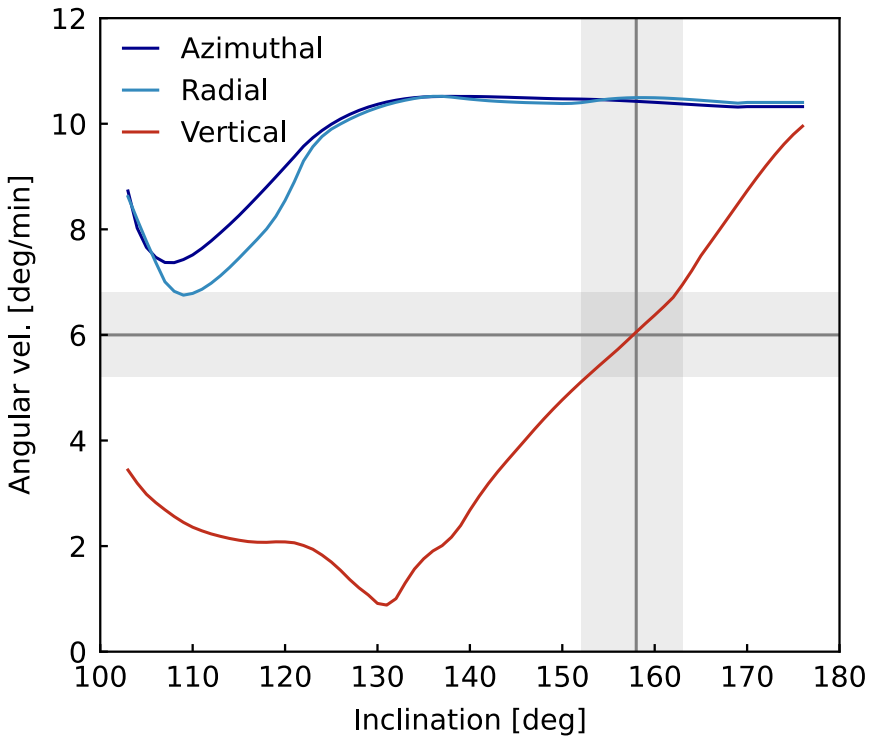

Figure 3.4: Comparison of the average angular velocity of the $Q-U$ loop for different magnetic field configurations as a function of inclination. Our measured values are consistent with a poloidal magnetic field and an inclination of $i = 157° \pm 5°$.

into account. Further, time delays and luminosity changes due to the combination of a non-flat spectral energy distribution and Doppler boosting are neglected.

As expected from the discussion above, the rotation speed distinguishes very well between the poloidal and toroidal/radial fields. Observing one polarimetric loop per astrometric loop only occurs for poloidal fields. The inclination can be constrained from the observed angular velocity with which the $Q-U$ loop is traversed (Fig. 3.4). The observed angular velocity of $6\,°$/min for the astrometry is only compatible with poloidal field configurations with an inclination of $i = 157° \pm 5°$.

Figure 3.5 shows that the model for $i = 157°$ is an excellent description of the observed polarization changes. This inclination matches the one measured by GRAVITY Collaboration et al., 2018a and the preferred inclination of the EHT ring (Event Horizon Telescope Collaboration et al., 2022). We allowed the position angle on the sky and the arbitrary zero point in time to be adjusted, and picked the combination that yields the smallest χ^2 to the data (Fig. 10). The best-matching position angle is $PA = 25°$. This value is consistent with the results from GRAVITY Collaboration et al., 2020d, Wielgus et al., 2022 and Michail et al., 2023. In summary, the analysis of the polarization loops gives robust constraints and a result compatible with the astrometric signature. In the following, we combine this information in a combined fit.

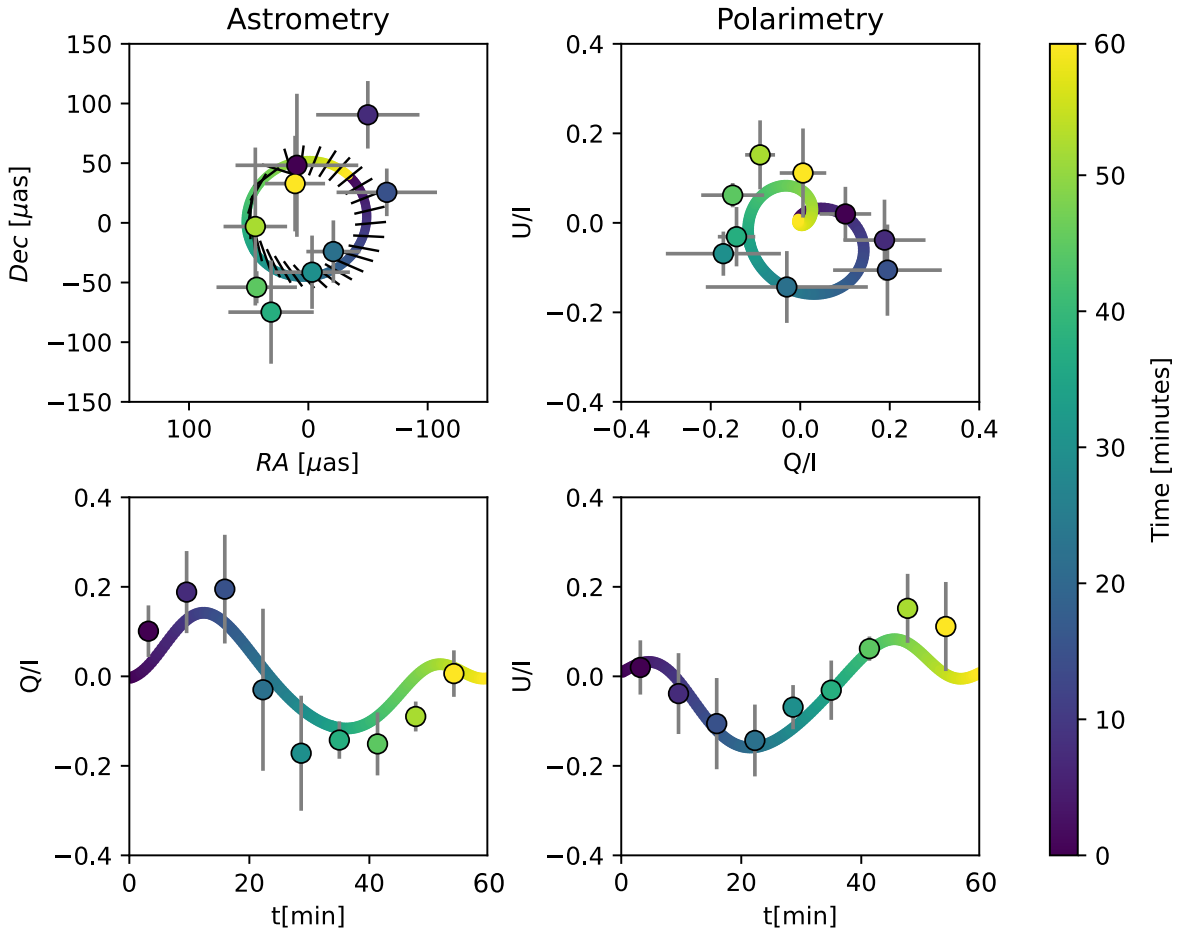

Figure 3.5: Comparison of the polarization model with $R = 9R_g$ and $i = 157°$ with the data from Fig. 3.3.

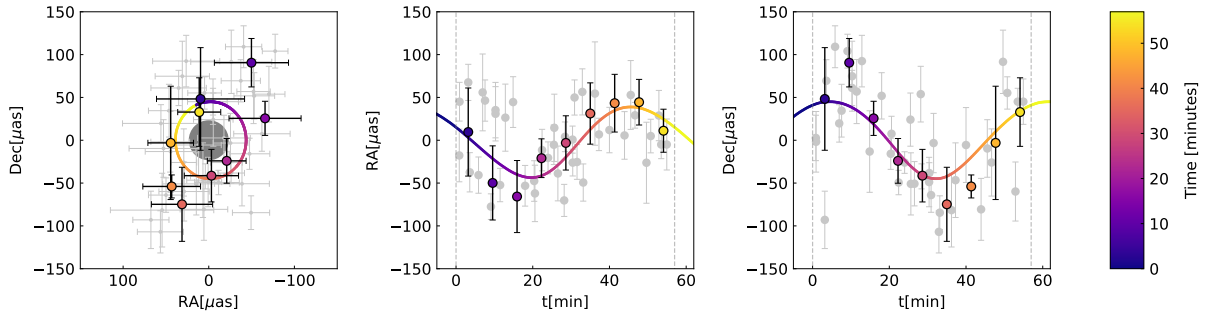

Figure 3.6: Combined fit of the astrometric flare data, taking into account the polarimetry constraints. Left: on-sky motion. The gray disk corresponds to the shadow size of a Schwarzschild black hole $3\sqrt{3}R_g$. Middle and right panels: individual coordinates as a function of time. The gray data points are the full data set and the colored points are bins of five minutes.

Table 3.2: Posterior mean values of the astrometry fit.

Parameter	Posterior mean
Radius	$R = 8.9^{+1.5}_{-1.3} R_g$
Inclination	$i = 154.9^{+4.6°}_{-4.6°}$
Position angle	$\Omega = 177.3^{+24°}_{-23°}$
Enclosed mass	$M_{enc} = 4.2^{+1.2}_{-0.9} \times 10^6 M_\odot$

Notes. The model corresponding to this set of parameters is displayed in Fig. 3.6 (for details of the Bayesian analysis see Appendix A2.4).

3.4.2 Combined fit

Our explicit combined fit (Fig. 3.6 and Fig. 11) uses the astrometric data and the constraints derived from the polarimetry. We obtained the set of parameters presented in Table 3.2. Within the uncertainties, the flare radius and the orientation agree with what GRAVITY Collaboration et al., 2018b; GRAVITY Collaboration et al., 2020d; GRAVITY Collaboration et al., 2020e found from the previous smaller data set. The novel result is the mass constraint, that stems from the new data, in particular from the strong independent period constraint from the polarimetry. The value for the mass inside $9R_g$ matches the simple estimate, and again also the mass derived using stellar orbits.

3.5 Results

The most important result we find is that the mass of Sgr A* measured from stellar orbits, $M = (4.297 \pm 0.012) \times 10^6\,\mathrm{M}_\odot$, is enclosed within 9 R_g, corresponding to 0.38 AU, or roughly

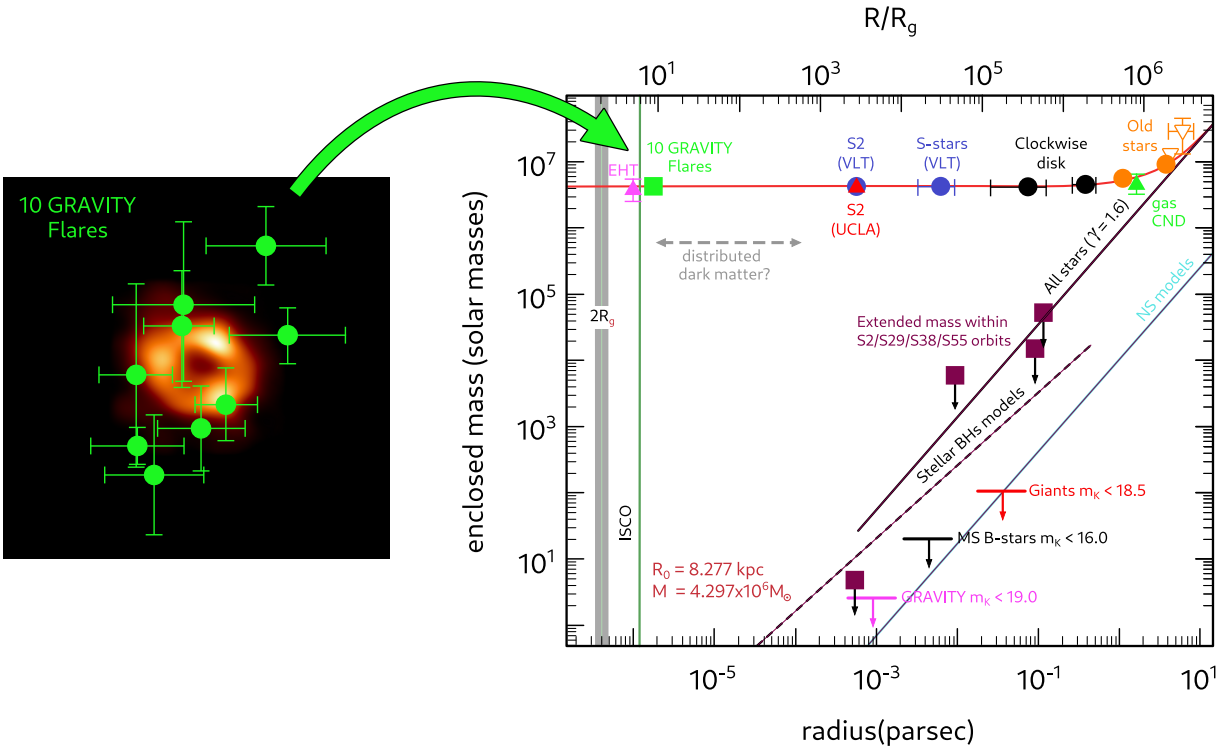

Figure 3.7: Central mass distribution in the GC. Right: enclosed mass in the GC as a function of radius. The flare motions constrain the black hole mass of $M = (4.2 \pm 2.0) \times 10^6\,\mathrm{M}_\odot$ to be enclosed within less than 9 R_g. Out to 10^6 R_g the potential is dominated by the MBH, as the comparison with theoretical estimates shows (solid and dashed lines). Left: astrometric flare data overlayed on the EHT observation of Sgr A* (Event Horizon Telescope Collaboration et al., 2022) that provides a constraint at a similar radius.

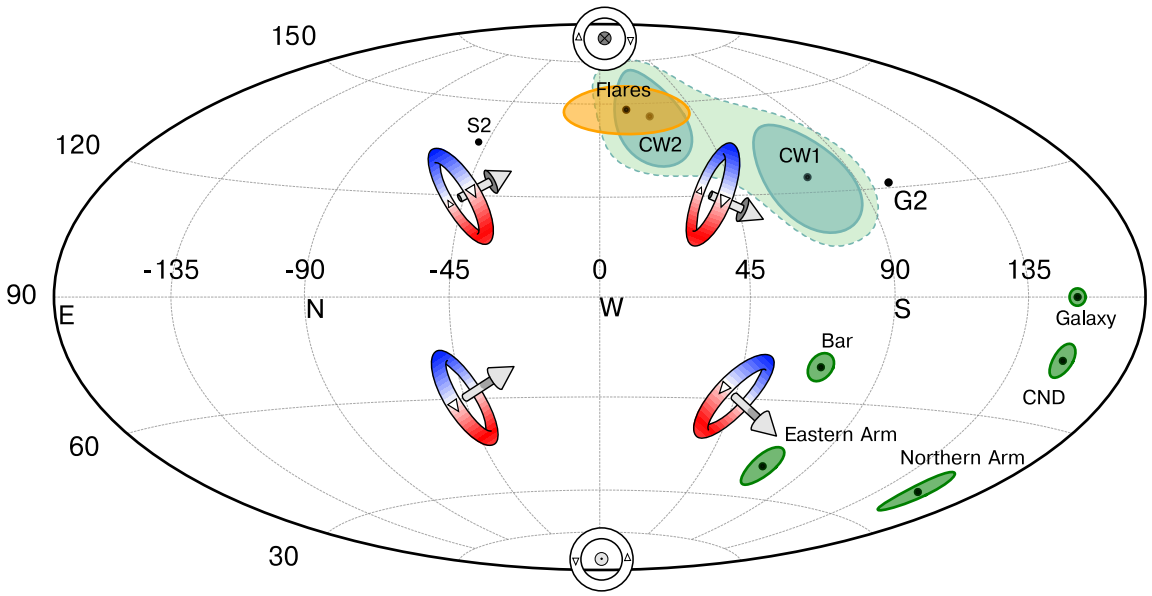

Figure 3.8: Compilation of orientations of angular momentum vectors of different dynamical structures in the GC. The colored tori illustrate the definitions of the angles. Inclinations between 0° and 90° correspond to counterclockwise motion on the sky (bottom half) and 90° – 180° to clockwise motion (upper half). The vectors of the clockwise stellar disk (shown are the features called CW1 and CW2 in von Fellenberg et al. 2022; see also Paumard et al. 2006,Lu et al. 2009), of the Sgr A* flares (this work), and of the gas cloud G2 (Gillessen et al., 2012a) are very close to each other. Other features shown are the rotation of the Galaxy, as well as the Circumnuclear Disk (CND) in the GC and the Eastern and Northern Arm gas features. The orientation of the flare angular momentum vector is consistent with the clockwise disk features.

the orbital radius of planet Mercury. A similarly strong constraint is obtained from the radio-VLBI image of Sgr A* (Event Horizon Telescope Collaboration et al., 2022).

The stellar orbits with the sub-percent precise mass measurement, on the other hand, limit the size of Sgr A* to be smaller than the smallest observed pericenter passages, which are those of S29 with 100 AU in 2021 (directly observed by GRAVITY Collaboration et al. 2022) and S14 with 26 AU in 2000 (well-determined orbit, but poorer coverage; Gillessen et al. 2017 and newer data). We show an updated version of the enclosed mass vs. radius in Fig. 3.7.

Other than the mass determination from the stellar orbits, both inner constraints are not assumption-free. The NIR flare constraint assumes that the motion of the emission is near Keplerian (i.e., governed by the forces of gravity), which is well motivated by accretion flow models (Yuan et al., 2003; Narayan and Quataert, 2023). The EHT image needs to assume a certain (again well-motivated) structure of the accretion flow, as other gas configurations could mimic the ring-like appearance. Taken together, these two independent estimates make the case for a black hole ever more convincing. Excluded are, for example, self-gravitating fermionic dark matter models with typical core radii of $\approx 10^{-3}\,\mathrm{pc} \approx 200\,\mathrm{AU}$ (Argüelles et al., 2019; Becerra-Vergara et al., 2020).

The fact that the azimuthal speed of the hot spots is near Keplerian is, however, non-trivial. In low-density advection-dominated accretion flows (ADAFs), the gas motions generally are assumed to be sub-Keplerian (e.g., Yuan and Narayan, 2014). The same is not true for magnetically dominated flows, where the speed can depend on the spin of the black hole, and both sub- and super-Keplerian motions occur. We note that a number of non-Keplerian models have also been proposed. Aimar et al., 2023 consider the outward motion of a hot spot along a conical trajectory, and Lin et al., 2023 propose that, similar to coronal mass ejections on the Sun, Sgr A* flux ropes are ejected out and filled with energetic electrons. Matsumoto et al., 2020 discuss whether the observed motions are actually pattern motions.

In addition to the enclosed mass, we also measured the orientation of the flare orbits (see Fig. 3.8). The measured orientation, which is the direction of orbital angular momentum, is close to that of the clockwise stellar disk (Levin and Beloborodov, 2003; Genzel et al., 2003b; Paumard et al., 2006; Lu et al., 2009; von Fellenberg et al., 2022, Fig. 9), suggesting a physical connection.

The stars that make up the disk are predominantly O–type and Wolf–Rayet–type stars that have strong winds. Simulations by Ressler et al., 2020 indeed show that the almost spherical accretion flow, fueled by the stellar winds from disk stars, carries the initial angular momentum down to event horizon scales, where the gas settles into a disk-like structure. This disk can tilt by a moderate angle with respect to the initial angular momentum, perhaps responsible for the misalignment between the stellar disk and flare angular momentum directions in Fig. 3.8. The simulations also predict that the infalling gas settles into a magnetically arrested disk (MAD), which naturally carries a poloidal field geometry. Only for strong fields can the geometry withstand the dragging with the fluid that would lead to a toroidal field geometry. Our data, favoring a poloidal field, directly support the MAD state. The MAD scenario is further supported by the estimated

magnetic field strength (30-80 G; Ripperda et al. 2020) and measured density profile (see Fig. 6 in Gillessen et al. 2019 and references therein). McKinney et al., 2013 and Ressler et al., 2023 find that for MAD situations, the innermost disk-like structure tends to align with the spin axis of the black hole. The dynamics of NIR flares may, in that case, actually carry information on the black hole spin rather than just on the initial conditions of the inflow.

Acknowledgements. We are very grateful to our funding agencies (MPG, ERC, CNRS [PNCG, PNGRAM], DFG, BMBF, Paris Observatory [CS, PhyFOG], Observatoire des Sciences de l'Univers de Grenoble, and the Fundação para a Ciência e Tecnologia), to ESO and the Paranal staff, and to the many scientific and technical staff members in our institutions, who helped to make NACO, SINFONI, and GRAVITY a reality. JS is supported by the Deutsche Forschungsgemeinschaft (DFG, German Research Foundation) under Germany's Excellence Strategy – EXC- 2094 – 390783311. A.A., A.F., P.G., and V.C. were supported by Fundação para a Ciência e a Tecnologia, with grants reference SFRH/BSAB/142940/2018, UIDB/00099/2020 and PTDC/FIS-AST/7002/2020. F.W. has received funding from the European Union's Horizon 2020 research and innovation programme under grant agreement No 101004719. Based on observations collected at the European Southern Observatory under the ESO programme IDs 109.22ZA.005, 109.22ZA.002, 105.20B2.004, 0103.B-0032(C), 0101.B-0576(E), 0101.B-0576(C).

Chapter 4

Monitoring stellar orbits in the Galactic Center with GRAVITY

4.1 Introduction

The Galactic Center, home to the supermassive black hole Sagittarius A* (Sgr A*), is a uniquely rich astrophysical laboratory. Hosting a dense cluster of stars, the S-star cluster, within just one arcsecond of Sgr A*, this region offers an exceptional opportunity to study astrophysical processes in the strong gravitational regime and to probe General Relativity (GR; Genzel et al., 2010) near a massive black hole. The near-infrared instrument GRAVITY (GRAVITY Collaboration et al., 2017) at the Very Large Telescope Interferometer (VLTI) makes it possible to overcome the diffraction limit of a single 8 m-class telescope, reaching an imaging resolution of ≈3 milli-arcseconds and an astrometric accuracy down to 30 micro-arcseconds, a factor 10–20 better compared to a single telescope of similar size. GRAVITY's high angular resolution and precision allow us to isolate individual stars near Sgr A*, trace their orbits at unprecedented precision, and directly probe relativistic effects in the stars' orbits.

Approximately 50 stars in the Galactic Center have known orbits, determined from stellar monitoring in imaging and spectroscopy over more than three decades (Schödel et al., 2002; Ghez et al., 2003; Ghez et al., 2005; Eisenhauer et al., 2005; Gillessen et al., 2017). The most prominent star is S2, due to its brightness of $m_K \approx 14$ and short period of 16 years. Following the motion of S2, in particular, during its pericenter in May 2018, allowed the detection of effects predicted by General Relativity (see Section 1.1.3). This was made possible by the high astrometric precision of GRAVITY, which was critical in resolving the subtle deviation from a Keplerian motion of S2 (GRAVITY Collaboration et al., 2020c).

Following the 2018 pericenter passage, S2 moved out of the ≈70 milli-arcsecond GRAVITY field of view centered on Sgr A*, clearing the way for deep interferometric imaging and the detection of fainter stars, which were previously obscured by S2's brightness (see Chapter 2). In March 2021, four stars were detected within the central 50 milli-arcseconds

of Sgr A*: S29, S55, S62, and S300 (GRAVITY Collaboration et al., 2022). Two stars, S29 with $m_K = 16.7$ and S55 with $m_K = 17.2$, reached their pericenters in 2021.4 and 2021.7, respectively. In particular, S29 approached Sgr A* even more closely than S2, with a distance of only ≈100 AU, while S55 orbits the black hole on a shorter period than S2, namely only 12 years. The monitoring of stars during their pericenters offers the opportunity to determine the mass of and distance to Sgr A*. In 2021, both S29 and S55 passed their pericenters as mentioned above, while S38 exhibited significant acceleration as it approached its pericenter in 2022.7. A combined fit of the four stars S2, S29, S38, and S55 has enabled the most recent and precise estimates of the gravitational potential (see Section 1.1.2; Gravity Collaboration et al., 2024). Finally, the images reconstructed from the 2021 GRAVITY data revealed the previously unknown, faint star, S300, with a magnitude of $m_K \approx 19.3$. S300 is even fainter than the star S62, a slowly moving star of magnitude $m_K = 18.9$, demonstrating the power of the imaging approach (GRAVITY Collaboration et al., 2021b; GRAVITY Collaboration et al., 2022). S300 moved to the west at high angular velocity and was strongly fiber-damped in July 2021, such that it was difficult to detect the star in the Sgr A*-centered field. To follow the star and provide an additional test for its detection, we moved the GRAVITY fiber such that S300 was close to the field center. This provided the first observed field not centered on Sgr A*. The discovery of S300 and the detection of pericenter passages of two more stars motivated a broader search for faint stars in the inner region of the Galactic Center and the monitoring of stars before and after their closest approach to the massive black hole.

Since the commissioning of GRAVITY in 2017, we have obtained high-precision positions of 15 S-stars in the inner 400 milli-arcseconds of Sgr A*. We have been observing S2 continuously since 2017, and the stars S29, S38, S42, S55, S60, S62, S63, and S300 since 2021. By April 2022, we had achieved high-precision astrometry of 11 stars, with S24 and S20 subsequently added to the sample. Since 2023, our monitoring campaign has expanded further, including the stars S4, S9, and S21. Most recently, our 2023 and 2024 datasets have revealed several previously unknown faint stars. The analysis of their orbits is ongoing and will be presented in a forthcoming publication (GRAVITY Collaboration et al. 2025, in prep.). One of these newly identified stars, S301, is included in the analysis presented in this chapter.

In this work, we provide updated orbits of 10 S-stars presented in Gillessen et al., 2017 and give one new orbit, which is that of S301. We investigate the resulting distribution of orbital parameters in the S-star cluster, including 30 stars from Gillessen et al., 2017 that were not observed with GRAVITY but for which orbital solutions exist. The main advancement compared to Gillessen et al., 2017 lies in the inclusion of GRAVITY data, which enables significantly more precise astrometric measurements of stellar positions and, consequently, more accurate determinations of stellar orbits. To observe these stars with GRAVITY from 2017 to 2025, modifications in the observing strategy were required, mainly due to the fast motions of the stars. Further, instrumental upgrades were implemented to improve the data quality and enable more precise and fainter observations. These adjustments are described in detail in this work.

In the following sections, we will present the steps necessary to determine the orbits

of S-stars in the Galactic Center observed with GRAVITY. Section 4.2 explains instrumental upgrades to GRAVITY under the GRAVITY+ project relevant to Galactic Center observations. Our observing strategy is illustrated in Section 5.3. Once the data is taken, we determine astrometric separations via single-beam or dual-beam astrometry, which we explain in Section 4.4. We give a summary of the data used for the analysis in this work in Section 4.5 and describe our analysis in Section 4.6. The updated and refined orbital parameters of 11 S-stars are presented in Section 4.7, where we also show the motions of four stars for which we have not yet determined orbits. Further, we discuss the distribution of orbital elements, which may preserve valuable information about the origin of the S-stars (see also Section 1.1.2). Finally, we summarize our findings in Section 4.8.

The work presented in this chapter is based on research carried out by the Gravity Collaboration during the course of my PhD. We are finalizing the results, including the astrometric analysis and updated orbits of S-stars in the Galactic Center, which form the basis of a forthcoming publication (GRAVITY Collaboration et al. 2025, in prep.).

4.2 Observational techniques and instrument upgrades

The setup for Galactic Center observations with GRAVITY has already been described in Section 1.3.3. This includes the observing window, spectral resolution, polarization mode, fringe tracking, and adaptive optics (AO) configuration. The observational techniques have evolved over the years due to instrumental upgrades to GRAVITY and the VLTI under the GRAVITY+ project (see Section 1.3.4; Eisenhauer, 2019; GRAVITY+ Collaboration et al., 2022), which started in 2019. Upgrades implemented in 2022 and 2023 are especially crucial for Galactic Center observations. Those are the pupil modulation and the implementation of a new observing mode, GRAVITY-Faint, which we will describe in more detail in the following.

4.2.1 Pupil modulation

In 2022, we introduced the so-called pupil modulation to maintain astrometric accuracy for flare observations in dual-beam astrometry. Before this, Sgr A* flares were observed in single-beam astrometry, which is doable when a bright star, such as S2, is within the same field of view as Sgr A*. In such cases, the flare motion is derived by fitting a binary model to the visibility amplitudes and closure phases without the need to fit the visibility phases. This approach was used for the 2018 flare observations when both Sgr A* and S2 were simultaneously visible in the interferometric field (GRAVITY Collaboration et al., 2018a). After 2018, however, S2 moved out of the Sgr A*-centered field of view, and no other bright star remained within the central field to serve as a reference. Consequently, flare analysis requires fitting the visibility phases, which are susceptible to systematic errors. In particular, high-order imperfections in the GRAVITY optics lead to significant systematic errors in the phase measurement. This is due to the limited coverage of the metrology sensors, which only measure four points across the telescope pupil. While these high-

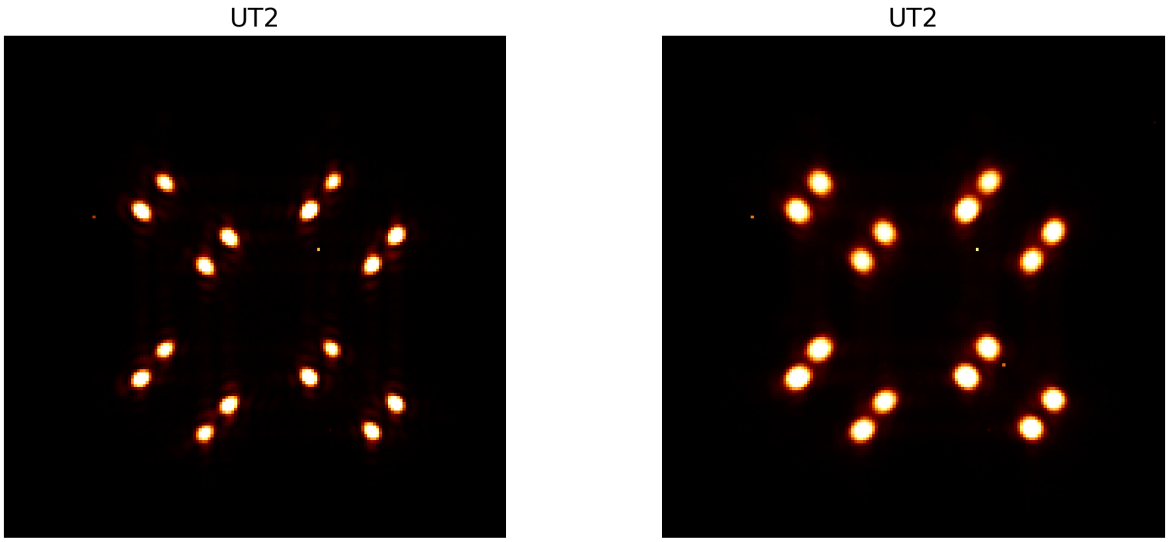

Figure 4.1: Pupil spots of UT2 imaged on the GRAVITY acquisition camera without (left) and with (right) pupil modulation. When the pupil modulation is activated, the continuous circular motion of the pupil averages out high-order aberrations introduced in the GRAVITY optics within a single DIT, resulting in smooth, symmetric spots. The pupil spots allow us to retrieve the pupil position along and perpendicular to the optical axis, thereby detecting pupil wander.

order aberrations average out for measurements of stellar positions collected throughout the night, thanks to the rotation of the pupil, this averaging does not occur for short exposures of flares. To mitigate this issue, we simultaneously modulate the pupil mirrors in the fiber coupler in a circular motion with a frequency of 1 Hz relative to the metrology receivers, effectively removing this source of systematic error within one DIT. Given the random occurrence of flares, we maintained the pupil modulation throughout the night. As a result, exposures on all fields were collected using pupil modulation. The effect of the pupil modulation is directly visible in the pupil spots, which are imaged on the acquisition camera by a 2×2 lenslet array (see Section 1.3.2). Figure 4.1 shows the pupil spots of UT2 with and without pupil modulation. When the pupil modulation is activated, the pupil mirrors are moved in a controlled circular pattern, effectively averaging out the described high-order aberrations over time. As a result, the imaged spots become smooth and symmetric. During the observations, we regularly verify that all pupil spots are visible and correctly positioned, allowing us to track lateral and longitudinal pupil motion in real-time.

4.2.2 Metrology ON and FAINT modes

To upgrade GRAVITY to a more sensitive instrument, GRAVITY+ also aims to eliminate existing noise sources as much as possible. One major improvement is the implementation

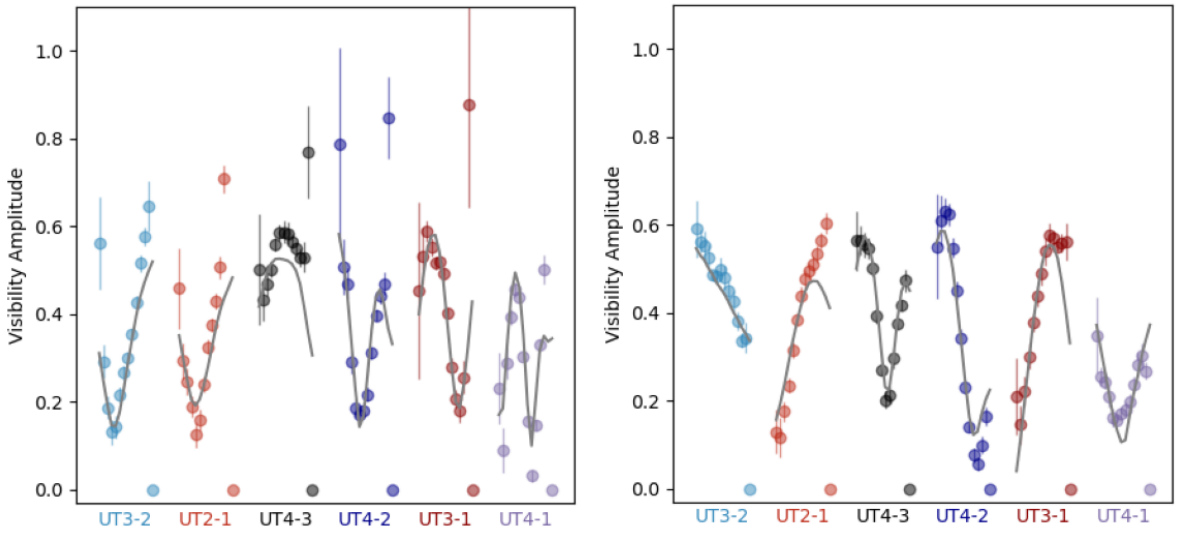

Figure 4.2: Comparison of measured visibility amplitudes in the GRAVITY-On (left) and GRAVITY-Faint (right) observing modes. Colored points show the observed data, while gray lines represent the best-fit models. The GRAVITY-On data (left) was obtained on the night of April 23rd, 2024, and modeled using Sgr A*, S62, S24, and S301. The GRAVITY-Faint data (right), from the night of June 2nd, 2023, includes an additional star, S38. In the GRAVITY-On mode, several spectral channels, particularly in the blue part of the spectrum, are affected by metrology laser back-scattering, resulting in increased noise. The GRAVITY-Faint mode suppresses this noise by damping the metrology laser during the DIT, resulting in more usable channels for model fitting. In this configuration, only the first and in some cases the last channel must be excluded from the fit.

of a new observing mode, GRAVITY-Faint (Widmann et al., 2022), which we have used for Galactic Center observations since 2023. The dominant source of instrumental noise is the back-scattering of metrology laser light on the detector. Although the wavelength of the metrology laser is outside the science spectrum, Raman scattering and back-scattering from elements in the optical fibers still lead to instrumental noise, which is particularly strong in the blue part of the spectrum. To mitigate this issue, we added optical attenuators to the science object (SC) and fringe tracking (FT) beams of the metrology laser. These attenuators allow us to dampen the laser power in the beams by applying a voltage to them. In GRAVITY-Faint, the SC and FT lasers are damped during a DIT, while between DITs, the laser is used at its usual power to maintain the stability of the metrology measurement. The decrease in instrumental noise by up to a factor of eight in the blue part of the spectrum allows us to use two more spectral channels for our analysis. The first and last of 14 channels remain excluded due to residual contamination and thermal noise from the telescope and VLTI optical train, respectively. The improvement in data quality is illustrated in Figure 4.2, which compares measured visibility amplitudes obtained in the previous implementation GRAVITY-On, where the laser power is kept constant throughout

the exposure, and in GRAVITY-Faint. In GRAVITY-Faint, fewer spectral channels are contaminated by metrology laser back-scattering, allowing more channels to be used in astrometric fitting. The increase in spectral channels enhances the (u, v)-coverage, which is crucial for reconstructing images of the Galactic Center (see Chapter 2; GRAVITY Collaboration et al., 2021b; GRAVITY Collaboration et al., 2022). When observing in GRAVITY-Faint, the DIT increases to 30 s with 12 NDITs, compared to 10 s and 32 NDITs in GRAVITY-On. For a detailed description of the instrumental changes in GRAVITY-Faint, see Widmann et al., 2022; GRAVITY+ Collaboration et al., 2022.

4.3 Observations and observing strategy

The strategy for Galactic Center observations is designed to achieve three complementary goals: first, to monitor stellar orbits with high astrometric precision; second, to detect new stars via deep imaging; and third, to catch flares and measure their orbits around Sgr A*.

Each observing night includes exposures centered on Sgr A*. Due to GRAVITY's high angular resolution of ≈3 milli-arcseconds, we can disentangle Sgr A* from nearby stars and detect it at all times. This central pointing provides a high-precision reference position of the black hole, which is used to determine the relative positions of nearby stars. We aim for uncertainties in the position measurement as low as 30 micro-arcseconds. This allows us to resolve stellar motions from night to night and refine orbital parameters, especially for stars approaching or leaving their pericenter passage.

In addition to the central field, we observe stars up to several hundred milli-arcseconds from Sgr A*. These are referenced back to Sgr A* by either pointing directly at it if the star is faint or requires maximal flux coupling, or between multiple stars if they are sufficiently close to be observed simultaneously. Because the GRAVITY fiber has a Gaussian acceptance profile, stars near the edge of the ≈70 milli-arcsecond field of view are coupled less efficiently. This leads to increased uncertainty in the stellar position, especially for faint, off-center stars, making field-centering a key part of the observing strategy. Importantly, the field pointings evolve continuously over time. Due to the high proper motions of many S-stars, the optimal field pointings change each year or even month as stars move out of shared fields and require individual pointings or, conversely, move close to other stars and can be observed together in a combined field. To detect flares, we revisit Sagittarius A* regularly throughout the night. Near-infrared flares occur roughly once or twice per day, and are detectable in real-time, mainly through an increased flux of Sgr A* on the GRAVITY acquisition camera. If a flare is detected, we continue integrating on Sgr A* throughout the flare duration.

Figure 4.3 illustrates our observing strategy, using the night of June 22nd, 2024, as an example. Each purple circle represents the ≈70 milli-arcsecond GRAVITY fiber field of view. The central Sgr A* field is shown together with surrounding fields that cover known S-stars. The field names correspond to the prominent stars they contain, except for the S2 and Sgr A* fields, which are labeled after their central target rather than all sources in the field. The stars are color-coded by spectral type, where blue indicates late-type stars,

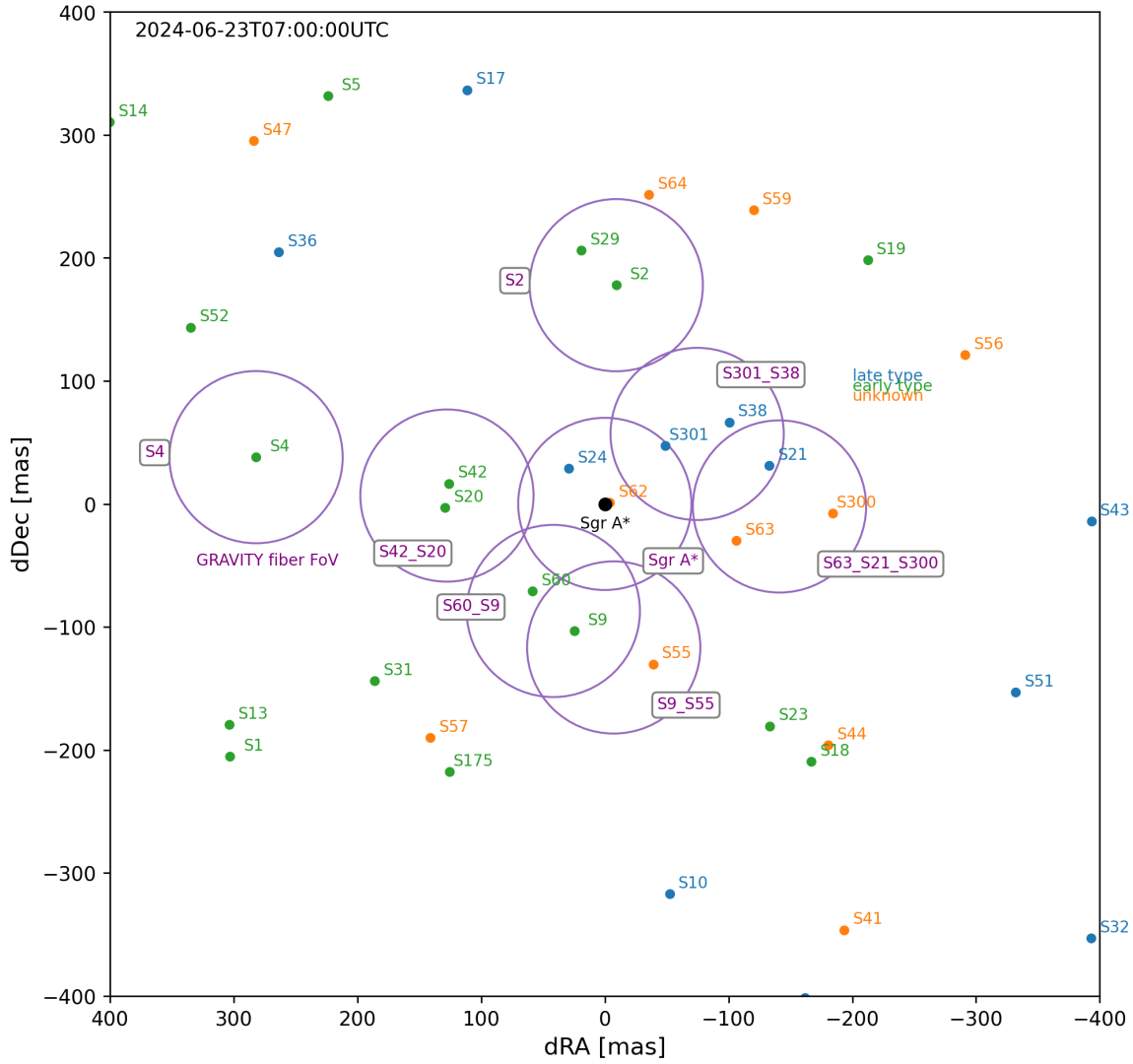

Figure 4.3: Example of our observing strategy on the night of June 22nd, 2024. Each purple circle marks the field of view of the GRAVITY fiber. The central Sgr A* field is shown together with surrounding fields covering known S-stars. Late-type stars are in blue, early-type stars in green, and stars of unknown spectral type are in orange. Each night, we collect exposures centered on Sgr A* to capture flares, determine a high-precision reference position of the black hole to reference stars further out to it, and potentially detect new stars through deep imaging. In addition, we observe fields containing stars up to several hundred milli-arcseconds from Sgr A*, prioritizing those near their pericenter to trace their orbital motion accurately.

green indicates early-type stars, and orange indicates stars of unknown spectral type. The observing templates are prepared in advance for all fields and each night of the observing run. The field selection and number of exposures per field are then adapted depending on the duration of the Galactic Center visibility window at the VLTI. We typically collect at least six exposures on Sgr A* each night to ensure a robust measurement of its position and of the positions of the stars in the central field. Additional fields are chosen based on science priority, the brightness of the stars in the field, and current observing conditions. In poor weather conditions, we favor fields with bright stars. In good weather conditions, we target fields containing faint stars, where we take multiple exposures to improve the (u, v)-coverage, which is crucial for interferometric imaging.

4.4 Determining astrometric separations

After having collected data over a night, we determine the astrometry of stars in the immediate vicinity of Sgr A*. The separation vector between Sgr A* and a star can be retrieved in three different ways, and the method chosen depends on the distance of the star to Sgr A* and whether the star is the only one in the interferometric field of view. The positions of S2 were derived using all three methods for the data from 2017 to 2025, whereas the positions of all other stars were derived in two different ways. One method is single-beam astrometry, which is used for stars in the same field of view as Sgr A*. The other method is dual-beam astrometry, which is used for stars outside the ≈70 milli-arcsecond field of view centered on Sgr A*and has two different approaches. All techniques will be explained in the following (see also Appendix A in GRAVITY Collaboration et al., 2020c and GRAVITY Collaboration et al., 2022). Additionally, we correct for static aberrations and bandwidth smearing introduced in the optical path of GRAVITY, as described in GRAVITY Collaboration et al., 2021c, and for a drift of the visibility phase resulting from the uncertainty of the FT–SC separation vector as explained in GRAVITY Collaboration et al., 2020c.

4.4.1 Single-beam astrometry

To determine the positions of stars within the same field of view as Sgr A* we use single-beam astrometry. In this case, the separation vector between Sgr A* and the star can be extracted by fitting the measured visibility amplitudes and closure phases with a multi-source model that includes Sgr A* and all stars within the interferometric field. An example is the observation of S2 and Sgr A* in 2018 and part of 2017, when both sources were within GRAVITY's ≈70 milli-arcsecond field of view. This configuration allowed for simultaneous observation of both sources. The geometry of this setup is illustrated in Figure 4.4, where Sgr A* (black cross at the origin) and S2 are within the same field, indicated by the black dashed circle.

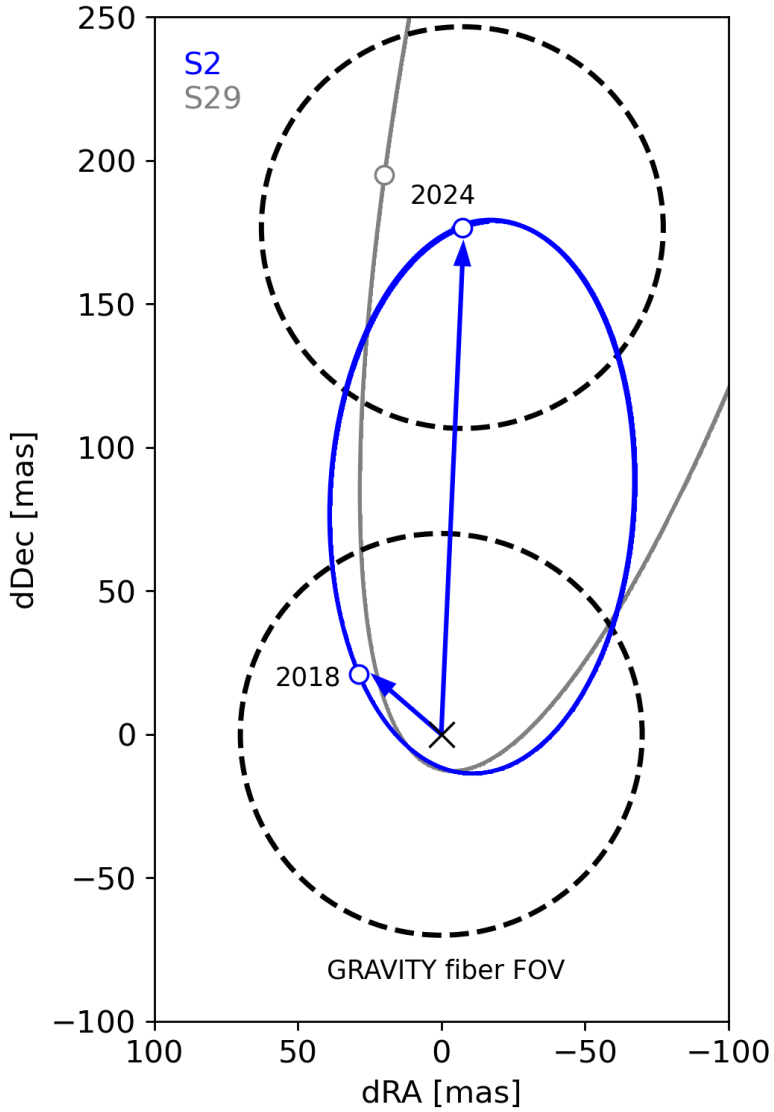

Figure 4.4: Illustration of single-beam and dual-beam astrometry using the orbits of S2 (blue) and S29 (gray) around Sgr A* (black cross at the origin) as an example. The dashed black circles represent the GRAVITY fiber's ≈70 milli-arcsecond field of view. In 2018, S2 and Sgr A* were within the same field of view, allowing us to derive the position of S2 to Sgr A* using single-beam astrometry. By 2024, S2 had moved farther from Sgr A*, and we used dual-beam astrometry, where both fields are observed separately and the separation between the two sources is determined from the fitted phase center vectors and the known fiber offset. The position of S29 is determined by adding the S29-S2 separation vector.

4.4.2 Dual-beam astrometry

Dual-beam astrometry is used to determine the position of a star to Sgr A* when the star is outside the 70 milli-arcsecond field of view of Sgr A*. In this case, we observe both sources separately within a night by offsetting the science fiber from Sgr A* to the star, described by the fiber offset, $\vec{s}_{\text{fiberoffset}}$, which is applied to the fiber differential delay lines. The two black dashed circles in Figure 4.4 represent the GRAVITY fiber field of view, which we point successively to Sgr A* and, in this case, S2. Further, each pointing is referenced to the fringe tracking star, which is IRS 16C in our observations. There are two different options for dual-beam astrometry:

- One option is to measure the separation of a star to Sgr A* by interferometrically calibrating the Sgr A* data with those of the star. The visibility phases of both pointings are referenced to the fringe tracking star, and by performing the calibration, the separation to the fringe tracking cancels out. As a result, we obtain visibility phases, which directly measure the separation vector between the star and Sgr A*. This technique is possible as long as the star is the only star in the field, thus, its visibility amplitudes are close to one, its closure phases are close to zero, and no modulation from other sources is seen in the interferometric observables. For example, this method was applied to S2 between 2019 and 2022, and to S4 in 2023 and 2024, allowing us to determine their positions relative to Sgr A* with high precision.

- The other option to determine the separation between a star and Sgr A* is by observing them separately and deriving their separation via vector addition in a post-fitting step. In this method, we fit the complex visibilities and closure phases of both the Sgr A*-centered field and the star-centered field, each using a model that includes all sources in the respective field. By fitting the visibility phases in each field, we obtain the phase center vector, $\vec{s}_{\text{PC}}$, which describes the offset between the actual position of the central object and the fiber center. The relative position between the star and Sgr A* is then computed by combining three vectors, namely the phase center vector of the Sgr A* field, $\vec{s}_{\text{PC,SgrA*}}$, the phase center vector of the S2 field, $\vec{s}_{\text{PC,S2}}$, and the applied fiber offset between the two pointings, $\vec{s}_{\text{fiberoffset}}$:

$$\vec{s}_{\text{S2-SgrA*}} = -\vec{s}_{\text{PC,SgrA*}} + \vec{s}_{\text{PC,S2}} + \vec{s}_{\text{fiberoffset}} \ . \tag{4.1}$$

  This dual-beam astrometry method has been used to derive the positions of all stars observed since July 2021, when we started following more stars than only S2 on their orbits. In particular, the position of S2 in 2023 and 2024 was derived using this method, as it was no longer the only star in the 70 milli-arcsecond field of view. By then, S29 had entered the same field, introducing a modulation in the interferometric observables of S2, which made S2 an unsuitable phase calibrator. Instead, S4 was used as the calibrator. This configuration is illustrated in Figure 4.4, where S2 and S29 are within the same field of view. In this case, the Sgr A*-centered and S2-centered fields are calibrated against S4, thereby effectively removing the separation

to S4 in the final vector addition. The phase center vectors of both fields are measured from the fits, and the separation vector between S2 and Sgr A* is calculated using Equation 4.1.

To derive the separation between S29 and Sgr A*, we add the separation vector between S2 and S29, $\vec{s}_{\text{S29-S2}}$, leading to the following equation:

$$\vec{s}_{\text{S2-SgrA*}} = -\vec{s}_{\text{PC,SgrA*}} + \vec{s}_{\text{PC,S2}} + \vec{s}_{\text{fiberoffset}} + \vec{s}_{\text{S29-S2}} \ . \tag{4.2}$$

Table 4.1: Astrometric and spectroscopic data used for the analysis of stellar motions.

Star	GRAVITY	NACO	SINFONI	ERIS
S2	118	118	92	10
S4	35	175	45	10
S9	16	191	33	7
S20	8	152	14	3
S21	10	185	24	7
S24	40	121	32	10
S29	65	72	17	2
S38	49	118	8	7
S42	20	123	8	2
S55	39	44	2	–
S60	17	92	6	5
S62	62	26	–	–
S63	12	28	–	–
S300	17	–	–	–
S301	10	–	–	–

Notes. For S2, we used in addition 3 Keck, 2 NACO, and 4 GNIRS/GEMINI radial velocity measurements. For S4, we additionally used 2 SHARP and 1 GEMINI data points. For S9, we added 8 SHARP and 1 GNIRS/GEMINI data points. For S24, we used, in addition, 8 SHARP and 1 GNIRS/GEMINI data points. For S29, we added two radial velocity measurements from GNIRS/GEMINI. For S38, we used two additional Keck data points.

4.5 Data

With the astrometric positions of stars around Sgr A* determined from GRAVITY data, we obtain high-precision measurements of their motion projected onto the plane of the sky.

To fully determine the stellar orbits in three dimensions, we also need information along the line of sight, that is, the radial component of the motion. To achieve this, we include radial velocity data in our analysis. Historically, we relied on the SINFONI integral-field spectrograph (Eisenhauer et al., 2005), which has provided extensive spectroscopic monitoring of the S-stars. Following the decommissioning of SINFONI in 2019, we transitioned to using the Enhanced Resolution Imager and Spectrograph (ERIS; Davies et al., 2023) at the VLT, which offers a state-of-the-art AO system and a significantly higher spectral resolution (R $\approx$ 10,000) compared to SINFONI (R $\approx$ 4,000). We combine radial velocity data points obtained with ERIS since 2022 with the existing SINFONI dataset, and complement the interferometric dataset obtained with GRAVITY with AO-assisted astrometric measurements from NACO at the VLT. The complete dataset used for the analysis of stellar orbits is summarized in Table 4.1.

4.6 Analysis

With the dataset described in Table 4.1, we determine each star's orbital motion around Sgr A*. For each star, we fit six orbital parameters (a, e, i, ω, Ω, t_0) that describe its Keplerian orbit. Two additional fit parameters are the mass of and distance to the central SMBH, $M_\bullet$ and R_0. Further, five parameters describe the on-sky position and three-dimensional velocity of Sgr A* relative to the AO imaging/spectroscopic reference frame, namely (x_0, y_0, vx_0, vy_0, vz_0). In the case of S2, we include a Schwarzschild precession term f_{SP} (see Section 1.1.3), which we fix to $f_{SP} = 1$ in our analysis. The orbital parameters then describe the initial osculating Keplerian orbit.

Table 4.2: Best-fit parameters of the S2 orbit fit to determine the mass of and distance to Sgr A*, and the reference frame parameters.

parameter	value	error	prior	error
$M_\bullet$ [$10^6 M_\odot$]	4.3192	0.0114	–	–
R_0 [pc]	8287.9	8.3	–	–
x_0 [mas]	-0.49330	0.06895	-7.79×10^{-4}	7.38×10^{-5}
y_0 [mas]	-0.14110	0.07329	-1.18×10^{-4}	7.93×10^{-5}
vx_0 [mas/yr]	0.075064	0.005545	6.64×10^{-5}	7.27×10^{-6}
vy_0 [mas/yr]	0.042458	0.005797	3.70×10^{-5}	7.76×10^{-6}
vz_0 [km/s]	-1.4763	1.2901	0	5

Notes. We adopt these values for the orbit fitting of all other stars, keeping the parameters fixed throughout the fitting process. The reference parameters x_0 and y_0 refer to J2000.

We determine the values of (x_0, y_0, vx_0, vy_0, vz_0), $M_\bullet$, and R_0 from an orbit fit of S2

presented in Table 4.2, which is the star that best constrains these parameters. For all other stars, we adopt these as fixed parameters and fit only the orbital parameters.

We used a Levenberg-Marquardt χ^2 minimization algorithm or a (Metropolis-Hastings) Markov chain Monte Carlo (MCMC) analysis for orbit fitting. For further details, we refer to GRAVITY Collaboration et al., 2018b; GRAVITY Collaboration et al., 2019a; GRAVITY Collaboration et al., 2020c; GRAVITY Collaboration et al., 2021c and Appendix A of GRAVITY Collaboration et al., 2022.

4.7 Stellar orbits in the Galactic Center

Our primary goal is to revisit and refine the orbital parameters of the S-stars presented in Gillessen et al. (2017), using the advanced capabilities of GRAVITY. Thanks to GRAVITY's milli-arcsecond resolution and micro-arcsecond-level astrometric precision, we can now determine stellar orbits with far greater accuracy than previously possible using single 8 m-class AO-assisted telescopes. With GRAVITY, we have monitored 15 stars in the inner 400 milli-arcseconds of Sgr A*. We present the orbits of all these stars in Figure 4.5. For 11 of the stars, we have sufficient astrometric and spectroscopic coverage to determine a complete orbital solution, assuming the gravitational potential derived from the S2 orbit fit. The updated orbital solutions are summarized in Table 4.3. We fit linear or quadratic motions for the remaining four stars, as the data do not yet allow us to constrain their orbits, and present the results in Table 4.4. The combination of dense temporal sampling and high-precision GRAVITY astrometry significantly improves the orbital parameter determination by factors ranging from 3 to more than 1000 compared to the results of Gillessen et al. (2017).

For a complete study of the distribution of orbital parameters, we include the S-stars presented in Gillessen et al., 2017, which were not observed with GRAVITY but have determined orbital parameters. Our sample of 41 stars with determined orbits consists of thirty early-type stars, eight late-type stars, and three stars of unknown spectral type, which are S39, S55, and S301.

We show the distribution of the angular momentum vectors for the 41 orbits in Figure 4.6, where we present the updated orientation of the orbital planes of the S-stars observed with GRAVITY. Early-type stars are shown in blue, late-type stars in red, and stars of unknown spectral type in gray. Further, of the 41 stars, eight stars have an orientation that is compatible with the clockwise stellar disk at ($\Omega = 104\,\mathrm{deg}$, $i = 126\,\mathrm{deg}$) (Bartko et al., 2009; Yelda et al., 2014): S66, S67, S83, S87, S91, S96, S97, and R44. The orbits of all other stars are randomly oriented. This finding is consistent with Gillessen et al., 2017.

In Figure 4.7, we show the cumulative eccentricity distribution of all stars that are not associated with the clockwise stellar disk. The left panel shows the eccentricity distribution of 22 early-type stars, and the right panel of seven late-type stars. We find that the early and late-type stars are thermally distributed with $n(e) \propto e$ (black line), which is compatible with Gillessen et al., 2017.

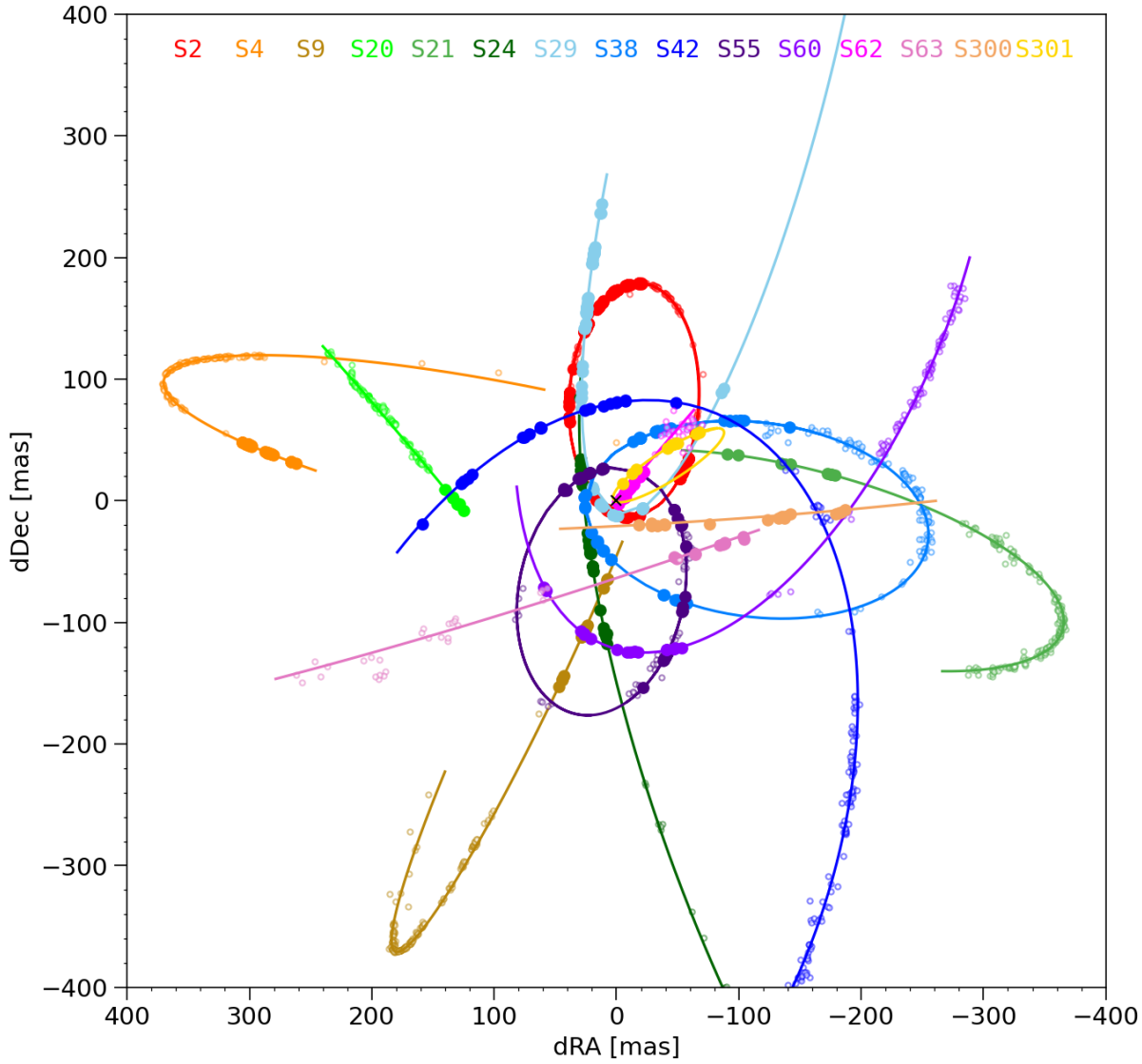

Figure 4.5: Motions of 15 S-stars in the inner 400 milli-arcseconds of Sgr A*with data from GRAVITY collected between 2017 and 2025. The filled circles represent GRAVITY data points. The small open circles are data from SHARP, GEMINI, or NACO.

Table 4.3: Orbital parameters for 11 stars for which we were able to determine orbits.

Star	a [as]	e	i [°]	Ω [°]	ω [°]	t_p [yr]	T [yr]	Sp	m_K
S2	$0.12503 \pm 3\times10^{-5}$	$0.88432 \pm 6\times10^{-5}$	134.715 ± 0.019	228.266 ± 0.026	66.378 ± 0.024	$2018.37912 \pm 8\times10^{-5}$	16.050 ± 0.001	e	13.95
S4	0.341 ± 0.001	0.403 ± 0.002	80.135 ± 0.024	258.748 ± 0.006	297.83 ± 0.41	1962.68 ± 0.33	72.13 ± 0.33	e	14.4
S9	$0.2709 \pm 7\times10^{-4}$	0.628 ± 0.002	82.523 ± 0.025	156.196 ± 0.019	153.37 ± 0.38	1977.23 ± 0.20	51.2 ± 0.2	e	15.1
S21	$0.2202 \pm 4\times10^{-4}$	0.753 ± 0.002	59.845 ± 0.157	259.111 ± 0.109	166.763 ± 0.352	2027.697 ± 0.012	37.505 ± 0.108	l	16.9
S24	0.8394 ± 0.0058	$0.8732 \pm 7\times10^{-4}$	104.019 ± 0.015	8.6312 ± 0.0197	292.589 ± 0.171	2024.582 ± 0.004	279.224 ± 2.926	l	15.6
S29	$0.3873 \pm 4\times10^{-4}$	$0.96880 \pm 4\times10^{-5}$	144.308 ± 0.071	4.71 ± 0.06	203.57 ± 0.07	$2021.4115 \pm 1\times10^{-4}$	87.5222 ± 0.1498	e	16.7
S38	$0.14205 \pm 2\times10^{-5}$	$0.81948 \pm 9\times10^{-5}$	167.505 ± 0.102	112.523 ± 0.673	30.894 ± 0.683	$2022.6892 \pm 4\times10^{-4}$	19.438 ± 0.004	l	17.0
S42	0.4124 ± 0.0018	$0.7697 \pm 9\times10^{-4}$	39.17 ± 0.07	308.46 ± 0.12	48.522 ± 0.141	2022.095 ± 0.003	96.155 ± 0.615	e	17.5
S55	$0.10423 \pm 4\times10^{-5}$	$0.731 \pm 2\times10^{-4}$	160.306 ± 0.112	325.981 ± 0.526	333.88 ± 0.51	2009.475 ± 0.007	12.218 ± 0.007	-	17.5
S60	0.358 ± 0.003	0.696 ± 0.002	127.655 ± 0.062	170.252 ± 0.122	31.009 ± 0.102	2024.132 ± 0.008	77.783 ± 0.835	e	16.3
S301	0.0768 ± 0.0122	0.978 ± 0.013	122.59 ± 8.59	81.82 ± 27.73	300.35 ± 16.17	2023.111 ± 0.058	7.73 ± 1.84	-	19.0–19.5

Notes. a is the semi-major axis, e the eccentricity, i the inclination, ω the longitude of the pericenter, Ω the position angle of the ascending node, t_P the epoch of pericenter passage, T the period, Sp the spectral type ('e' for early-type star, 'l' for late-type star), and m_K the K-band magnitude, which is taken from Gillessen et al., 2017. The K-band magnitude of S301 is determined using the improved imaging algorithm G^R (GRAVITY Collaboration et al. 2025, in prep.).

Table 4.4: Motions of stars for which we have not yet determined orbits.

Star	m_K	t_0	RA_0	vRA_0 [as yr^{-1}]	aRA [as yr^{-2}]	Dec_0	$vDec_0$ [as yr^{-1}]	$aDec$ [as yr^{-2}]
S20	2014.	180.547 ± 0.146	-4.86 ± 0.02	0.008 ± 0.003	58.337 ± 0.122	-5.749 ± 0.016	-0.003 ± 0.002	15.7
S62	2016.	-29.217 ± 0.196	3.151 ± 0.027	–	34.697 ± 0.229	-3.828 ± 0.030	–	18.9
S63	2014.	89.704 ± 0.579	-17.944 ± 0.092	-0.071 ± 0.009	-92.26 ± 0.93	5.562 ± 0.137	0.058 ± 0.014	17.5
S300	2023.	-110.931 ± 0.535	-51.145 ± 0.556	0.375 ± 0.504	-13.834 ± 0.56	3.83 ± 0.425	0.247 ± 0.407	19.0–19.3

Notes. The K-band magnitudes of S20, S62, and S63 are taken from Gillessen et al., 2017. The K-band magnitude of S300 is taken from GRAVITY Collaboration et al., 2022.

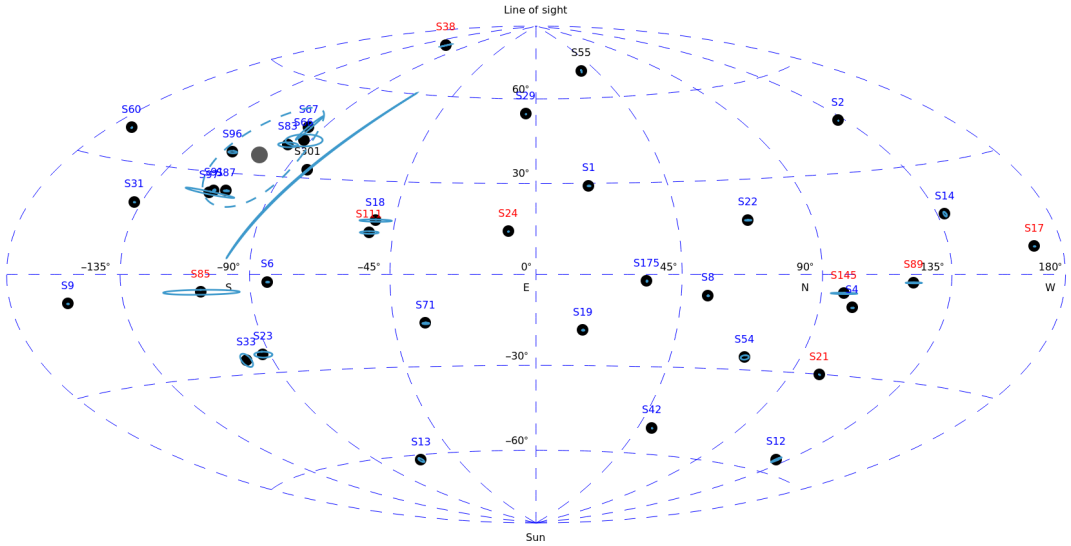

Figure 4.6: Distribution of angular momentum vectors of S-stars, for which we have orbits. The horizontal axis corresponds to the longitude of the ascending node, Ω, and the vertical axis to the inclination i. The error ellipses correspond to the statistical 1σ fit errors. We also show the clockwise stellar disk at ($\Omega = 104\,\mathrm{deg}$, $i = 126\,\mathrm{deg}$) (Bartko et al., 2009; Yelda et al., 2014), and its members S66, S67, S83, S87, S91, S96, S97, and R44. The other stars have randomly oriented orbits. The color of the labels indicates the star's spectral type, where blue corresponds to early-type stars, red to late-type stars, and gray to an unknown spectral type.

Investigating the orbital distribution of the S-stars can help understand their origin. One possible scenario is the Hills mechanism (see Section 1.1.2), which would create highly eccentric stars with $e \gtrsim 0.98$ (Hills, 1988). The observed eccentricity distribution, in contrast, is thermal. Therefore, subsequent relaxation processes must be involved to reproduce the observed eccentricity distribution of the S-stars. Generozov et al., 2025 find that indeed continuous disruption of binaries near Sgr A*, followed by orbital relaxation, can largely explain the observed thermal eccentricity distribution.

4.8 Conclusions

In this work, we presented a comprehensive analysis of the orbital motions of 15 S-stars in the inner 400 milli-arcseconds of Sgr A* observed with GRAVITY. Complementing GRAVITY data from 2017 to 2025 with spectroscopic and astrometric data from SINFONI, ERIS, and NACO, we derived orbital solutions for 11 stars and refined their orbital parameters. Compared to earlier studies with 8 m-class AO-assisted telescopes (Gillessen et al., 2017), we achieve improvements by up to three orders of magnitude in the determination of the orbital parameters.

Further, we presented observational techniques and observing strategies for monitoring

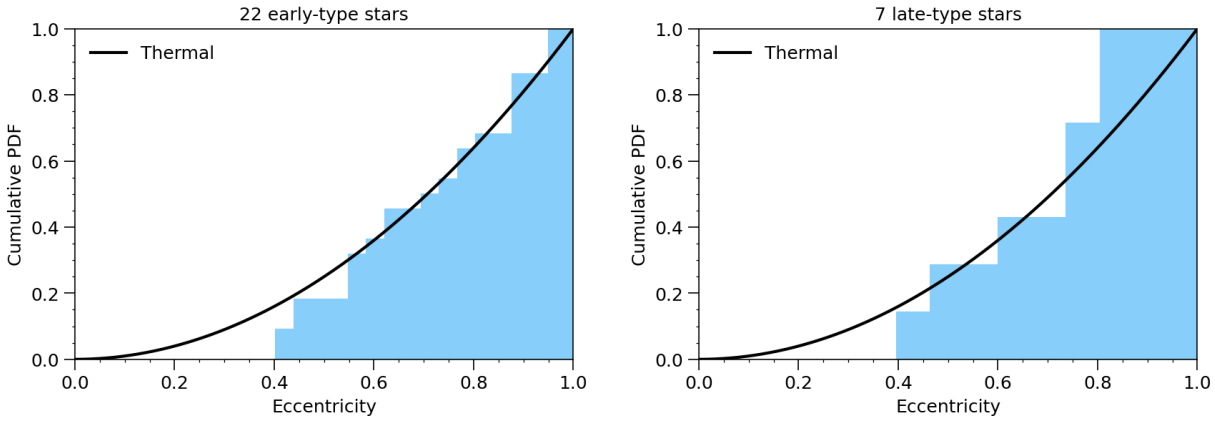

Figure 4.7: Cumulative probability density function (PDF) for the eccentricities of 22 early-type stars (left) and seven late-type stars (right), for which we have determined orbits. The distribution is compatible with a thermal eccentricity distribution (black line).

stars in the Galactic Center with GRAVITY, which have changed over the years, primarily for two reasons. First, instrumental upgrades to GRAVITY and the VLTI under the GRAVITY+ project (GRAVITY+ Collaboration et al., 2022) have enabled the pupil modulation to maintain astrometric accuracy for flare observations, and the implementation of a new observing mode, GRAVITY-Faint (Widmann et al., 2022), to reduce instrumental noise. We have adopted both instrumental upgrades for Galactic Center observations since 2022 and 2023, respectively. Second, different techniques for determining astrometric separations of the stars to Sgr A* were used. We presented the single-beam method, which is used to derive the positions of stars observed simultaneously with the supermassive black hole, and the dual-beam method, which is used to determine the positions of stars further away than ≈70 milli-arcseconds from Sgr A*.

We also analyzed the orbital parameter distributions of the S-stars. From our sample of 41 stars, eight have orientations consistent with the clockwise stellar disk, while the orientation of the other stars is random. Further, we analyzed the eccentricity distribution of 22 early-type and seven late-type stars and found both to be consistent with a thermal distribution. This matches earlier findings and suggests that while the stars may have been initially placed on highly eccentric orbits by the Hills mechanism, their orbits have since evolved. This evolution can be explained by resonant relaxation, where stars change their angular momentum due to coherent torques in highly symmetric, near-Keplerian gravitational potentials.

The continued astrometric and spectroscopic monitoring of S-stars in the Galactic Center is essential for probing any extended mass distribution around Sgr A*. Current constraints place a 1σ upper limit of $\approx 1200 M_\odot$ on the mass enclosed within S2's orbit (Gravity Collaboration et al., 2024), which is already approaching theoretical predictions of $1210 M_\odot$ for a dynamically relaxed stellar cusp made of white dwarfs, brown dwarfs, stars, neutron stars, and stellar-mass black holes. As S2 moves toward its apocenter in 2026, where the

influence of any extended mass component is strongest (Heißel et al., 2022), further observations with GRAVITY and ERIS will allow us to tighten these constraints and potentially detect this extended mass component directly.

With the continued collection of high-precision data with GRAVITY+, and, especially with MICADO at the ELT (Davies et al., 2018), we will increasingly be able to detect faint, previously unknown stars near Sgr A*, as demonstrated by the recent discovery of S300 and S301. This will be a crucial step toward confirming the presence of a stellar cusp and improving our understanding of the structure and evolution of the nuclear star cluster.

Chapter 5

First light for GRAVITY Wide. Large separation fringe tracking for the Very Large Telescope Interferometer

Original Publication: GRAVITY+ Collaboration: R. Abuter, F. Allouche, A. Amorim, C. Bailet, M. Bauböck, J.-P. Berger, P. Berio, A. Bigioli, O. Boebion, M.L. Bolzer, H. Bonnet, G. Bourdarot, P. Bourget, W. Brandner, Y. Clénet, B. Courtney-Barrer, Y. Dallilar, R. Davies, D. Defrère, A. Delboulbé, F. Delplancke, R. Dembet, P.T. de Zeeuw, A. Drescher, A. Eckart, C. Édouard, F. Eisenhauer, M. Fabricius, H. Feuchtgruber, G. Finger, N.M. Förster Schreiber, E. Garcia, P. Garcia, F. Gao, E. Gendron, R. Genzel, J.P. Gil, S. Gillessen, T. Gomes, F. Gonté, C. Gouvret, P. Guajardo, S. Guieu, M. Hartl, X. Haubois, F. Haußmann, G. Heißel, Th. Henning, S. Hippler, S. Hönig, M. Horrobin, N. Hubin, E. Jacqmart, L. Jochum, L. Jocou, A. Kaufer, P. Kervella, H. Korhonen, L. Kreidberg, S. Lacour, S. Lagarde, O. Lai, V. Lapeyrère, R. Laugier, J.-B. Le Bouquin, J. Leftley, P. Léna, D. Lutz, F. Mang, A. Marcotto, D. Maurel, A. Mérand, F. Millour, N. More, H. Nowacki, M. Nowak, S. Oberti, T. Ott, L. Pallanca, L. Pasquini, T. Paumard, K. Perraut, G. Perrin, R. Petrov, O. Pfuhl, N. Pourré, S. Rabien, C. Rau, S. Robbe-Dubois, S. Rochat, M. Salman, M. Schöller, J. Schubert, N. Schuhler, J. Shangguan, T. Shimizu, S. Scheithauer, A. Sevin, F. Soulez, A. Spang, E. Stadler, J. Stadler, C. Straubmeier, E. Sturm, L.J. Tacconi, K.R.W. Tristram, F. Vincent, S. von Fellenberg, S. Uysal, F. Widmann, E. Wieprecht, E. Wiezorrek, J. Woillez, S. Yazici, A. Young, and G. Zins
CORRESPONDING AUTHORS: A. Drescher, J. Woillez
DOI: 10.1051/0004-6361/202243941

ABSTRACT: GRAVITY+ is the upgrade for GRAVITY and the Very Large Telescope Interferometer (VLTI) with wide-separation fringe tracking, new adaptive

optics, and laser guide stars on all four 8 m Unit Telescopes (UTs) to enable ever-fainter, all-sky, high-contrast, milliarcsecond interferometry. Here we present the design and first results of the first phase of GRAVITY+, known as GRAVITY Wide. GRAVITY Wide combines the dual-beam capabilities of the VLTI and the GRAVITY instrument to increase the maximum separation between the science target and the reference star from 2 arcseconds with the 8 m UTs up to several 10 arcseconds, limited only by the Earth's turbulent atmosphere. This increases the sky-coverage of GRAVITY by two orders of magnitude, opening up milliarcsecond resolution observations of faint objects and, in particular, the extragalactic sky. The first observations in 2019 – 2022 include the first infrared interferometry of two redshift $z \sim 2$ quasars, interferometric imaging of the binary system HD 105913A, and repeat observations of multiple star systems in the Orion Trapezium Cluster. We find the coherence loss between the science object and fringe-tracking reference star well described by the turbulence of the Earth's atmosphere. We confirm that the larger apertures of the UTs result in higher visibilities for a given separation due to the broader overlap of the projected pupils on the sky and provide predictions for visibility loss as a function of separation to be used for future planning.

5.1 Introduction

Shao and Colavita (1992) described, for the first time, an optical interferometer simultaneously observing two widely separated targets contained inside the atmospheric turbulence isopistonic patch. The Palomar Testbed Interferometer (PTI) (Colavita et al., 1999) represents the first implementation of this dual-field technique, where star separators are located at the focus of the telescope and deliver two independent beams, which allow for the simultaneous operation of two interferometric instuments. At the time, however, the emphasis was primarily focused on astrometry, namely, measuring the angular distance between the two targets in preparation for NASA's space astrometry missions for exoplanets. The possibility to use the technique to observe much fainter targets was tentatively explored and presented in Lane and Colavita (2003), but remained within the limiting magnitudes of the PTI around $m_K = 5$. On the VLTI (Beckers, 1990), the dual-field instrument PRIMA (Delplancke, 2008) was foreseen to deliver astrometric and phase-referencing capabilities. The emphasis remained on astrometry, rather than pushing the sensitivity of the interferometer, until the project was discontinued in face of the competition with Gaia (Perryman et al., 2001), however the dual-field capability of the infrastructure was preserved. The first dual-field phase-referenced observations to demonstrate a sensitivity improvement were carried out by the ASTRA instrument (Woillez et al., 2014) of the Keck Interferometer (Colavita et al., 2013), reaching a magnitude of $\mathrm{m}_K = 12.5$, which was about ten times fainter than contemporaneous direct observations. The scientific exploitation of this nascent capability was, however, cut short by the early demise of this facility in July 2012.

The sensitivity revolution was finally delivered by the GRAVITY instrument (GRAVITY Collaboration et al., 2017) at the VLTI. It has transformed high angular resolution astronomy with the first interferometric instrument to routinely offer milliarcsecond (mas)

resolution imaging for objects as faint as $m_K = 19-20$, a sensitivity increase by more than a factor of a thousand over previous interferometers, 30-100 microarcsecond (μas) astrometry, and microarcsecond differential spectro-astrometry. The key to success are technical breakthroughs on several fronts, including the development of quasi-noiseless infrared detectors (Finger et al., 2019), infrared single-mode waveguides and integrated optics (Perraut et al., 2018), robust fringe tracking (Lacour et al., 2019), infrared adaptive optics (Scheithauer et al., 2016), and laser metrology (Gillessen et al., 2012b), as well as performance improvements all over the VLTI observatory (Woillez et al., 2018). GRAVITY is also the first interferometer to routinely offer dual-field interferometry, for which a bright reference star is used to stabilize and phase-reference the interferogram of the science object.

In the first five years of science operation, GRAVITY brought groundbreaking results covering a broad range of astrophysical science: It has provided the strongest experimental evidence that the compact mass in the Galactic Center (Sgr A*) is a black hole, including the first detection of the gravitational redshift (GRAVITY Collaboration et al., 2018b) and the Schwarzschild precession (GRAVITY Collaboration et al., 2020c) in the orbit of the star S2 around the black hole. Further, GRAVITY has detected orbital motion of hot gas close to the innermost stable orbit of the black hole (GRAVITY Collaboration et al., 2018a), and performed the most precise measurement of the black hole's mass and distance (GRAVITY Collaboration et al., 2019a), surrounding mass distribution (GRAVITY Collaboration et al., 2022), and tests of the Einstein equivalence principle (Amorim et al., 2019). GRAVITY has provided high resolution spectra of the atmosphere of several exoplanets, including HR8799e (GRAVITY Collaboration et al., 2019b) and β Pic b (GRAVITY Collaboration et al., 2020f). On the latter, the measured C/O ratio indicates that this planet has undergone substantial core accretion and planetesimal enrichment. Additionally, GRAVITY has delivered the first direct detection of a radial velocity planet β Pic c (Nowak et al., 2020) and the measurement of the mass of an exoplanet from the astrometry of a second planet (Lacour et al., 2021). GRAVITY was also the first instrument to spatially resolve a quasar broad line region (BLR, GRAVITY Collaboration et al. (2018d)) and to image at milliarcsecond resolution the dust sublimation region around a Seyfert 2 active galactic nucleus (AGN, GRAVITY Collaboration et al. (2020b)). It has also provided a comprehensive dataset of spatially resolved disks of young stellar objects (GRAVITY Collaboration et al., 2019c; GRAVITY Collaboration et al., 2021e; GRAVITY Collaboration et al., 2021h; GRAVITY Collaboration et al., 2021d; GRAVITY Collaboration et al., 2021g; GRAVITY Collaboration et al., 2021f) and spatially resolved the magnetospheric accretion onto a T Tauri star (GRAVITY Collaboration et al., 2020a). Furthermore, GRAVITY resolved for the first time the two images produced by gravitational microlenses (Dong et al., 2019).

Until now, the number of observable targets with the dual-feed mode is limited by the requirement that the fringe-tracking (FT) source and the science target (SC) have to be within the field of view of the VLTI, which is 2 arcseconds (arcsec) in diameter for the Unit Telescopes (UTs) and 4 arcsec in diameter for the Auxiliary Telescopes (ATs). This requirement can be overcome by implementing wide-angle off-axis fringe tracking, where we enlarge the separation between FT and SC up to about 30 arcsec, limited by the atmospheric turbulence. To break the limitation in separation between the two fields of

GRAVITY, they are separated at the telescope level and finally overlapped at the entrance of GRAVITY. This implementation, which we refer to as GRAVITY Wide, is one of the primary components of the ongoing upgrades to the VLTI and GRAVITY. This improved instrument is called GRAVITY+ (Eisenhauer, 2019). Besides GRAVITY Wide, GRAVITY+ also includes the implementation of new deformable mirrors and state-of-the-art adaptive optics (AO) wavefront sensors, an improved instrument throughput and vibration control, as well as laser guide stars on all four 8 m UTs. These upgrades will enable fringe tracking on objects as faint as $m_K = 13$ and, together with GRAVITY Wide, enable all-sky interferometry with high resolution imaging at milliarcsec accuracy with a limiting magnitude of $m_K = 22$.

The increased FT–SC angular separation will make it possible to observe faint targets with fringe tracking on a nearby bright source that can be picked from a much larger area. This will open up observations and discoveries in different areas of astronomy, such as: spatially resolving young stellar objects in their embedded phase; studying the multiplicity of massive stars in the Small and Large Magellanic Cloud; constraining, for the first time, intermediate mass black holes with accurate motions of stars in globular clusters; discovering single stellar-mass black holes and free floating planets via microlensing; and probing supermassive black holes in active galactic nuclei out to beyond $z \approx 2$ (Eisenhauer, 2019) and in nearby inactive galaxies with transient tidal disruption events.

The enlargement of the FT–SC separation, however, brings along a challenge. In ground-based optical and infrared interferometry, atmospheric turbulence plays an important role (Fried, 1966). Local changes in the temperature and humidity in the atmosphere lead to changes in the refractive index of air. When an initially flat wavefront from a distant science object enters the atmosphere, it gets distorted. Adaptive optics and the fringe tracker are able to correct these distortions. However, when the separation between SC and FT increases, the correction degrades on the SC due to residual wavefront errors in the direction of the SC. This effect is called anisoplanatism (Fried, 1982) and it becomes more severe for larger off-axis separations. Thus, it is important to understand the behaviour of the atmosphere and investigate the influence of atmospheric turbulence on large-separation fringe tracking.

In this paper, we present the first wide-angle interferometric observations with four telescopes performed with GRAVITY Wide. We describe the instrumental changes of GRAVITY to GRAVITY Wide in Sect. 5.2. In Sect. 5.3, we present the GRAVITY Wide data, and demonstrate first GRAVITY Wide science. From observations of multiple star systems in the Orion Trapezium Cluster, we derive a new orbit for θ^1 Ori B, and refine the orbits of θ^1 Ori C and θ^1 Ori D. We present the separation and flux ratio of the binary HD 105913A, and the successful detection of fringes across the Hα line for two $z > 2$ quasars, SDSS J161513.84+084914.4 ($z = 2.33$, hereafter SDSS1615) and LAMOST J092034.16+065717.9 ($z = 2.46$, hereafter, LAMOST09). In Sect. 5.4, we discuss the influence of atmospheric turbulence on the new large separation fringe tracking mode with 17 observed FT–SC pairs with separations up to 32 arcsec. Finally, we give a summary and an outlook for future GRAVITY+ science in Sect. 5.5.

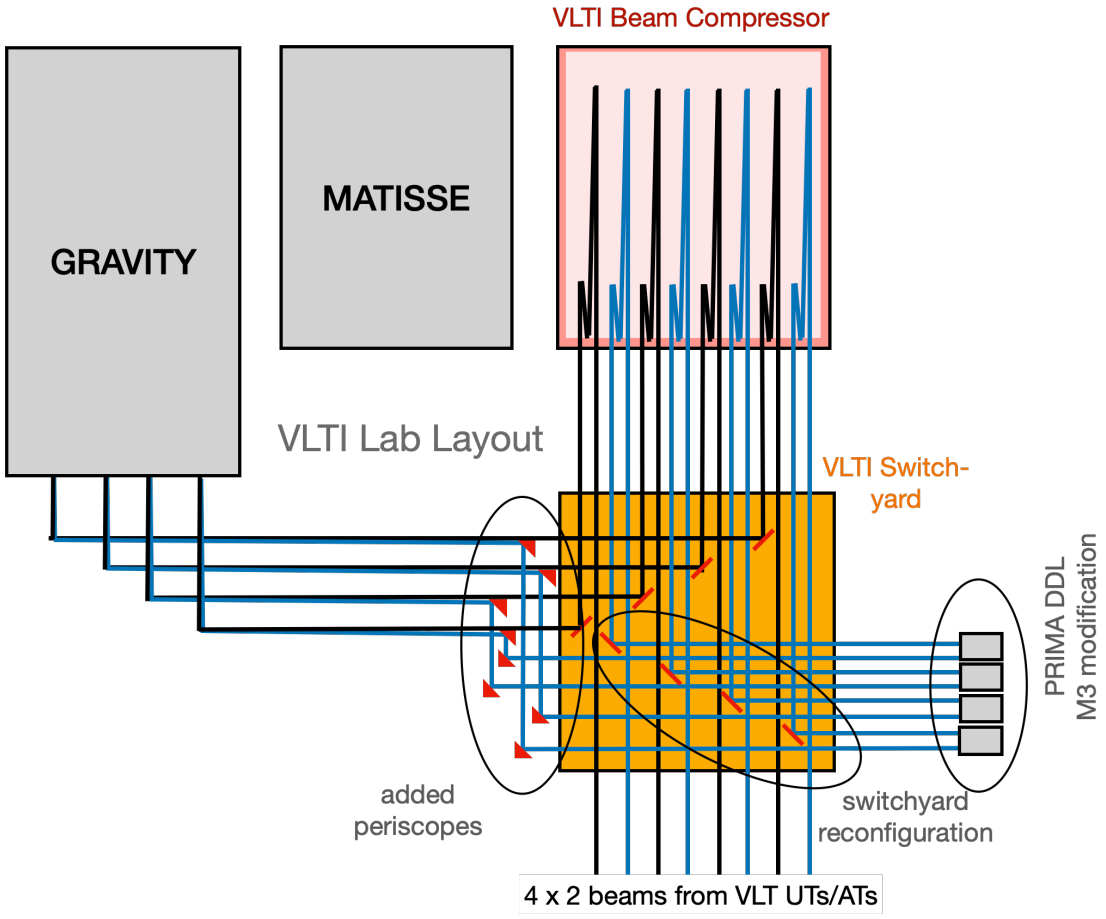

Figure 5.1: Modifications made to the VLTI switchyard in December 2021 to implement the first phase of GRAVITY Wide. Located in the VLTI laboratory underneath the VLTI platform, the switchyard receives the light from the main VLTI delay lines and directs the light to the various downstream instruments such as GRAVITY, MATISSE, and PIONIER. Typically, the light first enters the beam compressors to convert the beam diameters from 80 mm down to 18 mm. To allow for simultaneous observations of FT targets separated by more than 2 arcsec from the SC we enabled the use of the B beams from the VLTI. We added a four-fold periscope consisting of eight flat fold mirrors to merge the A (black) and B (blue) beams with a 2 arcsec separation. For this it was also necessary to rearrange four of the eight main switchyard mirrors, and reactivated the original PRIMA differential delay lines.

5.2 GRAVITY Wide upgrade

5.2.1 Instrumental changes

The original design of the VLTI incorporates dual-field interferometric capability. Two subsections of the telescopes' fields of view, each about 2 arcsec wide (4 arcsec for the ATs) and separated by up to 60 arcsec are picked up by the star separators (STS) located at the coudé focus of each telescope and propagated through the VLTI delay lines into the VLTI laboratory. The two beams are generally referred to as the A and B beams, where commonly only the A beams are used in non-dual-field applications.

To enable wide-mode observations we introduced new optics that merge the A and B beams on the VLTI switch yard before feeding them to GRAVITY. This is achieved through four periscopes that pick up the B beams and translate them laterally to bring them into overlap with the A beams (see Fig. 5.1). These periscopes are implemented through flat mirrors hanging upside down from two bridges, which are motorized and integrated into VLTI's ARAL (Morel et al., 2004) system for automated removal if not in use. The mirrors all ensure a peak-to-valley wavefront error of better than $\lambda/20$ ($\lambda = 632.8\,\mathrm{nm}$) within the footprint of the beam and were coated simultaneously to minimize differential polarization between the beams.

The main optical delay lines do not compensate for the differential optical path length (OPD) changes that result from the up to several 10 arcsec wide on-sky separation of the A and B beams. To correct for this, PRIMA (Delplancke, 2008) originally introduced the differential delay lines (DDLs, Launhardt et al., 2005). After the discontinuation of the PRIMA project the DDLs were turned off. We reactivated the DDLs for the use in GRAVITY Wide. This however required a modification to relay the pupil at the correct distance for the pickup by GRAVITY. The DDLs (see Fig. 5.2) consist of a three-mirror cat's eye system with five optical reflections (it's primary and secondary mirrors are passed twice). The tertiary mirror is located in the focus of the system and its radius of curvature directly controls the distance of the output pupil plane. We replaced the M3s with new mirrors with appropriately modified radii of curvature. The differential delay between the SC and FT is stabilized on the internal laser metrology of the PRIMA DDLs. The current GRAVITY Wide implementation does not propagate the GRAVITY laser metrology up to the telescope and, therefore, it does not yet provide the absolute phase and astrometry between the SC and FT. The upgrade with a full optical path length coverage by the GRAVITY metrology is foreseen for the next project phase.

With two beams entering GRAVITY, two sets of pupil beacons would appear in the acquisition camera pupil tracking images. Hence, in April 2022, we installed a narrow-band filter blocking the pupil beacon light from the A beam, such that only one set of pupil beacons appears in the acquisition camera from which to measure the lateral and longitudinal offsets. These offsets can then be used to adjust the pupil for both beams A and B. Finally, the VLTI switchyard itself required a reconfiguration to allow for this new beam routing. For this four of eight motorized flat mirrors were re-positioned.

All these modifications were carried out in December 2021 and concluded the hardware

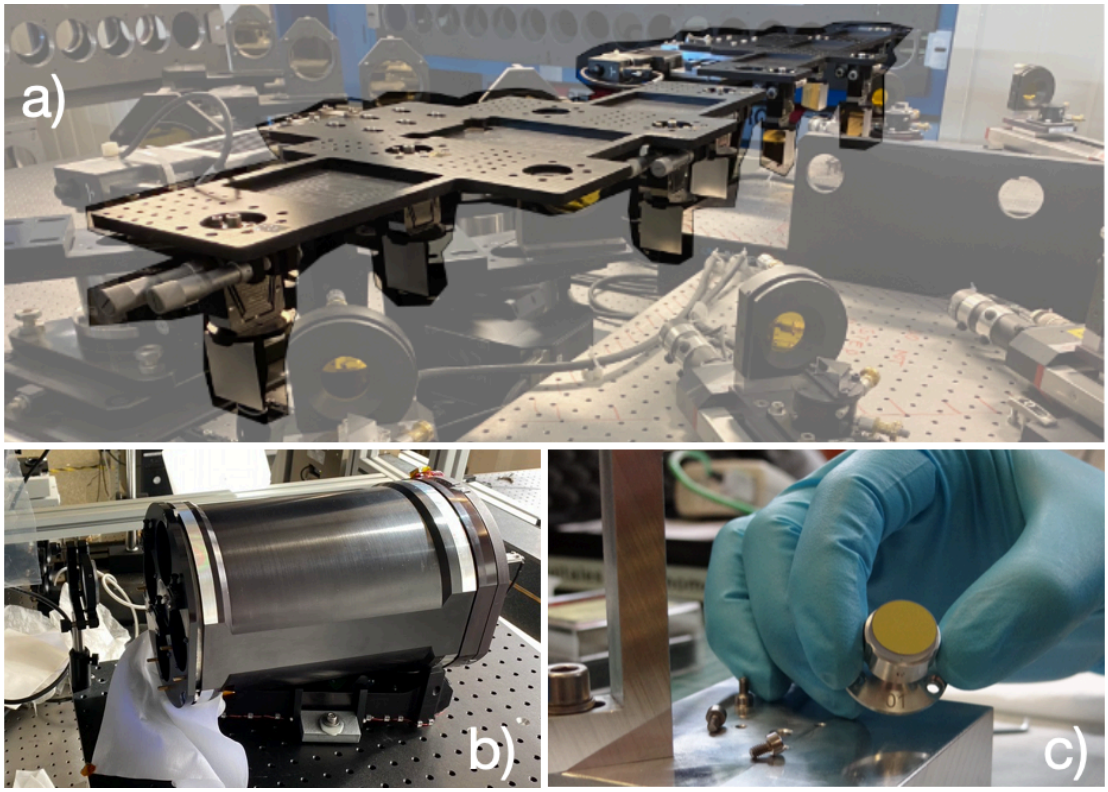

Figure 5.2: Photographs of the added or modified hardware for the implementation of GRAVITY Wide. *Panel a:* newly added periscopes merge the A and B beams of the respective four UT or ATs. Due to space constraints they were mounted hanging down from two motorized bridge structures. *Panel b:* to compensate for the differential optical path length between the A and B-beams, we now use the differential delay lines formerly belonging to PRIMA. *Panel c:* these DDLs, however, needed to be modified to relay the pupil to the appropriate location for GRAVITY. The PRIMA DDLs consist of a three mirror cat's eye with five optical reflections. We replaced the tertiary mirrors to adjust the pupil relay. Our beam path design allowed us to choose identical radii of curvature for all tertiary mirrors.

part of the first phase of the GRAVITY Wide implementation. We have begun to work on the second phase as part of the GRAVITY+ project which will remove the PRIMA DDLs entirely and save five optical reflections for the B beams. For this, in the second phase we will motorize the beam compressors of the VLTI (see again Fig. 5.1) to take over the differential optical path length compensation. The updated mechanics will ensure that the original optical specifications of the DDL system are met.

5.2.2 Software changes

Along with the instrumental changes, a number of software changes had to be made to bring GRAVITY Wide into operation. One general modification is to use the VLTI field selector mirrors (FSMs) and variable curvature mirrors (VCMs) as the actuators in all control loops instead of GRAVITY's internal mirrors. In particular, the field tracking and fringe tracker beam optimization loops are now controlled through FSM A and lateral pupil tracking is controlled through VCMs A and B. Furthermore, during the acquisition of the FT and SC targets, only FSMs A and B are moved in order to properly align them with the fibres.

We additionally developed and implemented a new "SC Tracking" control loop which is similar to the current field tracking loop. Here, we measure the SC target position through Gaussian fitting directly from the acquisition camera field images. The separation between the target position and SC fibre position is calculated and translated into the necessary FSM B offsets to bring the SC target back to the fibre. To help facilitate this for faint SC targets ($m_H < 17$), we added the option for a longer detector integration time (DIT) (2.8s) on the acquisition camera such that the SC target would be reliably detected on the field images.

5.2.3 Metrology OFF mode

When using GRAVITY Wide to observe extremely faint targets, it is important to reduce existing noise sources as much as possible. The dominant instrumental noise source in GRAVITY is the scattering of the metrology laser in the instrument. While the metrology laser wavelength lies outside the science wavelength, Raman scattering and backscattering from rare-earth elements in the optical fibers create a broad noise peak in the blue part of the K-band, as well as a constant background flux over the full detector (Lippa et al., 2018). The detector noise of GRAVITY is shown in Fig. 5.3. The direct back scattering is the dominant noise source from 2.0 µm to 2.1 µm and a diffuse background from the laser contributes to the noise above 2.1 µm.

The metrology system is only necessary for astrometric observations in the GRAVITY dual-beam mode. For observations where the science target is within a single beam, such as observations in GRAVITY on-axis or GRAVITY Wide, the metrology system is not needed. To avoid unnecessary noise in those observations, we developed a new instrument mode: the *Metrology OFF* mode. In this mode the laser amplifier of the metrology laser is turned off during the observation. This removes the back scattering of the laser on the

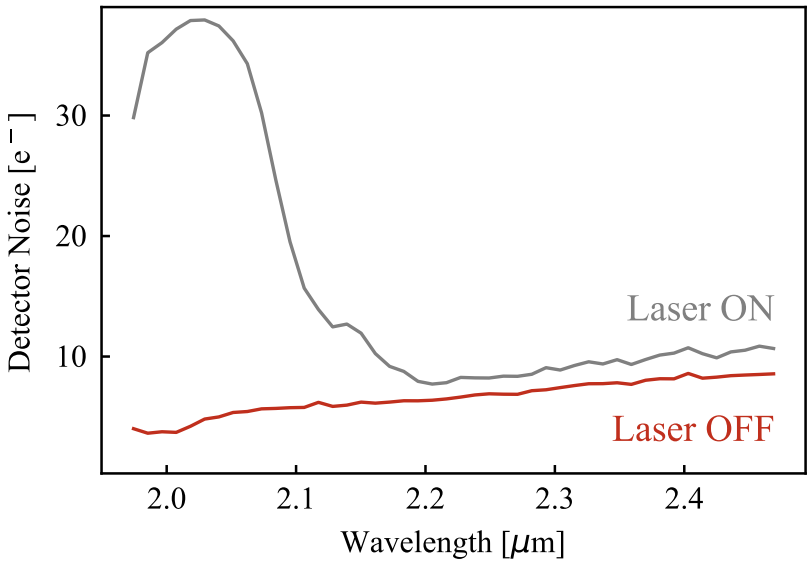

Figure 5.3: Detector noise of GRAVITY for a sky frame with an integration time of 30 s. The noise is shown with the metrology laser on (in grey) and the laser turned off (in red).

detector. The resulting noise for a 30 s sky frame is shown in Fig. 5.3. The noise decreases by a factor of eight in the blue part of the spectrum (from 2.0 µm to 2.1 µm) and on average by a factor of 2.5. The remaining dominant noise sources are the read-out noise from the detector as well as the thermal background from the telescopes, beam relay and sky.

5.3 First GRAVITY Wide observations

5.3.1 Data

The first wide-angle interferometric observations were performed in five runs. The first two runs were executed between November 2019 and March 2020 with a prototype implementation of GRAVITY Wide (no proper pupil relay to GRAVITY). Third and fourth runs were performed in December 2021 and January 2022, followed by a fifth run in April 2022. We used both the UTs and ATs. The ATs were mounted in the configuration A0-G1-J2-K0 in November 2019 and December 2021, and on the stations A0-G1-J2-J3 in March 2020. In November 2019 we carried out observations with the ATs on the Orion Trapezium Cluster. With the UTs, we performed GRAVITY Wide observations with the prototype implementation on the binary star HD 105913A in March 2020, and with the proper implementation of GRAVITY Wide on the quasars LAMOST09 in December 2021 and January 2022, and SDSS1615 in April 2022. We provide a detailed list of the observations and their parameters in Appendix A3.1 for the prototype implementation of GRAVITY Wide. In Appendix A3.1 we present the data for the later runs.

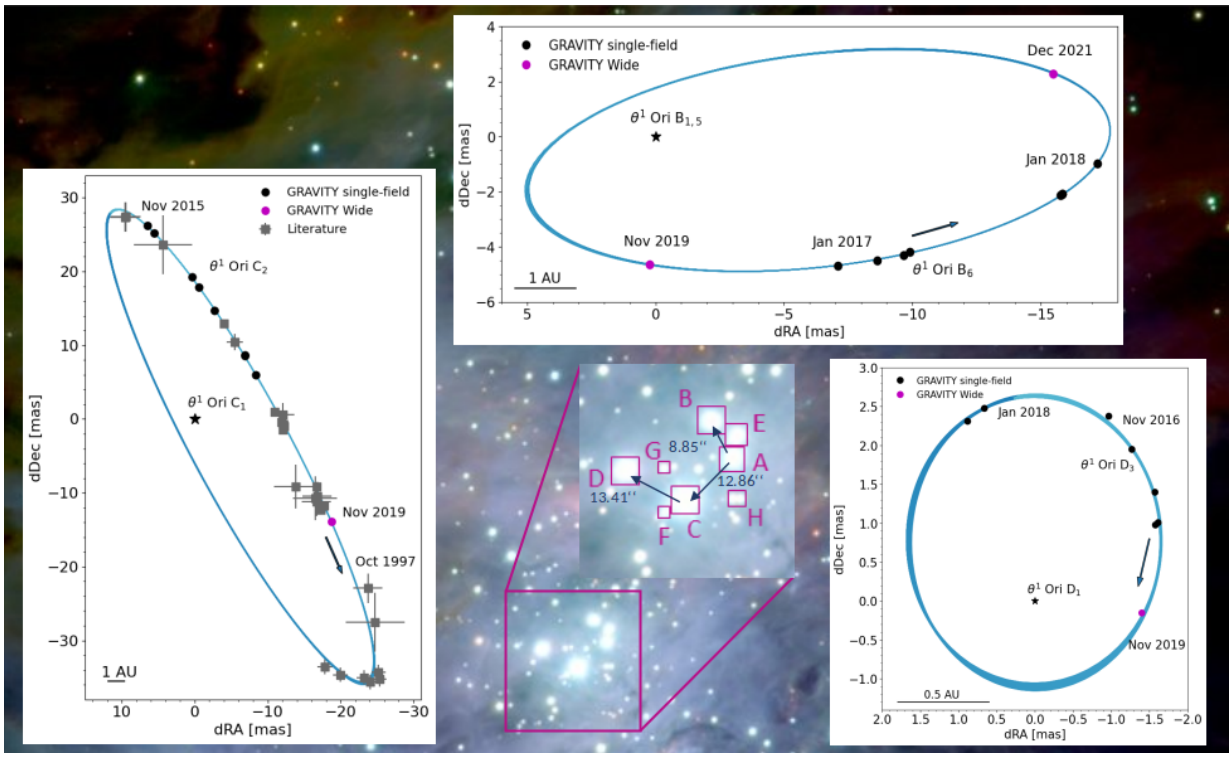

Figure 5.4: Summary of three observed multiple systems in the Orion Trapezium Cluster. *Middle:* Orion nebula in the background and zoom on the Orion Trapezium Cluster (θ^1) stars in the inset. Blue arrows mark the separation between FT and SC. *Upper:* Orbit of θ^1 Ori B_6 around the eclipsing binary θ^1 Ori $B_{1,5}$ at the center. We use θ^1 Ori A at a separation of 8.85 arcsec as the FT. Note that θ^1 Ori B_6 has completed more than one orbital revolution between 2017 and 2021. *Left:* orbit of θ^1 Ori C_2 around the primary star θ^1 Ori C_1 at the center. θ^1 Ori C_2 has completed more than two orbital revolutions. Literature data points are measurements taken from Weigelt et al. (1999), Schertl et al. (2003), Kraus et al. (2007), Patience et al. (2008), Kraus et al. (2009), and Grellmann et al. (2013). The observation was performed with θ^1 Ori A at a separation of 12.86 arcsec as the FT. *Right:* orbit of θ^1 Ori D_3 around the primary star θ^1 Ori D_1 at the center. We use θ^1 Ori C at a separation of 13.41 arcsec as the FT. θ^1 Ori D_3 has revolved 20 times between the first and last data point. Background image and zoom from ESO/M. McCaughrean et al. (AIP) 2001.

In total, we observed 36 FT–SC pairs with angular separations between 2 arcsec and 32 arcsec. The observations were performed in one of the three spectral resolutions offered: low with $R = \lambda/\Delta\lambda \approx 20$, medium with R $\approx$ 500, and high with R $\approx$ 4500. Furthermore, the light of the FT and SC was measured in either combined or split linear polarization. The integration time on the science spectrometer was between seconds and minutes, depending on the magnitude of the science target. The data allow us to demonstrate the performance of GRAVITY Wide on the one side, and evaluate the coherence loss for increasing off-axis separations due to atmosphere anisoplanatism on the other side. Further, the FT–SC pairs include faint objects that were observed to explore the current limit of the new observing mode. We used the GRAVITY pipeline (Lapeyrere et al., 2014; GRAVITY Collaboration et al., 2017) to reduce the data.

5.3.2 Binaries in the Orion Nebula

One of the main targets for science demonstration of GRAVITY Wide with the ATs is the Orion Trapezium Cluster. The cluster is located in the heart of the Orion Nebula at a distance of 414 $\pm$ 7 pc (Menten et al., 2007) from Earth. It is one of the closest regions of massive star formation (Genzel and Stutzki, 1989; Hillenbrand, 1997; Menten et al., 2007; Muench et al., 2008) and the best-studied cluster of massive stars. An interferometric study of the cluster stars was carried out with GRAVITY in single-field mode between November 2016 and January 2018 and it revealed that most of the massive stars are not single stars, but multiple star systems (GRAVITY Collaboration et al., 2018c). This finding is expected for massive O-type stars, as they are found more often in multiple systems than low mass stars (Sana et al., 2014).

These systems are good targets for GRAVITY Wide for several reasons. First, the binaries are located within the field of view of GRAVITY. Additionally, many of the main components of the cluster can be used as FT targets, since they all are separated by < 20 arcsec from each other. And lastly, the former GRAVITY observations provide orbits for some of the stars. This provides the unique opportunity to test and verify GRAVITY's new wide-field mode. We observed three principal components of the cluster, θ^1 Ori B, θ^1 Ori C, and θ^1 Ori D. Compared to GRAVITY single-field mode, where one multiple system serves as both FT and SC, in GRAVITY Wide, we use one multiple system as the FT and another multiple system as the SC. This is shown in the lower middle panel in Fig. 5.4. For the observation of θ^1 Ori B and θ^1 Ori C, we used θ^1 Ori A at a separation of 8.85 arcsec and 12.86 arcsec, respectively, as the FT. For the observation of θ^1 Ori D, the FT was θ^1 Ori C at a separation of 13.41 arcsec. For details about each multiple system we refer to GRAVITY Collaboration et al. (2018c). Here, we present the results from the observations with GRAVITY Wide, namely, the measured separation and flux ratio of the binary components, as well as orbital parameters for each of the systems, which were derived as described in Appendix A3.2.

We observed the multiple system θ^1 Ori B on the nights of November 1, 2019 and December 15, 2021 with GRAVITY Wide. The measured separation and flux ratio between θ^1 Ori B_6 and θ^1 Ori $B_{1,5}$ is given in Table 5.1. We use the measurements from GRAVITY

Table 5.1: Binary separation and flux ratio for θ^1 Ori B, θ^1 Ori C and θ^1 Ori D.

Object	Date	Sep. [mas]	f
θ^1 Ori B	Nov 1, 2019	4.65 ± 0.07	0.3224 ± 0.0006
	Dec 15, 2021	15.66 ± 0.01	0.3504 ± 0.0022
θ^1 Ori C	Nov 1, 2019	23.39 ± 0.14	0.3099 ± 0.0021
θ^1 Ori D	Nov 2, 2019	1.41 ± 0.02	0.3419 ± 0.0064

Notes. Here, we give the binary separation (sep.) and flux ratio (f) for the multiple star systems observed with GRAVITY Wide in November 2019 and December 2021.

single-field mode in 2017/18 (GRAVITY Collaboration et al., 2018c) and the new measurements from GRAVITY Wide to determine orbital parameters. Figure 5.4 presents the new orbit. The corresponding orbital parameters are shown in Table 5.2. We found a total system mass of $M_{B_{1,5}B_6} = 14.93 \pm 0.06$ $M_\odot$. This result is consistent with the sum of the masses of $M_{B_1} = 7$ $M_\odot$ (Weigelt et al., 1999), $M_{B_5} \sim 2$ $M_\odot$ (GRAVITY Collaboration et al., 2018c) and the upper limit of GRAVITY Collaboration et al. (2018c), which is $M_{B_6} \sim 6$ $M_\odot$.

In a second observation with GRAVITY Wide, we observed θ^1 Ori C in the night of November 1, 2019. Table 5.1 provides the measured separation and flux ratio of the binary components θ^1 Ori C_1 and θ^1 Ori C_2. We fit the orbit of θ^1 Ori C with the new GRAVITY Wide measurement and with measurements from GRAVITY single-field and the literature. The orbit is presented in Fig. 5.4. In Table 5.2, we compare our results with the results from GRAVITY Collaboration et al. (2018c). We found that they agree with each other and that our fit result supports the large mass of the binary θ^1 Ori C. Further, we obtain more constrained values for the orbital parameters, and a slightly larger total system mass, which is, nonetheless, within the uncertainties from GRAVITY Collaboration et al. (2018c).

Finally, we observed θ^1 Ori D in the night of November 2, 2019 with GRAVITY Wide. We give the measured separation and flux ratio between θ^1 Ori D_1 and θ^1 Ori D_3 in Table 5.1. We used the measurements from GRAVITY single-field observations (GRAVITY Collaboration et al., 2018c) and the new measurement with GRAVITY Wide and fit the orbit of θ^1 Ori D_3 around the primary θ^1 Ori D_1. We present the orbit in Fig. 5.4. We compare the fit results with the results from GRAVITY Collaboration et al. (2018c) in Table 5.2. We note that the uncertainties are smaller for a, e, i, ω, and Ω. Additionally, we found a larger total system mass.

The results presented above improve the results of previous observations of multiple star systems in the Trapezium. This verifies the functionality of GRAVITY Wide with the ATs and demonstrates that the new data points are of equal quality than the GRAVITY single-field points.

Table 5.2: Orbital parameters for θ^1 Ori B, θ^1 Ori C and θ^1 Ori D.

	This work	(1)
	θ^1 Ori B	
a [mas]	12.982 ± 0.018	–
e	0.67326 ± 0.00037	–
i [°]	69.233 ± 0.063	–
ω [°]	133.48 ± 0.13	–
Ω [°]	282.860 ± 0.028	–
P [yr]	3.22571 ± 0.00056	–
$t_{\rm P}$ [yr]	2019.3935 ± 0.0019	–
$M_{\rm tot}$ [$M_\odot$]	14.928 ± 0.057	–
	θ^1 Ori C	
a [mas]	44.47 ± 0.19	45 ± 2
e	0.5908 ± 0.0034	0.59 ± 0.04
i [°]	98.702 ± 0.050	98.6 ± 0.6
ω [°]	283.70 ± 0.14	283 ± 2
Ω [°]	27.516 ± 0.055	27.9 ± 0.7
P [yr]	11.4426 ± 0.0097	11.4 ± 0.2
$t_{\rm P}$ [yr]	2002.304 ± 0.019	2002.2 ± 0.2
$M_{\rm tot}$ [$M_\odot$]	47.70 ± 0.61	46.4 ± 5.9
	θ^1 Ori D	
a [mas]	1.94 ± 0.014	1.86 ± 0.06
e	0.391 ± 0.011	0.43 ± 0.03
i [°]	155.19 ± 0.70	160 ± 12
ω [°]	156.40 ± 12.03	166 ± 27
Ω [°]	339.56 ± 9.52	346 ± 24
P [yr]	0.1449059 ± 0.0000086	0.1452 ± 0.0002
$t_{\rm P}$ [yr]	2017.1004 ± 0.0015	2017.101 ± 0.001
$M_{\rm tot}$ [$M_\odot$]	24.91 ± 0.54	21.68 ± 0.05

Notes. a is the semi-major axis, e the eccentricity, i the inclination, ω the argument of periastron of the secondary's orbit, Ω the longitude of ascending node, P the period, $t_{\rm P}$ the time of periastron passage, and $M_{\rm tot}$ the total system mass assuming a parallax of 2.415 ± 0.040 mas (Menten et al., 2007).
References. (1) GRAVITY Collaboration et al. (2018c).

5.3.3 HD 105913A

We highlight the first GRAVITY Wide observation with the 8 m UTs. The binary HD 105913A was observed with GRAVITY Wide in the night of March 9th, 2020. A third companion star, HD 105913B, is located at a separation of 5.11 arcsec from HD 105913A

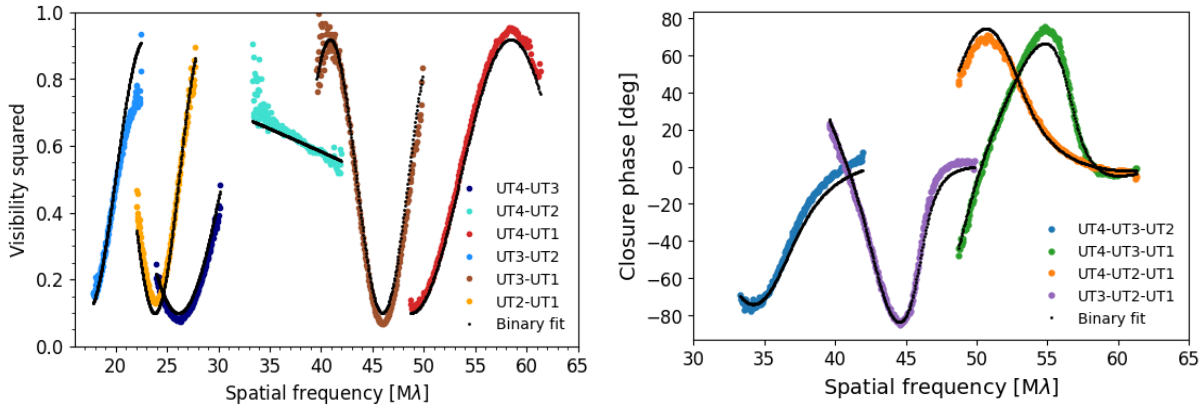

Figure 5.5: Observation of the binary HD 105913 A on March 9th, 2020. *Upper:* observed (color) and fitted (black) visibility squared, and *lower:* observed (color) and fitted (black) closure phases. The binary system Aa,Ab was observed with the UTs. The separation to the fringe tracker, HD 105913B, is 5.11 arcsec.

(Gaia Collaboration et al., 2018) and was used as the FT. The binary components in HD 105913A, Aa and Ab, have a period of 211.59 days and a mass ratio of $q = 0.874$. The triple system HD 105913 Aa,Ab,B is of spectral type K1 and located at 34 pc from the Sun (Tokovinin, 2019).

In Fig. 5.5, we show the observed and fitted visibility squared and closure phases, respectively. We find the position of the secondary star at (dRA, dDec) = (-5.83 ± 0.002, 24.11 ± 0.002) mas, with respect to the primary star fixed at the center; therefore, the measured binary separation is 24.8 ± 0.002 mas. The error on the position, thus separation, is statistical and does not include systematics. We observe a flux ratio $f = 0.64 \pm 0.039$, thus Aa at the center is the brighter star. We show an image of the binary reconstructed with the imaging code G^R (GRAVITY Collaboration et al., 2022) in Fig. 5.6, which is obtained from imaging with closure phases and visibility amplitudes.

5.3.4 Broad line region of redshift two quasars

GRAVITY has spatially resolved the broad-line region of low-redshift AGNs (GRAVITY Collaboration et al., 2018d; GRAVITY Collaboration et al., 2020i; GRAVITY Collaboration et al., 2021i). This is achieved by measuring the differential phase of the BLR referenced to the continuum emission from the hot dust closely surrounding the BLR. Before GRAVITY Wide, however, only the brightest and therefore nearby AGN could be observed with GRAVITY because it is nearly impossible to find a bright FT star within 2 arcsec of extragalactic objects. Therefore, only on-axis GRAVITY observations were possible, which imposed a $m_K < 10.5$ limit to enable fringe tracking on the AGN.

With GRAVITY Wide, we are able to observe fainter quasars at higher redshift given the increased sky coverage and ability to find off-axis FT stars. In particular, quasars at $z \approx 2 - 3$ are ideal targets, as the bright Hα line is redshifted into the K band. This

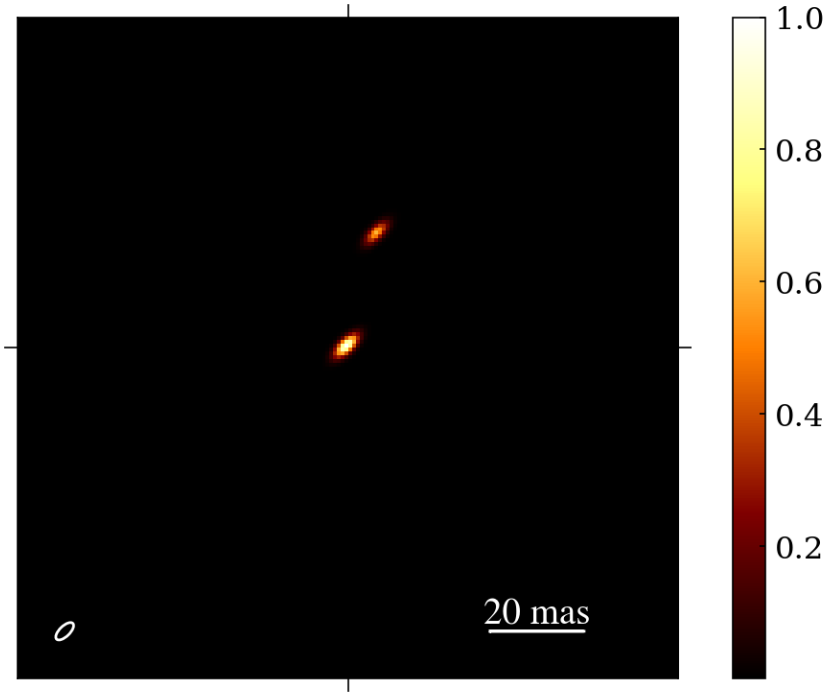

Figure 5.6: Image of the binary HD 105913A, reconstructed with the imaging code G^R (GRAVITY Collaboration et al., 2022). We indicate the FWHM of the corresponding dirty beam in the bottom left corner. The flux is normalized to the star Aa at the center.

line is very strong compared to the continuum which boosts the observed differential phase by a factor of $\gtrsim 10$ compared to the $z \lesssim 0.1$ AGN. $z \approx 2$ is often called "cosmic noon," namely, the epoch in galaxy evolution when both star formation and SMBH accretion peaked (Madau and Dickinson, 2014). Since SMBHs and their host galaxies are thought to co-evolve together (e.g., Heckman and Best, 2014), measuring SMBH masses throughout the history of the Universe and especially at cosmic noon is critical for understanding galaxy evolution.

We selected two quasars, LAMOST09 ($z = 2.33$, $m_K = 15.1$) and SDSS1615 ($z = 2.46$, $m_K = 15.6$), and observed them with the UT array and GRAVITY Wide. LAMOST09 has a FT star at a separation of 12.8 arcsec with $m_K = 10.4$ while SDSS1615's FT star is 7.5 arcsec away with $m_K = 10.45$. Observations took place on 18 December 2021, 19 January 2022, and 25 January 2022 for LAMOST09 and 17 April 2022 for SDSS1615 in MEDIUM spectral resolution. Atmospheric conditions ranged from poor to moderate over the three nights for LAMOST09, resulting in difficulties maintaining fringe tracking (especially on 18 December). Nonetheless, each night we were able to acquire, fringe-track, and detect fringes with the QSO-star pair resulting in 96 min of useable data. For SDSS1615, we had very good weather conditions for the single night of observing and were able to consistently fringe-track and integrate on the QSO over 1 hour. The left panel of Fig. 5.7 shows an example acquisition camera field image containing both the FT star and

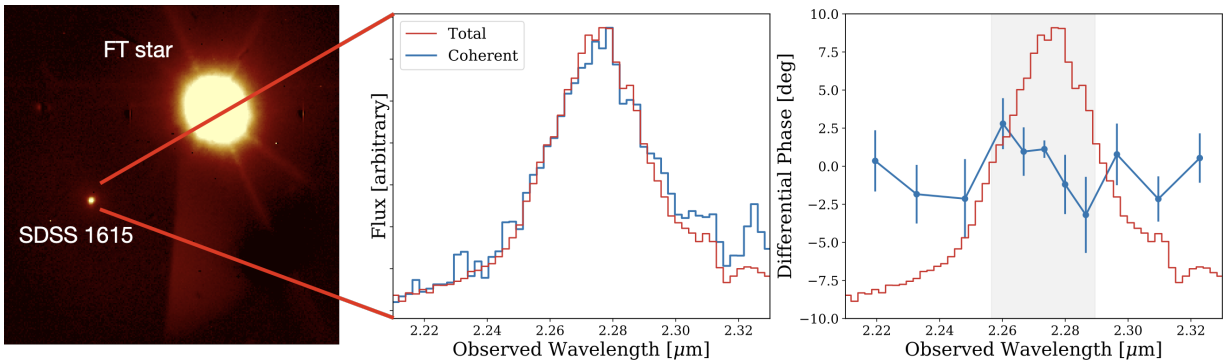

Figure 5.7: Observation of the $z = 2.46$ quasar SDSS1615. *Left:* acquisition camera field image during observations of SDSS1615, showing successful acquisition and detection of the quasar. *Middle:* average total flux spectrum (red) over all four telescopes showing the detection of the broad Hα line at 2.28 μm consistent with a redshift of $z = 2.46$. In blue is the average coherent flux spectrum using the UT4-UT1 and UT3-UT1 baseline and the post-processing explained in the text. Coherent flux is significantly detected across the entire spectrum. *Right:* average differential phase spectrum using the UT4-UT1 and UT3-UT1 baselines overlaid on the normalized total flux spectrum. With an RMS of $\approx 1 - 2°$within the FWHM of the line (gray shaded region), we tentatively detect the rotating disk signal of the BLR.

SDSS1615 demonstrating successful acquisition.

The raw data were reduced through the GRAVITY pipeline to produce complex visibilities for every DIT (60s for LAMOST09 and 100s for SDSS1615). Due to the low flux level, significant fringe jumps, and a slow drift in the OPD, we chose not to use the standard coherent integration within the pipeline and instead manually ran our own post-processing. This involved first running a 2D Discrete Fourier Transform on each individual night's dataset to determine an overall group delay accounting for the OPD drifts for each baseline. The drifts were removed for each DIT individually with the self-reference method from Tatulli et al., 2007; Millour et al., 2008, whereby the phase reference for each spectral channel is constructed from all other spectral channels. This post-processing significantly increased the coherent flux for each baseline. We note that once the cause of the drift can be identified and potentially fixed, even longer DITs will be possible to further increase the sensitivity of QSO observations.

In the middle panel of Fig. 5.7, we plot the average coherent flux overlaid on the total flux in the wavelength range of the expected Hα line for SDSS1615. The detected Hα line averaged over all four telescopes peaks around 2.28 µm and has a FWHM of 4300 km s^{-1}. The coherent flux is averaged over two of the longest baselines, UT4-UT1 and UT3-UT1 where we expect the strongest differential phase signal. We clearly detect coherent flux across the entire spectrum, which represents the first near-infrared interferometric fringes of a high redshift object. The right panel shows the average differential phase for the same two baselines. Within the FWHM of the Hα line (gray shaded region), we measure an

RMS noise of approximately 1–2°and observe a tentative "S-shaped" signal indicative of a rotating BLR. SDSS1615 is a high luminosity quasar with an estimated BLR size of ~ 1.1 pc and SMBH mass of $10^{9.9}$ $M_\odot$ based on the [CIV] line profile (Rakshit et al., 2020). Using these values, the differential phase peak should be between 3–6°, depending on the inclination and position angle on-sky of the BLR which matches well the emerging signal in Fig. 5.7.

5.4 Role of atmospheric seeing for wide-angle fringe tracking

5.4.1 Atmospheric coherence loss

Similarly to classical ground-based observations in the optical and near-infrared, atmospheric turbulence also plays an important role in near-infrared interferometry. Turbulence in the atmosphere of Earth leads to a blurred image of an astronomical object with a typical diameter of around 1 arcsec. The full width at half maximum (FWHM) of the blurred image is the so-called *seeing*, ϵ. It depends on the individual conditions at the observational site, and is given by (Kornilov et al., 2007)

$$\epsilon = 0.98\frac{\lambda}{\mathrm{r}_0} \ , \tag{5.1}$$

where r_0 is the Fried parameter, and λ the observed wavelength.

For interferometry, especially with off-axis fringe tracking as it is done in GRAVITY Wide, atmospheric effects are crucial. In this context, the isoplanatic angle becomes an important parameter, which defines how far from the SC the FT can be without losing coherence on the SC. Angular anisoplanatism occurs when the light from two targets separated by an angle θ experiences different phase variations as it travels through different parts of the atmosphere (Quirrenbach, 2000). The disturbed wavefront of the on-axis star can be corrected by AO, whereas the off-axis star has residual wavefront errors. Thus, the wavefront correction degrades if the science target is further away from the fringe tracking star, which leads to a loss in coherence, thus a loss in the signal-to-noise ratio (S/N). We therefore try to understand the effects of the isoplanatic angle on the observations to estimate which atmospheric conditions are best suited for observations with GRAVITY Wide.

The isoplanatic angle is given by (Quirrenbach, 2000):

$$\theta_0 = 0.314(\cos\ z)\frac{r_0}{H} \ , \tag{5.2}$$

where z is the zenith angle, and H the mean effective turbulence height which can be expressed as

$$H \equiv \left(\frac{\int dh\ C_N^2(h)h^{5/3}}{\int dh C_N^2(h)}\right)^{3/5} \ , \tag{5.3}$$

where C_N^2 is the strength of refractive index fluctuations, and h the height in the atmosphere.

Elhalkouj et al. (2008) and Esposito et al. (2000) developed a model that describes visibility reduction for off-axis fringe tracking as expected from atmosphere anisoplanatism.

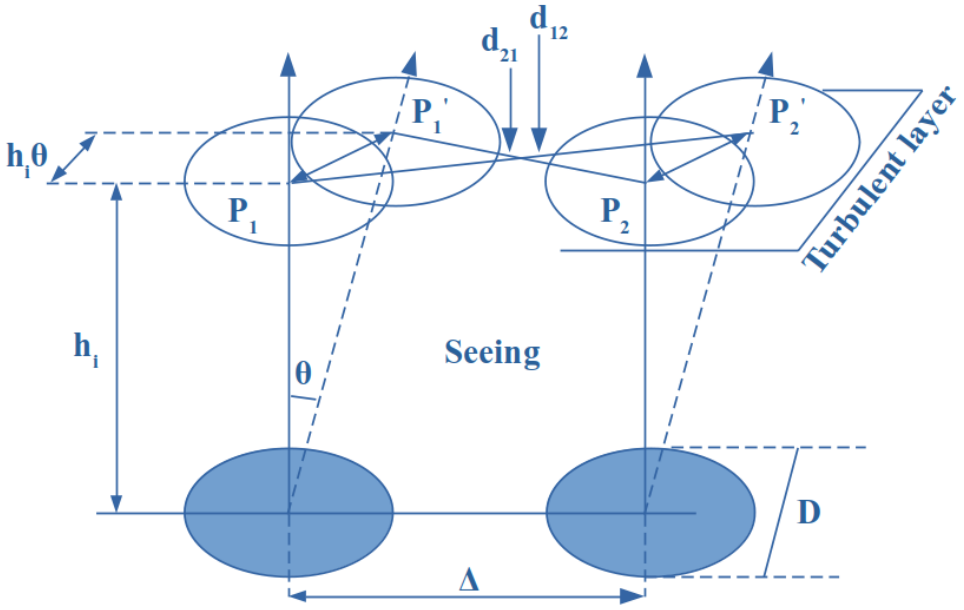

Figure 5.8: Two-aperture interferometer with baseline length Δ, and projected pupils onto a single turbulent layer at altitude h. The aperture diameter is D and science object and phase-reference star form an angle θ. Image adapted from Esposito et al. (2000).

Figure 5.8 illustrates the geometrical elements considered for the calculation. Here, we consider a two-aperture interferometer, each with an aperture diameter D, with a baseline length Δ. The science object and the phase-reference star are separated by θ, and P_1, P_2 and $P_1^{'}$, $P_2^{'}$ are the pupils projected onto a single turbulent layer at height h. Further, d_{12} and d_{21} are the distances between the pupils P_1 and $P_2^{'}$ as well as P_2 and $P_1^{'}$, respectively.

Assuming that angular anisoplanatism is the only effect that reduces the visibility, the loss of visibility as a function of FT–SC separation can be approximated (following Maréchal) as:

$$V_{\text{average}}(\theta) = V \, \exp\Big[- \frac{2\pi^2}{\lambda^2} \sigma_p^2(\theta) \Big] \, , \tag{5.4}$$

where V is the instant visibility for a delay time τ between the two optical paths, and $\sigma_p^2(\theta)$ is the anisopistonic error variance, which is the variance of the differential piston error. The expression for $\sigma_p^2(\theta)$ is derived in Elhalkouj et al. (2008) under the following assumptions: In long-baseline interferometry, the product $h\theta$ is in general much smaller than the baseline length Δ: for $h \simeq 10$ km, $\theta \simeq 15$ arcsec, the product results in $h\theta \simeq 0.75$ m, which is small compared to $\Delta_{UT1-UT4} = 130$ m. Thus, the distances d_{12} and d_{21} can be approximated by $\Delta \simeq d_{12} \simeq d_{21}$. Furthermore, the outer scale of turbulence L_0 is assumed to be infinity

(Buscher and Longair, 2015), following the Kolmogorov model. A full treatment taking into account the effect and statistics of the outer scale of turbulence can be found in Boskri et al., 2021. Elhalkouj et al. (2008) considered two different scenarios for deriving the isopistonic angle error. The decisive parameter for this is the fraction $\pi D/L_0$, which in our case is much smaller than one. Thus, we follow the "small-aperture case," which assumes that the apertures are small compared to the outer scale of turbulence L_0. Finally, the product $(h\theta)_{max}$ is equivalent to $h_{max}\theta_0$.

The expression for the isopistonic angle error in Eq. (5.4) is given by:

$$\sigma_p(\theta) \sim 0.12\pi^{1/3}\lambda \left(\frac{D}{r_0}\right)^{-1/6} \frac{\theta}{\theta_0} \qquad \text{for } L_0 \to \infty \ . \tag{5.5}$$

Under the assumptions described above, the anisopistonic error variance $\sigma_p(\theta)$ in Eq. (5.5) only depends on two geometrical elements, aperture diameter D and FT–SC separation θ, on two atmospheric parameters, the height of the turbulent layer H and the seeing ϵ, as well as on the wavelength λ when r_0 and θ_0 are replaced by Eq. (5.1) and Eq. (5.2). For observations with the VLTI the atmosphere profiler MASS-DIMM (Haguenauer et al., 2020) at the Paranal observatory measures θ_0 and ϵ, while D, θ, and λ are given by the telescopes, the FT–SC pair used, as well as the K-band wavelength observed with GRAVITY. We can therefore calculate the expected visibility of the SC for a given observation with GRAVITY Wide with Eq. (5.5).

5.4.2 Visibility as a function of FT–SC separation

To show how well the model for the visibilities matches the observed data, we provide an example in Fig. 5.9 for the science target HD 48543B observed with the ATs. We compare the measurement to the modeled visibilities from Eq. (5.4) and Eq. (5.5). At the time of observation, the seeing is 0.41 arcsec (at 500 nm), and the isoplanatic angle is 1.7 arcsec (at 500 nm), which corresponds to 10.0 arcsec in K-band. We use HD 48543A at a separation of 7.90 arcsec as the FT.

Figure 5.9 shows that the modeled visibility from atmosphere anisoplanatism matches the observed visibility very well. The visibility loss ranges from approximately 0.2–0.4, depending on the wavelength, in accordance with what is predicted by the model. The data presented in Fig. 5.9 are calibrated for instrumental effects inside GRAVITY, but not for atmospheric coherence loss in the main delay lines and coherence loss of optics in the beam train from the telescopes to the VLTI lab. Therefore, we can say that the visibility loss observed in this exposure comes mostly from atmosphere anisoplanatism. Just as in Fig. 5.9, we compute the atmospheric visibility loss at a wavelength of 2.2 μm of 60 GRAVITY Wide AT observations. In Fig. 5.10, we display each observation by either a cross (for observations from 2019) or a filled circle (for observations from 2021). Further, we sort the data in three groups based on their isoplanatic angle measured. The first group contains the highest values of θ_0 with 3.12 arcsec $< \theta_0 <$ 3.3 arcsec. The second group spans 2.02 arcsec $< \theta_0 <$ 2.7 arcsec, and the third group 1.23 arcsec $< \theta_0 <$ 1.93 arcsec.

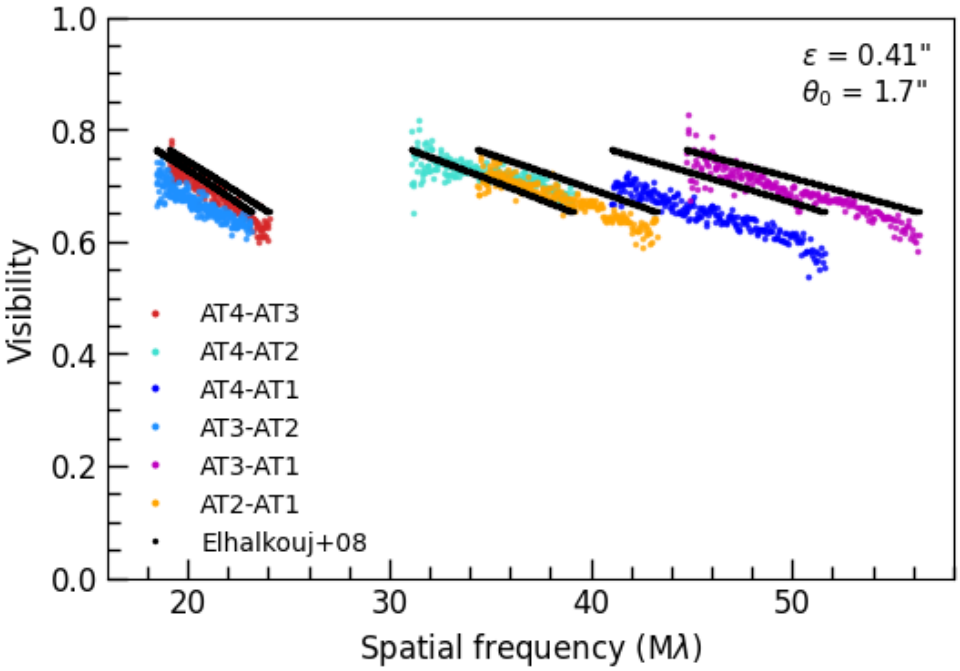

Figure 5.9: Observed (color) and modeled (black) visibility for the star HD 48543B. The FT, HD 48543A, is located at 7.90 arcsec from the SC. During the observation, the MASS-DIMM measured a seeing ϵ of 0.41 arcsec and an isoplanatic angle θ_0 of 1.7 arcsec (at 500 nm), which is 10.0 arcsec in K-band. AT1-AT2-AT3-AT4 correspond to the stations A0-G1-J2-K0. The model by Elhalkouj et al. (2008) is able to explain the visibility loss from atmosphere anisoplanatism.

Per group, we determine the mean value for both isoplanatic angle and seeing from the exposures and calculate the visibility loss with Eq. (5.4) for off-axis separations up to 30 arcsec, represented by the solid orange, blue and green curve, respectively. Additionally, we color the area of the minimum and maximum visibility reduction, given by the minimum and maximum seeing and isoplanatic angle per group, respectively.

We find that the coherence loss with increased FT–SC separation is well described by atmosphere anisoplanatism for a large outer scale of turbulence following Elhalkouj et al. (2008). We note two important aspects. Firstly, we find that the visibility is higher for larger isoplanatic angles. The reason for this is that a larger isoplanatic angle means a lower turbulent layer, and therefore a larger overlap of the projected pupils from the SC and FT target. This results in a better correction for wavefront aberrations by AO, as well as correction for the fringe motion of the SC. Secondly, we find that the model is more sensitive to the isoplanatic angle than to the seeing. A large isoplanatic angle is crucial for being able to observe at large off-axis separations. Until now, seeing and coherence time are taken into account for scheduling service mode observations. Based on our findings, we point out that the isoplanatic angle should be taken into account as well when executing

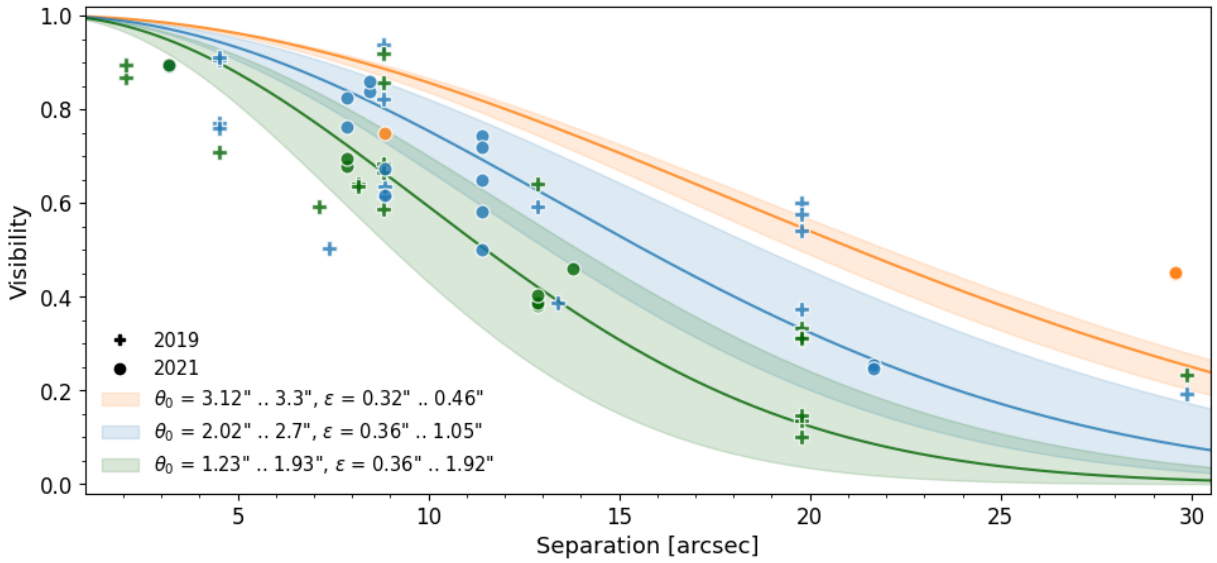

Figure 5.10: Observed contrast loss at 2.2 μm versus off-axis separation for the ATs. The three curves indicate the typical contrast loss for different seeing and isoplanatic angle values as expected from atmospheric turbulence following Elhalkouj et al. (2008). Crosses represent data from GRAVITY Wide observations with the prototype implementation in November 2019, while circles represent data from GRAVITY Wide commissioning in December 2021. Seeing and isoplanatic angle values are measured by the MASS-DIMM at the Paranal observatory, and are defined at 500 nm.

GRAVITY Wide observations.

5.4.3 Atmospheric conditions on Paranal

In Fig. 5.10, we see that while the overall trend is well matched by the model by Elhalkouj et al. (2008), only a few observations match the expected visibility exactly. We discuss possible reasons in the following.

First, the model assumes the outer scale of turbulence to be infinity, following the Kolmogorov model. However, this scale ranges from 12 to 50 m at all major astronomical sites (Ziad, 2016), and is about 22 m (Martinez et al., 2010) in the atmosphere model of Paranal. This leads to an underestimation of the maximum visibility in our calculations for large telescopes (Elhalkouj et al., 2008; Boskri et al., 2021), but does not affect much the visibility estimates for the comparably small ATs (Fig. 5.10). Another point is that the model might be too simple to describe the full effects. For example, it does not take parameters such as DIT, total exposure time, coherence time, airmass, or magnitude of the SC and FT into account. The target HD 10257 at 19.77 arcsec separation in Fig. 5.10 was observed with a sequence of DITs between 0.13 s and 10 s to investigate the influence of the DIT on the visibility. In the analysis, we omitted the shortest DITs of 0.13 s and 0.3 s, because they might be short enough to "freeze" the turbulence and thus artificially increase

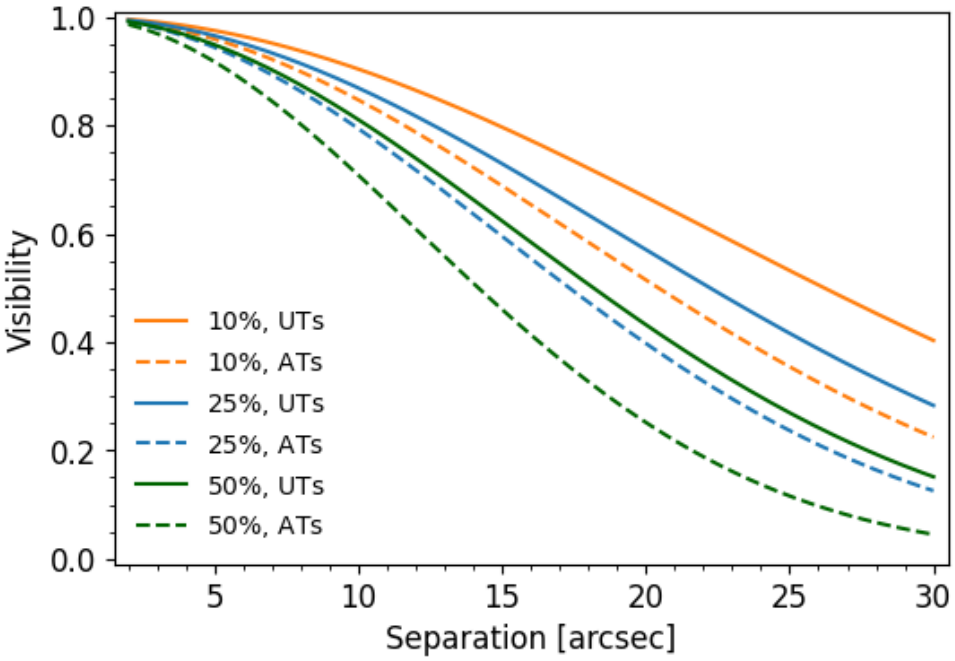

Figure 5.11: Visibility at a wavelength of 2.2 μm versus off-axis separation for different seeing and isoplanatic angle values given in Table 5.3. Solid lines represent the visibility loss for the UTs, and dashed lines for the ATs, respectively.

the measured visibilities. The 60 GRAVITY Wide observations (presented in Fig. 5.10) were performed with the ATs. For observations with the UTs we expect a higher visibility due to a larger overlap of the projected pupils on sky for given FT–SC separation. Table 5.3 presents the seeing categories for the median seeing and isoplanatic angle, respectively, for the percentiles of 10%, 25%, and 50% measured by the MASS-DIMM at the Paranal platform. Based on these values, we computed the visibility reduction for both UTs and ATs for separations up to 30 arcsec; we present the result in Fig. 5.11. We can see that for the same values of seeing and θ_0, the UTs provide a higher visibility.

Table 5.3: Statistics of seeing and isoplanatic angle θ_0 at Paranal.

Percentile	10%	25%	50%
Seeing [arcsec] at 500 nm	0.52	0.62	0.76
θ_0 [arcsec] at 500 nm	3.01	2.48	1.96
θ_0 [arcsec] at 2.2 μm	17.81	14.68	11.60

Notes. The seeing is given at 500 nm and the isoplanatic angle θ_0 at 500 nm and at 2.2 μm. Both parameters are measured by the MASS-DIMM at the Paranal observatory.

We conclude that the predictions from the model of Elhalkouj et al. (2008) are in good

agreement overall with the coherence loss we observe with GRAVITY Wide. This gives a good starting point to plan and execute observations. It also shows that it is not enough to check the seeing conditions and coherence time, but that we also need to take the isoplanatic angle into account. Considering the performance as theoretically predicted and observationally confirmed (see Fig. 5.9 and Fig. 5.10), for GRAVITY Wide operations we suggest a maximum separation of 30 arcsec, as for larger distances, the coherence loss is considered too large. Figure 5.10 also demonstrates that especially observations at the largest separations should be done at atmospheric conditions with a large isoplanatic angle and with a small zenith angle.

5.5 Summary and outlook

GRAVITY Wide has provided another breakthrough in near-infrared interferometry with the first observations using wide-angle separation fringe tracking up to about 30 arcsec across four telescopes. GRAVITY Wide significantly expands the sky coverage of GRAVITY and opens up near-infrared interferometry to new fields. In particular we demonstrate first near-infrared fringes of a $z = 2.46$ quasar. At $m_K = 15.6$, this is now the faintest extragalactic object observed by a factor of a hundred along with the highest redshift. In addition, we demonstrated interferometric imaging with this new observing mode on the binary system HD 105913A, and derived new and updated orbits for several binary stars in the Orion Trapezium Cluster.

We investigate here the influence of atmospheric turbulence on the new wide-angle fringe tracking mode and find that atmosphere anisoplanatism well describes the contrast loss in the GRAVITY Wide observations following Elhalkouj et al. (2008). In particular, we note higher visibilities for observations with the 8 m UTs compared to the 1.8 m ATs due to a larger overlap of the projected pupils on sky. Because wide-angle separation observations are more sensitive to the isoplanatic angle than to the seeing, we propose including the isoplanatic angle in future planning for GRAVITY Wide observations.

GRAVITY Wide is just the beginning of the full GRAVITY+ upgrade (Eisenhauer, 2019). The main limitation now is the performance of the adaptive optics which has a two-fold effect in both reducing the SC target light and preventing fringe tracking on fainter stars. The next phases of GRAVITY+ therefore will install a new state-of-the-art adaptive optics system in 2024 and laser guide stars on all four UTs in 2025. The combination will allow us to push to even fainter targets across the whole sky (Fig. 5.12). Together with enhanced vibration control for the telescopes and performance improvements of the GRAVITY instrument itself, we then expect fringe tracking on stars as faint as $m_K = 13$ both on-axis and off-axis, and observations of objects with a magnitude up to $m_K \approx 22$. The performance improvements from GRAVITY+ will open up key advances in many fields of astrophysics: for instance, the possibility to measure the spin of the Galactic Center black hole, to study SMBH growth and coevolution with galaxies over cosmic time, to directly detect exoplanets that are out of reach for traditional coronographs, to measure their atmospheric composition and orbital architecture to unprecedented precision, and to

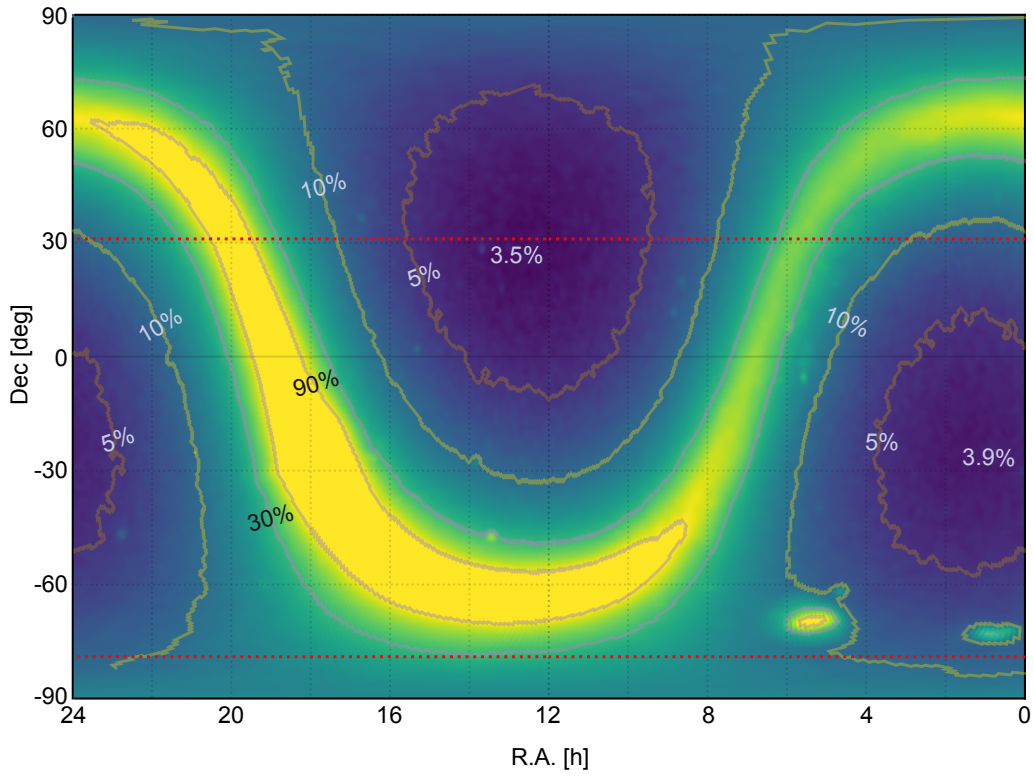

Figure 5.12: Sky coverage for laser guide star adaptive optics supported off-axis fringe tracking with a fringe tracking star as faint as $m_K = 13$, and a maximum allowed separation of 30 arcsec.

spatially resolve stars and planetary systems in formation. The leaps and bounds with regard to near-infrared interferometric AGN science can be best seen in the numbers of AGN that GRAVITY can observe at each step. GRAVITY with its original performance could observe ≈ 10 AGN at $z \sim 0$ (GRAVITY Collaboration et al., 2020h). GRAVITY Wide provides the same $10 - 20$ but now at $z = 2$. GRAVITY+, with its full expanded capabilities, will make the jump to over 1000 AGN across cosmic time.

The first GRAVITY Wide results presented in this paper prove the functionality of the new large-separation fringe-tracking mode, which will be offered to the community through ESO from October 2022 onwards [1]. These results provide a glimpse into the exciting future of near-infrared interferometry with GRAVITY+.

Acknowledgements. We are very grateful to our funding agencies (MPG, DFG, BMBF, ERC, CNRS (CSAA, ASHRA), Ile-de-France region (DIM ACAV+), Paris Observatory-PSL, Observatoire des Sciences de l'Univers de Grenoble, Université Grenoble Alpes, Ob-

[1]The JMMC tech group has developed a tool for finding FT targets in order to assist in GRAVITY Wide proposal preparations. Available at `https://searchftt.jmmc.fr/`

servatoire de la Côte d'Azur, Université Côte d'Azur, and the Fundação para a Ciência e Tecnologia) and the generous support from the Max Planck Foundation - an independent, non-profit organization of private supporters of top research in the Max Planck Society. A.A. and P.G. acknowledge support from grants UIDB/00099/2020 and PTDC/FIS-AST/7002/2020. We also thank ESO and the ESO/Paranal staff, and the many scientific and technical staff members in our institutions, who helped to make GRAVITY Wide a reality. This work was supported by the European Union through ERC grant Nos. 866070 (AB, DD, RL, and MS), and has made use of the Jean-Marie Mariotti Center `Aspro` and `LITpro` services (`http://www.jmmc.fr/`) and of the CDS astronomical Data Centers SIMBAD and VIZIER.

Chapter 6

Conclusions and Outlook

This thesis aims to investigate the motions of stars and flares around the supermassive black hole, Sgr A*, using data from the near-infrared beam combiner GRAVITY at the Very Large Telescope Interferometer (VLTI). By analyzing these motions, we investigate the properties of the gravitational potential around Sgr A* and test General Relativity (GR) in the strong gravitational regime. GRAVITY offers the unique opportunity to study the Galactic Center, with its unmatched resolution of ~ 3 milli-arcseconds, precision down to ~ 30 micro-arcseconds, and sensitivity to detect stars as faint as $m_K \sim 20$. Building on the success of detecting two GR effects using GRAVITY, the gravitational redshift and Schwarzschild precession in the S2 orbit, and of gas motions around Sgr A*'s event horizon, the work presented in this thesis aims to enhance our understanding of the central parts of our Galaxy through a larger sample of stellar motions and flares, improvements in the GRAVITY instrument, and advancements in data analysis techniques. These efforts have led to the detection of the faintest star in the Galactic Center, precise measurements of the mass enclosed within the flare radius, improved constraints on the accretion flow geometry, and the most precise determinations of S-star orbits.

Probing the gravitational potential of Sgr A* with stars.
In Chapter 2, we showed that pushing the boundaries of data analysis techniques, particularly imaging, brings us closer to the next primary goal of Galactic Center science, which is the detection of the spin of Sgr A*. This measurement requires a star on a highly eccentric, short-period orbit. However, none of the stars known from adaptive optics data, which detect stars as faint as $m_K \sim 18$, is on a suitable orbit. Therefore, it is necessary to find stars with magnitudes of $m_K = 19$ or fainter in the vicinity of Sgr A* through imaging. To address this challenge, we developed a new imaging tool called G^R, which is specifically designed for Galactic Center observations with GRAVITY. G^R takes into account instrumental effects that impact GRAVITY data and the variability of Sgr A*. We applied G^R to 2021 data, obtaining the deepest images until then of the inner 100 milli-arcseconds of the Galactic Center. In addition to the known stars S29, S38, S42, S55, S60, S62, and S63, we detected a new, faint star with a magnitude of $m_K \simeq 19.0$–19.3, which we refer to as S300. This detection demonstrates the capabilities of the new imaging tool. Furthermore, images

reconstructed with the CLEAN algorithm confirm the detection. Finding the star through other independent methods is crucial to validate the detection and judge the performance of the new imaging tool. We assessed the sensitivity of G^R through injection tests and found that sources as faint as $m_K = 20$ can be recovered under good conditions.

We have since then extended the observed field around Sgr A* to image the inner 400 milli-arcseconds of the Galactic Center. This significantly broadens the accessible search area for faint stars. We detected several previously unknown sources in the most recent GRAVITY data from 2023 and 2024. One is S301, with a magnitude of $m_K = 19.0$–19.5, which is even fainter than S300. The astrometric analysis of S301 is currently ongoing to derive its precise orbit. The discovery of new stars with G^R demonstrates the power of advanced imaging techniques in the Galactic Center. It opens the door to detecting additional stars on short-period, highly eccentric orbits, which are needed for measuring higher-order effects predicted by General Relativity, such as the spin of the black hole. This goal can be achieved by combining high-precision astrometry from GRAVITY+ with spectroscopic measurements from MICADO at the ELT (Davies et al., 2018).

While measuring higher-order relativistic effects requires finding stars on very close orbits around Sgr A*, the currently known S-stars can still constrain the gravitational potential at larger distances from the black hole. Precise orbital determinations of these stars allow us to constrain the extended mass distribution around Sgr A*, which is believed to consist of a stellar cusp of old stars, stellar remnants, and potentially a dark matter spike. So far, only an upper limit on this extended mass component around Sgr A* has been obtained. Continued monitoring of the S-stars is therefore essential to improve the precision of their orbital parameters and ultimately to measure the extended mass distribution around Sgr A*.

In Chapter 4, we presented the analysis of stellar motions of 15 S-stars within 400 milli-arcseconds of Sgr A*, observed with GRAVITY between 2017 and 2025. We described strategies and techniques for Galactic Center observations, highlighting key instrumental upgrades introduced under the GRAVITY+ project to maintain astrometric precision and improve GRAVITY's sensitivity. Complementing the GRAVITY data with data from SINFONI, ERIS, and NACO, we derived and refined orbital solutions for 11 S-stars and presented updated stellar motions for the remaining four. Thanks to the GRAVITY data, we achieved significant improvements by up to three orders of magnitude in the precision of orbital parameter determination compared to earlier studies with single 8 m-class telescopes. Beyond precise orbit determination, our work contributes to understanding the dynamical structure and origin of the S-star cluster. This can be achieved by investigating the distribution of the orbital parameters of the observed S-stars, as they are a valuable probe to discriminate between different formation scenarios. In our study, we include S-stars from Gillessen et al., 2017 that were not observed with GRAVITY, but have determined orbits. This gives us a sample of 41 stars, where eight are members of the clockwise stellar disk. The other stars are randomly oriented, which is consistent with earlier findings. In particular, the observed eccentricity distribution of 22 early-type and seven late-type stars is consistent with a thermal distribution. This points toward dynamical processes as the dominant S-stars formation mechanism. A combination of binary

disruption near Sgr A* through the Hills mechanism and an additional orbital relaxation process can largely explain the observed S-star orbital distribution. Our growing sample of precisely monitored orbits opens new possibilities for testing these theories, especially as additional faint stars are discovered and traced with high precision. Continued orbital monitoring in the coming years will further clarify the dynamical structure and history of the S-star cluster.

Probing the gravitational potential of Sgr A* with flares.
Sgr A* is known to exhibit flares, the sudden increase in its near-infrared emission, roughly once or twice per day. These flares are believed to originate from processes in the innermost region of the accretion flow, close to the event horizon. Understanding these flares' origin and physical nature has become a key objective in black hole accretion physics. Thanks to its microarcsecond-level astrometric precision and polarimetric capabilities, GRAVITY provides a unique window into this regime, enabling us to trace the dynamics of the flaring region in time. GRAVITY Collaboration et al., 2018a reported on the astrometric detection of orbital motions during flares and found a clockwise motion consistent with a compact emission region orbiting Sgr A*. In Chapter 3, we built on this result by presenting an expanded sample comprising four astrometric and six polarimetric flares observed between 2019 and 2022. Our analysis confirms the findings from 2018 and significantly strengthens the hot spot model, particularly through the additional polarimetric measurements, which provide independent constraints on the inclination and magnetic field structure of the accretion flow. We enhance our fit of the orbiting hot spot by incorporating prior information from the flare light curves, the Sgr A* image from the Event Horizon Telescope (Event Horizon Telescope Collaboration et al., 2022), and our polarimetric data. Most importantly, we find that the mass of Sgr A* of $4.3 \pm 0.012 \times 10^6 M_\odot$ is enclosed within less than 9 gravitational radii (R_g), which is consistent with the mass measured from stellar orbits at several thousand R_g. This measurement, together with the image of the EHT Collaboration supports a single black hole model. Further, we find an inclination close to face on and a predominantly vertical magnetic field configuration, therefore supporting the magnetically arrested disk scenario. In addition, we find a position angle that is close to the orientation of the clockwise stellar disk of predominantly O-type and Wolf-Rayet-type stars, and we suggest that the strong winds of these stars fuel the accretion flow.

Our high-precision astrometric and polarimetric measurements with GRAVITY provide key observational constraints for theoretical models of Sgr A* flares. Recent studies increasingly employ scenarios based on magnetic reconnection and/or magnetized turbulence in strongly magnetized accretion flows to explain the observed behavior (von Fellenberg et al., 2025). These models are now directly fitted to our measurements (Yfantis et al., 2024) or have been adopted as prior knowledge in several modeling efforts (Levis et al., 2024). Further, our polarimetric observations can be used to investigate the impact of special relativity on the observed polarization loops and probe spacetime curvature around Sgr A* (Vincent et al., 2024). Thus, our measurements help to constrain the accretion flow geometry, magnetic field configuration, and emission region structure, making GRAVITY data a cornerstone for developing and testing physically motivated flare models of Sgr A*.

All-sky, ever-fainter, milli-arcsecond interferometry with GRAVITY+.
I dedicated Chapter 5 to the development and first results of GRAVITY Wide, a new observing mode developed within the GRAVITY+ project. GRAVITY Wide extends the angular separation between the science target and the fringe tracking star from 2 arcseconds up to 30 arcseconds, increasing GRAVITY's sky coverage by two orders of magnitude. This opens the door for milli-arcsecond resolution studies of faint objects, in particular, the extragalactic sky.

In 2019 and 2021, we observed 36 FT–SC pairs with separations ranging from 2 arcseconds to 32 arcseconds. We used the data to validate the functionality of GRAVITY Wide on the one side and investigate the coherence loss for increasing separations on the other side. We showed that the coherence loss is well described by atmospheric turbulence and anisoplanatism. Further, a larger isoplanatic angle leads to a better wavefront correction by the adaptive optics, which is crucial for observations at large off-axis separations. These findings have successfully been included in the observation planning since GRAVITY Wide's commissioning in 2022.

One of the main targets observed for GRAVITY Wide science demonstration were multiple-star systems in the Orion Trapezium Cluster. This cluster is one of the closest regions of massive star formation and lies in the heart of the Orion Nebula. We fitted positions of stars in the cluster and derived orbits for three systems, θ^1 Ori B, θ^1 Ori C, and θ^1 Ori D, obtaining the first orbital solution for one of them, θ^1 Ori B. Our results are consistent and improve the results of previous observations, thereby verifying the functionality of the new observing mode and demonstrating that the data points are equally good as GRAVITY observations in the single-field observing mode.

The implementation of GRAVITY Wide has far-reaching implications for studying active galactic nuclei (AGN) and the relationship between the growth of supermassive black holes (SMBHs) and their host galaxies with time. With GRAVITY Wide, it is now possible to spatially resolve the broad-line region of redshift $\sim$ 2–3 quasars, thus measuring the mass of the central black hole at a time in galaxy evolution when star formation and black hole accretion peaked. The number of observable AGN has increased significantly with GRAVITY Wide, from only $\sim$ 10 AGN at redshift $z \sim 0$ with the original implementation to 10–20 AGN at $z \sim$ 2–3 with the new implementation of wide-field off-axis fringe tracking. As the GRAVITY+ upgrade continues to evolve, with the implementation of state-of-the-art adaptive optics and laser guide stars on all four UTs, it is expected to enable the observation of over 1000 AGN across cosmic time, revolutionizing our understanding of the co-evolution of galaxies and black holes. In fact, recent studies have already demonstrated the power of GRAVITY Wide. Abuter et al., 2024 report on the dynamical measurement of the black hole mass in a quasar at $z \sim 2$, a look back in time of 11 billion years. They find a mass of 3.2×10^8 solar masses and an undermassive black hole accreting at a super-Eddington rate. This finding suggests that the host galaxy grew faster than the SMBH, indicating different timelines for forming galaxies and black holes. More SMBH mass measurements are needed to reveal whether this is true for all or only some systems.

Appendix

A1 Appendix: Deep images of the Galactic center with GRAVITY

A1.1 Efficient response implementation

In the presence of static instrumental optical aberrations (GRAVITY Collaboration et al., 2021c) and bandwidth smearing, the simplified response function in Eq. (2.3) is generalized to:

$$v_{ij}\left(\boldsymbol{u}\right) = \frac{\int \mathrm{d}\lambda\, P_{\lambda_0}\left(\lambda\right) \int \mathrm{d}\boldsymbol{s}\, \Pi_i\left(\boldsymbol{s}\right) \Pi_j^*\left(\boldsymbol{s}\right)\, I\left(\boldsymbol{s},\lambda\right) \mathrm{e}^{-2\pi i \boldsymbol{b}\cdot\boldsymbol{s}/\lambda}}{\prod_{x=i,j} \sqrt{\int \mathrm{d}\lambda\; P_{\lambda_0}\left(\lambda\right) \int \mathrm{d}\boldsymbol{s}\;\left|\Pi_x\left(\boldsymbol{s}\right)\right|^2 I\left(\boldsymbol{s},\lambda\right)}}\,, \tag{1}$$

where i and j label the two telescopes forming the baseline, $\boldsymbol{b}$, and the Fourier coordinate is evaluated at the central wavelength λ_0, that is, $\boldsymbol{u} = \boldsymbol{b}/\lambda_0$. The spectral bandpass is normalized such that $\int \mathrm{d}\lambda\; P_{\lambda_0}\left(\lambda\right) = 1$. Finally, $\Pi_{i/j}$ summarizes the phase maps, $\phi_{i/j}$, and amplitude maps, $A_{i/j}$, of each telescope and is given by

$$\Pi_i\left(\boldsymbol{s}\right) = A_i\left(\boldsymbol{s}+\delta_i\right)\, \mathrm{e}^{i\phi_i(\boldsymbol{s}+\delta_i)}\,. \tag{2}$$

Since the fiber center is not necessarily aligned perfectly with the image center, a small offset δ_i can arise between the zero-coordinate of the phase and amplitude maps and the sky intensity distribution.

The position integral in the numerator of Eq. (1) can be computed very efficiently with the fast fourier transform (FFT) algorithm. However, the grid of rectangular frequencies does not necessarily align with the (u, v)-coordinates of the measurements. A common technique in radio and optical interferometry, known as gridding, is to interpolate the complex visibilities between the regular grid points of the FFT (Dutt and Rokhlin, 1993; Briggs et al., 1999).

To implement the phase and amplitude maps numerically, we produced a complex screen for each telescope, following the procedure in GRAVITY Collaboration et al., 2021c. The maps already account for the instrument's aperture and are smoothed with a 10 mas Gaussian kernel that models residual tip-tilt jitter from the AO system (Perrin and Woillez, 2019). The resulting complex screen has the same dimensions as the actual image, and both are multiplied pixel-wise before FFT and gridding are performed[1]. Because the aberrations differ between telescopes, we need to perform the computation separately on each baseline.

Taking into account the temporal and spectral variability naively would lead to a slightly different image for each exposure and each spectral channel and further curtail any computational gain achievable by gridding. To avoid this, we write the overall sky brightness distribution as

$$I\left(\boldsymbol{s},\lambda,t,p\right) = f_{\nu_1}\left(\lambda\right) I_{\mathrm{SgrA}}\left(t,p\right) \delta\left(\boldsymbol{s}-\boldsymbol{s}_{\mathrm{SgrA}}\right) + f_{\nu_2}\left(\lambda\right)\left[I_{\mathrm{Img}}\left(\boldsymbol{s}\right) + \sum_{j=1}^{N_{\mathrm{PS}}} I_j\, \delta\left(\boldsymbol{s}-\boldsymbol{s}_j\right)\right],$$

[1] We use the ducc0 library for FFT and gridding (Arras et al., 2021a) which provides C++17 code with a comprehensive Python interface, cf. `https://gitlab.mpcdf.mpg.de/mtr/ducc`.

where the first line corresponds to Sgr A*, a variable point source with spectral index ν_1 and the second line represents the image of faint sources plus N_{PS} additional point sources whose spectral index is ν_2. The spectral distributions are given by

$$f_\nu(\lambda) = \left(\frac{\lambda}{2.2\,\mu\mathrm{m}}\right)^{-\nu-1}, \tag{3}$$

where we choose the reference wavelength at the center of the K-band observed by GRAVITY. In this context, the spectral indices correspond to the observed spectrum, namely, the intrinsic spectrum of the sources altered by interstellar absorption and reddening, the Earth's atmosphere, and instrumental transmission. However, the complex visibilities in Eq. (1) are primarily sensitive to the difference $\nu_1 - \nu_2$, rather than to the individual spectral indices due to the normalization by the total flux.

We then approximate the bandpass integration by an average over N_λ points, distributed linearly over each channel such that the numerator of Eq. (1) becomes

$$\begin{aligned}\frac{1}{N_\lambda}\sum_{i=1}^{N_\lambda} P_{\lambda_0}(\lambda_i)\Bigg\{ & f_{\nu_1}(\lambda_i)\; I_{\mathrm{SgrA}}(t,\,p)\; \mathrm{e}^{-2\pi i \boldsymbol{b}\cdot\boldsymbol{s}_{\mathrm{SgrA}}/\lambda_i} + \\ & f_{\nu_2}\left[\sum_{j=1}^{N_{\mathrm{PS}}} I_j\, \mathrm{e}^{-2\pi i \boldsymbol{b}\cdot\boldsymbol{s}_j/\lambda_i} + \int \mathrm{d}\boldsymbol{s}\, I_{\mathrm{Img}}(\boldsymbol{s})\; \mathrm{e}^{-2\pi i \boldsymbol{b}\cdot\boldsymbol{s}/\lambda_i}\right]\Bigg\}.\end{aligned} \tag{4}$$

Because we implemented the last integral as an FFT and a subsequent gridding operation, evaluating it for a fine-gridded set of λ values is computationally not very expensive as long as the image inside the Fourier transform is mono-chromatic. The computational steps to evaluate Eq. (4) are summarized in the following.

1. We use a FFT followed by gridding to compute

$$\int \mathrm{d}\boldsymbol{s}\; A_i(\boldsymbol{s})\, A_j(\boldsymbol{s})\, I_{\mathrm{Img}}(\boldsymbol{s})\, \mathrm{e}^{-2\pi i \boldsymbol{b}\cdot\boldsymbol{s}/\lambda + i\phi_i(\boldsymbol{s}) - i\phi_j(\boldsymbol{s})} \tag{5}$$

   simultaneously for all exposures, all spectral channels, and all fine-grained λ values within a channel.

2. For all additional point sources, we obtain $\mathrm{e}^{-2\pi i \vec{b}\cdot\vec{s}/\lambda}$ at each exposure, channel and sub-resolution in λ and multiply it by the phase- and amplitude-maps at the position of the source. Hereby, we approximate the aberration maps at the sources' actual positions by the aberration maps at the center of their position prior. Since the maps are very flat on the scale of the position uncertainty, the error introduced by this approximation is small, however it significantly simplifies the computation.

3. We multiply the expression for the time-dependent point source by an exposure- and polarization-dependent brightness $I_{\mathrm{SgrA}}(t,p)$ and all further point sources by their constant brightness I_j which is independent of the spectral channel.

4. We then account for the spectral distribution by multiplying each source at each λ-coordinate with the appropriate value from Eq. (3). This multiplication is the same for all exposures.

5. Finally, we add up all components, multiply by the spectral bandpass and perform the wavelength integration or bandwidth smearing as an average over all fine-grained λ-steps within one channel.

6. The procedure is repeated independently for all six GRAVITY baselines due to the changing aberration maps between baselines.

This implementation is very flexible in that more complicated spectra than the power-law of Eq. (3) can easily be accommodated. It can also readily be generalized to accomodate additional spectral components and different bandpass shapes.

We use calibration measurements of the GRAVITY spectral transmission to investigate the effect of bandwidth smearing and to compare the full measured bandpass to a top hat approximation. We find that the top-hat affects the computed visibilities on a level much smaller than the typical GRAVITY error bars and, therefore, we chose the approximation for this work. To determine the required sub-sampling steps per spectral channel, we iteratively increase N_λ until the visibilities have converged to a stable value. This is the case by a good margin at $N_\lambda = 100$.

To implement the denominator term of Eq. (1), we note that the spectral and positional integration can be decoupled under the parametrization in Eq. (3). Furthermore, assuming a top-hat bandpass with center λ_0 and width $2\delta\lambda$:

$$P(\lambda) = \mathrm{rect}\left(\frac{\lambda - \lambda_0}{2\delta\lambda}\right) = \begin{cases} 1 & \text{if } |\lambda - \lambda_0| < 0 \\ 1/2 & \text{if } |\lambda - \lambda_0| = 0 \\ 0 & \text{otherwise,} \end{cases} , \tag{6}$$

the wavelength integral is evaluated analytically to:

$$\int \mathrm{d}\lambda P(\lambda)\ f_\nu(\lambda) = \frac{2.2\,\mu\mathrm{m}}{\nu}\left[\left(\frac{\lambda_0 - \delta\lambda}{2.2\,\mu\mathrm{m}}\right)^{-\nu} - \left(\frac{\lambda_0 + \delta\lambda}{2.2\,\mu\mathrm{m}}\right)^{-\nu}\right] . \tag{7}$$

The integral in the spatial directions, on the other hand, can be computed readily as a sum over all image pixels multiplied by the squared amplitude maps. To this, we add the intensity of potential extra point sources multiplied by the fiber damping. For the variable component, the spatial integral is simply given by the product between light curve and fiber damping. Either contribution is then multiplied by Eq. (7), then their summation gives the denominator of Eq. (1).

Once we have evaluated the deterministic part of the response function, we multiply it by the time- and baseline dependent amplitude calibration factor, introduced in Sect. 2.2.3.

With this setup, one full response evaluation, including all exposures, baselines, and channels of a typical observing night with 21 exposures takes 0.4 s on a single laptop CPU (Intel i7 1.90 GHz).

A1.2 Formal description of the inference scheme

Given the sky model from Sect. 2.2.1 (cf. also Eq. 3) and the self-calibration approach for the visibility amplitudes described in Sect. 2.2.3, the full set of model parameters to be inferred is

$$\theta = \{I_{\mathrm{Img}}(\boldsymbol{s}),\, I_{\mathrm{SgrA}}(t,p),\, \boldsymbol{s}_{\mathrm{SgrA}},\, I_1, ...I_{\mathrm{NP}},\, \boldsymbol{s}_1,\, ...\, \boldsymbol{s}_{\mathrm{NP}},\, \nu_1,\, \nu_2,\, C(t,\, b)\}\ .$$

For a clearer notation, we have written the spatial ($\vec{s}$), temporal (t), baseline (b) and the polarization (p) dependence of these quantities as functional arguments, but we use them, in particular, to label the discretized coordinates. The degrees of freedom inherent to each of these parameters are counted in Eq. (2.5). The prior model for the image of faint sources is provided in Eq. (2.2), and for the remaining parameters we have:

$$\ln I_{\mathrm{SgrA}}(t,p) \hookleftarrow \prod_{j=1}^{N_{\mathrm{exp}}} \prod_{p=1,2} \mathcal{G}\left[\ln I_{\mathrm{SgrA}}(t_j,p)\,|\,0,1\right]\ , \tag{8}$$

$$\boldsymbol{s}_{\mathrm{SgrA}} \hookleftarrow \mathcal{G}\left(\boldsymbol{s}_{\mathrm{SgrA}}\,|\,\mu_{\mathrm{SgrA}},\, \sigma_{\mathrm{SgrA}}\mathbb{1}\right)\ , \tag{9}$$

$$\ln I_i \hookleftarrow \mathcal{G}\left(\ln I_i|\ 0,1\right) \quad \text{for} \quad i=1,...\,N_{\mathrm{PS}}\,, \tag{10}$$

$$\boldsymbol{s}_i \hookleftarrow \mathcal{G}\left(\boldsymbol{s}_i\,|\,\mu_i,\, \sigma_i\mathbb{1}\right) \quad \text{for} \quad i=1,...\,N_{\mathrm{PS}}\,, \tag{11}$$

$$\nu_i \hookleftarrow \mathcal{G}\left(\nu_i|\ \mu_{\nu_{\mathrm{i}}},\, \sigma_{\nu_{\mathrm{i}}}\right) \quad \text{for} \quad i=1,2\,, \tag{12}$$

$$C_i(t,\, b) \hookleftarrow \prod_{b=1}^{6} \prod_{j=1}^{N_{\mathrm{exp}}} \mathcal{G}\left[C_i(t_j)|\ 1,\, \sigma_C\right]\ , \tag{13}$$

where the "$\hookleftarrow$" indicates the probability density function from which a variable is drawn a priori and N_{exp} counts the exposures in the data set. MGVI works with standardized coordinates, that is, all the model parameters are mapped to a set of auxiliary parameters ξ, which follow a standard normal distribution. This mapping is obtained by a two-step process,

$$\theta = \left[\mathcal{F}^{-1}_{\mathcal{P}(\theta)} \circ \mathcal{F}_{\mathcal{G}(\xi|0,\mathbb{1})}\right](\xi)\ , \tag{14}$$

where $\mathcal{F}$ and $\mathcal{F}^{-1}$ denote the cumulative probability density function and its inverse, respectively. The first step translates a standard normal distributed to an uniformly distributed variable. In the second step, this uniform distribution is transformed to the prior specified in Eq. (2.2) and Eqs. (8) to (13).

For brevity, we introduce an operator notation in which $\mathcal{S}$ is the signal operator and corresponds to the application of Eq. (14). The response operator, $\mathcal{R}$, computes complex visibilities for any realization of θ as specified by Eq. (1). Finally, the complex visibilities are transformed to visibility amplitudes and closure phases by the $\mathcal{A}$ and $\mathcal{C}$ operator, respectively.

In this notation, the negative logarithm of the likelihood discussed in Sect. 2.2.4 is

expressed as:

$$
\begin{aligned}
-\ln \mathcal{P}\left(\boldsymbol{d}|\xi\right) \mathrel{\widehat{=}} & \frac{1}{2}\left[\mathrm{e}^{i(\mathcal{C}\circ\mathcal{R}\circ\mathcal{S})(\xi)} - \mathrm{e}^{i\mathcal{C}(\boldsymbol{d})}\right] N_\Phi^{-1}\left[\mathrm{e}^{i(\mathcal{C}\circ\mathcal{R}\circ\mathcal{S})(\xi)} - \mathrm{e}^{i\mathcal{C}(\boldsymbol{d})}\right]^\dagger \\
& + \frac{1}{2}\left[\left(\mathcal{A}\circ\mathcal{R}\circ\mathcal{S}\right)(\xi) - \mathcal{A}\left(\boldsymbol{d}\right)\right] N_\rho^{-1}\left[\left(\mathcal{A}\circ\mathcal{R}\circ\mathcal{S}\right)(\xi) - \mathcal{A}\left(\boldsymbol{d}\right)\right]^\dagger ,
\end{aligned}
\tag{15}
$$

where "$\widehat{=}$" denotes equality up to addition of a constant and N_Φ^{-1} and N_ρ^{-1} are the diagonal covariance matrices of the closure phases and visibility amplitudes (see Sect. 2.2.4). In the first line, we approximate the closure phases by their position on the unit circle, which mitigates the problem of phase wraps. This represents an approximation to the full likelihood, which becomes precise in the limit of small differences and down-weights outliers. The corresponding negative log-prior, on the other hand, is now simply given by

$$
-\ln \mathcal{P}\left(\xi\right) \mathrel{\widehat{=}} \frac{1}{2}\xi\mathbb{1}\xi^\dagger . \tag{16}
$$

In the inference, MGVI approximates the full posterior by a multivariate Gaussian distribution with covariance $\Xi \simeq I\left(\xi\right)^{-1}$, where $I\left(\xi\right)$ is a generalization of the Fisher metric defined as

$$
\begin{aligned}
I\left(\xi\right) = \mathbb{1} & + \left[\frac{\partial\, \mathrm{e}^{i(\mathcal{C}\circ\mathcal{R}\circ\mathcal{S})(\xi)}}{\partial\xi}\right] N_\Phi^{-1}\left[\frac{\partial\, \mathrm{e}^{i(\mathcal{C}\circ\mathcal{R}\circ\mathcal{S})(\xi)}}{\partial\xi}\right]^\dagger \\
& + \left[\frac{\partial\, \left(\mathcal{A}\circ\mathcal{R}\circ\mathcal{S}\right)(\xi)}{\partial\xi}\right] N_\rho^{-1}\left[\frac{\partial\, \left(\mathcal{A}\circ\mathcal{R}\circ\mathcal{S}\right)(\xi)}{\partial\xi}\right]^\dagger .
\end{aligned}
\tag{17}
$$

Here, the first term originates from the prior and the latter two from the likelihood. The NIFTy package (Arras et al., 2019b), which we have used to implement the inference, facilitates auto-differentiation, such that only the derivatives of individual operators need to be implemented and an operator sequence can be differentiated automatically by applying the chain rule.

A1.3 Hyper-parameters of the inference

The performance of MGVI depends on a series of hyper-parameters which need to be set by the user. Among them is the number of MGVI iterations and the number of samples and minimization steps at each iteration which we jointly refer to as the iteration scheme. In addition, it is possible to choose between different minimizers and iteration controllers for the minimization of the KL and for drawing samples at a given position.

We determined these hyper-parameters in a two step procedure and first consider a mock data set, for which we took a representative (u, v)-coverage from the 2019 observing series. We then specified a model with a variable Sgr A* at the center, two faint sources in its vicinity and a brighter S2-like source to the north east. The model provides a prediction

Table 1: Iteration scheme for the posterior exploration with MGVI.

iteration step	# minimization steps	# samples
1 - 3	4	3
4 & 5	5	5
7 & 8	8	6
9 - 12	10	8
13 - 20	15	12
21 - 25	20	15
26 - 30	30	20

for closure phases and visibility amplitudes, to which we added a random Gaussian noise realization.

In the analysis of the mock data set, we varied all the aforementioned hyper-parameters with the aim to optimally recover the ground truth. We find that an iteration controller that checks the relative energy change between steps works best for drawing samples and minimizing the KL, and for the latter task we picked a Newton Conjugate Gradient minimizer. None of our results show significant changes after 30 MGVI iterations.

Arras et al., 2020 noted that tempering during the early MGVI iterations could improve their results and to this end, they iterated between minimizing the closure and amplitude likelihoods separately. We do not find a similar improvement in our reconstructions and thus consider the full likelihood at all MGVI steps.

The performance on the actual data can differ from the mock-imaging tests, for example, if not all noise correlations are modeled or if some residual systematic effects remain unaccounted for by the response function. Therefore, in a second step, we revised our iteration scheme now considering actual observations. This resulted in an overall decrease in the number of minimization steps and an increase in the number of samples at each MGVI iteration. Accordingly, MGVI reaches the minimum more slowly and overfitting is impeded. We can thus view this revision as the adoption of a less aggressive and more conservative approach.

We summarize the minimization scheme in Table 1. The consistency of our images across multiple nights and observing periods (cf. Sect. 2.4.3) and injection tests (cf. Sect. 2.4.5) verify that our result is not an artifact of the minimization routine.

A1.4 Identification of stars

The GRAVITY images illustrate how S29 flies through pericenter in 2021 and here we comment on the crossidentification of the star with the earlier, AO-based NACO data. For that purpose, we differentiate between $S29_{\mathrm{GRAVITY}}$ (i.e., the star labeled S29 throughout this publication and observed with GRAVITY) and $S29_{\mathrm{NACO}}$, the star label S29 in Gillessen et al. (2009).

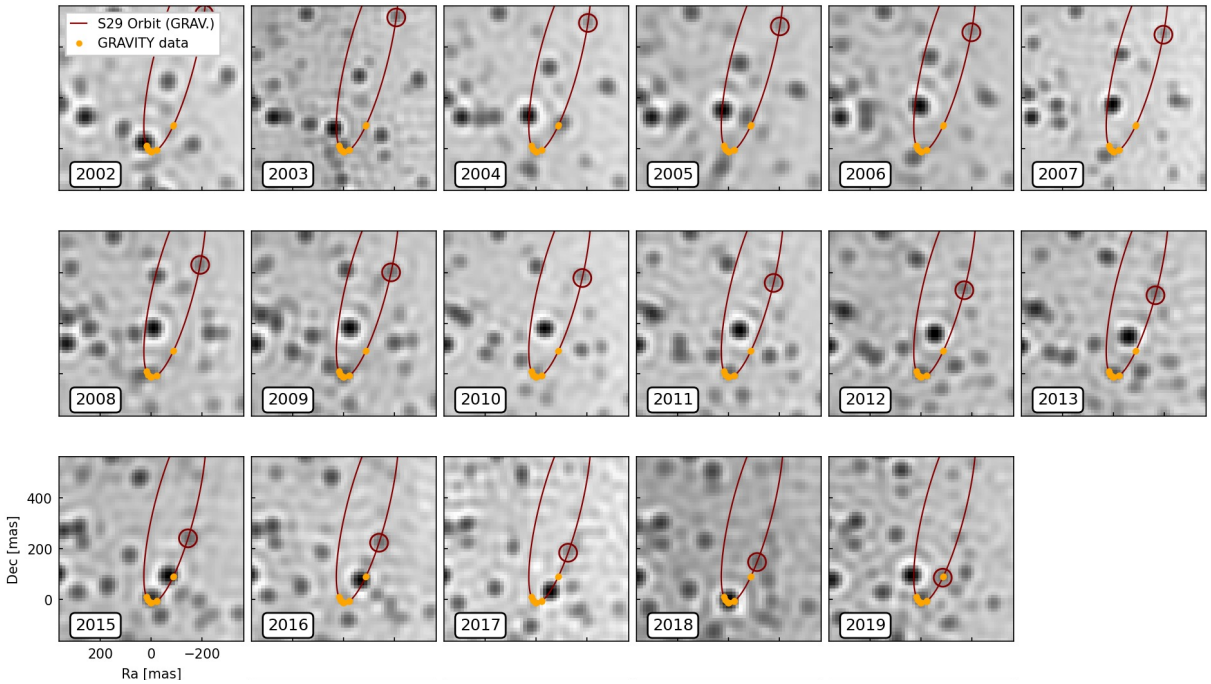

Figure 1: Compilation of deconvolved NACO images cut to the central ±400,mas. The small circle in dark red marks the position of S29 on its orbit (dark red ellipse) in each panel. The orange data points are the 2019 and 2021 GRAVITY measurements. Evidently, S29 can be traced consistently over two decades. We note that around 2015 - 2017 the star is confused with other stars, such that the astrometry becomes unreliable, but the identification remains unambiguous.

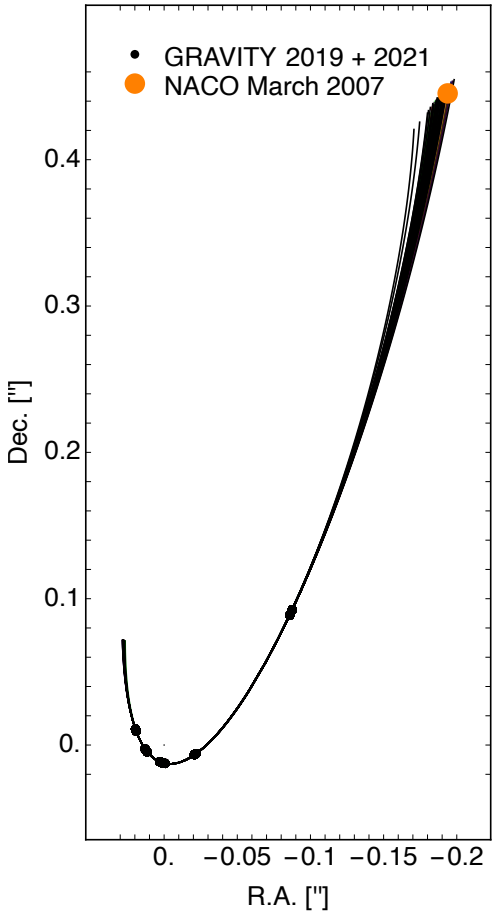

Figure 2: Backwards prediction of the GRAVITY data for $S29_{GRAVITY}$ leads to a position in March 2007 compatible with the position of $S29_{NACO}$. The black points show the GRAVITY data from 2021 and 2019. The set of black orbits is obtained by bootstrapping these data and fitting each of these mock data sets. The family of orbits naturally matches the position obtained from NACO (orange disk). The epoch March 2007 was chosen since it is the one used in Gillessen et al., 2009 to define the names of the S-stars.

Identifying $S29_{GRAVITY}$ with $S29_{NACO}$

In Fig. 1, we show a compilation of deconvolved NACO images from 2002 to 2019, which allow us to trace $S29_{NACO}$ through the years. In 2019, the star was observed with NACO and GRAVITY, and we obtain matching positions for $S29_{NACO}$ and $S29_{GRAVITY}$.

Using only the 2021 GRAVITY data for $S29_{GRAVITY}$, we can fit an orbit and extrapolate back to 2019, yielding a position consistent with the 2019 astrometric points of GRAVITY for $S29_{GRAVITY}$. Furthermore, the orbit from the full interfermetric data set, that is, GRAVITY astrometric positions from 2021 to 2019, reliably predicts the $S29_{NACO}$ position in earlier AO epochs. In particular, it agrees with the 2007 reference map in Gillessen et al., 2009, as demonstrated in Fig. 2.

We conclude that our identification of $S29_{GRAVITY}$ with $S29_{NACO}$ is robust and can be done both forwards from the AO epochs to GRAVITY as well as backwards from the GRAVITY data to the NACO images obtained $15-20$ years earlier.

Excluding other identifications for $S29_{GRAVITY}$

Conserved dynamical quantities can be used to tag stars, since the conserved quantity needs to apply at each point on the orbit for a given star. Here, we use the z-component of the angular momentum vector, $h_z = xv_y - yv_x$, which can be derived from astrometric data alone. For $S29_{GRAVITY}$, we can determine that value for four occasions in 2021: during each of the four observing campaigns, we were not only able to determine the positions, but also the proper motions. This yields $h_z = (-1.09 \pm 0.03) \times 10^{20}$ m^2/s, where the value is the mean over the four epochs and the error the corresponding standard deviation. The two 2019 points for $S29_{GRAVITY}$ yield $h_z \approx -1.1 \times 10^{20}$m^2/s, consistent with the 2021 value.

This excludes, for example, that $S29_{GRAVITY}$ is identical to the source candidate from Peißker et al., 2021, which we henceforth refer to as $S62_{Peissker}$. The latter star has a significantly smaller z-component for the angular momentum vector, $h_z \approx +1.4 \times 10^{19}$m^2/s. Indeed, a star with such a high value of h_z as $S29_{GRAVITY}$ would need to show an (tangential) on-sky motion of ≈ 880 km/s, for a projected radius of 0.1 mas, at appocenter.

We also inspected the two 2019 data sets obtained on $S29_{GRAVITY}$. Using the same imaging technique as in Sect. 2.5.1 and GRAVITY Collaboration et al., 2021b, we find that there is only one dominant source in the field. Furthermore, the residual level is fainter than $m_K = 19$. The structure of these residuals can be attributed to S2, which is significantly brighter than $S29_{GRAVITY}$ but located further away from the field center and thus appears significantly damped by the Gaussian acceptance profile of the GRAVITY fibers.

Looking for the counterpart of $S62_{Peissker}$

There are two sets of GRAVITY pointings which contain the position predicted by the $S62_{Peissker}$ orbit in Peißker et al., 2020. First, we would have expected it to show up in the 2019 GRAVITY pointings to $S29_{GRAVITY}$. Second, we pointed to the north-west of Sgr A* this year as part of the mosaicing data set (see Table 2.2 and Fig. 2.4). In the former,

we detect S29 at the expected position and with the expected velocity, as discussed in the previous sub-section. In the images from the latter data set (see Fig. 2.4), we can identify S42, S2 and Sgr A*. However, we do not find any further sources. Given the predicted brightness of $S62_{\text{Peissker}}$, it would have to be outside the FOV of either pointing. In 2022, the star is predicted even closer to Sgr A* and should then appear in the central pointing, that is, when positioning the GRAVITY fibers directly onto Sgr A*.

A1.5 Probabilistic view of the imaging results

In Figs. 2.1 and 2.5, we show the main imaging results of this publication. These images are computed as the mean over all samples in a single G^R run and have been convolved with a Gaussian of 1.6 standard deviation to account for the typical size of the CLEAN beam.

However, the MGVI samples contain information beyond the mean and can also be used to estimate the uncertainty of the result. Since our sky model for the GC is a collection of point sources and the main goal of the analysis is the search for faint, yet unknown stars, we visualize the information contained in the MGVI samples in the following way. In the mean image, we select all pixels whose flux exceeds the background by at least a factor of 10. This threshold is chosen to be below the optimal sensitivity found in Sect. 2.4.5. Then, for all potential sources identified in this way, we compute the flux variance in the corresponding pixel and express the mean flux in units of its standard deviation. We summarize the position of all potential sources in a RA-Dec plot, as the one shown in Fig. 3. Thereby, the symbol size indicates the mean flux in units of its standard deviation, that is, the significance of the source candidate, while the color signals its flux. For known sources with a Gaussian position prior, G^R directly infers the coordinates and the standard deviation of this estimate is overdrawn on the source symbol.

This statistical view of the imaging results is provided in Fig. 3 for the same G^R runs, which are shown in Fig. 2.1. As Fig. 3 demonstrates, S300 corresponds not only to the brightest pixel in the image of faint sources, but it is also the only pixel where flux is detected at a high significance. The only exception here is the July result, where S300 is most strongly affected by fiber damping and G^R fails to detect its flux in a single high-significance pixel. To evaluate the G^R results, we produce and inspect this type of figure for each of the ten G^R imaging runs separately. The results of this inspection are reported in Sect. 2.4.3.

Further, we also combine the samples from all ten G^R runs into a single figure for a joint representation. These are shown, for all nights considered in Tables 2.1 and 2.2, in Figs. 4 and 5 respectively. Here, we did not perform a selection of runs, which means that the figures also contain poorly converged runs and runs that failed to identify S300. Furthermore, as we report in Sect. 2.4.3, the position at which S300 is detected can vary by a single pixel. The same holds for sources in the mosaicing data set, which are not modeled as a point source which is superimposed on the image. Both effects, the inclusion of all runs and the position uncertainty, lead to a decrease in the significance estimate of faint sources in the joint representation. The effect is very apparent from the comparison

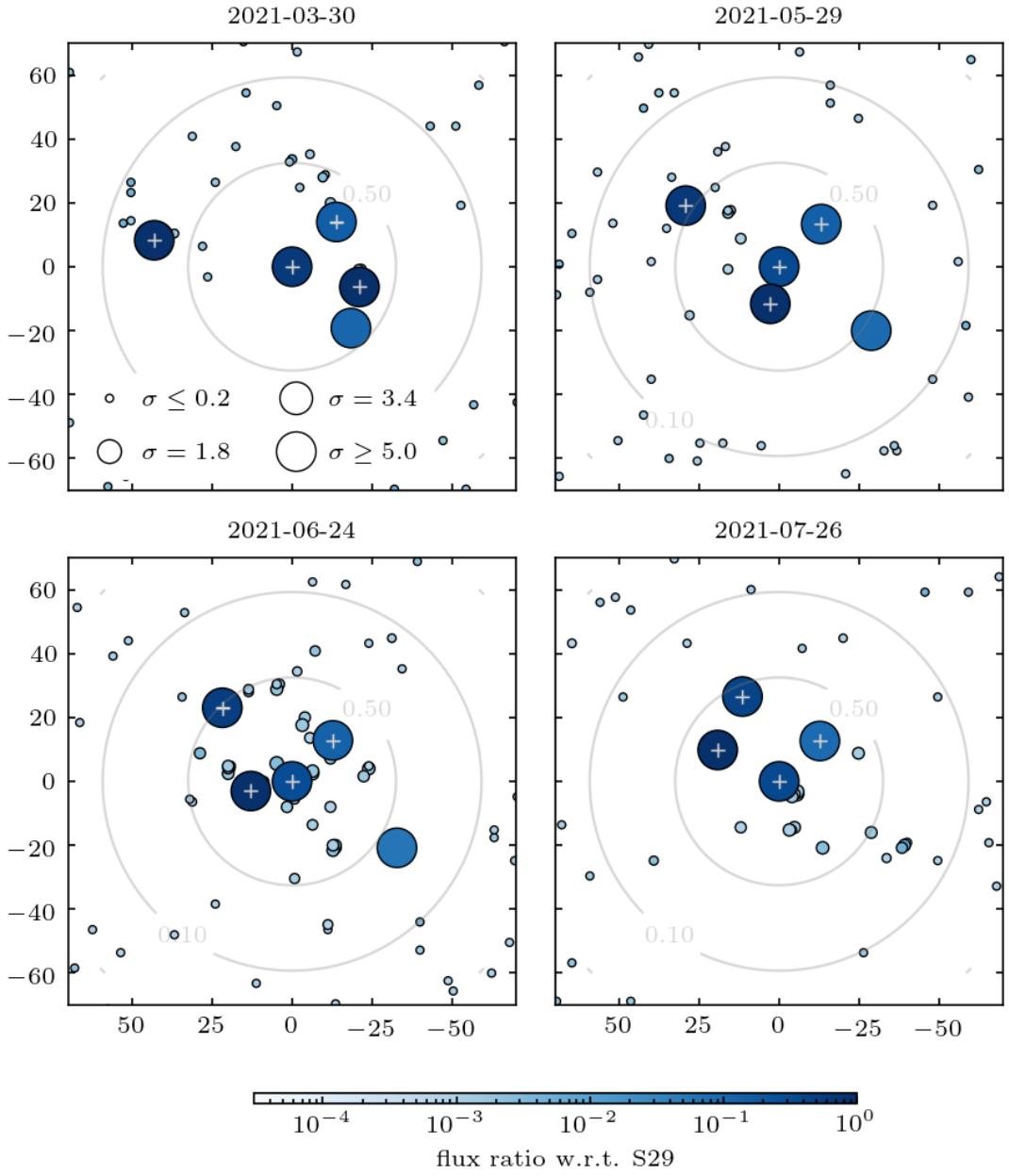

Figure 3: Statistical view of the imaging results shown in Fig. 2.1. The symbol color indicates the flux of a source candidate normalized to S29, while its size represents the significance (see Appendix A1.5 for details). The Sgr A* flux depicted here has to be multiplied by the light curve at each exposure to arrive at the true flux ratios. For stars which are modeled as a point source, the position uncertainty is indicated in gray.

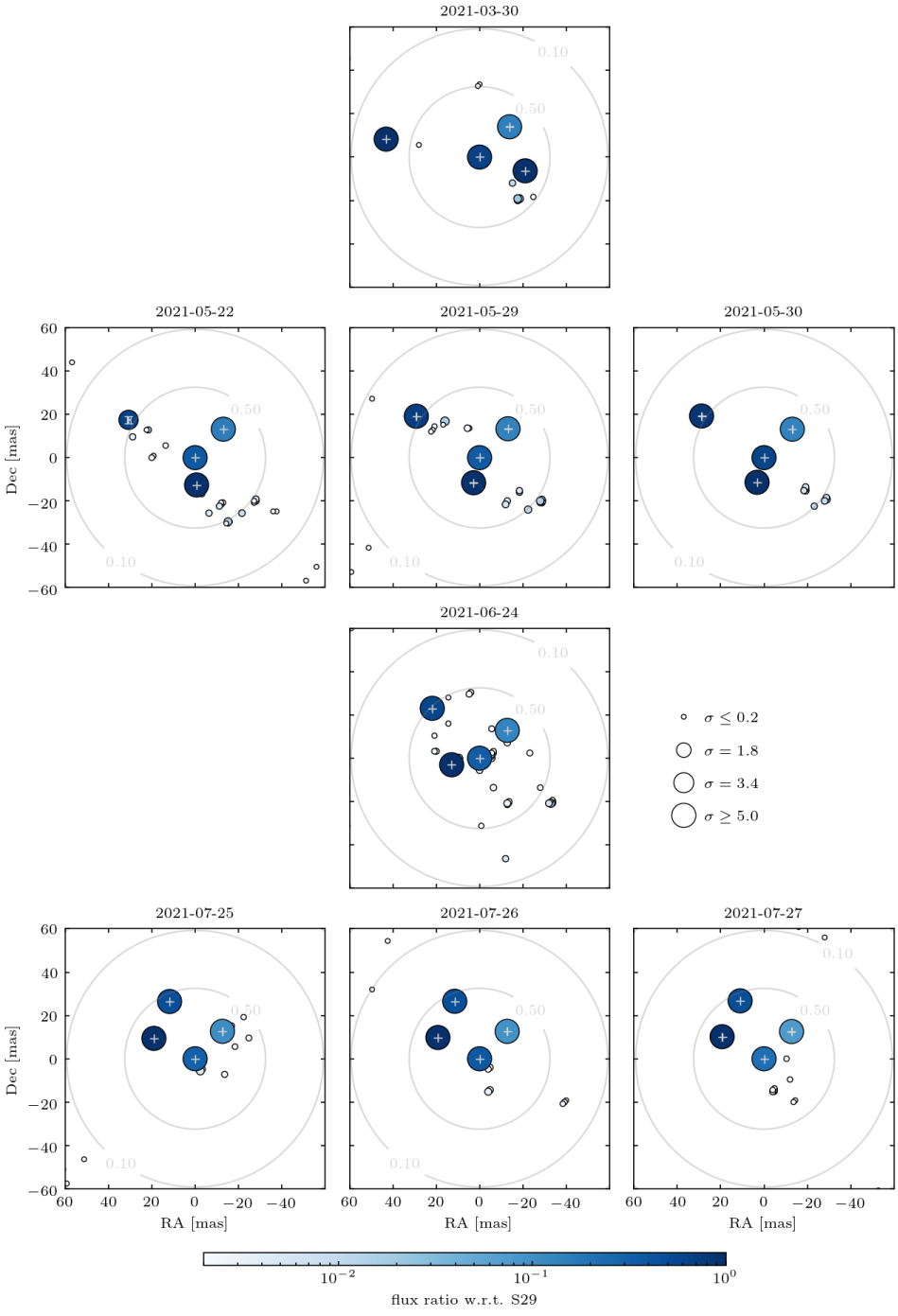

Figure 4: Summary of all imaging runs for Sgr A*-centered exposures. Each panel combines the samples from ten imaging runs with independent random seeds (see Appendix A1.5 for details). The symbol color indicates the flux of a source candidate normalized to S29, while its size represents the significance. The Sgr A* flux depicted here has to be multiplied by the light curve at each exposure to arrive at the true flux ratios. For stars modeled as a point source, the position uncertainty is indicated in gray.

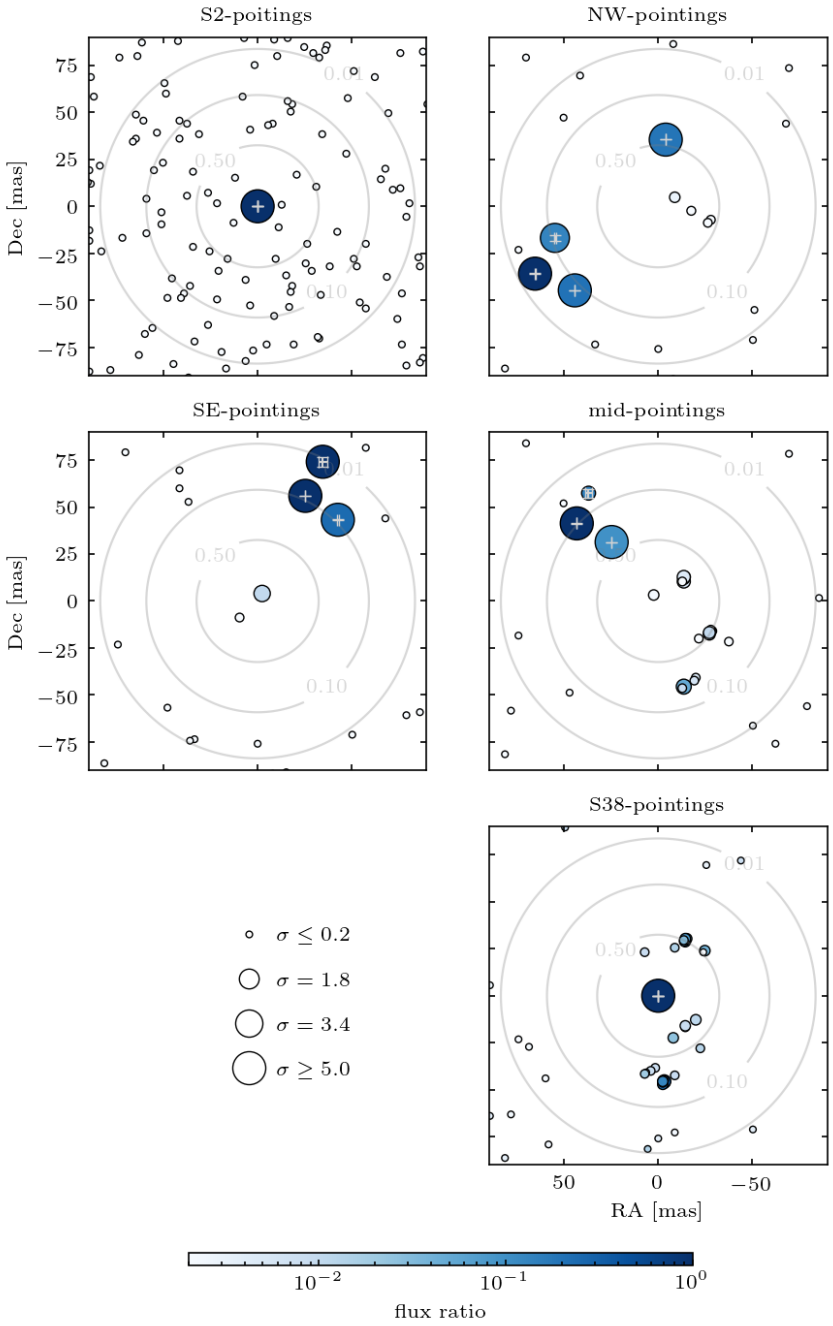

Figure 5: Summary of all imaging runs for the mosaicing data set. Each panel combines the samples from ten imaging runs with independent random seeds (see Appendix A1.5 for details). The symbol color indicates the flux of a source candidate, while its size represents the significance. The flux in the images is normalized to S2 in the top left panel, to S38 in the bottom right panel, and to S29 in all other instances. The Sgr A* flux depicted here has to be multiplied by the light curve at each exposure to arrive at the true flux ratios. For stars modeled as a point source, the position uncertainty is indicated in gray.

of Fig. 3 and Fig. 4. Also for this reason, the evaluation of the G^R results run-by-run as presented in Sect. 2.4.3 is a very important step of the analysis.

A1.6 Source injection tests

We performed a series of injection tests to further corroborate the result from Sect. 2.4.3. Injecting a source into the data and trying to recover it in the images has the additional benefit of making it possible to dial down the source's flux step-by-step and in this fashion test our sensitivity.

To create the data for the injection tests, we pick the imaging run with the cleanest result from the 2021-05-29 night, this corresponds to the image shown in Fig. 2.1. The posterior mean gives a model prediction for closure phases and visibility amplitudes, which we subtract from the data to obtain the residuals. We then augment the model by an additional faint source, again compute closures and amplitudes, and, finally, we add back the residuals. In comparison to creating mock data, where we would specify the model by hand and then add a random Gaussian noise realization, this approach preserves the effect of any instrumental systematics as well as correlations between individual data points, which are unaccounted for by the prior model and the likelihood.

In summary, we tested mock sources at two different positions, each with four values for its flux. The first position is at $\vec{s}_{\mathrm{mock1}} = (-15.0, 5.0)\,\mathrm{mas}$ from Sgr A* and thus relatively close to S300. The second location we pick at identical separation from the field center with $\vec{s}_{\mathrm{mock2}} = (5.0, 15.0)\,\mathrm{mas}$. The flux ratios with respect to S29 for each of these sources are 0.055, 0.037, 0.018, and 0.0037. With $m_{\mathrm{K}}\,(\mathrm{S29}) \simeq 16.6$, this corresponds to a 19.7, 20.2, 21.0 and a 22.7 magnitude mock source, respectively.

The most important results of the injection tests are summarized in Fig 6. From the first row of plots, that is, the injection tests at position 1, close to S300, it is very apparent that the algorithm struggles to properly disentangle both stars. For the highest flux ratio tested, the mock source is found in three runs as a single bright pixel at high significance and in another three smeared out over multiple pixels. Most importantly, however, the scatter around S300 and the amount of flux found in its side lobes increases significantly. The detection of S300 gets cleaner when the flux of the mock source is reduced. But it is already for the second highest flux ratio that the algorithm struggles to robustly detect the mock source and only infers it as flux spread out over multiple pixels at a low significance in six of the ten imaging runs. The result is thus very similar to S300 in the Sgr A*-centered July images. For a flux ratio of 0.018, the mock source at the first position is found only once at a low significance. At this point, it is clear that we have exceeded our sensitivity.

At the position of the second mock source, in contrast, the sensitivity is considerably higher. These results are shown in the second row of Fig. 6. For a flux ratio of 0.018 or magnitude of 21.0, all imaging runs infer flux at the correct position, five of them in a single pixel with high significance and the remaining spread out over multiple neighboring pixels. The faintest magnitude we tested is 22.7; at this point, only one of the ten imaging runs is able to identify the mock source and we would not be able to claim a detection. Interestingly, however, more flux is attributed to a spurious source in the side lobe west of

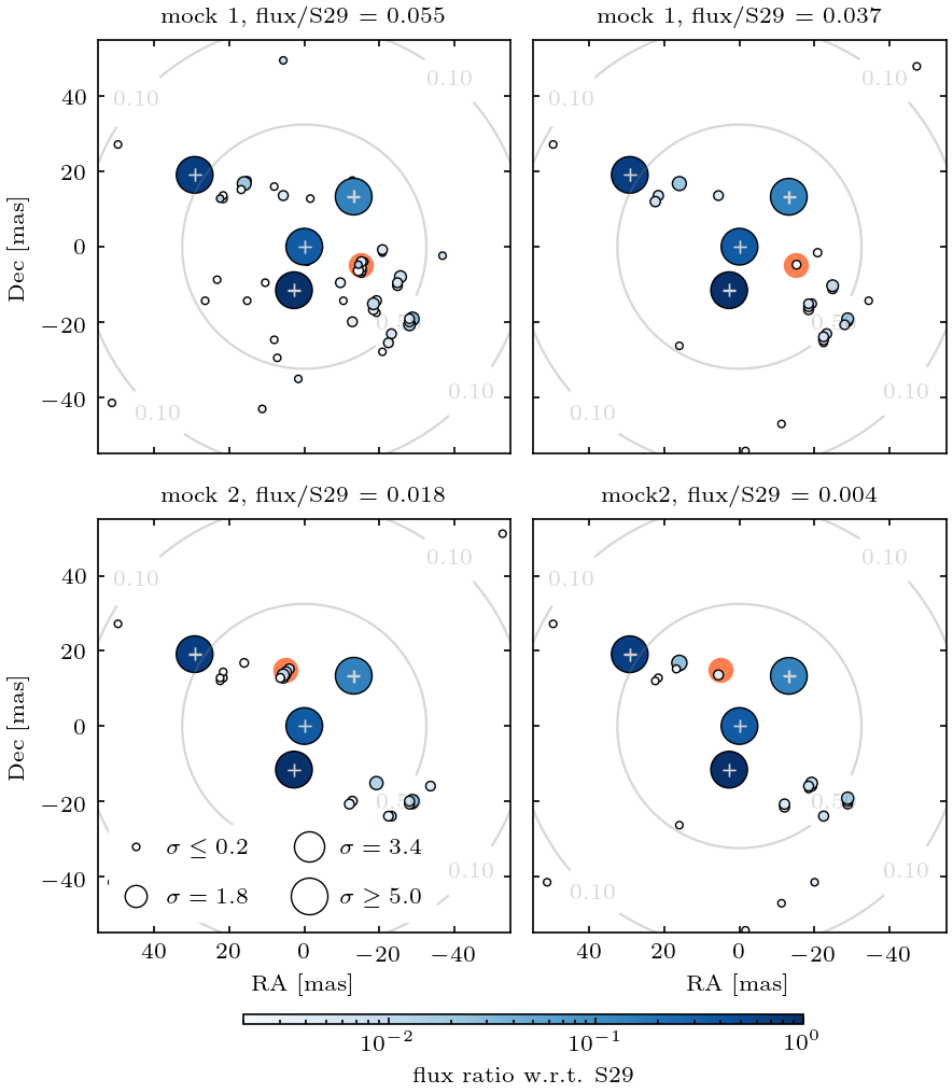

Figure 6: Results of injection tests for the May 29 data set. The position of the injected source is at $(-15.0, -5.0)$ mas from Sgr A* for mock 1, at $(5.0, 15.0)$ mas for mock 2 and marked by an orange circle in the respective plots. We show the combined samples from ten imaging runs with varying random seed and indicate the mean inferred flux, normalized by S29, by symbol color and the significance of a source candidate by the size of its symbol (see Appendix A1.5 for details). In this fashion of display, variation of a faint source's position by a pixel between the imaging runs leads to a decrease in the estimated significance, even if the detection is very robust ($> 5\sigma$) for individual runs. The Sgr A* flux depicted here has to be multiplied by the light curve at each exposure to arrive at the true flux ratios. For stars that are modeled as a point source, the position uncertainty is indicated in gray.

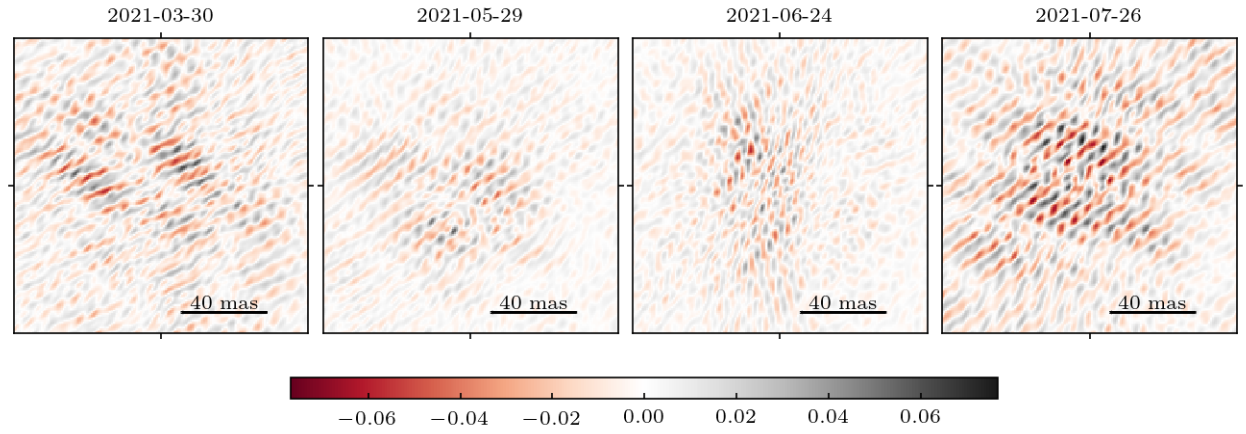

Figure 7: Residual images for the four observing epochs in 2021, where north is up, east to the left and the flux is normalized to S29. The images corresponding to the nights depicted here are shown in Fig. 2.1. We note that while our posterior model was optimized on closure phases and visibility amplitudes, here we compare it to the full complex visibility.

Table 2: Rms in the central 74×74 mas of the residual images in Fig. 7.

Date	rms/S29	magnitude
2021-03-30	1.6×10^{-2}	21.1
2021-05-29	1.2×10^{-2}	21.7
2021-06-24	1.3×10^{-2}	21.6
2021-07-26	2.2×10^{-2}	21.0

Notes. We convert the flux ratio with respect to S29 into a K-band magnitude, assuming that $m_{\mathrm{K}}\,(\mathrm{S29}) = 16.6$.

S55, which is rather close to the injected star.

A1.7 Residual images

Residual images play a crucial role for the CLEAN algorithm in that they guide the investigator when deciding where to place the clean box. Furthermore, the highest residual inside this box is understood as a physical source, and its signal is subtracted from the visibilities.

For the $\mathrm{G^R}$-code, residual images do not have the same significance. We worked with closure phases and visibility amplitudes and performed the comparison between the model and data directly in the data space by evaluating the likelihood. Indeed, to be able to compute a residual image, it is necessary to invert the Fourier transform in the response equation, namely, Eq. (2.3), which requires the full phase information of the complex visibilities. Even then, the normalization term, bandwidth smearing and aberration corrections (see Sect. 2.2.2 and Appendix A1.1) cannot be accounted for.

To maintain an understanding of the spatial structure of our residuals and to aid in the comparison of other methods, here we provide retroactively computed residual images. These make use of the absolute phase measurement which is provided by GRAVITY but was not considered in the imaging.

Closure phases are insensitive to a global translation and our model therefore fixes Sgr A* at the center of the image. In reality, a slight offset from zero is plausible and would reflect itself in the visibility phases. To correct for this offset, we compute a pseudo-dirty image from our model, and fit a Gaussian to its brightest peak. Doing the same in the dirty image, we can align the model with the data by shifting the coordinates of either Gaussian on top of each other.

We also need to fix the normalization term which is implemented in our model. To determine the overall scaling of the residual images, we use the flux in the brightest pixel of the pseudo-dirty image which corresponds to S29. Our final residual images are given by the inversely Fourier transformed residuals, divided by the S29 signal and are shown in Fig. 7.

The imaging analysis of GRAVITY GC data with CLEAN in GRAVITY Collaboration et al., 2021b used the residual images to estimate the noise level as the root mean square (rms) in the central 74×74 mas of the image. We provide the same values for all images shown in Fig. 7 in Table 2. We note that all images are found to be below the noise level reported in GRAVITY Collaboration et al., 2021b.

Although a comparison with CLEAN based on the residual images is tempting, we caution the reader against overinterpreting these results. Any telescope-based phase errors are reflected in the residual images, even though G^R is completely insensitive to them. The inversion of the measurement equation to translate the residuals into the image domain cannot account for several important effects such as normalization by the photometric flux, bandwidth smearing, or aberration maps. Finally, the alignment of our model with the absolute position information available from visibility phases is not perfect and may even have the effect of increasing the noise level by itself.

A2 Appendix: Dynamical probes for the mass of Sgr A*

A2.1 Rough mass estimate

The period P for an emitter on a circular orbit with radius r_e is simply given by the common Kepler formula

$$P^2 = \frac{4\pi^2 r_e^3}{GM} = \frac{4\pi^2}{c^2}\frac{r_e^3}{R_g} \,. \tag{18}$$

Following Gralla et al., 2019 and Gates et al., 2020, the observed loop radius on the sky r_0 is (to very good approximation) $r_0 = r_e + R_g$, meaning that the loop appears enlarged by roughly $1R_g$ due to the gravitational lensing. This yields

$$R_g = \left(\frac{2\pi}{Pc}\right)^2 (r_0 - R_g)^3 \,, \tag{19}$$

which, for an observed period and radius, can be solved for R_g, and thus yields a mass M.

A2.2 Depolarized hot spot model

The model used in Sect. 4.6 builds on the model presented in Gelles et al., 2021. The original model describes the non-fractional Stokes parameters Q and U for completely polarized light such that the total intensity of the hot spot is given by $\sqrt{Q^2+U^2}$. Experimentally we measure both polarized and non-polarized intensities such that the total intensity is $I = I_p + I_{np}$. While we assume that the flux is dominated by the hot spot, it still is only $10-40$ % polarized (GRAVITY Collaboration et al., 2020d). If the non-polarized intensity comes from some stochastic process (e.g., turbulence in the flow, chaotic local magnetic fields), the averaging process of the non-polarized intensity will average to a constant value $\langle I_{np}\rangle$ if enough flares are considered. The average fractional polarization will then be

$$\frac{Q}{I} = \frac{Q}{I_p + \langle I_{np}\rangle} \quad , \quad \frac{U}{I} = \frac{U}{I_p + \langle I_{np}\rangle} \,. \tag{20}$$

Although a simplification, this approach captures the fundamental features of the complex dynamics seen in more realistic hot spot models (see Vos et al., 2022; Dexter et al., 2020).

An example of how adding the non-polarized emission component can be used to match the observational average fractional polarization

$$\left\langle \frac{I_p}{I} \right\rangle = \left\langle \frac{\sqrt{Q^2+U^2}}{I} \right\rangle \tag{21}$$

is shown in Fig. 8. Matching the average polarization fraction of the data naturally represents the data points.

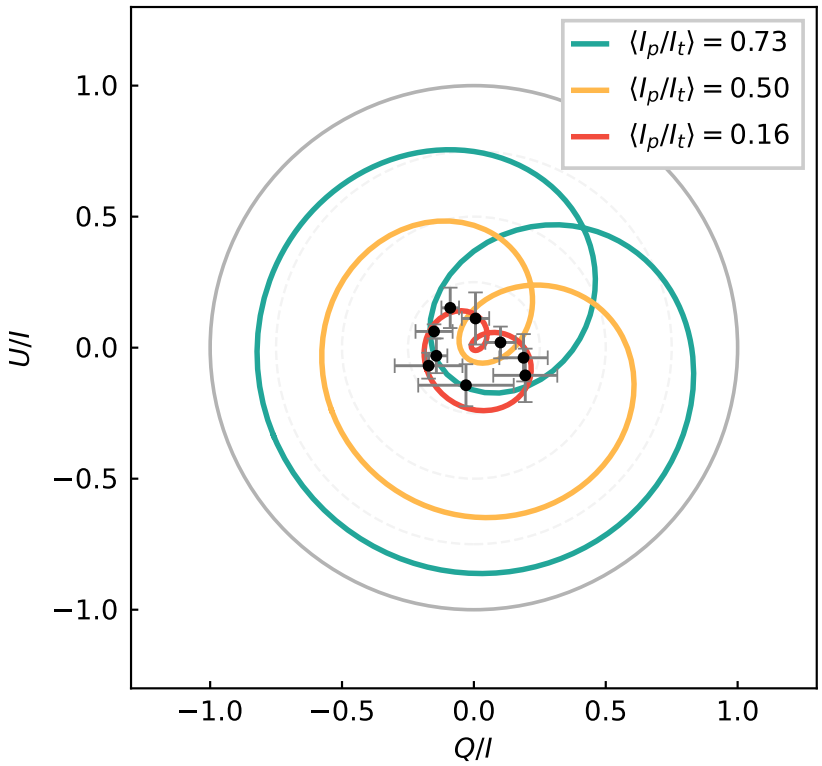

Figure 8: Effect of adding a constant depolarization term to the total intensity predicted by the hot spot model. The data points represent the averaged polarization data shown in Fig. 3.3, and the red line the model whose average polarization matches that of the observed value. The inclination and position angle used are respectively $i = 157°$ and $PA = 25°$.

A2.3 QU loop morphology

Regardless of the depolarization fraction used in the depolarized hot spot model (see Appendix A2.2), the predicted electric field position angle (EVPA) is always given by

$$\text{EVPA} = \frac{1}{2}\arctan\left(\frac{U}{Q}\right) , \tag{22}$$

and depends solely on the non-fractional Stokes parameters. The angular velocity with which the $Q-U$ loops are traversed (see Fig. 9) is thus independent of the non-polarized emission, and makes it a robust value for the inclination constraint presented in Fig. 3.4. By taking the inclination that matches the 6 °/min and fixing the polarization emission such that the average fractional polarization matches the observed value, we can fit for the position angle and time starting point of the loop. The χ^2 fit is displayed in Fig. 10 and the corresponding model in Fig. 3.5.

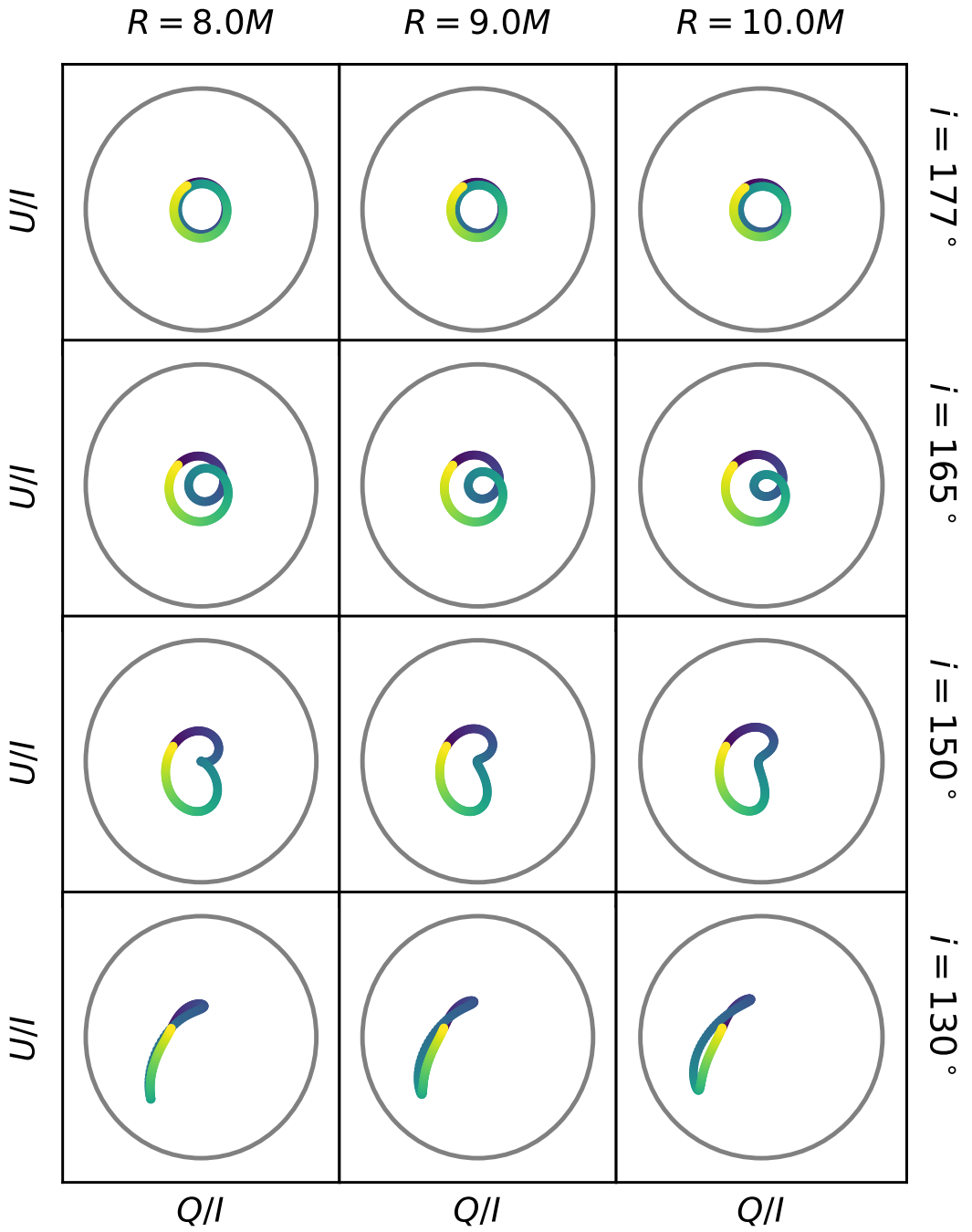

Figure 9: Illustration of $Q - U$ loops for different radii and inclinations for the case of a poloidal field geometry. The color-coding indicates time, as in Fig. 3.3. A single loop occurs for a narrow range of almost face-on inclinations. The gray circle represents unitary fractional polarization, and the average depolarized emission is $\langle I_{np} \rangle = 0.3$ for all plots.

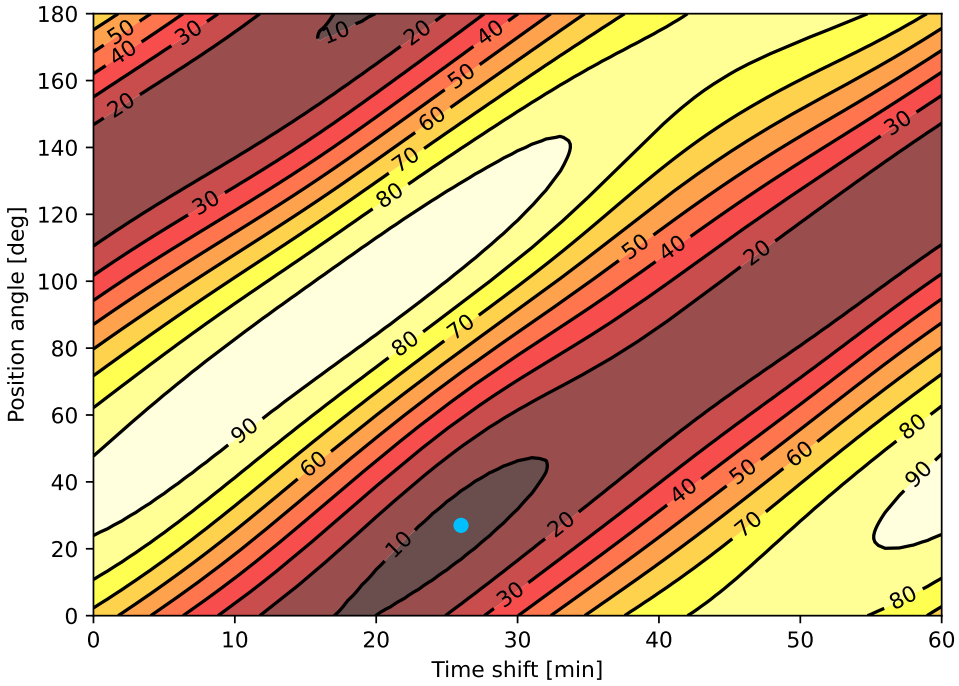

Figure 10: χ^2 contour map for the polarization model as a function of position angle and time shift for a fixed radius of $9R_g$. The blue dot represents the minimum at (27 min, 25°). A slight degeneracy between the two variables exists since, for each position angle, there is a corresponding optimum time shift that adjusts the model to start at the right time. The corresponding model is displayed in Fig. 3.5.

A2.4 Fitting model

The astrometric fit presented in Sect. 3.4.2 is similar to that presented in GRAVITY Collaboration et al., 2020e. In addition to the new constraints from the polarimetric data, we replaced the previously used χ^2 fit with a nested sampling fit. The posterior distributions are shown in Fig. 11 and the corresponding model in Fig. 3.6. We used flat priors for all quantities except the inclination, for which we used a sine prior. For the inclination and position angle we consider cyclic priors.

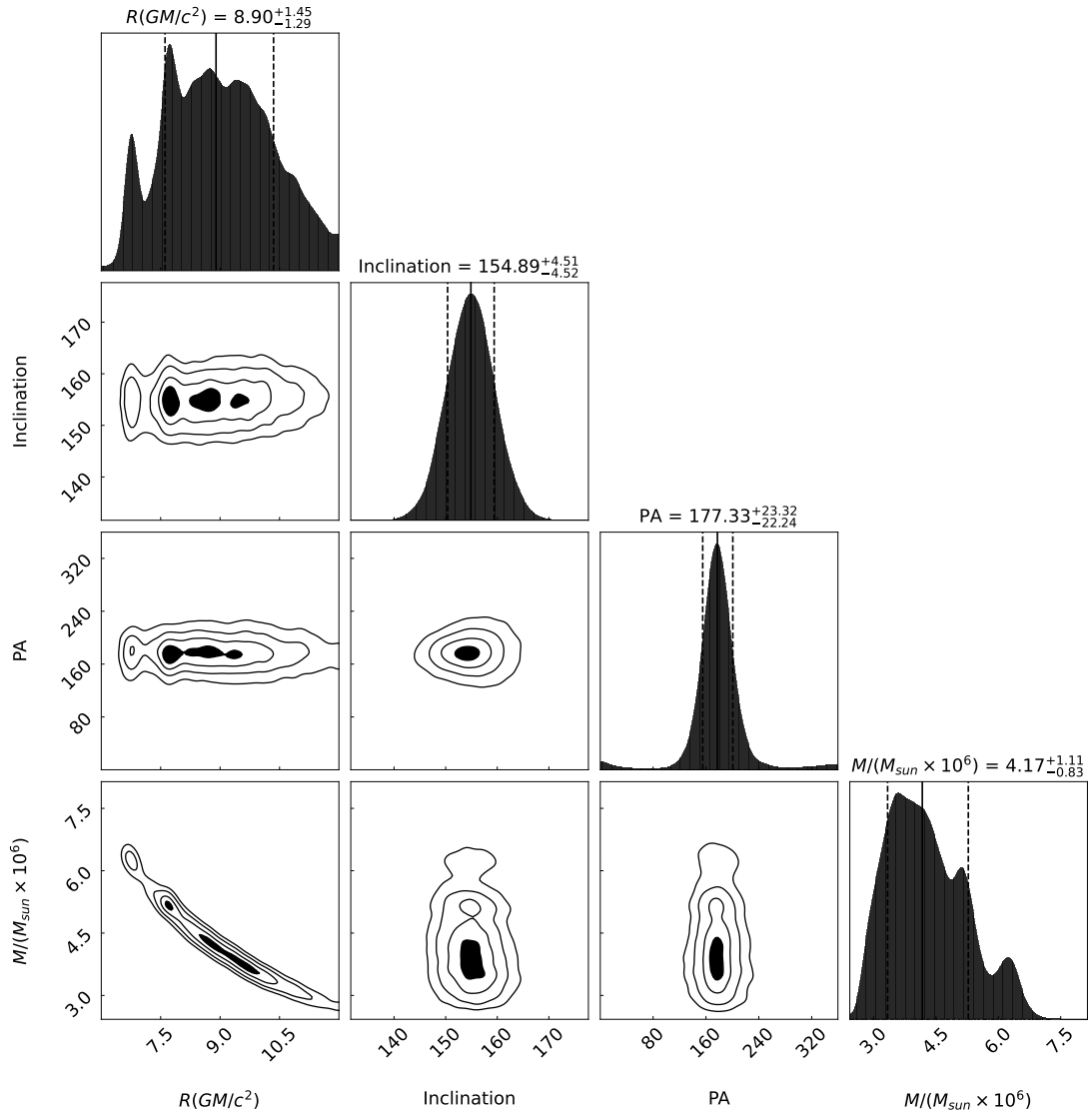

Figure 11: Two-dimensional posterior distributions of our combined fit with four free parameters: flare orbit radius, inclination, position angle, and enclosed mass. The posterior distribution of the radius parameter has multiple peaks, and hence the mean of the distribution is reported. There is a correlation between mass and radius, due to the strong period constraint in our data.

A3 Appendix: First light for GRAVITY Wide

A3.1 GRAVITY Wide data

Data from GRAVITY Wide prototype implementation

Here, we list the observations performed with the prototype implementation of GRAVITY Wide, i.e. no pupil relay, in the runs in November 2019 and March 2020.

Table 3: Observations with the GRAVITY Wide prototype implementation in November 2019 and March 2020.

SC	FT	Sep. [arcsec]	Date [UTC]	Pol.	Res.	Baseline Conf.	DIT [s]	NDIT
GJ 65B	GJ 65A	2.08	2019 Nov 01	S	MED	A0 G1 J2 K0	5.0	30
			2019 Nov 02	C	MED	A0 G1 J2 K0	0.3	300
HD 105913A	HD 105913B	5.11	2020 Mar 09	S	MED	U1 U2 U3 U4	1.0	128
HD 24071	HD 24072	8.16	2019 Nov 03	C	MED	A0 G1 J2 K0	5.0	16
HD 218268	HD 218269	8.83	2019 Nov 01	S	MED	A0 G1 J2 K0	1.0	32
			2019 Nov 02	C	MED	A0 G1 J2 K0	0.3	300
			2019 Nov 03	S	MED	A0 G1 J2 K0	1.0	64
			2019 Nov 03	C	MED	A0 G1 J2 K0	1.0	64
HD 10257	HD 10268	19.77	2019 Nov 01	S	MED	A0 G1 J2 K0	5.0	30
			2019 Nov 01	C	MED	A0 G1 J2 K0	0.13	500
			2019 Nov 02	C	MED	A0 G1 J2 K0	0.3	300
			2019 Nov 02	C	MED	A0 G1 J2 K0	1.0	64
			2019 Nov 02	C	MED	A0 G1 J2 K0	2.0	32
			2019 Nov 02	C	MED	A0 G1 J2 K0	5.0	32
			2019 Nov 02	C	MED	A0 G1 J2 K0	10.0	32
GJ1048B	HD 16270	12.06	2019 Nov 03	S	MED	A0 G1 J2 K0	10.0	32
LEDA 1264801	TYC 274-754-1	22.14	2020 Mar 04	S	MED	U1 U2 U3 U4	30.0	10
[VV96] J095516.0 -251732	2MASS 09551512 -2517108	23.93	2020 Mar 04	S	MED	U1 U2 U3 U4	30.0	10
QSO B0435-300	HD 29514	25.99	2019 Nov 01	C	MED	A0 G1 J2 K0	10.0	32
			2019 Nov 01	C	MED	A0 G1 J2 K0	30.0	16
TYC 8071-854-1	HD 26404	29.89	2019 Nov 02	C	MED	A0 G1 J2 K0	10.0	30
TCC 59	θ^1 Ori A	4.23	2019 Nov 02	C	MED	A0 G1 J2 K0	10.0	32
			2019 Nov 03	S	MED	A0 G1 J2 K0	10.0	16
θ^1 Ori E	θ^1 Ori A	4.51	2019 Nov 01	C	MED	A0 G1 J2 K0	5.0	32
			2019 Nov 02	C	MED	A0 G1 J2 K0	10.0	32
			2019 Nov 03	S	MED	A0 G1 J2 K0	10.0	16
θ^1 Ori F	θ^1 Ori C	4.52	2019 Nov 02	C	MED	A0 G1 J2 K0	10.0	32
			2019 Nov 03	S	MED	A0 G1 J2 K0	10.0	16
TCC 43	θ^1 Ori B	6.82	2019 Nov 02	C	MED	A0 G1 J2 K0	10.0	32
θ^1 Ori G	θ^1 Ori C	7.38	2019 Nov 02	C	MED	A0 G1 J2 K0	10.0	32
θ^1 Ori H	θ^1 Ori A	8.19	2019 Nov 02	C	MED	A0 G1 J2 K0	10.0	32
θ^1 Ori B	θ^1 Ori A	8.85	2019 Nov 01	C	MED	A0 G1 J2 K0	5.0	32
			2020 Mar 03	S	MED	A0 G1 J2 J3	10.0	16
			2020 Mar 03	S	MED	A0 G1 J2 J3	10.0	32
θ^1 Ori C	θ^1 Ori A	12.86	2019 Nov 01	C	MED	A0 G1 J2 K0	5.0	32
			2020 Mar 03	S	MED	A0 G1 J2 J3	10.0	32
θ^1 Ori D	θ^1 Ori C	13.41	2019 Nov 02	C	MED	A0 G1 J2 K0	10.0	32

Notes. The first block of SC–FT pairs are single and binary stars, the second block indicates a brown dwarf, three AGN, and a faint star with $m_K = 9.91$ (Cutri et al., 2003) (from top to bottom). Finally, the third block lists single and binary stars within the Orion Trapezium Cluster. Columns from left to right: name of the SC, name of the FT, separation (Sep.) between SC and FT in arcsec, date of observation night in UTC, polarization (Pol.) mode in combined (C) or split (S) linear polarization, resolution (Res.) in low (LOW), medium (MED) or high (HIGH), baseline configuration (Baseline Conf.), detector integration time (DIT) in seconds and number of DITs (NDIT).

Data from GRAVITY Wide commissioning

We list the observations during GRAVITY Wide commissioning in December 2021 and January 2022.

Table 4: Observations from GRAVITY Wide commissioning in December 2021, January 2022 and April 2022.

SC	FT	Sep. [arcsec]	Date [UTC]	Pol.	Res.	Baseline Conf.	DIT [s]	NDIT
HD 83368A	HD 83368B	3.28	2021 Dec 16	S	MED	A0 G1 J2 K0	10.0	12
			2021 Dec 16	C	MED	A0 G1 J2 K0	10.0	12
TYC6018-535-1	TYC6018-1742-1	3.91	2021 Dec 18	C	HIGH	U1 U2 U3 U4	1.0	200
			2021 Dec 19	C	HIGH	U1 U2 U3 U4	3.0	30
2MASS 09325130 -5548206	IRAS 09312-5534	4.83	2021 Dec 17	S	MED	A0 G1 J2 K0	30.0	4
HD 28255A	HD 28255B	5.52	2021 Dec 13	S	MED	A0 G1 J2 K0	10.0	12
SDSS J161513.84 +084914.4	2MASS 16151430 +0849167	7.50	2022 Apr 17	C	MED	U1 U2 U3 U4	100.0	6
HD 48543B	HD 48543A	7.90	2021 Dec 15	C	MED	A0 G1 J2 K0	10.0	12
			2021 Dec 15	S	MED	A0 G1 J2 K0	10.0	12
* f Eri A	* f Eri B	8.19	2021 Dec 16	S	MED	A0 G1 J2 K0	10.0	4
			2021 Dec 16	S	MED	A0 G1 J2 K0	10.0	12
			2021 Dec 16	S	MED	A0 G1 J2 K0	3.0	12
θ^1 Ori B	θ^1 Ori A	8.85	2021 Dec 15	S	MED	A0 G1 J2 K0	10.0	32
			2021 Dec 15	S	MED	A0 G1 J2 K0	30.0	12
HD 34750	HD 34749	10.65	2021 Dec 14	C	MED	A0 G1 J2 K0	30.0	4
* p Eri A	* p Eri B	11.46	2021 Dec 15	C	HIGH	A0 G1 J2 K0	3.0	32
* p Eri B	* p Eri A	11.46	2021 Dec 14	C	HIGH	A0 G1 J2 K0	10.0	16
			2021 Dec 14	S	MED	A0 G1 J2 K0	3.0	32
			2021 Dec 15	C	HIGH	A0 G1 J2 K0	3.0	32
θ^1 Ori C	θ^1 Ori A	12.85	2021 Dec 14	C	MED	A0 G1 J2 K0	10.0	32
LAMOST J092034.16 +065	Gaia 586750639 2466652	12.86	2021 Dec 18	S	MED	U1 U2 U3 U4	30.0	12
			2022 Jan 19	S	MED	U1 U2 U3 U4	30.0	12
			2022 Jan 25	S	MED	U1 U2 U3 U4	30.0	12
2MASS 05165352 -4811412 019	HD 34708	13.80	2021 Dec 14	S	MED	A0 G1 J2 K0	30.0	8
			2021 Dec 16	S	MED	A0 G1 J2 K0	30.0	12
			2021 Dec 16	S	MED	A0 G1 J2 K0	3.0	4
* gam01 Vol	* gam02 Vol	14.14	2021 Dec 13	S	HIGH	A0 G1 J2 K0	10.0	12
HD 10268	HD 10257	19.77	2021 Dec 14	S	MED	A0 G1 J2 K0	10.0	12
RMC 141	W61 7-8	21.58	2021 Dec 15	C	MED	A0 G1 J2 K0	30.0	12
PKS0435-300	HD 29514	25.99	2021 Dec 14	S	MED	A0 G1 J2 K0	30.0	12
			2021 Dec 15	C	MED	A0 G1 J2 K0	30.0	12
2MASS J07300800 -3939086	HD 59867	29.11	2021 Dec 15	S	MED	A0 G1 J2 K0	3.0	32
HD 42092	HD 42111	29.17	2021 Dec 15	S	MED	A0 G1 J2 K0	10.0	12
BAT99 113	W61 7-8	31.92	2021 Dec 15	S	LOW	A0 G1 J2 K0	30.0	12
			2021 Dec 15	C	MED	A0 G1 J2 K0	30.0	12

Notes. Columns from left to right: name of the SC, name of the FT, separation (Sep.) between SC and FT in arcsec, date of observation night in UTC, polarization (Pol.) mode in combined (C) or split (S) linear polarization, resolution (Res.) in low (LOW), medium (MED) or high (HIGH), baseline configuration (Baseline Conf.), detector integration time (DIT) in seconds and number of DITs (NDIT).

A3.2 Analysis of binary star systems

The analysis of binary star systems detailed in Sect. 5.3.2 proceeds in two steps. First, we use LITpro (Tallon-Bosc et al., 2007) to fit a binary model to our data. In the second step, we use `orbitize!` (Blunt et al., 2020) for θ^1 Ori B and θ^1 Ori C, and the fitting code from Gillessen et al. (2009) for θ^1 Ori D to determine orbital parameters from our separation measurements and measurements from the literature.

Binary Fitting with LITpro

For fitting a binary model to our data, we use the model fitting software LITpro which is based on the modified Levenberg–Marquardt Algorithm (Dennis and Schnable, 1983) and includes a Trust Region Method (Moré and Sorensen, 1983). It was developed by the Jean-Marie Mariotti Center (JMMC) [2], the french center for optical interferometry. LITpro uses the same OI Exchange format as the GRAVITY pipeline, thus we can directly upload our data and fit observables, such as squared visibilities, closure phases or visibility amplitudes.

We can choose the types of data to be fitted and take the interferometric observables visibility squared, visibility amplitude, or closure phase (or a combination of the three). The visibility squared for a binary model is.

$$\begin{aligned}\nu^2_{\text{binary}} &= \nu^*_{\text{binary}}\nu_{\text{binary}} \\ &= \frac{\nu_a^2 + f^2\nu_b^2 + 2f|\nu_a||\nu_b|\cos(2\pi(u\Delta\alpha + v\Delta\beta))}{(1+f)^2} \\ &= \frac{\nu_a^2 + f^2\nu_b^2 + 2f|\nu_a||\nu_b|\cos(2\pi\mathbf{B}\cdot\mathbf{s}_{\text{binary}}/\lambda)}{(1+f)^2}\ ,\end{aligned} \tag{23}$$

where ν_a and ν_b are the primary star and companion star's visibility, respectively, λ, is the wavelength, $f = f_b/f_a$, is the flux ratio between both stars, $\mathbf{B}$, is the baseline and $\mathbf{s}_{\text{binary}} \equiv (\Delta\alpha, \Delta\beta)$ is the position of the companion star with respect to the primary star in dRA and dDEC.

The closure phase is determined by taking the argument from the *bispectrum*

$$\begin{aligned}B_{123} &= \nu_{12}^{measured}\nu_{23}^{measured}\nu_{31}^{measured} \\ &= |F_1|\ |F_2|e^{i(\Phi_1-\Phi_2)}\nu_{12}^{true}\cdot|F_2|\ |F_3|e^{i(\Phi_2-\Phi_3)}\nu_{23}^{true}\cdot \\ &\quad |F_3|\ |F_1|e^{i(\Phi_3-\Phi_1)}\nu_{31}^{true} \\ &= |F_1|^2\ |F_2|^2\ |F_3|^2\ \nu_{12}^{true}\cdot\nu_{23}^{true}\cdot\nu_{31}^{true}\ ,\end{aligned} \tag{24}$$

between three telescopes 1,2 and 3:

$$\phi_{1-2-3} = \arg(\nu_{\text{binary,1-2}}\ \nu_{\text{binary,2-3}}\ \nu_{\text{binary,3-1}})\ , \tag{25}$$

where ν_{binary} is computed with Eq. (23).

[2] Available at `https://www.jmmc.fr/english/tools/data-analysis/litpro/`

From Eqs. (23) and (25), the parameters $\Delta\alpha$ and $\Delta\beta$ give the distance from the primary star located at (dRA, dDec) = (0, 0) mas to the companion star, and are together with the flux ratio, f, and a background, $f_{\text{background}}$, the parameters to be fitted. The latter variable represents the effect of visibility loss from atmospheric turbulence. We give a starting value for the companion star position, and let LITpro's fitting engine iteratively find the minimum χ^2 value. At the end of the fitting procedure, we obtain the final χ^2, values and standard deviations for the fitted parameters, and covariance and correlation matrices for outlining possible parameter degeneracies.

Orbit modeling with `orbitize!`

`orbitize!` is an open-source Python package for orbit fitting of directly imaged exoplanets, which can also be applied to binary star systems. `orbitize!` is comprised of a parallel-tempered Affine-invariant Markov Chain Monte Carlo (MCMC) algorithm (Vousden et al., 2016; Foreman-Mackey et al., 2013), and is based on Bayesian statistics. In `orbitize!` the input data used in the orbit-fitting includes the date of the observation in MJD, and the dRA and dDec offsets from the primary star at (0,0) mas with corresponding uncertainties of the secondary star in mas. The posterior distribution over the orbital parameters are then computed using Bayes' theorem.

The MCMC algorithm in `orbitize!` represents an efficient sampling method to explore the likelihood over a multidimensional parameter space and to determine expectation values of the model parameters, i.e. the orbital parameters. Further, it is possible to use several Markov chains, called "walkers," in parallel to fully explore the parameter space at different "temperatures". A higher temperature helps the walkers not to become stuck in regions of local minima. A larger number of walkers increases the samples used, but also increases the computation time.

We use 20 temperatures, 1000 walkers, and 1 million steps to ensure convergence. Further, we impose a Gaussian prior on the measurement for the mass, and we use the parallax of 2.415 ± 0.040 mas from Menten et al. (2007), which is fixed in our analysis. If we have an initial guess for best-fit orbital parameters, for example from the literature, we use lower and upper bounds of a uniform prior around this value. This was done for the orbit of θ^1 Ori C (see Sect. 5.3.2), where we set bounds around orbital parameters that were already determined in the literature (GRAVITY Collaboration et al., 2018c). In the case of θ^1 Ori B (see Sect. 5.3.2), there are no previously determined orbital parameters, and therefore we let `orbitize!` find the best-fit orbit without giving an initial guess.

Bibliography

Abuter, R. et al. (Mar. 2024). "A dynamical measure of the black hole mass in a quasar 11 billion years ago". In: *Nature* 627.8003, pp. 281–285. DOI: 10.1038/s41586-024-07053-4. arXiv: 2401.14567 [astro-ph.GA].

Aimar, N. et al. (Apr. 2023). "Magnetic reconnection plasmoid model for Sagittarius A* flares". In: *Astronomy & Astrophysics* 672, A62, A62. DOI: 10.1051/0004-6361/202244936. arXiv: 2301.11874 [astro-ph.HE].

Allen, David A., Hyland, A. R., and Hillier, D. J. (June 1990). "The source of luminosity at the Galactic Centre." In: *Monthly Notice of the Royal Astronomical Society* 244, p. 706.

Amaro Seoane, Pau, Lin, Yiren, and Tzanavaris, Kostas (Sept. 2024). "Mono- and oligochromatic extreme-mass-ratio inspirals". In: *Physical Review D* 110.6, 064011, p. 064011. DOI: 10.1103/PhysRevD.110.064011. arXiv: 2403.12134 [astro-ph.CO].

Amorim, A. et al. (Mar. 2019). "Test of the Einstein Equivalence Principle near the Galactic Center Supermassive Black Hole". In: *Phys. Rev. Lett.* 122.10, 101102, p. 101102. DOI: 10.1103/PhysRevLett.122.101102. arXiv: 1902.04193 [astro-ph.GA].

Amorim, Antonio et al. (July 2012). "The final design of the GRAVITY acquisition camera and associated VLTI beam monitoring strategy". In: *Optical and Infrared Interferometry III*. Ed. by Françoise Delplancke, Jayadev K. Rajagopal, and Fabien Malbet. Vol. 8445. Society of Photo-Optical Instrumentation Engineers (SPIE) Conference Series, 844534, p. 844534. DOI: 10.1117/12.925993.

Argüelles, C. R., Krut, A., Rueda, J. A., and Ruffini, R. (Jan. 2019). "Can fermionic dark matter mimic supermassive black holes?" In: *International Journal of Modern Physics D* 28.14, 1943003, p. 1943003. DOI: 10.1142/S021827181943003X. arXiv: 1905.09776 [astro-ph.GA].

Arras, Philipp, Frank, Philipp, Leike, Reimar, Westermann, Rüdiger, and Enßlin, Torsten A. (July 2019a). "Unified radio interferometric calibration and imaging with joint uncertainty quantification". In: *Astronomy & Astrophysics* 627, A134, A134. DOI: 10.1051/0004-6361/201935555. arXiv: 1903.11169 [astro-ph.IM].

Arras, Philipp, Knollrnüller, Jakob, Junklewitz, Henrik, and Enßlin, Torsten A. (2018). "Radio Imaging with Information Field Theory". In: *2018 26th European Signal Processing Conference (EUSIPCO)*, pp. 2683–2687. DOI: 10.23919/EUSIPCO.2018.8553533.

Arras, Philipp, Reinecke, Martin, Westermann, Rüdiger, and Enßin, Torsten A. (Feb. 2021a). "Efficient wide-field radio interferometry response". In: *Astronomy & Astro-*

physics 646, A58, A58. DOI: 10.1051/0004-6361/202039723. arXiv: 2010.10122 [astro-ph.IM].

Arras, Philipp et al. (Mar. 2019b). *NIFTy5: Numerical Information Field Theory v5*. ascl: 1903.008.

Arras, Philipp et al. (Feb. 2020). "M87* in space, time, and frequency". In: *arXiv e-prints*, arXiv:2002.05218, arXiv:2002.05218. arXiv: 2002.05218 [astro-ph.IM].

Arras, Philipp et al. (Feb. 2021b). "Comparison of classical and Bayesian imaging in radio interferometry. Cygnus A with CLEAN and resolve". In: *Astronomy & Astrophysics* 646, A84, A84. DOI: 10.1051/0004-6361/202039258.

Arsenault, Robin et al. (Feb. 2003). "MACAO-VLTI: An Adaptive Optics system for the ESO VLT interferometer". In: *Adaptive Optical System Technologies II*. Ed. by Peter L. Wizinowich and Domenico Bonaccini. Vol. 4839. Society of Photo-Optical Instrumentation Engineers (SPIE) Conference Series, pp. 174–185. DOI: 10.1117/12.458836.

Baganoff, F. K. et al. (Sept. 2001). "Rapid X-ray flaring from the direction of the supermassive black hole at the Galactic Centre". In: *Nature* 413.6851, pp. 45–48. DOI: 10.1038/35092510. arXiv: astro-ph/0109367 [astro-ph].

Baganoff, F. K. et al. (July 2003). "Chandra X-Ray Spectroscopic Imaging of Sagittarius A* and the Central Parsec of the Galaxy". In: *ApJ* 591.2, pp. 891–915. DOI: 10.1086/375145. arXiv: astro-ph/0102151 [astro-ph].

Balick, B. and Brown, R. L. (Dec. 1974). "Intense sub-arcsecond structure in the galactic center." In: *ApJ* 194, pp. 265–270. DOI: 10.1086/153242.

Baron, Fabien, Monnier, John D., and Kloppenborg, Brian (July 2010). "A novel image reconstruction software for optical/infrared interferometry". In: *Optical and Infrared Interferometry II*. Ed. by William C. Danchi, Françoise Delplancke, and Jayadev K. Rajagopal. Vol. 7734. Society of Photo-Optical Instrumentation Engineers (SPIE) Conference Series, 77342I, p. 77342I. DOI: 10.1117/12.857364.

Bartko, H. et al. (June 2009). "Evidence for Warped Disks of Young Stars in the Galactic Center". In: *ApJ* 697.2, pp. 1741–1763. DOI: 10.1088/0004-637X/697/2/1741. arXiv: 0811.3903 [astro-ph].

Bartko, H. et al. (Jan. 2010). "An Extremely Top-Heavy Initial Mass Function in the Galactic Center Stellar Disks". In: *ApJ* 708.1, pp. 834–840. DOI: 10.1088/0004-637X/708/1/834. arXiv: 0908.2177 [astro-ph.GA].

Becerra-Vergara, E. A., Argüelles, C. R., Krut, A., Rueda, J. A., and Ruffini, R. (Sept. 2020). "Geodesic motion of S2 and G2 as a test of the fermionic dark matter nature of our Galactic core". In: *Astronomy & Astrophysics* 641, A34, A34. DOI: 10.1051/0004-6361/201935990. arXiv: 2007.11478 [astro-ph.GA].

Beckers, J. M. (June 1990). "Planning the VLT interferometer." In: *The Messenger* 60, pp. 1–9.

Becklin, E. E., Gatley, I., and Werner, M. W. (July 1982). "Far-infrared observations of Sagittarius A - The luminosity and dust density in the central parsec of the Galaxy". In: *ApJ* 258, pp. 135–142. DOI: 10.1086/160060.

Becklin, E. E., Matthews, K., Neugebauer, G., and Willner, S. P. (Jan. 1978). "Infrared observations of the galactic center. I. Nature of the compact sources." In: *ApJ* 219, pp. 121–128. DOI: 10.1086/155761.

Becklin, E. E. and Neugebauer, G. (Jan. 1968). "Infrared Observations of the Galactic Center". In: *ApJ* 151, p. 145. DOI: 10.1086/149425.

Becklin, E. E. and Neugebauer, G. (Sept. 1975). "High-resolution maps of the galactic center at 2.2 and 10 microns." In: *The Astrophysical Journal Letters* 200, pp. L71–L74. DOI: 10.1086/181899.

Berdeu, Anthony et al. (Aug. 2024). "Simplified model(s) of the GRAVITY+ adaptive optics system(s) for performance prediction". In: *Adaptive Optics Systems IX*. Ed. by Kathryn J. Jackson, Dirk Schmidt, and Elise Vernet. Vol. 13097. Society of Photo-Optical Instrumentation Engineers (SPIE) Conference Series, 130976G, 130976G. DOI: 10.1117/12.3019865. arXiv: 2410.08563 [astro-ph.IM].

Bhatnagar, S., Cornwell, T. J., Golap, K., and Uson, J. M. (Aug. 2008). "Correcting direction-dependent gains in the deconvolution of radio interferometric images". In: *Astronomy & Astrophysics* 487.1, pp. 419–429. DOI: 10.1051/0004-6361:20079284. arXiv: 0805.0834 [astro-ph].

Blackburn, Lindy et al. (May 2020). "Closure Statistics in Interferometric Data". In: *ApJ* 894.1, 31, p. 31. DOI: 10.3847/1538-4357/ab8469. arXiv: 1910.02062 [astro-ph.IM].

Blum, R. D., Depoy, D. L., and Sellgren, K. (Mar. 1995). "A Comparison of Near-Infrared Spectra of the Galactic Center Compact He i Emission-Line Sources and Early-Type Mass-losing Stars". In: *ApJ* 441, p. 603. DOI: 10.1086/175386.

Blunt, Sarah et al. (Mar. 2020). "orbitize!: A Comprehensive Orbit-fitting Software Package for the High-contrast Imaging Community". In: *The Astronomical Journal* 159.3, 89, p. 89. DOI: 10.3847/1538-3881/ab6663. arXiv: 1910.01756 [astro-ph.EP].

Bonnell, I. A. and Rice, W. K. M. (Aug. 2008). "Star Formation Around Supermassive Black Holes". In: *Science* 321.5892, p. 1060. DOI: 10.1126/science.1160653. arXiv: 0810.2723 [astro-ph].

Booth, Michael Tucker et al. (2024). "Infrastructure upgrade of Antu, Kueyen, and Melipal for the implementation of laser guide stars for the GRAVITY+ project". In: *Ground-based and Airborne Instrumentation for Astronomy X*. Ed. by Julia J. Bryant, Kentaro Motohara, and Joël R. D. Vernet. Vol. 13096. International Society for Optics and Photonics. SPIE, 130969A. DOI: 10.1117/12.3020005. URL: https://doi.org/10.1117/12.3020005.

Boskri, Abdelkarim et al. (Sept. 2021). "Potential and sky coverage for off-axis fringe tracking in optical long baseline interferometry". In: *Monthly Notice of the Royal Astronomical Society* 506.1, pp. 1364–1388. DOI: 10.1093/mnras/stab1505. arXiv: 2107.04729 [astro-ph.IM].

Bourdarot, G. et al. (Sept. 2024). "GRAVITY+ Wavefront Sensors: High-Contrast, Laser Guide Star, Adaptive Optics systems for the VLTI". In: *arXiv e-prints*, arXiv:2409.08438, arXiv:2409.08438. DOI: 10.48550/arXiv.2409.08438. arXiv: 2409.08438 [astro-ph.IM].

Bower, Geoffrey C. et al. (Aug. 2019). "ALMA Observations of the Terahertz Spectrum of Sagittarius A*". In: *The Astrophysical Journal Letters* 881.1, L2, p. L2. DOI: 10.3847/2041-8213/ab3397. arXiv: 1907.08319 [astro-ph.HE].

Briggs, Daniel S., Schwab, Frederic R., and Sramek, Richard A. (Jan. 1999). "Imaging". In: *Synthesis Imaging in Radio Astronomy II*. Ed. by G. B. Taylor, C. L. Carilli, and R. A. Perley. Vol. 180. Astronomical Society of the Pacific Conference Series, p. 127.

Broderick, A. E. and Loeb, A. (Apr. 2006). "Imaging optically-thin hotspots near the black hole horizon of Sgr A* at radio and near-infrared wavelengths". In: *Monthly Notice of the Royal Astronomical Society* 367.3, pp. 905–916. DOI: 10.1111/j.1365-2966.2006.10152.x. arXiv: astro-ph/0509237 [astro-ph].

Broderick, Avery E. and Loeb, Abraham (Oct. 2005). "Imaging bright-spots in the accretion flow near the black hole horizon of Sgr A*". In: *Monthly Notice of the Royal Astronomical Society* 363.2, pp. 353–362. DOI: 10.1111/j.1365-2966.2005.09458.x. arXiv: astro-ph/0506433 [astro-ph].

Brown, R. L. and Lo, K. Y. (Feb. 1982). "Variability of the compact radio source at the Galactic Center." In: *ApJ* 253, pp. 108–114. DOI: 10.1086/159615.

Buscher, David F. and Longair, Foreword by Malcolm (July 2015). *Practical Optical Interferometry*. Cambridge, UK: Cambridge University Press.

Christopher, M. H., Scoville, N. Z., Stolovy, S. R., and Yun, Min S. (Mar. 2005). "HCN and HCO^+ Observations of the Galactic Circumnuclear Disk". In: *ApJ* 622.1, pp. 346–365. DOI: 10.1086/427911. arXiv: astro-ph/0502532 [astro-ph].

Colavita, M. M. et al. (Jan. 1999). "The Palomar Testbed Interferometer". In: *ApJ* 510.1, pp. 505–521. DOI: 10.1086/306579. arXiv: astro-ph/9810262 [astro-ph].

Colavita, M. M. et al. (Oct. 2013). "The Keck Interferometer". In: *PASP* 125.932, p. 1226. DOI: 10.1086/673475.

Crawford, M. K. et al. (June 1985). "Mass distribution in the galactic centre". In: *Nature* 315.6019, pp. 467–470. DOI: 10.1038/315467a0.

Cutri, R. M. et al. (June 2003). "VizieR Online Data Catalog: 2MASS All-Sky Catalog of Point Sources (Cutri+ 2003)". In: *VizieR Online Data Catalog*, II/246, pp. II/246.

Davies, R. et al. (July 2018). "The MICADO first light imager for the ELT: overview, operation, simulation". In: *Ground-based and Airborne Instrumentation for Astronomy VII*. Ed. by Christopher J. Evans, Luc Simard, and Hideki Takami. Vol. 10702. Society of Photo-Optical Instrumentation Engineers (SPIE) Conference Series, 107021S, 107021S. DOI: 10.1117/12.2311483. arXiv: 1807.10003 [astro-ph.IM].

Davies, R. et al. (June 2023). "The Enhanced Resolution Imager and Spectrograph for the VLT". In: *Astronomy & Astrophysics* 674, A207, A207. DOI: 10.1051/0004-6361/202346559. arXiv: 2304.02343 [astro-ph.IM].

Delplancke, F. et al. (Oct. 2004). "Star separator system for the dual-field capability (PRIMA) of the VLTI". In: *New Frontiers in Stellar Interferometry*. Ed. by Wesley A. Traub. Vol. 5491. Society of Photo-Optical Instrumentation Engineers (SPIE) Conference Series, p. 1528. DOI: 10.1117/12.551873.

Delplancke, Françoise (June 2008). "The PRIMA facility phase-referenced imaging and micro-arcsecond astrometry". In: *New A Rev.* 52.2-5, pp. 199–207. DOI: 10.1016/j.newar.2008.04.016.

Dennis, J. E. and Schnable, Robert B. (1983). *Numerical methods for unconstrained optimization and nonlinear equations*. U.S.: Society for Industrial & Applied Mathematics.

Dexter, J. et al. (Oct. 2020). "Sgr A* near-infrared flares from reconnection events in a magnetically arrested disc". In: *Monthly Notice of the Royal Astronomical Society* 497.4, pp. 4999–5007. DOI: 10.1093/mnras/staa2288. arXiv: 2006.03657 [astro-ph.HE].

Do, T. et al. (Feb. 2009). "A Near-Infrared Variability Study of the Galactic Black Hole: A Red Noise Source with NO Detected Periodicity". In: *ApJ* 691.2, pp. 1021–1034. DOI: 10.1088/0004-637X/691/2/1021. arXiv: 0810.0446 [astro-ph].

Do, T. et al. (Feb. 2013). "Stellar Populations in the Central 0.5 pc of the Galaxy. I. A New Method for Constructing Luminosity Functions and Surface-density Profiles". In: *ApJ* 764.2, 154, p. 154. DOI: 10.1088/0004-637X/764/2/154. arXiv: 1301.0539 [astro-ph.SR].

Do, Tuan et al. (Aug. 2019a). "Relativistic redshift of the star S0-2 orbiting the Galactic Center supermassive black hole". In: *Science* 365.6454, pp. 664–668. DOI: 10.1126/science.aav8137. arXiv: 1907.10731 [astro-ph.GA].

Do, Tuan et al. (Sept. 2019b). "Unprecedented Near-infrared Brightness and Variability of Sgr A*". In: *The Astrophysical Journal Letters* 882.2, L27, p. L27. DOI: 10.3847/2041-8213/ab38c3. arXiv: 1908.01777 [astro-ph.GA].

Dodds-Eden, K. et al. (June 2009). "Evidence for X-Ray Synchrotron Emission from Simultaneous Mid-Infrared to X-Ray Observations of a Strong Sgr A* Flare". In: *ApJ* 698.1, pp. 676–692. DOI: 10.1088/0004-637X/698/1/676. arXiv: 0903.3416 [astro-ph.GA].

Dodds-Eden, K. et al. (Feb. 2011). "The Two States of Sgr A* in the Near-infrared: Bright Episodic Flares on Top of Low-level Continuous Variability". In: *ApJ* 728.1, 37, p. 37. DOI: 10.1088/0004-637X/728/1/37. arXiv: 1008.1984 [astro-ph.GA].

Dodds-Eden, Katie et al. (Dec. 2010). "Time-Dependent Models of Flares from Sagittarius A*". In: *ApJ* 725.1, pp. 450–465. DOI: 10.1088/0004-637X/725/1/450. arXiv: 1005.0389 [astro-ph.GA].

Doeleman, Sheperd S. et al. (Sept. 2008). "Event-horizon-scale structure in the supermassive black hole candidate at the Galactic Centre". In: *Nature* 455.7209, pp. 78–80. DOI: 10.1038/nature07245. arXiv: 0809.2442 [astro-ph].

Dong, Subo et al. (Jan. 2019). "First Resolution of Microlensed Images". In: *ApJ* 871.1, 70, p. 70. DOI: 10.3847/1538-4357/aaeffb. arXiv: 1809.08243 [astro-ph.SR].

Drescher, Antonia et al. (Aug. 2022). "GRAVITY+ Wide: towards hundreds of z 2 AGN". In: *Optical and Infrared Interferometry and Imaging VIII*. Ed. by Antoine Mérand, Stephanie Sallum, and Joel Sanchez-Bermudez. Vol. 12183. Society of Photo-Optical Instrumentation Engineers (SPIE) Conference Series, 121830T, 121830T. DOI: 10.1117/12.2628921. arXiv: 2209.11602 [astro-ph.IM].

Dutt, A. and Rokhlin, V. (1993). "Fast Fourier Transforms for Nonequispaced Data". In: *SIAM Journal on Scientific Computing* 14.6, pp. 1368–1393.

Eatough, R. P. et al. (Sept. 2013). "A strong magnetic field around the supermassive black hole at the centre of the Galaxy". In: *Nature* 501.7467, pp. 391–394. DOI: 10.1038/nature12499. arXiv: 1308.3147 [astro-ph.GA].

Eckart, A. and Genzel, R. (Oct. 1996). "Observations of stellar proper motions near the Galactic Centre". In: *Nature* 383.6599, pp. 415–417. DOI: 10.1038/383415a0.

Eckart, A. and Genzel, R. (Jan. 1997). "Stellar proper motions in the central 0.1 PC of the Galaxy". In: *Monthly Notice of the Royal Astronomical Society* 284.3, pp. 576–598. DOI: 10.1093/mnras/284.3.576.

Eckart, A. et al. (Aug. 2006a). "Polarimetry of near-infrared flares from Sagittarius A*". In: *Astronomy & Astrophysics* 455.1, pp. 1–10. DOI: 10.1051/0004-6361:20064948. arXiv: astro-ph/0610103 [astro-ph].

Eckart, A. et al. (May 2006b). "The flare activity of Sagittarius A*. New coordinated mm to X-ray observations". In: *Astronomy & Astrophysics* 450.2, pp. 535–555. DOI: 10.1051/0004-6361:20054418. arXiv: astro-ph/0512440 [astro-ph].

Eckart, A. et al. (Mar. 2008a). "Polarized NIR and X-ray flares from Sagittarius A*". In: *Astronomy & Astrophysics* 479.3, pp. 625–639. DOI: 10.1051/0004-6361:20078793. arXiv: 0712.3165 [astro-ph].

Eckart, A. et al. (Dec. 2008b). "Simultaneous NIR/sub-mm observation of flare emission from Sagittarius A*". In: *Astronomy & Astrophysics* 492.2, pp. 337–344. DOI: 10.1051/0004-6361:200810924. arXiv: 0811.2753 [astro-ph].

Einstein, A. (Jan. 1916). "Die Grundlage der allgemeinen Relativitätstheorie". In: *Annalen der Physik* 354.7, pp. 769–822. DOI: 10.1002/andp.19163540702.

Eisenhauer, F. et al. (July 2005). "SINFONI in the Galactic Center: Young Stars and Infrared Flares in the Central Light-Month". In: *ApJ* 628.1, pp. 246–259. DOI: 10.1086/430667. arXiv: astro-ph/0502129 [astro-ph].

Eisenhauer, Frank (July 2019). "GRAVITY+: Towards faint science". In: *The Very Large Telescope in 2030*, 30, p. 30. DOI: 10.5281/zenodo.3356274. URL: https://www.mpe.mpg.de/7480772/GRAVITYplus_WhitePaper.pdf.

Eisenhauer, Frank et al. (Mar. 2003). "SINFONI - Integral field spectroscopy at 50 milliarcsecond resolution with the ESO VLT". In: *Instrument Design and Performance for Optical/Infrared Ground-based Telescopes*. Ed. by Masanori Iye and Alan F. M. Moorwood. Vol. 4841. Society of Photo-Optical Instrumentation Engineers (SPIE) Conference Series, pp. 1548–1561. DOI: 10.1117/12.459468. arXiv: astro-ph/0306191 [astro-ph].

Elhalkouj, T. et al. (Jan. 2008). "Isopistonic angle for multi-aperture interferometers from isoplanatic angle". In: *A&A* 477.1, pp. 337–344. DOI: 10.1051/0004-6361:20078173.

Enßlin, Torsten A. (Mar. 2019). "Information Theory: Information Theory for Fields (Ann. Phys. 3/2019)". In: *Annalen der Physik* 531.3, p. 1970017. DOI: 10.1002/andp.201970017.

Esposito, Simone, Riccardi, Armando, and Femenía, Bruno (Jan. 2000). "Differential piston angular anisoplanatism for astronomical optical interferometers". In: *A&A* 353, pp. L29–L32.

Event Horizon Telescope Collaboration et al. (May 2022). "First Sagittarius A* Event Horizon Telescope Results. I. The Shadow of the Supermassive Black Hole in the Center of the Milky Way". In: *The Astrophysical Journal Letters* 930.2, L12, p. L12. DOI: 10.3847/2041-8213/ac6674.

Fabricius, Maximilian et al. (Aug. 2024). "GRAVITY+ Wide: towards hundreds of z ∼ 2 AGN, larger throughput and improved vibrational control". In: *Optical and Infrared Interferometry and Imaging IX*. Ed. by Jens Kammerer, Stephanie Sallum, and Joel Sanchez-Bermudez. Vol. 13095. Society of Photo-Optical Instrumentation Engineers (SPIE) Conference Series, 130950B, 130950B. DOI: 10.1117/12.3019984.

Falcke, Heino et al. (May 1998). "The Simultaneous Spectrum of Sagittarius A* from 20 Centimeters to 1 Millimeter and the Nature of the Millimeter Excess". In: *ApJ* 499.2, pp. 731–734. DOI: 10.1086/305687. arXiv: astro-ph/9801085 [astro-ph].

Finger, G. et al. (July 2019). "On-sky performance verification of near infrared eAPD technology for wavefront sensing at ground based telescopes, demonstration of e-APD pixel performance to improve the sensitivity of large science focal planes and possibility to use this technology in space". In: *International Conference on Space Optics — ICSO 2018*. Vol. 11180. Society of Photo-Optical Instrumentation Engineers (SPIE) Conference Series, 111806L, p. 111806L. DOI: 10.1117/12.2536156.

Foreman-Mackey, Daniel, Hogg, David W., Lang, Dustin, and Goodman, Jonathan (Mar. 2013). "emcee: The MCMC Hammer". In: *Publications of the Astronomical Society of the Pacific* 125.925, p. 306. DOI: 10.1086/670067. arXiv: 1202.3665 [astro-ph.IM].

Fried, D. L. (Oct. 1966). "Optical Resolution Through a Randomly Inhomogeneous Medium for Very Long and Very Short Exposures". In: *Journal of the Optical Society of America (1917-1983)* 56.10, p. 1372.

Fried, David L. (1982). "Anisoplanatism in adaptive optics". In: *J. Opt. Soc. Am.* 72.1, pp. 52–61. DOI: 10.1364/JOSA.72.000052. URL: https://opg.optica.org/abstract.cfm?URI=josa-72-1-52.

GRAVITY Collaboration et al. (June 2017). "First light for GRAVITY: Phase referencing optical interferometry for the Very Large Telescope Interferometer". In: *Astronomy & Astrophysics* 602, A94, A94. DOI: 10.1051/0004-6361/201730838. arXiv: 1705.02345 [astro-ph.IM].

GRAVITY Collaboration et al. (Oct. 2018a). "Detection of orbital motions near the last stable circular orbit of the massive black hole SgrA*". In: *Astronomy & Astrophysics* 618, L10, p. L10. DOI: 10.1051/0004-6361/201834294. arXiv: 1810.12641 [astro-ph.GA].

GRAVITY Collaboration et al. (July 2018b). "Detection of the gravitational redshift in the orbit of the star S2 near the Galactic centre massive black hole". In: *Astronomy & Astrophysics* 615, L15, p. L15. DOI: 10.1051/0004-6361/201833718. arXiv: 1807.09409 [astro-ph.GA].

GRAVITY Collaboration et al. (Dec. 2018c). "Multiple star systems in the Orion nebula". In: *Astronomy & Astrophysics* 620, A116, A116. DOI: 10.1051/0004-6361/201833575. arXiv: 1809.10376 [astro-ph.SR].

GRAVITY Collaboration et al. (Nov. 2018d). "Spatially resolved rotation of the broad-line region of a quasar at sub-parsec scale". In: *Nature* 563.7733, pp. 657–660. DOI: 10.1038/s41586-018-0731-9. arXiv: 1811.11195 [astro-ph.GA].

GRAVITY Collaboration et al. (May 2019a). "A geometric distance measurement to the Galactic center black hole with 0.3% uncertainty". In: *Astronomy & Astrophysics* 625, L10, p. L10. DOI: 10.1051/0004-6361/201935656. arXiv: 1904.05721 [astro-ph.GA].

GRAVITY Collaboration et al. (Mar. 2019b). "First direct detection of an exoplanet by optical interferometry. Astrometry and K-band spectroscopy of HR 8799 e". In: *Astronomy & Astrophysics* 623, L11, p. L11. DOI: 10.1051/0004-6361/201935253. arXiv: 1903.11903 [astro-ph.EP].

GRAVITY Collaboration et al. (Dec. 2019c). "The GRAVITY Young Stellar Object survey. I. Probing the disks of Herbig Ae/Be stars in terrestrial orbits". In: *Astronomy & Astrophysics* 632, A53, A53. DOI: 10.1051/0004-6361/201936403. arXiv: 1911.00611 [astro-ph.SR].

GRAVITY Collaboration et al. (Aug. 2020a). "A measure of the size of the magnetospheric accretion region in TW Hydrae". In: *Nature* 584.7822, pp. 547–550. DOI: 10.1038/s41586-020-2613-1. arXiv: 2104.06441 [astro-ph.SR].

GRAVITY Collaboration et al. (Feb. 2020b). "An image of the dust sublimation region in the nucleus of NGC 1068". In: *Astronomy & Astrophysics* 634, A1, A1. DOI: 10.1051/0004-6361/201936255. arXiv: 1912.01361 [astro-ph.GA].

GRAVITY Collaboration et al. (Apr. 2020c). "Detection of the Schwarzschild precession in the orbit of the star S2 near the Galactic centre massive black hole". In: *Astronomy & Astrophysics* 636, L5, p. L5. DOI: 10.1051/0004-6361/202037813. arXiv: 2004.07187 [astro-ph.GA].

GRAVITY Collaboration et al. (Nov. 2020d). "Dynamically important magnetic fields near the event horizon of Sgr A*". In: *Astronomy & Astrophysics* 643, A56, A56. DOI: 10.1051/0004-6361/202038283. arXiv: 2009.01859 [astro-ph.HE].

GRAVITY Collaboration et al. (Mar. 2020e). "Modeling the orbital motion of Sgr A*'s near-infrared flares". In: *Astronomy & Astrophysics* 635, A143, A143. DOI: 10.1051/0004-6361/201937233. arXiv: 2002.08374 [astro-ph.HE].

GRAVITY Collaboration et al. (Jan. 2020f). "Peering into the formation history of β Pictoris b with VLTI/GRAVITY long-baseline interferometry". In: *Astronomy & Astrophysics* 633, A110, A110. DOI: 10.1051/0004-6361/201936898. arXiv: 1912.04651 [astro-ph.EP].

GRAVITY Collaboration et al. (June 2020g). "The flux distribution of Sgr A*". In: *Astronomy & Astrophysics* 638, A2, A2. DOI: 10.1051/0004-6361/202037717. arXiv: 2004.07185 [astro-ph.GA].

GRAVITY Collaboration et al. (Mar. 2020h). "The resolved size and structure of hot dust in the immediate vicinity of AGN". In: *Astronomy & Astrophysics* 635, A92, A92. DOI: 10.1051/0004-6361/201936767. arXiv: 1910.00593 [astro-ph.GA].

GRAVITY Collaboration et al. (Nov. 2020i). "The spatially resolved broad line region of IRAS 09149-6206". In: *Astronomy & Astrophysics* 643, A154, A154. DOI: 10.1051/0004-6361/202039067. arXiv: 2009.08463 [astro-ph.GA].

GRAVITY Collaboration et al. (Oct. 2021a). "Constraining particle acceleration in Sgr A* with simultaneous GRAVITY, Spitzer, NuSTAR, and Chandra observations". In: *Astronomy & Astrophysics* 654, A22, A22. DOI: 10.1051/0004-6361/202140981. arXiv: 2107.01096 [astro-ph.HE].

GRAVITY Collaboration et al. (Jan. 2021b). "Detection of faint stars near Sagittarius A* with GRAVITY". In: *A&A* 645, A127, A127. DOI: 10.1051/0004-6361/202039544. arXiv: 2011.03058 [astro-ph.GA].

GRAVITY Collaboration et al. (Mar. 2021c). "Improved GRAVITY astrometric accuracy from modeling optical aberrations". In: *Astronomy & Astrophysics* 647, A59, A59. DOI: 10.1051/0004-6361/202040208. arXiv: 2101.12098 [astro-ph.GA].

GRAVITY Collaboration et al. (Jan. 2021d). "The GRAVITY young stellar object survey. IV. The CO overtone emission in 51 Oph at sub-au scales". In: *Astronomy & Astrophysics* 645, A50, A50. DOI: 10.1051/0004-6361/202038000. arXiv: 2011.05955 [astro-ph.SR].

GRAVITY Collaboration et al. (Apr. 2021e). "The GRAVITY young stellar object survey. V. The orbit of the T Tauri binary star WW Cha". In: *Astronomy & Astrophysics* 648, A37, A37. DOI: 10.1051/0004-6361/202039599. arXiv: 2102.00122 [astro-ph.SR].

GRAVITY Collaboration et al. (Oct. 2021f). "The GRAVITY young stellar object survey. VI. Mapping the variable inner disk of HD 163296 at sub-au scales". In: *Astronomy & Astrophysics* 654, A97, A97. DOI: 10.1051/0004-6361/202039600. arXiv: 2107.02391 [astro-ph.SR].

GRAVITY Collaboration et al. (Nov. 2021g). "The GRAVITY young stellar object survey. VII. The inner dusty disks of T Tauri stars". In: *Astronomy & Astrophysics* 655, A73, A73. DOI: 10.1051/0004-6361/202141624. arXiv: 2109.11826 [astro-ph.SR].

GRAVITY Collaboration et al. (Nov. 2021h). "The GRAVITY young stellar object survey. VIII. Gas and dust faint inner rings in the hybrid disk of HD141569". In: *Astronomy & Astrophysics* 655, A112, A112. DOI: 10.1051/0004-6361/202141103. arXiv: 2109.10070 [astro-ph.SR].

GRAVITY Collaboration et al. (Apr. 2021i). "The central parsec of NGC 3783: a rotating broad emission line region, asymmetric hot dust structure, and compact coronal line region". In: *Astronomy & Astrophysics* 648, A117, A117. DOI: 10.1051/0004-6361/202040061. arXiv: 2102.00068 [astro-ph.GA].

GRAVITY Collaboration et al. (Jan. 2022). "Deep images of the Galactic center with GRAVITY". In: *Astronomy & Astrophysics* 657, A82, A82. DOI: 10.1051/0004-6361/202142459. arXiv: 2112.07477 [astro-ph.GA].

GRAVITY+ Collaboration et al. (Sept. 2022). "First light for GRAVITY Wide. Large separation fringe tracking for the Very Large Telescope Interferometer". In: *Astronomy & Astrophysics* 665, A75, A75. DOI: 10.1051/0004-6361/202243941. arXiv: 2206.00684 [astro-ph.IM].

GRAVITY Collaboration et al. (Jan. 2022). "Mass distribution in the Galactic Center based on interferometric astrometry of multiple stellar orbits". In: *Astronomy & Astrophysics* 657, L12, p. L12. DOI: 10.1051/0004-6361/202142465. arXiv: 2112.07478 [astro-ph.GA].

GRAVITY Collaboration et al. (Jan. 2024). "Polarization analysis of the VLTI and GRAVITY". In: *Astronomy & Astrophysics* 681, A115, A115. DOI: 10.1051/0004-6361/202347238. arXiv: 2311.03472 [astro-ph.IM].

Gaia Collaboration et al. (Aug. 2018). "Gaia Data Release 2. Summary of the contents and survey properties". In: *A&A* 616, A1, A1. DOI: 10.1051/0004-6361/201833051. arXiv: 1804.09365 [astro-ph.GA].

Gaia Collaboration et al. (May 2021). "Gaia Early Data Release 3. Summary of the contents and survey properties". In: *Astronomy & Astrophysics* 649, A1, A1. DOI: 10.1051/0004-6361/202039657. arXiv: 2012.01533 [astro-ph.GA].

Gallego-Cano, E. et al. (Jan. 2018). "The distribution of stars around the Milky Way's central black hole. I. Deep star counts". In: *Astronomy & Astrophysics* 609, A26, A26. DOI: 10.1051/0004-6361/201730451. arXiv: 1701.03816 [astro-ph.GA].

Gates, Delilah E. A., Hadar, Shahar, and Lupsasca, Alexandru (Nov. 2020). "Maximum observable blueshift from circular equatorial Kerr orbiters". In: *Physical Review D* 102.10, 104041, p. 104041. DOI: 10.1103/PhysRevD.102.104041. arXiv: 2009.03310 [gr-qc].

Gelles, Zachary, Himwich, Elizabeth, Johnson, Michael D., and Palumbo, Daniel C. M. (Aug. 2021). "Polarized image of equatorial emission in the Kerr geometry". In: *Physical Review D* 104.4, 044060, p. 044060. DOI: 10.1103/PhysRevD.104.044060. arXiv: 2105.09440 [gr-qc].

Generozov, Aleksey et al. (Apr. 2025). "The S stars' zone of avoidance in the Galactic center". In: *Astronomy & Astrophysics* 696, A68, A68. DOI: 10.1051/0004-6361/202453272. arXiv: 2412.02752 [astro-ph.GA].

Genzel, R., Eisenhauer, F., and Gillessen, S. (Apr. 2024). "Experimental studies of black holes: status and future prospects". In: *The Astronomy and Astrophysics Review* 32.1, 3, p. 3. DOI: 10.1007/s00159-024-00154-z. arXiv: 2404.03522 [astro-ph.GA].

Genzel, R., Pichon, C., Eckart, A., Gerhard, O. E., and Ott, T. (Sept. 2000). "Stellar dynamics in the Galactic Centre: proper motions and anisotropy". In: *Monthly Notice of the Royal Astronomical Society* 317.2, pp. 348–374. DOI: 10.1046/j.1365-8711.2000.03582.x. arXiv: astro-ph/0001428 [astro-ph].

Genzel, R., Thatte, N., Krabbe, A., Kroker, H., and Tacconi-Garman, L. E. (Nov. 1996). "The Dark Mass Concentration in the Central Parsec of the Milky Way". In: *ApJ* 472, p. 153. DOI: 10.1086/178051.

Genzel, R. and Townes, C. H. (Jan. 1987). "Physical conditions, dynamics, and mass distribution in the center of the galaxy." In: *Annual Review of Astronomy and Astrophysics* 25, pp. 377–423. DOI: 10.1146/annurev.aa.25.090187.002113.

Genzel, R. et al. (Oct. 2003a). "Near-infrared flares from accreting gas around the supermassive black hole at the Galactic Centre". In: *Nature* 425.6961, pp. 934–937. DOI: 10.1038/nature02065. arXiv: astro-ph/0310821 [astro-ph].

Genzel, R. et al. (Sept. 2003b). "The Stellar Cusp around the Supermassive Black Hole in the Galactic Center". In: *ApJ* 594.2, pp. 812–832. DOI: 10.1086/377127. arXiv: astro-ph/0305423 [astro-ph].

Genzel, Reinhard (Feb. 2021). "A Forty Year Journey". In: *arXiv e-prints*, arXiv:2102.13000, arXiv:2102.13000. DOI: 10.48550/arXiv.2102.13000. arXiv: 2102.13000 [astro-ph.GA].

Genzel, Reinhard, Eisenhauer, Frank, and Gillessen, Stefan (Oct. 2010). "The Galactic Center massive black hole and nuclear star cluster". In: *Reviews of Modern Physics* 82.4, pp. 3121–3195. DOI: 10.1103/RevModPhys.82.3121. arXiv: 1006.0064 [astro-ph.GA].

Genzel, Reinhard and Stutzki, Juergen (Jan. 1989). "The Orion molecular cloud and star-forming region." In: *Annual Review of Astronomy and Astrophysics* 27, pp. 41–85. DOI: 10.1146/annurev.aa.27.090189.000353.

Ghez, A. M., Klein, B. L., Morris, M., and Becklin, E. E. (Dec. 1998). "High Proper-Motion Stars in the Vicinity of Sagittarius A*: Evidence for a Supermassive Black Hole at the Center of Our Galaxy". In: *ApJ* 509.2, pp. 678–686. DOI: 10.1086/306528. arXiv: astro-ph/9807210 [astro-ph].

Ghez, A. M., Morris, M., Becklin, E. E., Tanner, A., and Kremenek, T. (Sept. 2000). "The accelerations of stars orbiting the Milky Way's central black hole". In: *Nature* 407.6802, pp. 349–351. DOI: 10.1038/35030032. arXiv: astro-ph/0009339 [astro-ph].

Ghez, A. M. et al. (Sept. 2003). "Full Three Dimensional Orbits For Multiple Stars on Close Approaches to the Central Supermassive Black Hole". In: *Astronomische Nachrichten Supplement* 324.1, pp. 527–533. DOI: 10.1002/asna.200385103. arXiv: astro-ph/0303151 [astro-ph].

Ghez, A. M. et al. (Feb. 2004). "Variable Infrared Emission from the Supermassive Black Hole at the Center of the Milky Way". In: *The Astrophysical Journal Letters* 601.2, pp. L159–L162. DOI: 10.1086/382024. arXiv: astro-ph/0309076 [astro-ph].

Ghez, A. M. et al. (Feb. 2005). "Stellar Orbits around the Galactic Center Black Hole". In: *ApJ* 620.2, pp. 744–757. DOI: 10.1086/427175. arXiv: astro-ph/0306130 [astro-ph].

Gillessen, S. et al. (Apr. 2006). "Variations in the Spectral Slope of Sagittarius A* during a Near-Infrared Flare". In: *The Astrophysical Journal Letters* 640.2, pp. L163–L166. DOI: 10.1086/503557. arXiv: astro-ph/0511302 [astro-ph].

Gillessen, S. et al. (Feb. 2009). "Monitoring Stellar Orbits Around the Massive Black Hole in the Galactic Center". In: *ApJ* 692.2, pp. 1075–1109. DOI: 10.1088/0004-637X/692/2/1075. arXiv: 0810.4674 [astro-ph].

Gillessen, S. et al. (Jan. 2012a). "A gas cloud on its way towards the supermassive black hole at the Galactic Centre". In: *Nature* 481.7379, pp. 51–54. DOI: 10.1038/nature10652. arXiv: 1112.3264 [astro-ph.GA].

Gillessen, S. et al. (Mar. 2017). "An Update on Monitoring Stellar Orbits in the Galactic Center". In: *ApJ* 837.1, 30, p. 30. DOI: 10.3847/1538-4357/aa5c41. arXiv: 1611.09144 [astro-ph.GA].

Gillessen, S. et al. (Jan. 2019). "Detection of a Drag Force in G2's Orbit: Measuring the Density of the Accretion Flow onto Sgr A* at 1000 Schwarzschild Radii". In: *ApJ* 871.1, 126, p. 126. DOI: 10.3847/1538-4357/aaf4f8.

Gillessen, Stefan et al. (July 2012b). "GRAVITY: metrology". In: *Optical and Infrared Interferometry III*. Ed. by Françoise Delplancke, Jayadev K. Rajagopal, and Fabien Malbet. Vol. 8445. Society of Photo-Optical Instrumentation Engineers (SPIE) Conference Series, 84451O, 84451O. DOI: 10.1117/12.926813. arXiv: 1209.2624 [astro-ph.IM].

Glindemann, Andreas (2011). *Principles of Stellar Interferometry*. DOI: 10.1007/978-3-642-15028-9.

Gralla, Samuel E., Holz, Daniel E., and Wald, Robert M. (July 2019). "Black hole shadows, photon rings, and lensing rings". In: *Physical Review D* 100.2, 024018, p. 024018. DOI: 10.1103/PhysRevD.100.024018. arXiv: 1906.00873 [astro-ph.HE].

Gralla, Samuel E. and Lupsasca, Alexandru (Feb. 2020). "Lensing by Kerr black holes". In: *Physical Review D* 101.4, 044031, p. 044031. DOI: 10.1103/PhysRevD.101.044031. arXiv: 1910.12873 [gr-qc].

Gravity+ Collaboration et al. (Dec. 2022). "The GRAVITY+ Project: Towards All-sky, Faint-Science, High-Contrast Near-Infrared Interferometry at the VLTI". In: *The Messenger* 189, pp. 17–22. DOI: 10.18727/0722-6691/5285. arXiv: 2301.08071 [astro-ph.IM].

Gravity Collaboration et al. (Sept. 2023a). "Polarimetry and astrometry of NIR flares as event horizon scale, dynamical probes for the mass of Sgr A*". In: *Astronomy & Astrophysics* 677, L10, p. L10. DOI: 10.1051/0004-6361/202347416. arXiv: 2307.11821 [astro-ph.GA].

Gravity Collaboration et al. (Apr. 2023b). "Where intermediate-mass black holes could hide in the Galactic Centre. A full parameter study with the S2 orbit". In: *Astronomy & Astrophysics* 672, A63, A63. DOI: 10.1051/0004-6361/202245132. arXiv: 2303.04067 [astro-ph.GA].

Gravity Collaboration et al. (Dec. 2024). "Improving constraints on the extended mass distribution in the Galactic center with stellar orbits". In: *Astronomy & Astrophysics* 692, A242, A242. DOI: 10.1051/0004-6361/202452274. arXiv: 2409.12261 [astro-ph.GA].

Greisen, E. W. (2003). "AIPS, the VLA, and the VLBA". In: *Information Handling in Astronomy - Historical Vistas*. Ed. by André Heck. Vol. 285, p. 109. DOI: 10.1007/0-306-48080-8_7.

Grellmann, R. et al. (Feb. 2013). "The multiplicity of massive stars in the Orion Nebula Cluster as seen with long-baseline interferometry". In: *A&A* 550, A82, A82. DOI: 10.1051/0004-6361/201220192. arXiv: 1301.3045 [astro-ph.SR].

Guesten, R. et al. (July 1987). "Aperture Synthesis Observations of the Circumnuclear Ring in the Galactic Center". In: *ApJ* 318, p. 124. DOI: 10.1086/165355.

Guyon, O. (May 2002). "Wide field interferometric imaging with single-mode fibers". In: *Astronomy & Astrophysics* 387, pp. 366–378. DOI: 10.1051/0004-6361:20020387. arXiv: astro-ph/0204259 [astro-ph].

Habibi, M. et al. (Oct. 2017). "Twelve Years of Spectroscopic Monitoring in the Galactic Center: The Closest Look at S-stars near the Black Hole". In: *ApJ* 847.2, 120, p. 120. DOI: 10.3847/1538-4357/aa876f. arXiv: 1708.06353 [astro-ph.SR].

Haguenauer, Pierre, Guesalaga, Andres, and Butterley, Timothy (Dec. 2020). "Comparison of atmosphere profilers at Paranal and atmosphere parameters statistics: AOF-profiler, STEREO-SCIDAR, MASS-DIMM, LGS-WFS". In: *Society of Photo-Optical Instrumentation Engineers (SPIE) Conference Series*. Vol. 11448. Society of Photo-Optical Instrumentation Engineers (SPIE) Conference Series, 114481K, 114481K. DOI: 10.1117/12.2562267.

Hamaus, N. et al. (Feb. 2009). "Prospects for Testing the Nature of Sgr A*'s Near-Infrared Flares on the Basis of Current Very Large Telescope—and Future Very Large Telescope

Interferometer—Observations". In: *ApJ* 692.1, pp. 902–916. DOI: 10.1088/0004-637X/692/1/902. arXiv: 0810.4947 [astro-ph].

Heckman, T. M. and Best, P. N. (Aug. 2014). "The Coevolution of Galaxies and Supermassive Black Holes: Insights from Surveys of the Contemporary Universe". In: *Annual Review of Astronomy and Astrophysics* 52, pp. 589–660. DOI: 10.1146/annurev-astro-081913-035722. arXiv: 1403.4620.

Heißel, G., Paumard, T., Perrin, G., and Vincent, F. (Apr. 2022). "The dark mass signature in the orbit of S2". In: *Astronomy & Astrophysics* 660, A13, A13. DOI: 10.1051/0004-6361/202142114. arXiv: 2112.07778 [astro-ph.GA].

Herrnstein, Robeson M., Zhao, Jun-Hui, Bower, Geoffrey C., and Goss, W. M. (June 2004). "The Variability of Sagittarius A* at Centimeter Wavelengths". In: *AJ* 127.6, pp. 3399–3410. DOI: 10.1086/420711. arXiv: astro-ph/0402543 [astro-ph].

Hillenbrand, Lynne A. (May 1997). "On the Stellar Population and Star-Forming History of the Orion Nebula Cluster". In: *Astronomical Journal* 113, pp. 1733–1768. DOI: 10.1086/118389.

Hills, J. G. (Feb. 1988). "Hyper-velocity and tidal stars from binaries disrupted by a massive Galactic black hole". In: *Nature* 331.6158, pp. 687–689. DOI: 10.1038/331687a0.

Hobbs, Alexander and Nayakshin, Sergei (Mar. 2009). "Simulations of the formation of stellar discs in the Galactic Centre via cloud-cloud collisions". In: *Monthly Notice of the Royal Astronomical Society* 394.1, pp. 191–206. DOI: 10.1111/j.1365-2966.2008.14359.x. arXiv: 0809.3752 [astro-ph].

Högbom, J. A. (June 1974). "Aperture Synthesis with a Non-Regular Distribution of Interferometer Baselines". In: *Astronomy & Astrophysics Supplement* 15, p. 417.

Jackson, J. M. et al. (Jan. 1993). "Neutral Gas in the Central 2 Parsecs of the Galaxy". In: *ApJ* 402, p. 173. DOI: 10.1086/172120.

Jocou, L. et al. (July 2014). "The beam combiners of Gravity VLTI instrument: concept, development, and performance in laboratory". In: *Optical and Infrared Interferometry IV*. Ed. by Jayadev K. Rajagopal, Michelle J. Creech-Eakman, and Fabien Malbet. Vol. 9146. Society of Photo-Optical Instrumentation Engineers (SPIE) Conference Series, 91461J, 91461J. DOI: 10.1117/12.2054159.

Johnson, Michael D. et al. (Dec. 2015). "Resolved magnetic-field structure and variability near the event horizon of Sagittarius A*". In: *Science* 350.6265, pp. 1242–1245. DOI: 10.1126/science.aac7087. arXiv: 1512.01220 [astro-ph.HE].

Kammerer, J., Mérand, A., Ireland, M. J., and Lacour, S. (Dec. 2020). "Increasing the achievable contrast of infrared interferometry with an error correlation model". In: *Astronomy & Astrophysics* 644, A110, A110. DOI: 10.1051/0004-6361/202038563. arXiv: 2011.01209 [astro-ph.IM].

Kendrew, S. et al. (Sept. 2012). "GRAVITY Coudé Infrared Adaptive Optics (CIAO) system for the VLT Interferometer". In: *Ground-based and Airborne Instrumentation for Astronomy IV*. Ed. by Ian S. McLean, Suzanne K. Ramsay, and Hideki Takami. Vol. 8446. Society of Photo-Optical Instrumentation Engineers (SPIE) Conference Series, 84467W, 84467W. DOI: 10.1117/12.926558. arXiv: 1207.2945 [astro-ph.IM].

Knollmüller, Jakob and Enßlin, Torsten A. (Jan. 2019). "Metric Gaussian Variational Inference". In: *arXiv e-prints*, arXiv:1901.11033, arXiv:1901.11033. arXiv: 1901.11033 [stat.ML].

Kornilov, V. et al. (Dec. 2007). "Combined MASS-DIMM instruments for atmospheric turbulence studies". In: *Mon. Not. R. Astron. Soc.* 382.343, pp. 1268–1278. DOI: 10.1111/j.1365-2966.2007.12467.x. arXiv: 0709.2081 [astro-ph].

Krabbe, A., Genzel, R., Drapatz, S., and Rotaciuc, V. (Nov. 1991). "A Cluster of He i Emission-Line Stars in the Galactic Center". In: *The Astrophysical Journal Letters* 382, p. L19. DOI: 10.1086/186204.

Krabbe, A. et al. (July 1995). "The Nuclear Cluster of the Milky Way: Star Formation and Velocity Dispersion in the Central 0.5 Parsec". In: *The Astrophysical Journal Letters* 447, p. L95. DOI: 10.1086/309579.

Kraus, S. et al. (May 2007). "Visual/infrared interferometry of Orion Trapezium stars: preliminary dynamical orbit and aperture synthesis imaging of the θ^1 Orionis C system". In: *A&A* 466.2, pp. 649–659. DOI: 10.1051/0004-6361:20066965. arXiv: astro-ph/0702462 [astro-ph].

Kraus, S. et al. (Apr. 2009). "Tracing the young massive high-eccentricity binary system $\theta\hat{1}$Orionis C through periastron passage". In: *A&A* 497.1, pp. 195–207. DOI: 10.1051/0004-6361/200810368. arXiv: 0902.0365 [astro-ph.SR].

Kunneriath, D. et al. (Oct. 2008). "Coordinated mm/sub-mm observations of Sagittarius A* in May 2007". In: *Journal of Physics Conference Series*. Vol. 131. Journal of Physics Conference Series. IOP, 012006, p. 012006. DOI: 10.1088/1742-6596/131/1/012006. arXiv: 0810.0177 [astro-ph].

Lacour, S. et al. (Apr. 2019). "The GRAVITY fringe tracker". In: *Astronomy & Astrophysics* 624, A99, A99. DOI: 10.1051/0004-6361/201834981. arXiv: 1901.03202 [astro-ph.IM].

Lacour, S. et al. (Oct. 2021). "The mass of β Pictoris c from β Pictoris b orbital motion". In: *Astronomy & Astrophysics* 654, L2, p. L2. DOI: 10.1051/0004-6361/202141889. arXiv: 2109.10671 [astro-ph.EP].

Lacy, J. H., Townes, C. H., Geballe, T. R., and Hollenbach, D. J. (Oct. 1980). "Observations of the motion and distribution of the ionized gas in the central parsec of the Galaxy. II." In: *ApJ* 241, pp. 132–146. DOI: 10.1086/158324.

Lacy, J. H., Townes, C. H., and Hollenbach, D. J. (Nov. 1982). "The nature of the central parsec of the Galaxy". In: *ApJ* 262, pp. 120–134. DOI: 10.1086/160402.

Lane, Benjamin F. and Colavita, M. Mark (Mar. 2003). "Phase-referenced Stellar Interferometry at the Palomar Testbed Interferometer". In: *AJ* 125.3, pp. 1623–1628. DOI: 10.1086/367793.

Lapeyrere, V. et al. (July 2014). "GRAVITY data reduction software". In: *Optical and Infrared Interferometry IV*. Ed. by Jayadev K. Rajagopal, Michelle J. Creech-Eakman, and Fabien Malbet. Vol. 9146. Society of Photo-Optical Instrumentation Engineers (SPIE) Conference Series, 91462D, p. 91462D. DOI: 10.1117/12.2056850.

Laplace, Pierre-Simon (June 1795). "Exposition du système du monde". In: *Cahiers Clairaut: Bulletin du Comité de Liaison Enseignants et Astronomes* 74, pp. 23–29.

Laugier, Romain et al. (2024). "VLTI Unit Telescope coudé train vibration control upgrade for GRAVITY+". In: *Optical and Infrared Interferometry and Imaging IX*. Ed. by Jens Kammerer, Stephanie Sallum, and Joel Sanchez-Bermudez. Vol. 13095. International Society for Optics and Photonics. SPIE, p. 130950M. DOI: 10.1117/12.3018146. URL: https://doi.org/10.1117/12.3018146.

Launhardt, R. et al. (Oct. 2005). "Towards High-Precision Ground-Based Astrometry: Differential Delay Lines for PRIMA@VLTI". In: *Astrometry in the Age of the Next Generation of Large Telescopes*. Ed. by P. K. Seidelmann and A. K. B. Monet. Vol. 338. Astronomical Society of the Pacific Conference Series, p. 167.

Levin, Yuri and Beloborodov, Andrei M. (June 2003). "Stellar Disk in the Galactic Center: A Remnant of a Dense Accretion Disk?" In: *The Astrophysical Journal Letters* 590.1, pp. L33–L36. DOI: 10.1086/376675. arXiv: astro-ph/0303436 [astro-ph].

Levis, Aviad, Chael, Andrew A., Bouman, Katherine L., Wielgus, Maciek, and Srinivasan, Pratul P. (June 2024). "Orbital polarimetric tomography of a flare near the Sagittarius A* supermassive black hole". In: *Nature Astronomy* 8, pp. 765–773. DOI: 10.1038/s41550-024-02238-3. arXiv: 2310.07687 [astro-ph.HE].

Li, Juan et al. (July 2009). "The Variability of Sagittarius A* at 3 Millimeter". In: *ApJ* 700.1, pp. 417–425. DOI: 10.1088/0004-637X/700/1/417. arXiv: 0905.2654 [astro-ph.GA].

Lin, Xi, Li, Ya-Ping, and Yuan, Feng (Mar. 2023). "A 'coronal-mass-ejection' model for flares in Sagittarius A*". In: *Monthly Notice of the Royal Astronomical Society* 520.1, pp. 1271–1284. DOI: 10.1093/mnras/stad176. arXiv: 2301.05925 [astro-ph.HE].

Lippa, Magdalena et al. (Aug. 2016). "The metrology system of the VLTI instrument GRAVITY". In: *Optical and Infrared Interferometry and Imaging V*. Ed. by Fabien Malbet, Michelle J. Creech-Eakman, and Peter G. Tuthill. Vol. 9907. Society of Photo-Optical Instrumentation Engineers (SPIE) Conference Series, 990722, p. 990722. DOI: 10.1117/12.2232272. arXiv: 1608.04888 [astro-ph.IM].

Lippa, Magdalena et al. (July 2018). "Learnings from the use of fiber optics in GRAVITY". In: *Optical and Infrared Interferometry and Imaging VI*. Ed. by Michelle J. Creech-Eakman, Peter G. Tuthill, and Antoine Mérand. Vol. 10701. Society of Photo-Optical Instrumentation Engineers (SPIE) Conference Series, 107011Y, 107011Y. DOI: 10.1117/12.2312477.

Lo, K. Y. and Claussen, M. J. (Dec. 1983). "High-resolution observations of ionized gas in central 3 parsecs of the Galaxy: possible evidence for infall". In: *Nature* 306.5944, pp. 647–651. DOI: 10.1038/306647a0.

Lo, K. Y., Shen, Zhi-Qiang, Zhao, Jun-Hui, and Ho, Paul T. P. (Nov. 1998). "Intrinsic Size of Sagittarius A*: 72 Schwarzschild Radii". In: *The Astrophysical Journal Letters* 508.1, pp. L61–L64. DOI: 10.1086/311726. arXiv: astro-ph/9809222 [astro-ph].

Lu, J. R. et al. (Dec. 2006). "Galactic Center Youth: Orbits and Origins of the Young Stars in the Central Parsec". In: *Journal of Physics Conference Series*. Ed. by Rainer Schödel, Geoffrey C. Bower, Michael P. Muno, Sergei Nayakshin, and Thomas Ott. Vol. 54. Journal of Physics Conference Series. IOP, pp. 279–287. DOI: 10.1088/1742-6596/54/1/044.

Lu, J. R. et al. (Jan. 2009). "A Disk of Young Stars at the Galactic Center as Determined by Individual Stellar Orbits". In: *ApJ* 690.2, pp. 1463–1487. DOI: 10.1088/0004-637X/690/2/1463. arXiv: 0808.3818 [astro-ph].

Lynden-Bell, D. (Aug. 1969). "Galactic Nuclei as Collapsed Old Quasars". In: *Nature* 223.5207, pp. 690–694. DOI: 10.1038/223690a0.

Lynden-Bell, D. and Rees, M. J. (Jan. 1971). "On quasars, dust and the galactic centre". In: *Monthly Notice of the Royal Astronomical Society* 152, p. 461. DOI: 10.1093/mnras/152.4.461.

Macquart, Jean-Pierre and Bower, Geoffrey C. (Apr. 2006). "Understanding the Radio Variability of Sagittarius A*". In: *ApJ* 641.1, pp. 302–318. DOI: 10.1086/500317. arXiv: astro-ph/0512288 [astro-ph].

Madau, Piero and Dickinson, Mark (Aug. 2014). "Cosmic Star-Formation History". In: *Annual Review of Astronomy and Astrophysics* 52, pp. 415–486. DOI: 10.1146/annurev-astro-081811-125615. arXiv: 1403.0007 [astro-ph.CO].

Marrone, D. P. et al. (July 2008). "An X-Ray, Infrared, and Submillimeter Flare of Sagittarius A*". In: *ApJ* 682.1, pp. 373–383. DOI: 10.1086/588806. arXiv: 0712.2877 [astro-ph].

Marrone, Daniel P., Moran, James M., Zhao, Jun-Hui, and Rao, Ramprasad (Mar. 2006). "Interferometric Measurements of Variable 340 GHz Linear Polarization in Sagittarius A*". In: *ApJ* 640.1, pp. 308–318. DOI: 10.1086/500106. arXiv: astro-ph/0511653 [astro-ph].

Martinez, P., Kolb, J., Sarazin, M., and Tokovinin, A. (Sept. 2010). "On the Difference between Seeing and Image Quality: When the Turbulence Outer Scale Enters the Game". In: *The Messenger* 141, pp. 5–8.

Martins, F. et al. (Jan. 2008). "On the Nature of the Fast-Moving Star S2 in the Galactic Center". In: *The Astrophysical Journal Letters* 672.2, p. L119. DOI: 10.1086/526768. arXiv: 0711.3344 [astro-ph].

Matsumoto, Tatsuya, Chan, Chi-Ho, and Piran, Tsvi (Sept. 2020). "The origin of hotspots around Sgr A*: orbital or pattern motion?" In: *Monthly Notice of the Royal Astronomical Society* 497.2, pp. 2385–2392. DOI: 10.1093/mnras/staa2095. arXiv: 2004.13029 [astro-ph.HE].

McKinney, Jonathan C., Tchekhovskoy, Alexander, and Blandford, Roger D. (Jan. 2013). "Alignment of Magnetized Accretion Disks and Relativistic Jets with Spinning Black Holes". In: *Science* 339.6115, p. 49. DOI: 10.1126/science.1230811. arXiv: 1211.3651 [astro-ph.CO].

Menten, K. M., Reid, M. J., Forbrich, J., and Brunthaler, A. (Nov. 2007). "The distance to the Orion Nebula". In: *A&A* 474.2, pp. 515–520. DOI: 10.1051/0004-6361:20078247. arXiv: 0709.0485 [astro-ph].

Merritt, David, Alexander, Tal, Mikkola, Seppo, and Will, Clifford M. (Mar. 2010). "Testing properties of the Galactic center black hole using stellar orbits". In: *Physical Review D* 81.6, 062002, p. 062002. DOI: 10.1103/PhysRevD.81.062002. arXiv: 0911.4718 [astro-ph.GA].

Meyer, L. et al. (Dec. 2006). "Near-infrared polarimetry setting constraints on the orbiting spot model for Sgr A* flares". In: *Astronomy & Astrophysics* 460.1, pp. 15–21. DOI: 10.1051/0004-6361:20065925. arXiv: astro-ph/0610104 [astro-ph].

Meyer, L. et al. (Oct. 2012). "The Shortest-Known-Period Star Orbiting Our Galaxy's Supermassive Black Hole". In: *Science* 338.6103, p. 84. DOI: 10.1126/science.1225506. arXiv: 1210.1294 [astro-ph.GA].

Michail, Joseph M., Yusef-Zadeh, Farhad, Wardle, Mark, and Kunneriath, Devaky (Apr. 2023). "Polarized signatures of adiabatically expanding hotspots in Sgr A*'s accretion flow". In: *Monthly Notice of the Royal Astronomical Society* 520.2, pp. 2644–2654. DOI: 10.1093/mnras/stad291. arXiv: 2301.10243 [astro-ph.HE].

Michell, John (Jan. 1784). "On the Means of Discovering the Distance, Magnitude, &c. of the Fixed Stars, in Consequence of the Diminution of the Velocity of Their Light, in Case Such a Diminution Should be Found to Take Place in any of Them, and Such Other Data Should be Procured from Observations, as Would be Farther Necessary for That Purpose. By the Rev. John Michell, B. D. F. R. S. In a Letter to Henry Cavendish, Esq. F. R. S. and A. S." In: *Philosophical Transactions of the Royal Society of London Series I* 74, pp. 35–57.

Millour, Florentin, Petrov, Romain G., Vannier, Martin, and Kraus, Stefan (July 2008). "AMBER closure and differential phases: accuracy and calibration with a beam commutation". In: *Optical and Infrared Interferometry*. Ed. by Markus Schöller, William C. Danchi, and Françoise Delplancke. Vol. 7013. Society of Photo-Optical Instrumentation Engineers (SPIE) Conference Series, 70131G, 70131G. DOI: 10.1117/12.788689. arXiv: 0806.4833 [astro-ph].

Millour, Florentin et al. (2024). "GRAVITY+ adaptive optics (GPAO) tests in Europe". In: *Optical and Infrared Interferometry and Imaging IX*. Ed. by Jens Kammerer, Stephanie Sallum, and Joel Sanchez-Bermudez. Vol. 13095. International Society for Optics and Photonics. SPIE, p. 1309520. DOI: 10.1117/12.3020269. URL: https://doi.org/10.1117/12.3020269.

Miyazaki, Atsushi, Tsutsumi, Takahiro, and Tsuboi, Masato (Aug. 2004). "Intraday Variation of Sagittarius A* at Short Millimeter Wavelengths". In: *The Astrophysical Journal Letters* 611.2, pp. L97–L100. DOI: 10.1086/424004. arXiv: astro-ph/0407252 [astro-ph].

Moré, J. J. and Sorensen, D. C. (Jan. 1983). "Computing a Trust Region Step". In: *SIAM J. Sci. and Stat. Comput.* 4.3, pp. 553–572. DOI: 10.1137/0904038.

More, Nikhil et al. (Aug. 2024). "Opto-mechanical design of GRAVITY+ wavefront sensor". In: *Optical and Infrared Interferometry and Imaging IX*. Ed. by Jens Kammerer, Stephanie Sallum, and Joel Sanchez-Bermudez. Vol. 13095. Society of Photo-Optical Instrumentation Engineers (SPIE) Conference Series, 130952E, 130952E. DOI: 10.1117/12.3018880.

Morel, Sebastien et al. (Oct. 2004). "ARAL: a facility to fuel VLTI instruments with photons". In: *New Frontiers in Stellar Interferometry*. Ed. by Wesley A. Traub. Vol. 5491. Society of Photo-Optical Instrumentation Engineers (SPIE) Conference Series, p. 1079. DOI: 10.1117/12.550175.

Muñoz, D. J., Marrone, D. P., Moran, J. M., and Rao, R. (Feb. 2012). "The Circular Polarization of Sagittarius A* at Submillimeter Wavelengths". In: *ApJ* 745.2, 115, p. 115. DOI: 10.1088/0004-637X/745/2/115. arXiv: 1105.0427 [astro-ph.HE].

Muench, A., Getman, K., Hillenbrand, L., and Preibisch, T. (2008). "Star Formation in the Orion Nebula I: Stellar Content". In: *Handbook of Star Forming Regions, Volume I*. Ed. by B. Reipurth. Vol. 4. The Northern Sky ASP Monograph Publications, p. 483.

Najarro, F. et al. (Sept. 1997). "Quantitative spectroscopy of the HeI cluster in the Galactic center." In: *Astronomy & Astrophysics* 325, pp. 700–708.

Narayan, Ramesh and Quataert, Eliot (Mar. 2023). "Black holes up close". In: *Nature* 615.7953, pp. 597–604. DOI: 10.1038/s41586-023-05768-4. arXiv: 2303.13229 [astro-ph.HE].

Narayan, Ramesh et al. (May 2021). "The Polarized Image of a Synchrotron-emitting Ring of Gas Orbiting a Black Hole". In: *ApJ* 912.1, 35, p. 35. DOI: 10.3847/1538-4357/abf117. arXiv: 2105.01804 [astro-ph.HE].

Neilsen, J. et al. (Sept. 2013). "A Chandra/HETGS Census of X-Ray Variability from Sgr A* during 2012". In: *ApJ* 774.1, 42, p. 42. DOI: 10.1088/0004-637X/774/1/42. arXiv: 1307.5843 [astro-ph.HE].

Nowak, M. et al. (Oct. 2020). "Direct confirmation of the radial-velocity planet β Pictoris c". In: *Astronomy & Astrophysics* 642, L2, p. L2. DOI: 10.1051/0004-6361/202039039. arXiv: 2010.04442 [astro-ph.EP].

Nowak, M. et al. (Apr. 2024). "Upgrading the GRAVITY fringe tracker for GRAVITY+. Tracking the white-light fringe in the non-observable optical path length state-space". In: *Astronomy & Astrophysics* 684, A184, A184. DOI: 10.1051/0004-6361/202348771. arXiv: 2402.03594 [astro-ph.IM].

Patience, J. et al. (Feb. 2008). "Optical Interferometric Observations of θ^1 Orionis C from NPOI and Implications for the System Orbit". In: *The Astrophysical Journal Letters* 674.2, p. L97. DOI: 10.1086/529041. arXiv: 0801.2584 [astro-ph].

Paumard, T., Maillard, J. P., Morris, M., and Rigaut, F. (Feb. 2001). "New results on the helium stars in the galactic center using BEAR spectro-imagery". In: *Astronomy & Astrophysics* 366, pp. 466–480. DOI: 10.1051/0004-6361:20000227. arXiv: astro-ph/0011215 [astro-ph].

Paumard, T. et al. (June 2006). "The Two Young Star Disks in the Central Parsec of the Galaxy: Properties, Dynamics, and Formation". In: *ApJ* 643.2, pp. 1011–1035. DOI: 10.1086/503273. arXiv: astro-ph/0601268 [astro-ph].

Peißker, Florian, Eckart, Andreas, and Ali, Basel (Sept. 2021). "Observation of the Apoapsis of S62 in 2019 with NIRC2 and SINFONI". In: *ApJ* 918.1, 25, p. 25. DOI: 10.3847/1538-4357/ac0efc. arXiv: 2109.00798 [astro-ph.SR].

Peißker, Florian, Eckart, Andreas, and Parsa, Marzieh (Jan. 2020). "S62 on a 9.9 yr Orbit around SgrA*". In: *ApJ* 889.1, 61, p. 61. DOI: 10.3847/1538-4357/ab5afd. arXiv: 2002.02341 [astro-ph.GA].

Perraut, K. et al. (June 2018). "Single-mode waveguides for GRAVITY. I. The cryogenic 4-telescope integrated optics beam combiner". In: *Astronomy & Astrophysics* 614, A70, A70. DOI: 10.1051/0004-6361/201732544.

Perrin, G. and Woillez, J. (May 2019). "Single-mode interferometric field of view in partial turbulence correction. Application to the observation of the environment of Sgr A* with GRAVITY". In: *Astronomy & Astrophysics* 625, A48, A48. DOI: 10.1051/0004-6361/201834013. arXiv: 1903.10937 [astro-ph.IM].

Perrin, G. et al. (Jan. 2024). "Single-mode waveguides for GRAVITY. II. Single-mode fibers and Fiber Control Unit". In: *Astronomy & Astrophysics* 681, A26, A26. DOI: 10.1051/0004-6361/202347587. arXiv: 2401.10613 [astro-ph.IM].

Perryman, M. A. C. et al. (Apr. 2001). "GAIA: Composition, formation and evolution of the Galaxy". In: *Astronomy & Astrophysics* 369, pp. 339–363. DOI: 10.1051/0004-6361:20010085. arXiv: astro-ph/0101235 [astro-ph].

Pfuhl, O. et al. (July 2014). "The fiber coupler and beam stabilization system of the GRAVITY interferometer". In: *Optical and Infrared Interferometry IV*. Ed. by Jayadev K. Rajagopal, Michelle J. Creech-Eakman, and Fabien Malbet. Vol. 9146. Society of Photo-Optical Instrumentation Engineers (SPIE) Conference Series, 914623, p. 914623. DOI: 10.1117/12.2055080. arXiv: 1412.1696 [astro-ph.IM].

Ponti, G. et al. (June 2017). "A powerful flare from Sgr A* confirms the synchrotron nature of the X-ray emission". In: *Monthly Notice of the Royal Astronomical Society* 468.2, pp. 2447–2468. DOI: 10.1093/mnras/stx596. arXiv: 1703.03410 [astro-ph.HE].

Porquet, D. et al. (Aug. 2003). "XMM-Newton observation of the brightest X-ray flare detected so far from Sgr A*". In: *Astronomy & Astrophysics* 407, pp. L17–L20. DOI: 10.1051/0004-6361:20030983. arXiv: astro-ph/0307110 [astro-ph].

Quirrenbach, A. (Jan. 2000). "Observing Through the Turbulent Atmosphere". In: *Principles of Long Baseline Stellar Interferometry*. Ed. by Peter R. Lawson, p. 71.

Rakshit, Suvendu, Stalin, C. S., and Kotilainen, Jari (July 2020). "Spectral Properties of Quasars from Sloan Digital Sky Survey Data Release 14: The Catalog". In: *The Astrophysical Journal Supplement Series* 249.1, 17, p. 17. DOI: 10.3847/1538-4365/ab99c5. arXiv: 1910.10395 [astro-ph.GA].

Rees, Martin J. (Jan. 1984). "Black Hole Models for Active Galactic Nuclei". In: *Annual Review of Astronomy and Astrophysics* 22, pp. 471–506. DOI: 10.1146/annurev.aa.22.090184.002351.

Reid, M. J. and Brunthaler, A. (Dec. 2004). "The Proper Motion of Sagittarius A*. II. The Mass of Sagittarius A*". In: *ApJ* 616.2, pp. 872–884. DOI: 10.1086/424960. arXiv: astro-ph/0408107 [astro-ph].

Reid, Mark J. (Jan. 2009). "Is There a Supermassive Black Hole at the Center of the Milky Way?" In: *International Journal of Modern Physics D* 18.6, pp. 889–910. DOI: 10.1142/S0218271809014820. arXiv: 0808.2624 [astro-ph].

Ressler, S. M., White, C. J., and Quataert, E. (May 2023). "Wind-fed GRMHD simulations of Sagittarius A*: tilt and alignment of jets and accretion discs, electron thermodynamics, and multiscale modelling of the rotation measure". In: *Monthly Notice of the Royal Astronomical Society* 521.3, pp. 4277–4298. DOI: 10.1093/mnras/stad837. arXiv: 2303.15503 [astro-ph.HE].

Ressler, Sean M., White, Christopher J., Quataert, Eliot, and Stone, James M. (June 2020). "Ab Initio Horizon-scale Simulations of Magnetically Arrested Accretion in Sagittarius

A* Fed by Stellar Winds". In: *The Astrophysical Journal Letters* 896.1, L6, p. L6. DOI: 10.3847/2041-8213/ab9532. arXiv: 2006.00005 [astro-ph.HE].

Ripperda, B. et al. (Jan. 2022). "Black Hole Flares: Ejection of Accreted Magnetic Flux through 3D Plasmoid-mediated Reconnection". In: *The Astrophysical Journal Letters* 924.2, L32, p. L32. DOI: 10.3847/2041-8213/ac46a1. arXiv: 2109.15115 [astro-ph.HE].

Ripperda, Bart, Bacchini, Fabio, and Philippov, Alexander A. (Sept. 2020). "Magnetic Reconnection and Hot Spot Formation in Black Hole Accretion Disks". In: *ApJ* 900.2, 100, p. 100. DOI: 10.3847/1538-4357/ababab. arXiv: 2003.04330 [astro-ph.HE].

Rogers, A. E. E. et al. (Oct. 1974). "The structure of radio sources 3C 273B and 3C 84 deduced from the "closure" phases and visibility amplitudes observed with three-element interferometers." In: *ApJ* 193, pp. 293–301. DOI: 10.1086/153162.

Rousset, Gerard et al. (Feb. 2003). "NAOS, the first AO system of the VLT: on-sky performance". In: *Adaptive Optical System Technologies II*. Ed. by Peter L. Wizinowich and Domenico Bonaccini. Vol. 4839. Society of Photo-Optical Instrumentation Engineers (SPIE) Conference Series, pp. 140–149. DOI: 10.1117/12.459332.

Sana, H. et al. (Nov. 2014). "Southern Massive Stars at High Angular Resolution: Observational Campaign and Companion Detection". In: *The Astrophysical Journal Supplement Series* 215.1, 15, p. 15. DOI: 10.1088/0067-0049/215/1/15. arXiv: 1409.6304 [astro-ph.SR].

Sanchez-Bermudez, Joel et al. (2024). "BrG studies at high-spectral resolution with GRAVITY+: the design of a new high-resolution Germanium grism". In: *Optical and Infrared Interferometry and Imaging IX*. Ed. by Jens Kammerer, Stephanie Sallum, and Joel Sanchez-Bermudez. Vol. 13095. International Society for Optics and Photonics. SPIE, 130952F. DOI: 10.1117/12.3020375. URL: https://doi.org/10.1117/12.3020375.

Scheithauer, Silvia et al. (July 2016). "CIAO: wavefront sensors for GRAVITY". In: *Adaptive Optics Systems V*. Ed. by Enrico Marchetti, Laird M. Close, and Jean-Pierre Véran. Vol. 9909. Society of Photo-Optical Instrumentation Engineers (SPIE) Conference Series, 99092L, p. 99092L. DOI: 10.1117/12.2232997.

Schertl, D., Balega, Y. Y., Preibisch, Th., and Weigelt, G. (Apr. 2003). "Orbital motion of the massive multiple stars in the Orion Trapezium". In: *A&A* 402, pp. 267–275. DOI: 10.1051/0004-6361:20030225.

Schmidt, M. (Mar. 1963). "3C 273 : A Star-Like Object with Large Red-Shift". In: *Nature* 197.4872, p. 1040. DOI: 10.1038/1971040a0.

Schödel, R. et al. (Oct. 2002). "A star in a 15.2-year orbit around the supermassive black hole at the centre of the Milky Way". In: *Nature* 419.6908, pp. 694–696. DOI: 10.1038/nature01121. arXiv: astro-ph/0210426 [astro-ph].

Schwarzschild, K. (Jan. 1916). "On the Gravitational Field of a Mass Point According to Einstein's Theory". In: *Abh. Konigl. Preuss. Akad. Wissenschaften Jahre 1906,92, Berlin,1907* 1916, pp. 189–196.

Shahzamanian, B. et al. (Apr. 2015). "Polarized light from Sagittarius A* in the near-infrared K_s-band". In: *Astronomy & Astrophysics* 576, A20, A20. DOI: 10.1051/0004-6361/201425239. arXiv: 1411.0006 [astro-ph.GA].

Shaklan, Stuart and Roddier, Francois (June 1988). "Coupling starlight into single-mode fiber optics". In: *Applied Optics* 27, pp. 2334–2338. DOI: 10.1364/AO.27.002334.

Shao, M. and Colavita, M. M. (Aug. 1992). "Potential of long-baseline infrared interferometry for narrow-angle astrometry". In: *Astronomy & Astrophysics* 262.1, pp. 353–358.

Shen, Zhi-Qiang, Lo, K. Y., Liang, M. C., Ho, Paul T. P., and Zhao, J. H. (Nov. 2005). "A size of ∼1AU for the radio source Sgr A* at the centre of the Milky Way". In: *Nature* 438.7064, pp. 62–64. DOI: 10.1038/nature04205. arXiv: astro-ph/0512515 [astro-ph].

Smirnov, O. M. (Mar. 2011). "Revisiting the radio interferometer measurement equation. I. A full-sky Jones formalism". In: *Astronomy & Astrophysics* 527, A106, A106. DOI: 10.1051/0004-6361/201016082. arXiv: 1101.1764 [astro-ph.IM].

Tallon-Bosc, I., Tallon, M., Thiébaut, E., and Béchet, C. (Oct. 2007). "Model fitting tutorial". In: *New Astronomy Reviews* 51.8-9, pp. 697–705. DOI: 10.1016/j.newar.2007.06.011.

Tamblyn, Peter et al. (Jan. 1996). "The Peculiar Population of Hot Stars at the Galactic Center". In: *ApJ* 456, p. 206. DOI: 10.1086/176641.

Tatulli, E. et al. (Mar. 2007). "Interferometric data reduction with AMBER/VLTI. Principle, estimators, and illustration". In: *A&A* 464.1, pp. 29–42. DOI: 10.1051/0004-6361:20064799. arXiv: astro-ph/0603046 [astro-ph].

Thiébaut, Eric (July 2008). "MIRA: an effective imaging algorithm for optical interferometry". In: *Optical and Infrared Interferometry*. Ed. by Markus Schöller, William C. Danchi, and Françoise Delplancke. Vol. 7013. Society of Photo-Optical Instrumentation Engineers (SPIE) Conference Series, 70131I, p. 70131I. DOI: 10.1117/12.788822.

Thorpe, James Ira et al. (Sept. 2019). "The Laser Interferometer Space Antenna: Unveiling the Millihertz Gravitational Wave Sky". In: *Bulletin of the American Astronomical Society*. Vol. 51, 77, p. 77. DOI: 10.48550/arXiv.1907.06482. arXiv: 1907.06482 [astro-ph.IM].

Tokovinin, Andrei (Dec. 2019). "Spectroscopic Orbits of Subsystems in Multiple Stars. VI." In: *The Astronomical Journal* 158.6, 222, p. 222. DOI: 10.3847/1538-3881/ab4c94. arXiv: 1910.04143 [astro-ph.SR].

Trippe, S. et al. (Mar. 2007). "A polarized infrared flare from Sagittarius A* and the signatures of orbiting plasma hotspots". In: *Monthly Notice of the Royal Astronomical Society* 375.3, pp. 764–772. DOI: 10.1111/j.1365-2966.2006.11338.x. arXiv: astro-ph/0611737 [astro-ph].

Vincent, F. H., Wielgus, M., Aimar, N., Paumard, T., and Perrin, G. (Apr. 2024). "Polarized signatures of orbiting hot spots: Special relativity impact and probe of spacetime curvature". In: *Astronomy & Astrophysics* 684, A194, A194. DOI: 10.1051/0004-6361/202348016. arXiv: 2309.10053 [astro-ph.HE].

Vos, J., Mościbrodzka, M. A., and Wielgus, M. (Dec. 2022). "Polarimetric signatures of hot spots in black hole accretion flows". In: *Astronomy & Astrophysics* 668, A185, A185. DOI: 10.1051/0004-6361/202244840. arXiv: 2209.09931 [astro-ph.HE].

Vousden, W. D., Farr, W. M., and Mandel, I. (Jan. 2016). "Dynamic temperature selection for parallel tempering in Markov chain Monte Carlo simulations". In: *Monthly Notices of the Royal Astronomical Society* 455.2, pp. 1919–1937. DOI: 10.1093/mnras/stv2422. arXiv: 1501.05823 [astro-ph.IM].

Waisberg, Idel et al. (May 2018). "What stellar orbit is needed to measure the spin of the Galactic centre black hole from astrometric data?" In: *Monthly Notice of the Royal Astronomical Society* 476.3, pp. 3600–3610. DOI: 10.1093/mnras/sty476. arXiv: 1802.08198 [astro-ph.GA].

Weigelt, G. et al. (July 1999). "Bispectrum speckle interferometry of the Orion Trapezium stars: detection of a close (33 mas) companion of Theta (1) ORI C". In: *A&A* 347, pp. L15–L18. arXiv: astro-ph/9906233 [astro-ph].

Widmann, Felix et al. (Aug. 2022). "GRAVITY faint: reducing noise sources in GRAVITY+ with a fast metrology attenuation system". In: *Optical and Infrared Interferometry and Imaging VIII*. Ed. by Antoine Mérand, Stephanie Sallum, and Joel Sanchez-Bermudez. Vol. 12183. Society of Photo-Optical Instrumentation Engineers (SPIE) Conference Series, 121830U, 121830U. DOI: 10.1117/12.2628813. arXiv: 2209.05593 [astro-ph.IM].

Wielgus, M. et al. (Sept. 2022). "Orbital motion near Sagittarius A* . Constraints from polarimetric ALMA observations". In: *Astronomy & Astrophysics* 665, L6, p. L6. DOI: 10.1051/0004-6361/202244493. arXiv: 2209.09926 [astro-ph.HE].

Witzel, G. et al. (Jan. 2011). "The instrumental polarization of the Nasmyth focus polarimetric differential imager NAOS/CONICA (NACO) at the VLT. Implications for time-resolved polarimetric measurements of Sagittarius A*". In: *Astronomy & Astrophysics* 525, A130, A130. DOI: 10.1051/0004-6361/201015009. arXiv: 1010.4708 [astro-ph.IM].

Witzel, G. et al. (Aug. 2018). "Variability Timescale and Spectral Index of Sgr A* in the Near Infrared: Approximate Bayesian Computation Analysis of the Variability of the Closest Supermassive Black Hole". In: *ApJ* 863.1, 15, p. 15. DOI: 10.3847/1538-4357/aace62. arXiv: 1806.00479 [astro-ph.HE].

Witzel, G. et al. (Aug. 2021). "Rapid Variability of Sgr A* across the Electromagnetic Spectrum". In: *ApJ* 917.2, 73, p. 73. DOI: 10.3847/1538-4357/ac0891. arXiv: 2011.09582 [astro-ph.HE].

Wizinowich, P. et al. (Mar. 2000). "First Light Adaptive Optics Images from the Keck II Telescope: A New Era of High Angular Resolution Imagery". In: *PASP* 112.769, pp. 315–319. DOI: 10.1086/316543.

Woillez, J. et al. (Mar. 2014). "First Faint Dual-field Off-axis Observations in Optical Long Baseline Interferometry". In: *ApJ* 783.2, 104, p. 104. DOI: 10.1088/0004-637X/783/2/104.

Woillez, J. et al. (Sept. 2019). "NAOMI: the adaptive optics system of the Auxiliary Telescopes of the VLTI". In: *Astronomy & Astrophysics* 629, A41, A41. DOI: 10.1051/0004-6361/201935890. arXiv: 1908.06651 [astro-ph.IM].

Woillez, Julien et al. (July 2018). "VLTI status update: three years into the second generation". In: *Optical and Infrared Interferometry and Imaging VI*. Ed. by Michelle J.

Creech-Eakman, Peter G. Tuthill, and Antoine Mérand. Vol. 10701. Society of Photo-Optical Instrumentation Engineers (SPIE) Conference Series, 1070103, p. 1070103. DOI: 10.1117/12.2312042.

Wollman, E. R., Geballe, T. R., Lacy, J. H., Townes, C. H., and Rank, D. M. (Dec. 1977). "Ne II 12.8 micron emission from the galactic center. II." In: *The Astrophysical Journal Letters* 218, pp. L103–L107. DOI: 10.1086/182585.

Yazici, Senol et al. (2021). "GRAVITY upgrade with high-performance grisms with factor >2 enhanced throughput". In: *Optical and Infrared Interferometry and Imaging VII*. Ed. by Peter G. Tuthill, Antoine Mérand, and Stephanie Sallum. Vol. 11446. International Society for Optics and Photonics. SPIE, p. 114461X. DOI: 10.1117/12.2561387. URL: https://doi.org/10.1117/12.2561387.

Yelda, S. et al. (Mar. 2014). "Properties of the Remnant Clockwise Disk of Young Stars in the Galactic Center". In: *ApJ* 783.2, 131, p. 131. DOI: 10.1088/0004-637X/783/2/131. arXiv: 1401.7354 [astro-ph.GA].

Yfantis, A. I., Wielgus, M., and Mościbrodzka, M. (Nov. 2024). "Hot spots around Sagittarius A*: Joint fits to astrometry and polarimetry". In: *Astronomy & Astrophysics* 691, A327, A327. DOI: 10.1051/0004-6361/202451884. arXiv: 2408.07120 [astro-ph.HE].

Yuan, Feng, Lin, Jun, Wu, Kinwah, and Ho, Luis C. (June 2009). "A magnetohydrodynamical model for the formation of episodic jets". In: *Monthly Notice of the Royal Astronomical Society* 395.4, pp. 2183–2188. DOI: 10.1111/j.1365-2966.2009.14673.x. arXiv: 0811.2893 [astro-ph].

Yuan, Feng and Narayan, Ramesh (Aug. 2014). "Hot Accretion Flows Around Black Holes". In: *Annual Review of Astronomy and Astrophysics* 52, pp. 529–588. DOI: 10.1146/annurev-astro-082812-141003. arXiv: 1401.0586 [astro-ph.HE].

Yuan, Feng, Quataert, Eliot, and Narayan, Ramesh (Nov. 2003). "Nonthermal Electrons in Radiatively Inefficient Accretion Flow Models of Sagittarius A*". In: *ApJ* 598.1, pp. 301–312. DOI: 10.1086/378716. arXiv: astro-ph/0304125 [astro-ph].

Yusef-Zadeh, F., Roberts, D., Wardle, M., Heinke, C. O., and Bower, G. C. (Oct. 2006). "Flaring Activity of Sagittarius A* at 43 and 22 GHz: Evidence for Expanding Hot Plasma". In: *ApJ* 650.1, pp. 189–194. DOI: 10.1086/506375. arXiv: astro-ph/0603685 [astro-ph].

Yusef-Zadeh, F. et al. (July 2008). "Simultaneous Chandra, CSO, and VLA Observations of Sgr A*: The Nature of Flaring Activity". In: *ApJ* 682.1, pp. 361–372. DOI: 10.1086/588803. arXiv: 0712.2882 [astro-ph].

Yusef-Zadeh, F. et al. (Nov. 2009). "Simultaneous Multi-Wavelength Observations of Sgr A* During 2007 April 1-11". In: *ApJ* 706.1, pp. 348–375. DOI: 10.1088/0004-637X/706/1/348. arXiv: 0907.3786 [astro-ph.GA].

Zamaninasab, M. et al. (Jan. 2010). "Near infrared flares of Sagittarius A*. Importance of near infrared polarimetry". In: *Astronomy & Astrophysics* 510, A3, A3. DOI: 10.1051/0004-6361/200912473. arXiv: 0911.4659 [astro-ph.GA].

Zernike, F. (Aug. 1938). "The concept of degree of coherence and its application to optical problems". In: *Physica* 5.8, pp. 785–795. DOI: 10.1016/S0031-8914(38)80203-2.

Zhang, Fupeng and Iorio, Lorenzo (Jan. 2017). "On the Newtonian and Spin-induced Perturbations Felt by the Stars Orbiting around the Massive Black Hole in the Galactic Center". In: *ApJ* 834.2, 198, p. 198. DOI: 10.3847/1538-4357/834/2/198. arXiv: 1610.09781 [astro-ph.GA].

Zhao, Jun-Hui, Bower, G. C., and Goss, W. M. (Jan. 2001). "Radio Variability of Sagittarius A*-a 106 Day Cycle". In: *The Astrophysical Journal Letters* 547.1, pp. L29–L32. DOI: 10.1086/318877. arXiv: astro-ph/0011169 [astro-ph].

Zhao, Jun-Hui et al. (Mar. 2003). "Variability of Sagittarius A*: Flares at 1 Millimeter". In: *The Astrophysical Journal Letters* 586.1, pp. L29–L32. DOI: 10.1086/374581. arXiv: astro-ph/0302062 [astro-ph].

Ziad, Aziz (July 2016). "Review of the outer scale of the atmospheric turbulence". In: *Adaptive Optics Systems V*. Ed. by Enrico Marchetti, Laird M. Close, and Jean-Pierre Véran. Vol. 9909. Society of Photo-Optical Instrumentation Engineers (SPIE) Conference Series, 99091K, 99091K. DOI: 10.1117/12.2231375.

Zucker, Shay, Alexander, Tal, Gillessen, Stefan, Eisenhauer, Frank, and Genzel, Reinhard (Mar. 2006). "Probing Post-Newtonian Physics near the Galactic Black Hole with Stellar Redshift Measurements". In: *The Astrophysical Journal Letters* 639.1, pp. L21–L24. DOI: 10.1086/501436. arXiv: astro-ph/0509105 [astro-ph].

van Cittert, P. H. (Jan. 1934). "Die Wahrscheinliche Schwingungsverteilung in Einer von Einer Lichtquelle Direkt Oder Mittels Einer Linse Beleuchteten Ebene". In: *Physica* 1.1, pp. 201–210. DOI: 10.1016/S0031-8914(34)90026-4.

von Fellenberg, S. D. et al. (Jan. 2023). "General relativistic effects and the near-infrared and X-ray variability of Sgr A* I". In: *Astronomy & Astrophysics* 669, L17, p. L17. DOI: 10.1051/0004-6361/202245575. arXiv: 2301.02558 [astro-ph.HE].

von Fellenberg, Sebastiano D. et al. (June 2022). "The Young Stars in the Galactic Center". In: *The Astrophysical Journal Letters* 932.1, L6, p. L6. DOI: 10.3847/2041-8213/ac68ef. arXiv: 2205.07595 [astro-ph.GA].

von Fellenberg, Sebastiano D. et al. (Jan. 2025). "First Mid-infrared Detection and Modeling of a Flare from Sgr A*". In: *The Astrophysical Journal Letters* 979.1, L20, p. L20. DOI: 10.3847/2041-8213/ada3d2. arXiv: 2501.07415 [astro-ph.HE].

Acknowledgements

First and foremost, I want to thank my family, my parents, Dorothea and Mick, my siblings, Emilia and Fritz, and my Oma. Thank you for believing in me from the moment I mentioned I wanted to become a physicist. Thank you for your infinite support, being there for me, and going through thick and thin together. Ich habe euch unendlich lieb. Further, I want to thank Reinhard Genzel, Frank Eisenhauer, and Stefan Gillessen for supervising my PhD and for your challenging questions, fruitful discussions, and scientific support. I've truly learned a lot. I especially want to thank Frank for sending me around the world and giving me the opportunity to present our fantastic results to the community and work on the most fascinating instrument, your open door and ears, and for your trust. Many thanks to the Gravity Collaboration and infrared group, particularly the infrarats. Thank you for your support. I love our many emotional, serious, and incredibly funny moments. Thank you to Guillaume for your open ears, friendship, guidance, and chocolate, and Felix for your support and patience in answering my questions for the hundredth time. I thank Sebastiano, Shangguan, and Taro for always taking the time to discuss GRAVITY and the Galactic Center. Thank you to Matteo for your friendship and our breakfast tradition, and to Matteo and Simran for your very helpful thesis feedback. Thank you to Diogo for all the CMZ and laughter, to Felix for being a great office mate, to Daryl for going through the final PhD steps together, and to Federico for our Japan experience, espresso breaks, and all the fun. So many people have supported me over the last years, and I am deeply thankful for this. Thank you to Lena, Anki, Sarah, Julia, Lotte, Dani, Caro, Simran, Margo, Kateryna, and Alice for being you and for believing in me. You are strong and amazing. Thank you, Lena, for all the laughter and tears we shared. Thank you to my Gießen and Austrian family for your welcoming heart and teaching me the gumo and boadwisch languages. Thank you to Arthur for being part of my family and for your amazing questions about connecting astrophysics and movies. I also thank the boulderers. Our climbing Tuesdays with dinner and beers have been an anchor over the last years. Thank you to Fulvio for your friendship and being a great thesis submission and defense buddy. And I want to thank the sacrificers deeply. Thank you, Soumya, Jed, and Bob, for your strength, love, creativity, and encouragement. It's hard to describe how grateful I am that you are in my life. Thank you, Soumya, for the light you brought to dark moments. And lastly, from the bottom of my heart, I want to express my deepest thank you to Luki. You are wonderful. Thank you for your love, unconditional support, and truly knowing me. You are a source of strength and inspiration, and I feel so lucky to have you in my life.